Ultracold Atoms, Circular Waveguides, and Cavity QED with Millimeter-scale Electromagnetic Traps

by

Kevin Lawrence Moore

B.S. (Harvey Mudd College) 1999
M.A. (University of California, Berkeley) 2005

A dissertation submitted in partial satisfaction of the
requirements for the degree of
Doctor of Philosophy

in

Physics

in the

GRADUATE DIVISION
of the
UNIVERSITY OF CALIFORNIA, BERKELEY

Committee in charge:
Professor Dan M. Stamper-Kurn, Chair
Professor Dmitry Budker
Professor Brigitta Whaley

Spring 2007

The dissertation of Kevin Lawrence Moore is approved:

Chair Date

Date

Date

University of California, Berkeley

Spring 2007

Ultracold Atoms, Circular Waveguides, and Cavity QED with Millimeter-scale Electromagnetic Traps

Kevin Lawrence Moore

Abstract

Ultracold Atoms, Circular Waveguides, and Cavity QED with Millimeter-scale Electromagnetic Traps

by

Kevin Lawrence Moore

Doctor of Philosophy in Physics

University of California, Berkeley

Professor Dan M. Stamper-Kurn, Chair

The construction of a laser cooling/trapping apparatus with a versatile mm-scale magnetic trap for ultracold atoms is described herein. The design, operation, and performance of this unique trap are presented. The manipulation of this magnetic trapping system facilitated the Bose-condensation of ^{87}Rb atoms in a variety of magnetic traps, most notably a millimeter radius circular magnetic trap for ultracold atoms. The dynamics of the quantum degenerate atom beam in this geometry are explored, as well as future applications with refinements of this system. A new probe of the phase space distribution of a generalized atomic beam is presented, and this probe was employed in the circular magnetic waveguide to characterize the quantum state of the system. Finally, this mm-scale magnetic trap was integrated with a mm-scale high-finesse optical cavity which accesses the strong coupling regime of cavity quantum electrodynamics (QED). Large ensembles of ultracold atoms were delivered to this cavity, and the first experimental results of this new dispersive regime of many-atom cavity QED are described.

Professor Dan M. Stamper-Kurn
Dissertation Committee Chair

To my father,

Maurice Joseph Moore

(1932 - 2007)

Contents

List of Figures

List of Tables

Acknowledgments

'Ndanka, ndanka' mo jappa golo. - Wolof proverb

'Slowly, slowly' catches the monkey. I'm quite certain that this phrase, frequently invoked during my time in Africa, did not have graduate school in mind when it was first uttered. Nevertheless, the counsel of patience and thoughtfulness could hardly have been better advice for six years of trying to build and operate the complicated apparatus that resulted in the work presented in this thesis. These are, unfortunately, not virtues to which I naturally tend, but perhaps on my best days I approached this ideal. Rather, these virtues (and many others) may certainly be applied to those who knew me during this time, and it is my great privilege in these opening pages to thank those who helped me along this path.

First and foremost, I am grateful beyond words to my advisor, Dan Stamper-Kurn, with whom my working relationship began 20,000 miles away in the wilds of West Africa before he was a professor and before I was Berkeley student. I contacted him in November of 2000 through the nascent technique of internet stalking, as I saw his name on the Berkeley Physics website as a professor who was looking for graduate students. Since we started working together in June 2001, my appraisal of his scientific acumen has morphed continuously and monotonically along the spectrum from "impressed by" to "in utter awe of." He's been an amazing advisor, a good friend, and I will miss our conversations a great deal.

This thesis would be a much thinner without the help of Kater Murch and Deep Gupta, the two of whom I cannot thank enough for all of the years of fun we had together down in the lab. I am not naturally a superstitious person, but some lucky turn of fate

brought these two incredible individuals into my graduate life at nearly the same time. Deep, who is probably the most pleasant person to work with on the planet, brought his immense good nature and some desperately needed maturity to the effort, as well as a much-needed Lebowski enthusiast to properly appreciate my oft-repeated quotes. Kater, who is a few years younger than I yet somehow vastly wiser, brought his incredible spirit and astounding variety of talents ("Oh, you play the cello and the guitar? Hmm, you can paint? Oh, you've renovated your entire house? Oh look, you're our best soccer player. What's that, you organically farm, too? Hey, how's that pre-iPod Apple stock doing for you?"). Of everything that's changing as I complete my time at Berkeley, seeing this team of three come to an end is the saddest. I look forward to their company in different contexts in the coming years, preferably in the daytime now that we don't have to pull the all-nighters together anymore.

Another individual to whom this work is largely indebted is Tom Purdy, who joined the millitrap effort at precisely the right time (i.e. when I was about to torch 75 LeConte in frustration). With his deft hands added to the project, we were finally able to put together a workable millitrap which became the workhorse of this these. Beyond his intelligence, skill, and affability, Tom also wins hands down for the most creative birthday cake I've ever seen in my entire life. Complete with an army of gummy bears storming the frosting hill in coordinated assault on the unsuspecting Peeps barracks, his "Comment on the Human Condition" cake is still making me laugh even as I write this many years later.

Mukund Vengalattore, affectionately referred to as "Butters," has been my officemate for the last year, and a better companion with whom to finish my doctoral work I truly cannot imagine. That said, I will give warning to any future co-workers that they should not be fooled by his calm demeanor and gentle spirit. This act belies his intense competitive and sporadically malevolent nature, as evidenced by his intentional crippling of my ankle because I was beating him at racquetball. You'll pay for that, Butters... one of these days, you'll pay.

And way back to the beginning, of course, there were three. James Higbie, Lorraine Sadler, and I were Dan's first graduate students, and a surely a motley crew we made back in 2001 before we knew what we were getting into. The sense of shared history with these

founding members is strong, and while our scientific experiences remained mostly parallel in space and time (except for my haphazard constructions which are probably still slowing down E1), they have been wonderful coworkers from Day 1 and I wish them very well as they respectively embark on their next adventures.

I would imagine it poor form to allow one's Acknowledgements to exceed the length of the thesis itself, so quite reluctantly I must issue a most sincere blanket thank you to everyone who's passed through the Stamper-Kurn fellowship these past six years. It was a privilege to play soccer, get coffee, eat birthday cakes, solve anagrams, and occasionally do some science with you all.

Similarly, as I am technically finishing 22nd grade, I have a laundry list of former teachers who deserve my unqualified thanks for their contributions to my intellectual development. While space ever constrains me, I would be woefully remiss if I did not recognize three individuals to whom I am especially grateful.

For the generally ungraceful years I endured junior high school, Joel Narva sparked my interest in a myriad of subjects ranging from logic to computer programming to feedback to prime numbers, and of course the subject of algebra which was his charge. Far more than just learning about math, his classes positively buzzed with enthusiasm about the subject matter and no opportunity was missed to bring in interesting tangents. I've yet to lose the excitement for such intellectual digressions, and outside of my immediate family no teacher is more responsible than Joel Narva for my since-discovered penchant to seek out my own tangents.

On into high school, where my lazy academic philosophy hit a very significant roadblock in Kevin Connell's English class. It was here that I first discovered what really makes the written word worth reading, and haven't viewed it the same since. All of a sudden Stephen King seemed like a hack and I found myself turning to the likes of Orwell, Hemingway, Vonnegut, and Heller to satisfy my newfound requirement that books boast not just a plot but artistry, depth, and humanity. That said, I still think The Scarlet Letter is horrible.

Halfway into my tenure at Harvey Mudd College, I had the great fortune of working closely with Tom Donnelly, then a brand new professor. In addition to teaching me quan-

tum mechanics, guiding my haphazard calculations on non-equilibrium electron systems, and shipping me off to face the fire at the 1999 American Physical Society meeting in Atlanta, Tom became one of my closest friends from the college years (and has remained so). Both then and now, I have been continually envious of his ability to lead a full life as an exceptional scientist, teacher, and human being.

As for my role models at Berkeley, one need look no further than the amazing cadre of individuals I've had the fortune of calling my friends in the last six years: Mike Grobis, who never missed an opportunity to organize and manage memorable events such as the physics holiday party, the physics softball team, or the daily insertion of his foot into his own mouth. In addition to being a great roommate, friend, and co-discoverer of the croc-o-duck, Ryan "Bonesaw" Lindberg has proven that the reports of the death of plasma physics have probably been somewhat exaggerated (maybe). Michael Boylan-Kolchin, as a savvy poker player, softball all-star, and cosmologist extraordinaire, has proven that Delaware actually has more to offer than that joke in Wayne's World. Nadir Jeevanjee, who I first encountered dancing in my living room in a hot orange dress, has proven to the world the astonishing fact that there is actually a career out there which pays less than graduate school. And, filed under the heading of "unparalleled patience," Jess Walter endured my flakiness as a friend *and* band member, yet was always ready for the next round of cheap sushi. At longer distances, I must briefly and profusely thank the Peace Corps crowd, Jeff Johannes, the Eugene crew, and my many second families amidst the Gherty clan. Finally, Liz Powell deserves more thanks than anyone for keeping me sane during the actual writing of this thesis. (I can assure the reader it was no small task.)

I remain further indebted to the following people, places, and/or things which all provided considerable aid and comfort to me during my time at Berkeley: the Cal Triathlon team, my former band Five Little Words/The Infidels/(all the other unmentionable names we embraced for brief periods of time), the Psi Stars, the Berkeley physics poker guys, The Daily Show/Colbert Report, my Cannondale R-1000, the SF music scene, the iPod, Rhapsody (which I've somehow been using for free for the last two years), The Big Lebowski, Kingpin Donuts, Cafe Strada, the 21st Amendment to the Constitution and its logical progeny, the Bud Light Fan Club.

I've been blessed with wonderful home fires burning in the Northwest, and a special note of thanks must go to my family, Dave, Amy, and little Wyatt. The most special note of gratitude and love must go to my mother, who has been the most wonderful support to me from the day I was born right up to the submission day when she checked the document for spelling, typographical, and grammatical errors[1].

Underneath the undeniably happy occasion of completing my Ph.D. is a deep sadness that my father, Maurice Joseph Moore, did not live to see me become the second Dr. Moore. I know how much he would have loved seeing this day come, and it is to him that I dedicate this work.

[1]Their was plennty.

Chapter 1

Introduction

During my tenure at Berkeley, there has been a palpable shift in the ultracold atom "community" to progress from studies *of* Bose-Einstein condensates (BECs) to studies *with* them. While much work continues in the understanding of more exotic systems such as spinor condensates [1, 2, 3, 4, 5], lower dimensional systems [6, 7, 8, 9], dipolar BECs [10, 11], and bosons in lattices [12, 13], *scalar* Bose condensates are now primarily thought of as "sources" of coherent beams of ultracold atoms. This shift is analogous to the history of the laser, where what began as an object of research and rapidly became a ubiquitous component in the experimental physicist's toolbox. Some of the prominent work which makes use of a BEC as a bright source of ultracold atoms include measurements of fundamental constants [14], studies of sympathetic cooling of fermions [15] (which itself resulted in a secondary BEC of molecules [16, 17] and high-T_c fermionic superfluidity [18]), and even magnetometery [19].

The work described in this thesis should be considered firmly in this context, as while the early chapters of this thesis are concerned with the design and construction of an apparatus to make BECs, the remaining four chapters are concerned with how we used and studied ultracold atoms after their humble origins as a BEC in a simple magnetic trap. The last two chapters especially represent this "second generation" thinking, as the first experiments with loading ultracold atomic ensembles into a strongly coupled cavity QED system are presented.

1.1 Exploring Frontiers with Ultracold Atoms

To begin, we examine the state of matter that describes Bose condensates[1]. A gas of N bosons at zero temperature forces all particles to occupy the same spatial wavefunction $\phi(\mathbf{r})$, under the Hamiltonian [20]

$$\mathcal{H} = \sum_{j=1}^{N} \left(-\frac{\hbar^2}{2m}\nabla_j^2 + U(\mathbf{r}_j) \right) + \mathcal{U}_o \sum_{j<k} \delta(\mathbf{r}_j - \mathbf{r}_k)\,, \tag{1.1}$$

where $U(\mathbf{r}_j)$ is the external potential and the point-like interaction strength is $\mathcal{U}_o$. We may also define the condensate wavefunction $\psi(\mathbf{r}) = \sqrt{N}\,\phi(\mathbf{r})$, and the energy of the system is then readily computed to be

$$E(\psi) = \int \left(\frac{\hbar^2}{2m}|\nabla\psi(\mathbf{r})|^2 + U(\mathbf{r})|\psi(\mathbf{r})|^2 + \frac{N\mathcal{U}_o}{2}|\psi(\mathbf{r})|^4 \right) d^3\mathbf{r}\,, \tag{1.2}$$

where we assume $N \gg 1$. This equation is written as a functional on ψ, the complex conjugate of which can be exploited as a variational parameter subject to the normalization constraint $\int \psi^*(\mathbf{r})\psi(\mathbf{r})\, d^3\mathbf{r} = N$. With the chemical potential μ serving as the Lagrange multiplier which enforces particle conservation, the quantity $E - \mu N$ is minimized at a fixed chemical potential and we arrive at the Gross-Pitaevskii equation [22, 23]:

$$\left(-\frac{\hbar^2}{2m}\nabla^2 + U(\mathbf{r}) + \mathcal{U}_o|\psi(\mathbf{r})|^2 - \mu \right) \psi(\mathbf{r}) = 0\,. \tag{1.3}$$

Extensions of this equation will be encountered in Chapter 5, but the crucial point is that the Bose-condensed system is a product of N identical wavefunctions $\psi(\mathbf{r})/\sqrt{N}$, with the form of $\psi(\mathbf{r})$ given by Equation (1.3) and the particular experimental parameters $U(\mathbf{r})$ (determined by the external trapping potential), $\mathcal{U}_o$ (determined by the atom/molecule of the system), and N (number of particles in the condensate). Regardless of the value of the particular experimental parameters, the solution to Equation (1.3) can be written, in complex polar form, as

$$\psi(\mathbf{r}) = \sqrt{n(\mathbf{r})}\, e^{i\vartheta(\mathbf{r})}\,, \tag{1.4}$$

where $n(\mathbf{r})$ is the density and $\vartheta(\mathbf{r})$ is the spatially varying phase. That a single phase function characterizes the system is the basis for considering a BEC as a coherent source.

[1] As the statistical mechanics of BECs has been explored extensively elsewhere [20, 21], we refer the reader to these references for theoretical justification of the statements and equations in this subsection.

In most instances, one seeks to maximize atom number to enhance the experimental signal[2]. This leaves just $\mathcal{U}_o$ and $U(\mathbf{r})$ as an experimentalist's tuning parameters. $\mathcal{U}_o$ is adjusted by either choosing a boson with the desired scattering properties [26] or cleverly adjusting the interactions between atoms/molecules with external fields [27]. This thesis is, to a degree, a story of the second approach as we employ various new containers $\mathcal{U}(\mathbf{r})$ to house a condensate of the most commonly used atom for BEC experiments, rubidium-87.

As is the case with the vast majority of experimental ultracold atom experiments, our rubidium BEC is *formed* in a harmonic trap:

$$U(x_1, x_2, x_3) = \frac{1}{2} m \left(\omega_1^2 x_1^2 + \omega_2^2 x_2^2 + \omega_3^2 x_3^2 \right). \tag{1.5}$$

As will be described in this thesis, the magnetic trap used for this work has an uncharacteristically wide tuning range for the trapping frequencies $\omega_1, \omega_2, \omega_3$, but the BEC is nonetheless ordinary in its beginnings. There are certainly more interesting containers than that of Equation (1.5), including optical lattice potentials [28], quasi-lower dimensional trapping [9], and even a box-like potential [29].

In this line of thinking, two "new" potentials will concern this thesis. The first is a circular waveguide, with an idealized potential of the form

$$U(z, \rho) = \frac{1}{2} m \omega_z^2 z^2 + \frac{1}{2} m \omega_\rho^2 (\rho - \rho_o)^2 , \tag{1.6}$$

expressed in (z, ρ, θ) cylindrical coordinates. This is harmonic about the waveguide center, but perfectly flat in the θ dimension. Quantum degenerate matter in this system must obey periodic boundary conditions, a consequence of Equation (1.6) representing a multiply connected geometry (as opposed to the simply connected geometry of Equation (1.5)).

The second "new" potential is perhaps more exotic than the first, with a form

$$U(z, \rho) = U_1 \, \phi_1(\rho) \, \sin^2 k_1 z + U_2 \, \phi_2(\rho) \, \sin^2 k_2 z \, , \tag{1.7}$$

also expressed in cylindrical coordinates. This is an equation for overlapping optical standing wave potentials, where $\phi_{1,2}(\rho)$ are the transverse mode functions, $k_{1,2}$ are the respective wavevectors, and $U_{1,2}$ are the optical potential depths (dependent on the light intensity, polarization, detuning from atomic resonance, etc.). There is nothing immediately exotic

[2] The work of Oberthaler *et al.* [24, 25] is a notable exception.

about this potential, as many studies of ultracold atoms in one-dimensional optical lattices were carried out over the last decade [30, 31]. The novelty of Equation (1.7) comes if one or both of the optical fields is sensitive to the quantized nature of the electromagnetic field. This comes about when the influence of a single photon is energetically relevant as compared to the other energy scales of the system. This is a case not found in free space, and manufacturing a system where the energy contribution per photon is relevant for an ultracold atomic system leads us to the following section.

1.2 Cavity Quantum Electrodynamics (CQED)

Some seventy years after Einstein's resurrection of the idea of corpuscular light, advances in lasers and non-linear optics allowed the exploration of correlation experiments with light [32] which definitively proved the existence of the photon, leaving "quantum optics" as the only viable theory of light. The detection of a single photon is usually[3] a destructive process whereby a photon is absorbed by some material and detected either through heat or electric current generation. While the creation and destruction of photons is integral to the theory of quantum electrodynamics, it remains dissonant with the more familiar quantum mechanical notion of unitary evolution of a system under a Hamiltonian.

At its core, cavity QED is the attempt to make the influence of single photons felt *coherently*, in that a quantum system undergoes unitary evolution due to the action of the quantized electromagnetic field. Typically this quantum system is an atom, though recent CQED experiments have utilized other quantum systems such as quantum dots [34] and superconducting circuits [35, 36]. As the quantum system is presumably sensitive to the electric field, e.g. through a Hamiltonian such as $\mathcal{H} = -e\hat{\mathbf{r}}\cdot\mathbf{E}$, the difficulty in realizing this goal is mainly one of scale. In free space the electric field of a monochromatic single photon is infinitesimally small, and cavity QED seeks a regime where the interaction between a photon and a quantum system is at least a significant, if not the dominant, part of the Hamiltonian evolution.

Interestingly, the idealized case of cavity QED is encountered immediately when the

[3] To date, only cavity QED has demonstrated the completely non-destructive detection of a photon [33]. High-energy photons may be detected without full absorption (e.g. Compton scattering), but the original photon is "destroyed" in lieu of another photon of lower energy.

quantization of electromagnetic field is considered theoretically, a brief treatment of which will be presented in Chapter 6. It is from this point that we begin to develop the theoretical framework necessary to motivate the use of ultracold atoms to explore novel many-atom cavity QED regimes.

1.2.1 Experimental CQED, ca. 2001

Reaching the strongly coupled CQED regime may be achieved by working with a dipole transition with large dipole moment d, utilizing a cavity of small mode volume V, or both. Pioneering work in the Haroche group [37] made use of superconducting cavities and large dipole Rydberg atomic states with microwave transition frequencies. Optical cavity QED involves the use cavities with very small mode volume; the fundamental work in this implementation has been led by Kimble *et al.* [38, 39, 40, 41, 42, 43], but numerous other groups have made important contributions in the last six years [44, 45, 46, 47, 48, 49, 50].

The mm-scale[4] optical cavities which have proven useful in this cavity QED incarnation had, at the time that the work presented in this thesis began, only been used with atoms delivered ballistically from laser-cooled thermal sources [38, 51]. Efforts to trap atoms inside a cavity was nearly operational [41], and other groups [49] were working on the delivery of atomic samples to optical cavities with far off-resonance optical traps (FORTs).

It is in this context that our experimental endeavor began in early 2002. In an attempt to make use of the established techniques of laser cooling, magnetic trapping, and evaporative cooling of atomic ensembles, we sought to use a magnetically trapped, ultracold gas as a reservoir of quantum objects for optical cavity QED. The central goal was the repeatable delivery of cold atoms to a strongly coupled cavity, allowing access to many unexplored regimes of cavity QED. The reliable delivery of many atoms, perhaps even precisely determined numbers of atoms, to a cavity could eliminate the stochastic nature of the current generation of cavity experiments. Single atom CQED could potentially be restored by a controlled promotion from weakly coupled states[5], allowing *multiple* CQED

[4]The millimeter-scale is in reference to the size of the optical element used to make the cavity, i.e. the outer diameter of the mirror substrate is $\sim 3\,\mathrm{mm}$. The optical *mode* has a scale better represented by 10's of μm, as this is the typical size scale of the cavity mode waist and length.

[5]The decoupling of the ensemble may be accomplished either by physical placement of the atoms in very

experimental cycles for each atom cooling cycle. Finally, with its single atom sensitivity, the cavity could be used as a new probe of many-body physics.

1.3 "E2" - A History

Upon my arrival at Berkeley in June 2001, James Higbie and Lorraine Sadler were already hard at work on the construction of the basic hardware for a Rubidium-87 BEC machine. While still a little disoriented after completing two years in West Africa with the Peace Corps (and somewhat inconvenienced by a persistent case of giardiasis), I began my work in the nascent Stamper-Kurn group on this first experimental effort. By luck of the draw, I got to tackle the implementation of the homemade external cavity diode laser (ECDL) systems used for rubidium laser cooling. My youthful dabblings left many dead diodes, PZTs, and circuit boards in my wake, but thankfully I stayed below the maximum allowable screw-ups to remain in the group. As 2001 gave way to 2002, Keshav Dani and I began the process of designing the second experiment (E2, as it came to be known). As we sketched out the design for the required magnetic trapping system (outlined in Chapter 3), we acknowledged that the millimeter scale magnetic trap was a substantial technical challenge requiring a few extra months work beyond that required to assemble a more standard design. While there were many scheduling underestimates and deadlines missed in my graduate career, none were as significant as the underbid time to construct what came to be known as the "millitrap." Throughout the many dark days of trial and error, I was blessed with an outstanding cadre of individuals who shared my agony on the millitrap project. Keshav and I worked through the summer and into the fall of 2002, a time when it dawned on all of us just how difficult this project was going to be. Into 2003, we were lucky enough to steal theorist Ken Brown away from the Whaley group for a few months, with the upshot that, together, he and I were finally able to put the first viable version of the millitrap into the chamber and achieve ultra-high vacuum conditions (UHV). I owe Ken Brown a special debt of gratitude, as not only was he a fantastic lab mate and natural physicist, but his ear for indie music and willingness to bring in mix CDs

weakly coupled parts of the cavity or outside the mode entirely. Utilizing internal states which are weakly coupled to the cavity is also possible, although the collective action of large ensembles can still significantly affect the cavity resonances even in the far-detuned limit.

packed with Pavement, The Pixies, and Guided By Voices opened up to me to the world of pretentious music criticism/snobbery, a religion to which I have since converted with a fundamentalist's zeal.

In 2003, E2 was very lucky to sign a first round rookie draft pick in Tom Purdy, who proved himself the consummate experimental physicist in every way. He suffered the musical dominance that Ken and I cast over 75 LeConte without complaint and, when Ken left for a post-doc at MIT, Tom signed on as the fourth (and thankfully last) grad student thrown at the millitrap project. With his eye for detail and impressive mechanical aptitude, we finally turned the tide on the project and, with the help of the pros in the Physics Machine Shop (most notably Dave Murai and the very missed Armando Baeza), we put together the second generation millitrap which now resides in the main science chamber of B167 Birge.

And, of course, while the operation the millitrap was a critical part of the experiment, parallel to this effort was the required assembly of an entire lab full of optics, electronics, computer control, and vacuum equipment. In the summer of 2003, E2 was again blessed with two incredible personnel additions. Kater Murch, renaissance man extraordinaire, arrived and immediately began proving his immense worth by assembling the power supply interlock system at a staggering clip. With this in place we were able to observe the lab's first collection of cold atoms in a magneto-optical trap (fed by a rubidium dispenser). As summer waned, the long-awaited arrival of E2's post-doc – Dr. Subhadeep Gupta – finally came to pass. With his "Deep"[6] expertise, the next few months involved an attempt to magnetically trap and transfer a significant population of cold atoms into the 1^{st} generation millitrap region. After much investigation and many depleted rubidium dispensers, we came to the conclusion at the end of 2003 that the current implementation of the system (a getter-loaded MOT[7] and vertical magnetic transfer from the paired quadrupole traps) was simply inadequate to deliver large populations of atoms to the millitrap. As the second generation millitrap was complete and ready for installation, we decided to take the opportunity for a major overhaul of the entire system. The rubidium dispenser was

[6] He also Deep-ly loves puns.

[7] Our work with the rubidium dispensers was not completely fruitless, as it resulted in the group's first experimental publication (KLM *et al.*, RSI **76**, 023106 (2005)) and is included in Appendix E.

eliminated in favor of an oven/Zeeman-slower system, the magnetic transfer coils were redesigned to provide tighter and more versatile trapping, we invested in more laser power via a home-built tapered amplifier system and, most critically, we changed the orientation of the entire vacuum system from a vertical transfer to the millitrap to a horizontal transfer. This proved a very fateful decision as, besides the factor of two improvement in field gradient, it inadvertently made possible the ultracold atom storage ring work presented in Chapters 4 and 5. This change was did have the downside of reducing the versatility of the CQED work in Chapter 6 and 7 due to the preclusion of long time-of-flight imaging out of the cavity, but on the whole the overhaul was a huge win for the experiment.

In the blindingly fast winter of 2003, E2 became nearly unrecognizable compared to its first incarnation. By the end of summer the atom number in the reworked MOT exceeded a few billion atoms and the new millitrap was installed and had passed all heat/field tests with flying colors. While we had lost Tom to E3 (the planned atom chip-based replacement for E2), the final roster of Kater, Deep and I plowed ahead into the fall. On October 28th, 2004, the millitrap captured its first collection of cold atoms in a spherical quadrupole trap, and within a month we had achieved a Bose-Einstein condensate of over a million atoms in an Ioffe-Pritchard trap. Just a few short weeks later, Kater and I (somewhat academically) lowered the current in the gradient bars and made the astonishing discovery that the atoms not only remain trapped but that they filled in a circular-looking shape. We quickly realized what the source of this circular trapping was (presented in Chapter 4), and in short order worked how this "quadrupolar ring" trap could be modified to produce a Bose condensate in the circular geometry. The subsequent nine months were unbelievably productive, with the millitrap proving well worth the trouble by resulting in four publications [52, 53, 54, 55] in the course of $1\frac{1}{2}$ years.

The design for the cavity system necessarily had occurred in parallel with the millitrap, predating Deep Gupta's arrival in the group. Working within the constraints of the mechanical pieces that I designed and that Dave Murai had constructed, Deep had assembled and tested the cavity in parallel to all of the the millitrap/ring work[8]. By fall of 2005, it was time to finally make E2 whole with the integration of the high-finesse optical

[8]Indeed, Deep's influence is felt throughout this thesis, but nowhere more so than in Chapter 6 where the experimental elements of the cavity system are discussed.

cavity system. In September, we officially closed the book on the ring trap and cracked the vacuum chamber to add the cavity (described in Chapter 6). By January 2006, the cavity system was functional and we were poised to finally realize the experimental goals laid out four years prior. We found reconfiguring the millitrap to make a time-orbiting potential (TOP) trap was the best method for this application. By May we were reliably transferring Bose-condensates of $40,000+$ atoms into the heart of the high-finesse optical cavity. With these early explorations we found even more uncharted territory when we discovered the efficient transfer of the magnetically trapped atoms to optically trapped atoms (bound by the red-detuned potential from the 850 nm cavity locking light). This was well into the wilderness of a completely new physical system, with tens of thousands of $\sim 1\,\mu$K atoms interacting with a strongly coupled cavity QED system. As discussed in Chapter 6, the atomic cooperativity[9] was over two orders of magnitude larger than any other reported system [49, 56]. The subsequent six months involved many all-nighters and Kingpin runs ("But the cavity is quieter at night!") in an attempt to get a handle on the system. As my graduate career draws to a close, E2's history is still very much being written, but with two papers on the verge of submission and two bulky chapters at the end of this thesis, the future looks as bright as it can when you're dealing with fluxes of only 10^4 photons/sec.

1.4 Outline

The structure of this thesis closely mirrors the chronology of my graduate work. I have been fortunate enough to have the opportunity to encounter a variety of physical systems in my graduate career, and the relative diversity amongst the chapters is reflective of this. The construction and operation of the hybrid BEC-CQED apparatus will be presented in chapter 2. The operation, performance, and capabilities of the most unique technical part of this apparatus, the "millitrap," will be presented in chapter 3. In chapter 4, the use of this device to form a circular magnetic waveguide for ultracold atoms will be discussed, as well as future prospects for utilizing this technique for Sagnac atom interferometry and Bose condensation of ultracold atoms in a fully circularized magnetic trap. A close

[9] The atomic cooperativity is a measure of the coherent evolution of the many-atom cavity system.

experimental and theoretical consideration of the state of the propagating atom laser in the circular waveguide is discussed in chapter 5, including a new technique for diagnosing atom beams which is not restricted to our particular experiment. In chapter 6, the theoretical basis for CQED with many atoms is outlined, and the relevant experimental elements necessary to access this system are detailed. Finally, in Chapter 7 the first experimental results from the BEC-CQED apparatus will be presented, with a look toward the future of many-atom cavity QED in the system described herein. Crucial design drawings, as well as the relevant publications for this work are included in the Appendices.

Chapter 2

Ultracold Atom Production

This chapter describes the critical elements and functionality of the laser cooling apparatus which produces and delivers cold atomic ensembles to the mm-scale magnetic trap which is described in the next chapter. As ultracold atom experiments have proliferated over the last decade, much of the basic infrastructure has become very established technology. The aim of this section is to lay out the specific design considerations and peculiarities of our apparatus with the theoretical background behind each subsystem referenced to the giants upon whose shoulders we stood when constructing the apparatus.

Ultracold atom production is built upon a number of integrated primary physical elements. Crucial systems found in these experiments include:

Ultra-high vacuum (UHV) chamber - This must be able to achieve pressures $\leq 10^{-10}$ torr and accommodate all necessary experimental elements (e.g. atomic sources, optical access, electronic control).

Bright atom source - This must provide a sufficiently high-flux source of atoms to be laser-cooled.

Frequency-locked laser system - These lasers must have sufficient coherence (linewidth $\leq$ MHz), tunability, and power to laser-cool a large atom population. Also included in this system are the various optics and optical control elements necessary to cool, address, and image a cloud of atoms.

Atom trapping - This can be either an optical trapping system or a magnetic trap-

ping system.

Electronic control - Because of the immense complexity and time-ordered sequencing of ultracold atomic experiments, substantial electronic infrastructure is required to operate the myriad control elements, e.g. beam shutters, acousto-optic modulators (AOMs), power supplies, etc.[1]

Imaging system - This optical probe is the main diagnostic and data collection system, allowing interrogation of the atomic ensemble.

The description of these systems and their performance will occupy the bulk of this chapter. The underlying physics of manipulating atoms with external electromagnetic fields that makes this work possible is well described elsewhere [20, 57].

2.1 The UHV Chamber

That a floating cloud of gas $1/10,000$th the density of air can achieve nK temperatures while surrounded by a 300 K steel vacuum chamber is at least counterintuitive, if not magical. The reason this is possible is the extremely low pressures achievable with modern vacuum technology, providing the requisite insulation from heating or loss due to collisions between the ultracold gas and 300 K background molecules. Reaching the UHV regime of pressure ($\lesssim 10^{-9}$ torr) is an absolute requirement for ultracold atomic physics experiments, and $< 10^{-10}$ torr is usually needed for most experiments.

The vacuum chamber in which this work was carried out accommodates a "loading region" where the cold atoms would be collected in a magneto-optical trap (MOT) and the "millitrap/cavity region" to which the atom population would be subsequently transported. As the optical beams which form the MOT are roughly 1" in diameter, this set a separation scale between these regions on the order of a few inches. The rationale behind the decision to incorporate both regions in the same steel chamber is one of simplicity, where only two magnetic trapping coils (described later in this chapter) are required to effect the displacement from loading to the science region.

The main pumping elements are a 110 L/s ion pump (Thermionics TP-110) and two

[1] This is included for completeness, but as the computer control system used for this work was designed and programmed by Dan Stamper-Kurn while he was at MIT [21] and implemented on this experiment by Tom Purdy, it will not be outlined in this thesis.

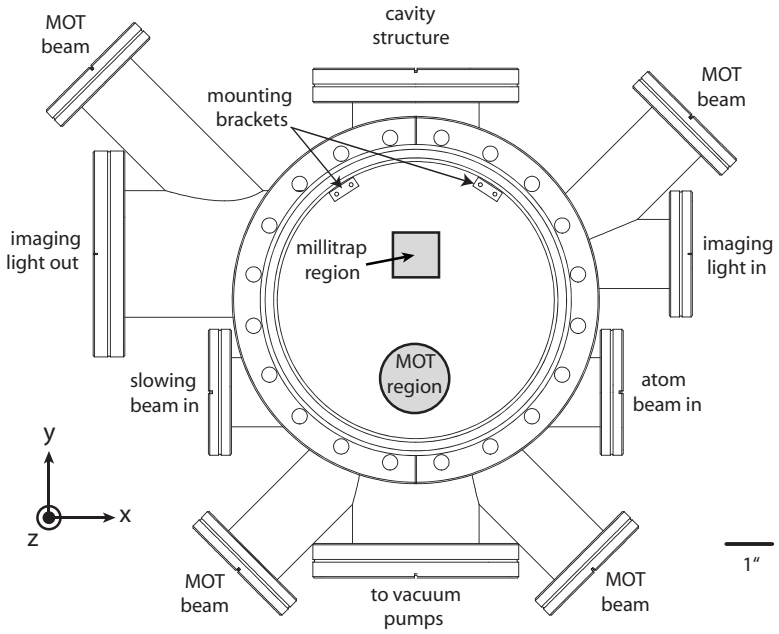

Figure 2.1: Sketch of the main chamber with the two focii of the system. The vacuum ports are labeled by primary function.

titanium sublimation (Ti:sub) pumps. The primary Ti:sub pump is surrounded by a "shroud" (Thermionics SS400/275) which is cooled by liquid nitrogen during experimental operation, increasing the pumping speed. The secondary Ti:sub pump is mounted on a retractable vacuum piece (Thermionics LMA-8) along the "slowing beam" arm of the main chamber. This allows the deposition of titanium on the interior of the main chamber and along the slower tube. With a standard bakeout [58], the system reached the final pressures shown in Table 2.1.

2.2 Optical System

In addition to the simple hydrogen-like atomic structure and collisional properties which make it a good atom for evaporative cooling [59, 60], the major selling point for using rubidium in laser-cooling experiments is the relative ease with which the necessary laser light is produced with external cavity diode laser (ECDL) systems [61]. By the time the work presented in the last two chapters of this thesis commenced, no less than six

Integrated	Final Pressure
millitrap only (Ch. 3-5), room temp	3×10^{-11} torr
millitrap only (Ch. 3-5), lN_2 flowing	2×10^{-11} torr
millitrap and cavity (Ch. 6), room temp	7×10^{-11} torr
millitrap and cavity (Ch. 6), lN_2 flowing	5×10^{-11} torr

Table 2.1: Final experimental pressures. The relatively higher pressure after the cavity installation (discussed in chapter 6) is likely due to extra outgassing from the some of the construction materials used in the mounting structure, e.g. Viton, Teflon, piezoelectric ceramics, and the cavity mirrors. These pressures were measured with an ion gauge that was relatively far from the main chamber and very close to the vacuum pumps. While the values are probably best considered lower bounds, the vacuum-limited lifetime of the atoms did roughly conform to these pressures.

distinct diode laser systems (three commercial, three home-built) were actively used in the experimental cycle. Four of these were used entirely for laser-cooling/imaging and will be discussed in this section; the remaining cavity-related light sources are introduced in chapter 6.

For a discussion of magnetic-optical traps, we refer the reader to the treatment in Ref. [57]. The three important elements for a sizable magneto-optical trap are a high flux of atoms capable of being captured by a MOT (discussed in Sections 2.3 and 2.4), a spherical quadrupole magnetic field (discussed in Section 2.5) and many 10's of mW/cm^2 of $F = 2$ laser light. The effective saturation intensity of the $F = 2 \rightarrow F' = 3$ cycling transition is $I_{sat} = 3.05\,\mathrm{mW/cm^2}$, and to confine a large population several times this value is desirable.

A schematic of the laser system with an accompanying diagram of the relevant atomic structure of rubidium-87 is presented in Figure 2.2. The $F = 2$ slowing laser and the $F = 1$ repump laser are commercial Toptica DL100 ECDL systems with a nominal output power of nominal 50 mW. The diode systems were purported to be self-contained "plug-and-play" units, though we developed several patches to optimize the performance of the lasers. Primarily, patching into the bypass of the electronic control unit was necessary after the Toptica PID controller (PID110) failed to achieve a robust lock. The patch was designed to access the piezoelectric transducer (PZT) which controls the orientation of the external

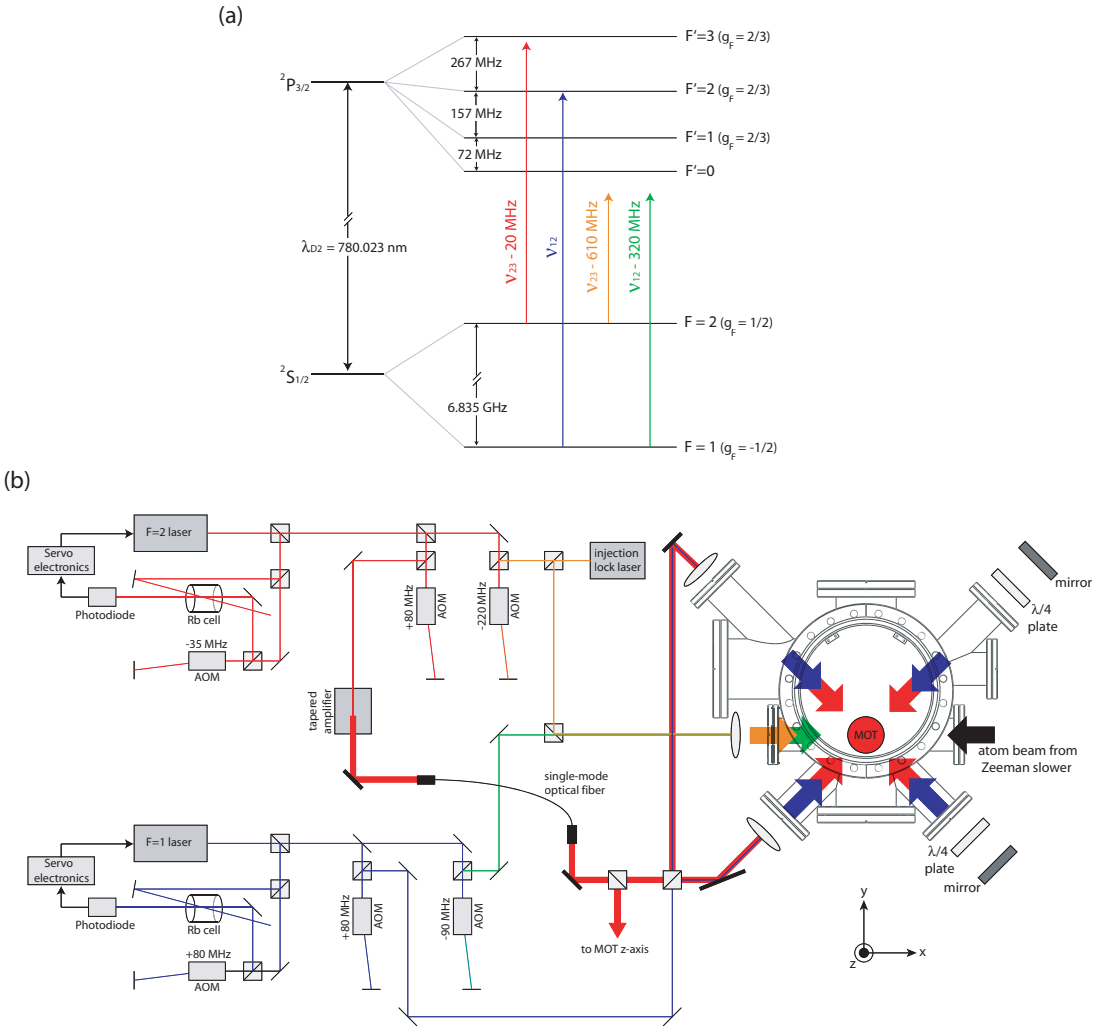

Figure 2.2: The laser-cooling system. (a) Shown are the ground and relevant excited hyperfine states of rubidium-87. (The closely-related D1 transitions – $|^2S_{1/2}\rangle \rightarrow |^2P_{1/2}\rangle$ at $\lambda_{D1} = 795\,\text{nm}$ – are omitted.) Associated with each state is the quantum number F (specified by the eigenvalue equation $(\mathbf{L}+\mathbf{S}+\mathbf{I})^2|F\rangle = F(F+1)\hbar^2|F\rangle$) and, in the limit of a Zeeman shift much less than the hyperfine energy splitting, the "g-factor" for each state (given by the equation $E_B = \mu_B g_F m_z B_z$). The laser frequencies used for the MOT and Zeeman slower are shown on this scale, with false color distinguishing each beam. The optical setup, depicted in (b), shows the crucial laser elements and frequency controls. The two ECDL systems (labeled $F = 2$ and $F = 1$, respectively) are frequency-locked to rubidium vapor cells. The $F = 2$ laser injection locks a 50 mW diode laser to provide the Zeeman slowing light, while the $\sim 200\,\text{mW}$ of MOT light comes from an injection-locked tapered amplifier system which is, in turn, coupled into a single-mode optical fiber. A sketch of the geometric layout of the three beam reflection MOT is shown, relative to the main chamber layout.

grating and thereby the optical feedback. With this control and the current modulation input on the front face of the current control module (DCC110) we were able to utilize home-built PI lockboxes to stabilize the laser frequency. The feedback signal is obtained by frequency modulating the probe beam in the saturation-absorption spectroscopy (SAS) of a rubidium vapor cell. The probe beam is focused onto a photodiode, the output current of which can be mixed down at the modulation frequency to obtain Doppler-free error signals of the hyperfine transitions and their SAS crossover peaks [62]. Activation of the PI lockbox's negative feedback stabilizes the laser frequency to the rubidium reference with a bandwidth of $\sim 1\,\mathrm{MHz}$.

To realize the full laser cooling capabilities of the apparatus, far more than 50 mW of $F = 2$ light is needed to operate a Zeeman slower (Section 2.4) and a MOT well past saturation. After downshifting the $F = 2$ laser frequency by $-610\,\mathrm{MHz}$, a standard master-slave injection lock is established between the locked $F = 2$ and a free-running laser diode, boosting the input slower intensity to 25 mW of laser power[2]. The slower laser beam diameter at the MOT region is $\sim 2.5\,\mathrm{cm}$, yielding a slower saturation parameter of $s = I/I_{sat} \geq 1.7$. The $\geq$ sign is relevant because the slower laser beam converges into the oven region, meaning that the saturation parameter will always exceed 1.7 over the slowing region.

To obtain a large saturation parameter for the MOT as well, an injection-locked tapered amplifier laser diode chip is utilized to boost $\sim 20\,\mathrm{mW}$ of input $F = 2$ laser power to $\sim 350\,\mathrm{mW}$. The mounting and control of the tapered amplifier chip follows that of Ref. [63], with minor design changes for electrical and mechanical isolation. The light produced by the tapered amplifier is then coupled into a single-mode optical fiber, yielding 200 mW of MOT light. As depicted in Figure 2.2, we employed a three-beam retroreflection MOT, which has the advantage of nearly doubling the power per beam. At $\sim 70\,\mathrm{mW}$ per 1 inch diameter laser beam, we obtain a saturation parameter of $s = 4.7$ and ultimately observed MOT populations of ~ 5 billion atoms (as measured by fluorescence [64]).

[2]The free-running laser is capable of 50 mW of output power, but half is lost to the 50-50 beamsplitter which combines the light with the slower repump beam. This intensity cost is required to maintain the proper polarization correlation between the two light fields.

2.3 The Oven

After determining rubidium dispensers to be inadequate for our full experimental requirements [65], we employed a recirculating rubidium oven [66] as the atomic source. The layout of this system is presented in Figure 2.3, which also display the Zeeman slower system that is described in the subsequent section.

The elbow containing the liquid rubidium and the recirculating nozzle have been described elsewhere [63, 66]. The remaining elements of the oven chamber are unique to this experiment however, and deserve mention here. The overarching goal in the construction of the oven chamber was to allow a shuttered atomic beam while minimizing the distance to the entrance of the slower. A custom 6-way cross designed with a minimal length along one axis was employed to accomplish this task. A TEC-cooled two-plate cold catcher was enclosed by the 6-way cross and traps the bulk of the oven-emitted rubidium which does not travel through to the differential pumping tube separating the oven chamber from the Zeeman slower/main chamber region. Between the two cold plates is an aluminum "flag" which acts as a mechanical shutter. The shutter position is controlled by a rotary vacuum feedthrough (Varian L6691-301), rotating the flag into and out of the ballistic path of the atomic beam.

The differential pumping tube is 2.75 inches long with an inner diameter of 5 mm, promising a conductance of 0.2 liters/sec. This allows the oven pressure to exceed 10^{-8} torr with no discernable affect on the main chamber pressure, and the pressure was in the 10^{-9} torr range during normal operation. With the gate valve as the only remaining element separating the oven aperture and the main chamber, the oven-to-slower distance is merely 7.6 inches. The full distance to the MOT center is 42.3 inches.

2.4 Zeeman Slower

The theory behind the functionality of a Zeeman slower is described elsewhere [67, 68, 63]. Briefly stated, an inhomogeneous $B(x)$ is shaped to maintain atomic resonance with a fixed laser slowing beam, despite the ever-reduced Doppler shift of the atoms as they propagate along the x-axis and are slowed from the oven exit velocities of $v \sim 300\,\mathrm{m/s}$ to

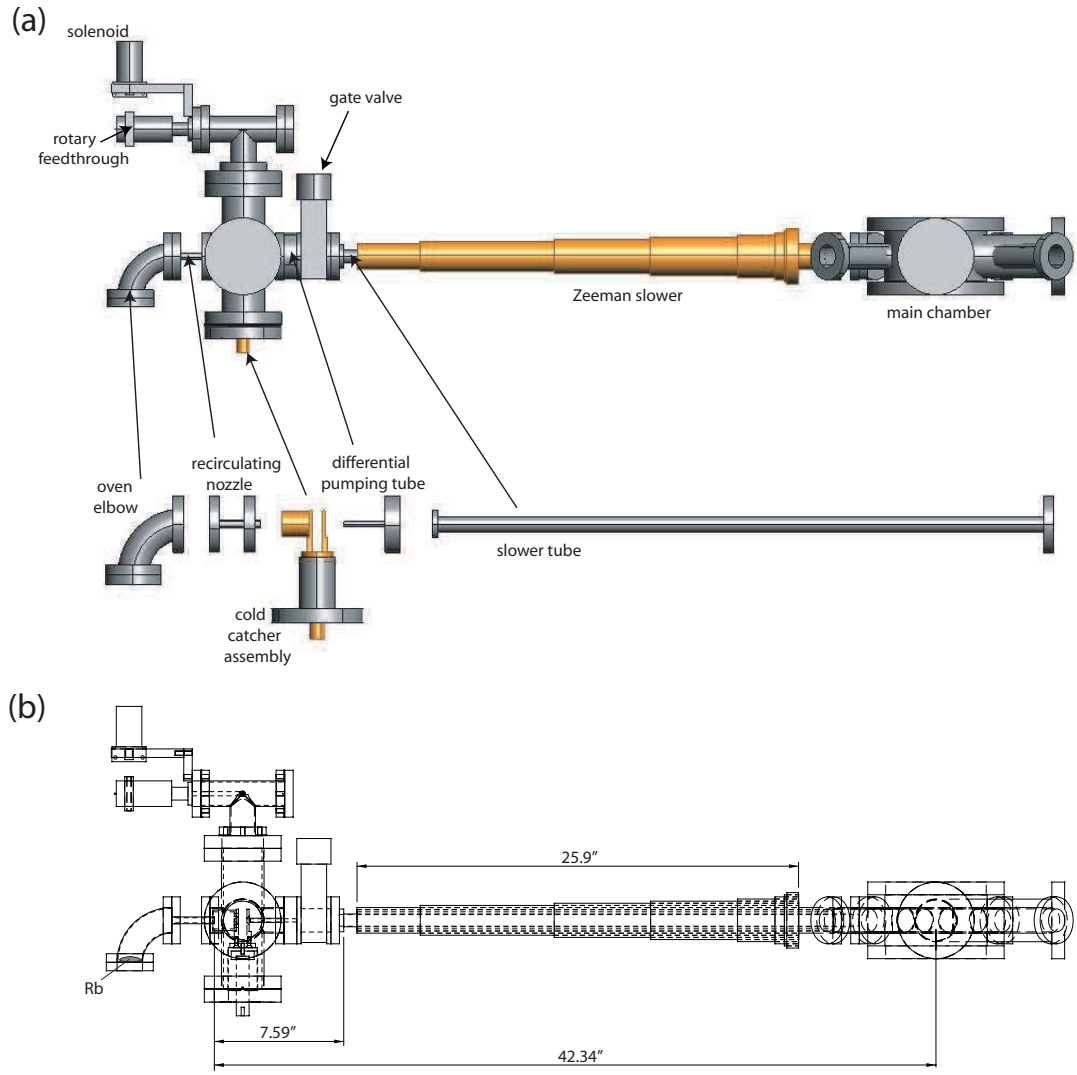

Figure 2.3: Diagram of the skeletal system of the atom delivery systems, the rubidium oven and the Zeeman slower. (a) This diagram shows the critical elements which determine the atomic beam which reaches the main chamber center, 42.3 in. from the oven nozzle opening. (b) Relevant dimensions are shown in this "x-ray" image of the system, including the free propagation distance from oven to Zeeman slower entrance (7.6 in.) and the full slower length (26 in.).

MOT-capturable velocities of $v \lesssim 30\,\mathrm{m/s}$. The maximum deceleration given by dissipative laser cooling is $a_{max} = \hbar k\gamma/2m = 1.15 \times 10^5\,\mathrm{m/s}$, also setting the minimum length $L_{min} = \bar{v}^2/2a_{max} = 0.39\,\mathrm{m}$ of the slower. Given the difficulty in precisely matching the field profile necessary to attain a_{max}, the length of the slower can be increased to yield a uniform deceleration of $a = fa_{max}$. The desired field profile is thus given by

$$B_{slower}(z) = B_v\sqrt{1 - x/L_{slower}} + B_o \tag{2.1}$$

where $B_v \equiv \hbar k\bar{v}/\Delta\mu$, $L_{slower} = L_{max}/f$, and B_o is an arbitrary bias field. The use of a bias field B_o necessitates an accompanied retuning of the slowing laser to $\delta_{slower} = \nu_{laser} - \nu_{eg} = -kv - \Delta\mu B_o$. The layout of the oven and Zeeman slower system is shown in Figure 2.3, and the relevant experimental parameters are summarized in Table 2.2.

Variable	Definition	Value
$\Delta\mu$	magnetic moment difference	$-\mu_B$
$\bar{v}$	avg. entrance atomic velocity	$\sim 300\,\mathrm{m/s}$
B_v	slower capture field	$290\,\mathrm{G}$
v_{cap}	capture velocity	$230\,\mathrm{m/s}$
B_o	bias field	$200\,\mathrm{Gauss}$
δ_{slower}	slower laser detuning	$-610\,\mathrm{MHz}$
f	slower parameter	0.6
a	slower deceleration	$fa_{max} = 6.9 \times 10^4\,\mathrm{m/s}$
L_{slower}	slower length	$L_{max}/f = 0.66\,\mathrm{m}$

Table 2.2: The Zeeman slower parameters for the rubidium $|F = 2, -2\rangle \rightarrow |F' = 3, -3\rangle$ transition. The value of $f = 0.6$ was chosen based on the more sophisticated treatment in Ref. [63].

2.5 Magnetic Trapping and Transfer

The physics of magnetic trapping can be seen directly in the Zeeman energy shifts of the $F = 1$ and $F = 2$ ground states in Figure 2.4. Three of the eight magnetic sublevels $-\{|F = 1, m_F = -1\rangle, |F = 2, m_F = +1\rangle, |F = 2, m_F = +2\rangle\}-$ experience a positive energy shift $\Delta E = g_F m_F \mu_B B$ for an applied field B. In a spatially-inhomogeneous magnetic field $\mathbf{B}(\mathbf{r})$, the force on an atom is given by $\mathbf{F}_B = -g_F m_F \mu_B \nabla|\mathbf{B}(\mathbf{r})|$ and the

aforementioned subset of states are dubbed "weak-field seekers" as the force experienced is along the negative gradient of $|\mathbf{B}(\mathbf{r})|$.

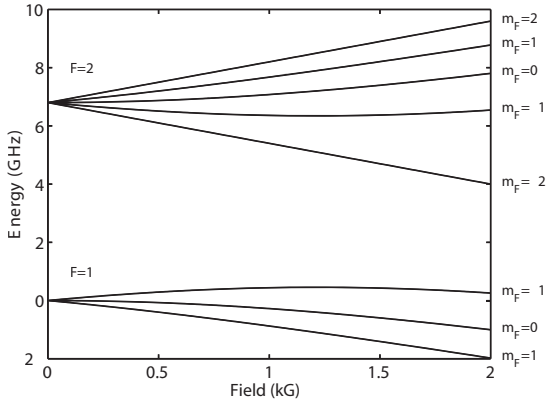

Figure 2.4: Rb-87 Zeeman splitting for hyperfine ground states

Maxwell's equations in free space require $\nabla \cdot \mathbf{B}(\mathbf{r}) = 0$ and $\nabla \times \mathbf{B}(\mathbf{r}) = 0$. If $\mathbf{B}(\mathbf{r})$ has a minimum at $\mathbf{r} = 0$, then Taylor expansion of the field is

$$\mathbf{B}(\mathbf{r}) = \mathbf{B}(\mathbf{r}=0) + [(\mathbf{r}\cdot\nabla)\mathbf{B}]_{\mathbf{r}=0} + \frac{1}{2}\left[(\mathbf{r}\cdot\nabla)^2\mathbf{B}\right]_{\mathbf{r}=0} + \mathcal{O}(r^3). \tag{2.2}$$

The magnetic trapping of atoms is achieved for weak-field seeking atoms orbiting about a magnetic field minimum. There is a class of magnetic field arrangements which are prevalent in atom trapping [20, 69], four of which were employed in this thesis. We begin with the simplest configuration, the spherical quadrupole trap, and will introduce the remaining trapping configurations in chapters 2 and 3 in the context of the millitrap.

2.5.1 Spherical Quadrupole Trap

Considering the specific case of Equation (2.2) where $\mathbf{B}(0) = 0$, the lowest order expansion of the field is given by

$$\mathbf{B}(\mathbf{r}) = [(\mathbf{r}\cdot\nabla)\mathbf{B}]_{\mathbf{r}=0} + \mathcal{O}(r^2). \tag{2.3}$$

This is a generalized quadrupole field, so named because two magnetic dipoles are required to obtain zero field at a specific location or, equivalently, because the field looks quadrupolar, i.e. $B(r,\theta) \propto 1/r^4$ for large r. A *spherical* quadrupole field is obtained in the case of

cylindrical symmetry, i.e. the coils which produce the field are co-axial. The lowest-order field profile is specified by a single gradient B':

$$\mathbf{B}(\mathbf{r}) = B'\,(x, y, -2z)\,. \tag{2.4}$$

This can be achieved by two identical coils of radius R, separated by distance $2d$, carrying current I_c in opposite directions. At the center of the coils, the field is that of Equation (2.4) with $B' = 6\mu_o I_c R^2/(d^2 + R^2)^{5/2}$.

A magneto-optical trap which collects and cools the initial gaseous sample requires just such a spherical quadrupole field and appropriate laser-cooling light [57, 70]. To trap the cold atomic sample for delivery to the millitrap/cavity region, the same coils which form the fields necessary for the MOT can be employed to form a spherical quadrupole trap. It is important to mention at this point that, first and foremost, a magnetic trap on Earth must support the atoms against gravity. Incorporating gravitational energy, the potential seen by a ^{87}Rb atom in a spherical quadrupole trap is given by

$$U = mgz + g_F m_F \mu_B B' \sqrt{x^2 + y^2 + 4z^2}, \tag{2.5}$$

where $g = 9.8\,\mathrm{m/s^2}$, the gravitational acceleration at the earth's surface. To trap against this force, a minimum gradient of $B'_{min} = mg/2g_F m_F \mu_B$ is required, and realizing a B' significantly larger than B'_{min} is desirable to prevent significant vertical asymmetry in the trap. For $|F = 1, m_F = -1\rangle$ ^{87}Rb atoms, $B'_{min} = 31\,\mathrm{G/cm}$.

2.5.2 Quadrupole Transfer System

Greiner *et al.* [71] developed an elegant method to transport atoms trapped in spherical quadrupole traps. To transfer the atoms from one location to another, the cylindrical symmetry of a single quadrupole trap is broken with the addition of a second quadrupole coil pair with its balanced trap center in the same $x-y$ plane as the first coil pair. Without loss of generality, the center of the second coil pair is placed at $(0, y_o, 0)$. Powering both coils with currents I_1 and I_2, respectively, leads to superposed spherical quadrupole fields. These coils can have distinct geometries, i.e. different radii $R_{1,2}$ and coil separations $2d_{1,2}$, leading to differing gradient/current ratios. If $y_o \leq R_1 + R_2$, then the field vanishes in only

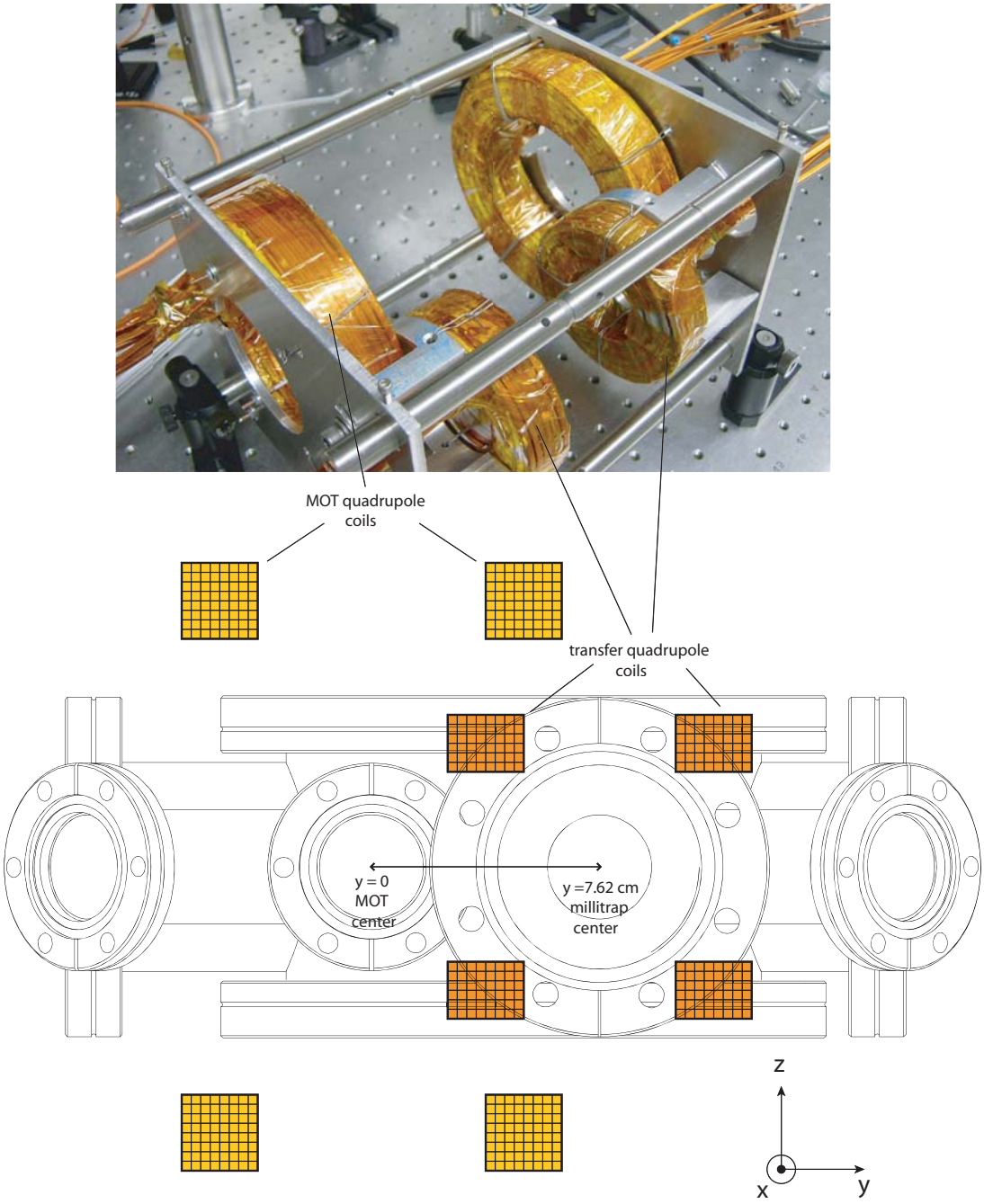

Figure 2.5: Magnetic quadrupole transfer system. A side view of the chamber is overlaid for perspective.

one location and, as the ratio of coil currents I_1/I_2 is varied from 0 to ∞, the location of this field zero is mapped from $y = 0$ to $y = y_o$.

This is precisely the process by which magnetically trapped atoms, loaded in the MOT region, are moved to the millitrap/cavity region. The size and shape of the two spherical quadrupole coil pairs are constrained by the physical dimensions of the vacuum chamber. The coil pairs were dubbed the "MOT quadrupole coils" and the "cavity quadrupole coils," respectively, with latter so named because they were coaxial with the high-finesse cavity that was ultimately installed in the chamber (described in chapter 6). A reentrant "bucket"[3] is utilized to minimize the coil separation of the transfer coils, but the MOT quadrupole coils are forced to a front-face separation of 6 inches. The relevant physical dimensions of the coils are presented in Table 2.3.

Coil Pair	y_o	**ID**	**OD**	d_{front}	d_{back}	**No. of turns**	B'/Amp
MOT coils	0	3 in.	5 in.	3 in.	4 in.	8×8	0.25 G/cm/A
Transfer coils	3 in.	2 in.	4 in.	1.5 in.	2.25 in.	8×6	0.55 G/cm/A

Table 2.3: Magnetic transfer coil parameters.

Despite the many turns of wire which make up the two coil pairs, the relatively low B'/Amp ratios requires large currents to exceed B'_{min}. Experimentally, hundreds of Amps are needed for optimal performance, necessitating large current power supplies and water-cooled wire (Kapton-insulated, square $\frac{1}{8}" \times \frac{1}{8}"$ hollow copper wire). A 300 psi high-pressure water pump (300 psi) flows water through the MOT and cavity coil assemblies, broken up into 2×8 turns to maintain sufficient water flow. The Joule heating generated during the $20 - 30$ seconds of magnetic trapping and transfer is sizeable, and Kater's interlock system would interrupt the supply current if either the water temperature or flow rate fell outside of their normal operational tolerances.

The gradient fields and trap positions are presented in Table 2.5.2, with the information organized in a matrix such that each cell gives the quadrupole field parameters for given coil currents.

[3]The "bucket" moniker is applied because the element consists of an 8" conflat flange welded to a recessed steel platform which extends 0.75" past the flange face into the chamber. See Appendix B for engineering drawings.

KEY	I_{CQ}
I_{MOT}	y_o (cm) dB/dy (G/cm) dB/dx (G/cm) -dB/dz (G/cm)

	0 **A**	40 **A**	80 **A**	120 **A**	160 **A**	200 **A**	240 **A**	280 **A**	320 **A**	360 **A**	400 **A**
		7.62	7.62	7.62	7.62	7.62	7.62	7.62	7.62	7.62	7.62
0		22.6	45.3	67.9	90.6	113.2	135.9	158.5	181.2	203.8	226.5
A		22.6	45.3	67.9	90.6	113.2	135.9	158.5	181.2	203.8	226.5
		45.3	90.6	135.9	181.2	226.5	271.8	317.1	362.4	407.7	453.0
	0.0	5.52	6.67	7.00	7.16	7.26	7.32	7.36	7.40	7.42	7.44
40	10.3	15.0	40.8	64.3	87.4	110.3	133.1	155.8	178.6	201.3	224.0
A	10.3	26.7	50.2	73.0	95.7	118.4	141.1	163.7	186.4	209.1	231.7
	20.6	41.8	90.7	137.3	183.1	228.7	274.1	319.6	365.0	410.3	455.7
	0.0	1.78	5.52	6.32	6.67	6.87	7.00	7.10	7.16	7.22	7.26
80	20.7	9.8	30.1	57.1	81.6	105.3	128.6	151.8	174.8	197.7	220.5
A	20.7	26.1	53.4	77.3	100.3	123.2	146.0	168.7	194.4	214.1	236.8
	41.1	36.0	83.5	134.4	181.9	228.5	274.6	320.5	366.2	411.8	457.3
	0.0	0.92	3.64	5.52	6.14	6.47	6.67	6.82	6.92	7.00	7.07
120	31.0	22.1	12.3	45.1	72.8	98.1	122.4	146.2	170.0	192.9	216.1
A	31.0	35.0	51.6	80.1	104.2	127.5	150.5	173.4	196.2	218.9	214.7
	62.1	57.1	63.9	125.3	177.0	225.6	272.9	319.6	365.8	411.9	457.8
	0.0	0.63	1.77	4.43	5.52	6.02	6.32	6.53	6.67	6.79	6.87
160	41.4	33.2	19.7	27.3	60.2	88.3	114.2	139.0	163.2	187.0	210.6
A	41.4	45.0	52.3	79.9	106.9	131.1	154.5	177.7	200.7	223.5	246.4
	82.7	78.2	71.9	107.2	167.0	219.4	268.7	316.7	363.9	410.6	457.0
	0.0	0.48	1.20	2.76	4.74	5.52	5.94	6.22	6.41	6.56	6.64
200	51.7	43.9	32.5	17.1	43.0	75.2	103.6	130.0	155.3	179.9	204.0
A	51.7	55.1	60.5	75.0	107.2	133.6	157.9	181.5	204.8	227.9	250.8
	103.5	99.0	93.0	92.1	150.2	208.8	261.5	311.5	360.0	407.7	454.8
	0.0	0.39	0.92	1.77	3.64	4.92	5.52	5.88	6.14	6.32	6.47
240	62.1	54.5	44.2	29.5	24.6	58.5	90.3	118.9	145.6	171.3	196.2
A	62.1	65.4	70.0	78.4	103.3	134.3	160.3	184.7	208.4	231.8	255.0
	124.2	119.9	114.3	107.9	127.9	192.7	250.6	303.6	354.0	403.0	451.2
	0.0	0.33	0.75	1.34	2.42	4.14	5.03	5.52	5.84	6.07	6.24
280	72.4	65.0	55.5	42.6	26.0	39.0	73.8	105.3	135.1	161.1	187.1
A	72.4	75.6	79.9	86.3	99.9	131.8	161.2	187.0	211.5	235.3	258.8
	144.9	140.7	135.4	128.9	125.9	170.8	235.0	292.3	345.5	396.4	445.9
	0.0	0.28	0.63	1.09	1.78	3.09	4.43	5.10	5.52	5.81	6.02
320	82.8	75.5	66.4	54.8	39.3	27.3	54.6	89.7	120.3	149.2	176.5
A	82.8	85.9	89.9	95.4	104.6	126.1	159.7	188.0	213.7	238.3	262.2
	165.6	161.4	156.3	150.2	143.9	153.4	214.3	277.1	334.1	387.5	438.7

Table 2.4: The table of positions and field gradients for the magnetic transfer system. The cylindrical symmetry is of course broken with two quadrupole coil pairs, so with both sets running current the three cartesian gradients are unequal about the field zero. Three typical experimental configurations (the latter two of which are explained in chapter 3) are the following:

MOT loading : $I_{MOT} = 75\,\mathrm{A}$, $I_{CQ} = 0$, $y = 0$, $B' = 18.1\,\mathrm{G/cm}$

Quadrupole evaporation : $I_{MOT} = 200\,\mathrm{A}$, $I_{CQ} = 240\,\mathrm{A}$, $y = 5.94\,\mathrm{cm}$,
$\nabla|\mathbf{B}| = (104\,\mathrm{G/cm},\ 158\,\mathrm{G/cm},\ -262\,\mathrm{G/cm})$

Millitrap handoff : $I_{MOT} = 0$, $I_{CQ} = 240\,\mathrm{A}$, $y = 7.62\,\mathrm{cm}$, $B' = 136\,\mathrm{G/cm}$

2.6 Imaging

With the atoms being formed in the loading region and then transported to the millitrap/cavity region, diagnostic imaging is possible at several chamber locations. Table 2.5

summarizes the physical apertures constraining the imaging system, though typically the image quality is experimentally limited by the optics and CCD camera pixelation (Roper Scientific Photometrics CoolSNAP ES, 6.5 μm×6.5 μm pixel size).

Imaging location	**NA**
MOT region (top)	0.16
Outside millitrap (side)	0.19
Inside millitrap (top)	0.16
Inside millitrap (top, 40 ms TOF)	0.11
Inside millitrap (side)	0.10
Inside cavity (side)	0.10

Table 2.5: Limiting numerical apertures for the imaging system.

2.7 The Full Cooling Apparatus

With all of the elements presented in the preceding sections, the full system is depicted in Figure A. The figure also shows the integration of two elements, namely the millitrap electrical feedthrough port and the liquid nitrogen feedthrough, both of which will be described in the next chapter. Finally, a recent picture of the experiment (shown in Figure 2.7) obscures the elements discussed in this chapter, but shows the substantial infrastructure in which the system resides.

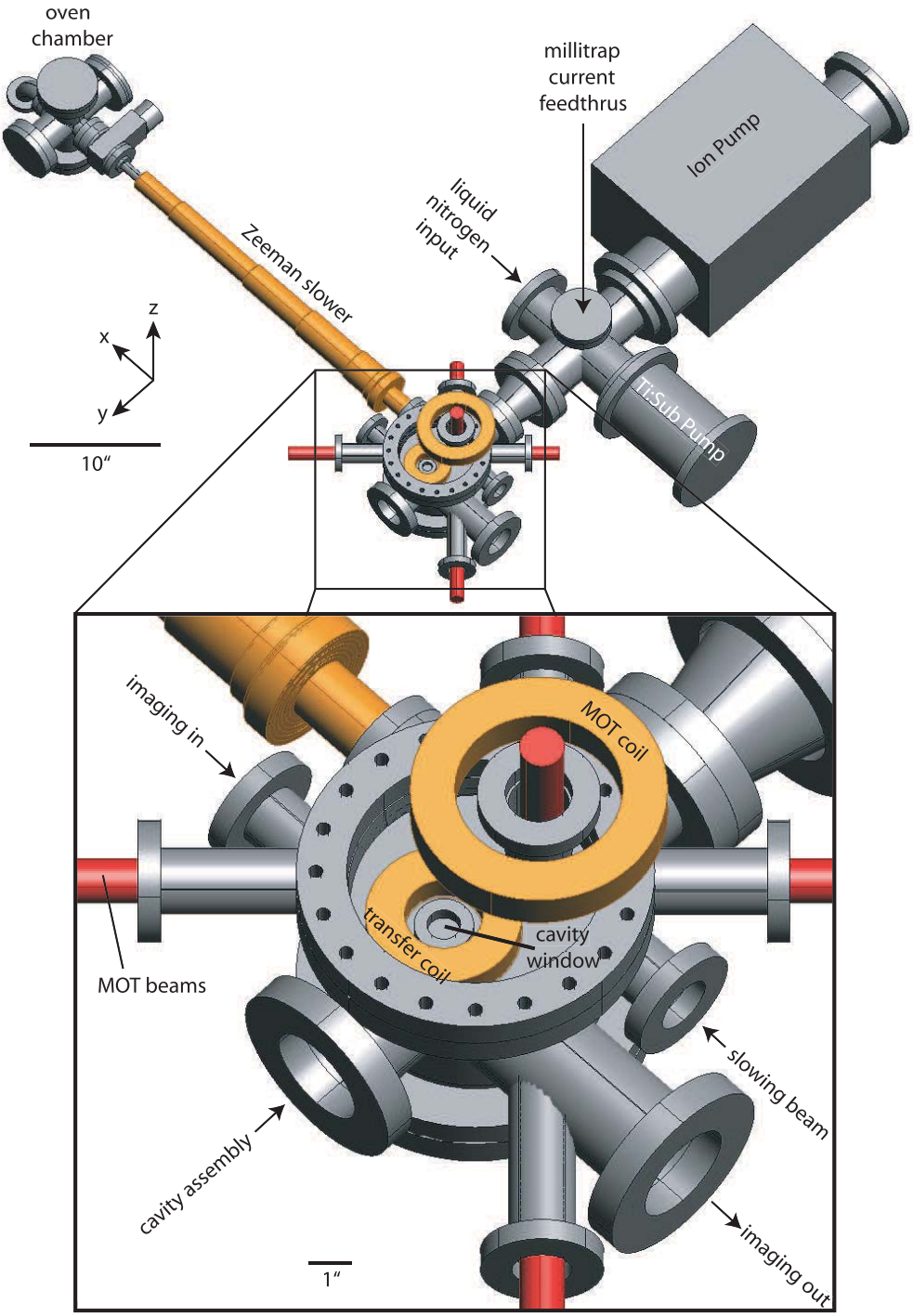

Figure 2.6: The full vacuum chamber layout.

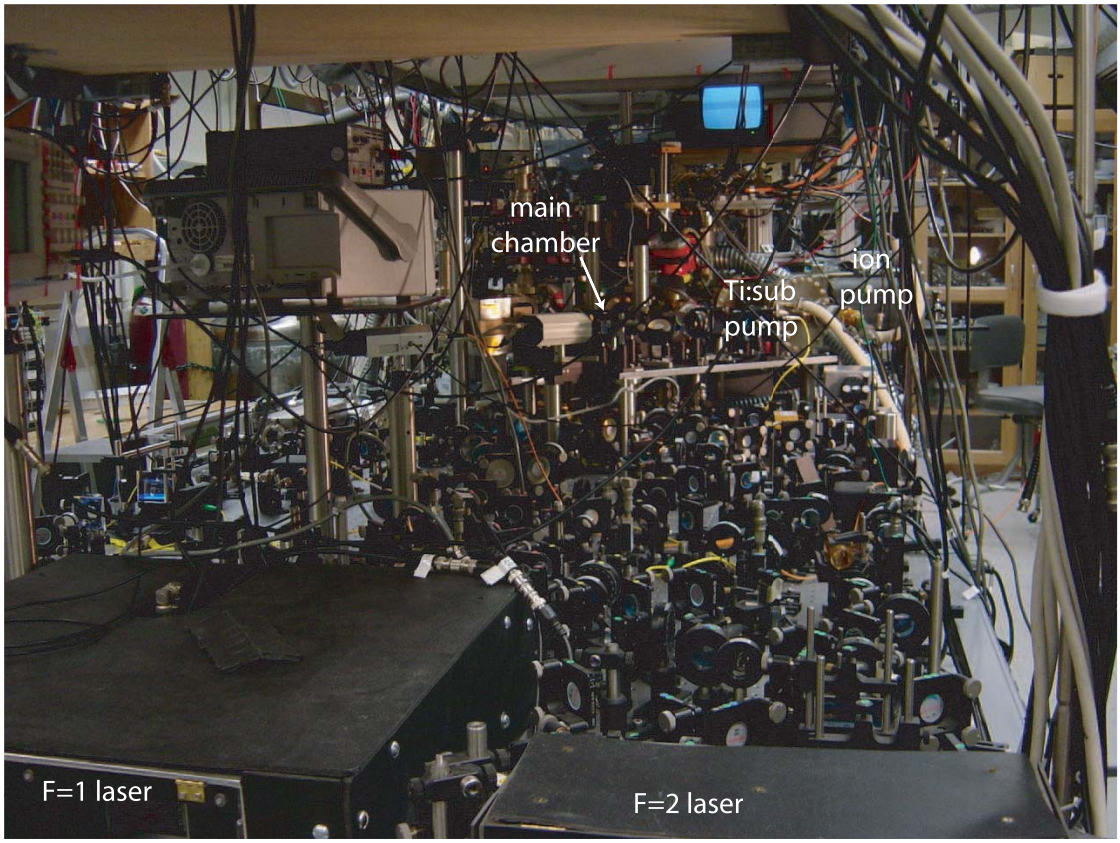

Figure 2.7: Photo of the experiment.

Chapter 3

The Millitrap

This chapter discusses the design, operation, and performance of the mm-scale magnetic trap; portions of this chapter were presented in the publication:

- *K. L. Moore, T. P. Purdy, K. W. Murch, K. R. Brown, K. Dani, S. Gupta, and D. M. Stamper-Kurn, "Bose-Einstein condensation in a mm-scale Ioffe-Pritchard trap," Applied Physics B* ***82****, 533-538 (2006). Included in Appendix F.*

As discussed in chapters 1 and 2, the main design criterion for the magnetic trapping system is the integration with a high-finesse optical cavity. In the 2002 review article "Cavity QED - Coherence in Context," the authors discuss a number of high-finesse optical cavity systems with the potential to access the strong atom-photon coupling regime [72]. However, at that time, only one cavity implementation had successfully proven its worth for optical cavity QED with laser-cooled atoms[1]– namely, the optical Fabry-Perot cavities developed by Jeff Kimble *et al.* and manufactured by Research Electro-Optics (REO) [73]. These cavities are formed by $\sim 3\,\mathrm{mm}$ outer diameter (OD) glass substrates which have been coned down to a 1 mm concave surface, superpolished, and coated with a numerous alternating layers of high-index (Ta_2O_5, $n_H = 2.04$) and low-index (SiO_2, $n_L = 1.46$) dielectric material [74]. The mirror separation of the substrates could vary from 10's to 100's of microns depending on the desired implementation, but the size scale of interest

[1]The pioneering experiments of Haroche *et al.* [37] with Rydberg atoms and *microwave* cavities should be mentioned here as an excellent cavity QED implementation, but an inappropriate one for a magnetically-trapped atoms.

for the design of the magnetic trapping system that will deliver the cold atoms into the cavity was the OD of the mirrors. The basic structure of the REO mirrors used in this work is presented in Figure 3.1.

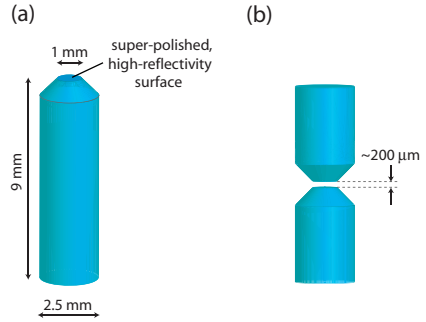

Figure 3.1: The high-finesse optical cavity mirrors. (a) A single mirror, with the critical dimensions listed. The outer diameter is approximately 2.5 mm, and the super-polished, dielectric-coated face is coned down to 1 mm. (b) Two mirrors facing each other form a Fabry-Perot cavity. The optical properties of the mirrors are presented in chapter 6.

The optical properties of the cavity will be discussed in chapter 6, but for the purposes of this chapter we are concerned with the dimensions of the mirrors which will dictate the design of the magnetic trap. Engineers at REO claimed that significantly narrowing the OD from the 3 mm used by the Kimble group was not possible with the current manufacturing capabilities of their plant, but they felt comfortable going as low as 2.5 mm. The second nonstandard request we made was for a relatively long substrate, finally settling on 9 mm, twice the normal length[2]. The substrates built by REO were ultimatel two 4.5 mm long substrates epoxied together[3]. With the crucial dimensions of the cavity being the 2.5 mm OD and the 9 mm substrate length, the *millimeter* became the natural length scale for the engineering task that was required. The magnetic trap which resulted from this thinking also had characteristic dimensions expressed in millimeters, and the verbal contraction of the length scale and intended function became both the name of the device and the title

[2]The extra length was required because the millitrap assembly eventually occupied the front 4 mm of the substrate, and the cavity length and mounting structure were pushed back substantially (see chapter 6).

[3]This does not compromise the cavity properties because any reflection/scattering only occurs on, at most a single pass. Scattering losses on the mirror face, while presumably much smaller than the losses at this interface, are compounded like the finesse, $\mathcal{F} = 580,000$ in our case.

of this chapter.

3.1 Design Considerations

The design began with the following initial criteria:

1. Maintain mechanical decoupling from cavity
2. Accommodate 2.5 mm mirror OD and support structure
3. Match long axis (and if possible, magnetic bias field) of trap with the cavity axis
4. Obtain the largest possible magnetic field curvatures so that an ultracold cloud will be smaller than the mirror separation

The third consideration led us to consider an Ioffe-Pritchard (IP) trap [69], which generates the following field profile

$$\mathbf{B}(\rho, z) = \left[B_o + \frac{B_z''}{2}\left(z^2 - \frac{\rho^2}{2}\right)\right]\hat{z} + \left(B_\rho' - \frac{B_z''}{2}z\right)\rho\,\hat{\rho}, \tag{3.1}$$

where $\rho = \sqrt{x^2 + y^2}$, and the axial curvature ($B_z'' = d^2B_z/dz^2$) and transverse gradient ($B' = dB_\rho/d\rho$) are tunable trap parameters[4]. To lowest order about the origin, the field magnitude is given by

$$B(\rho, z) = B_o + \frac{1}{2}B_z''z^2 + \frac{1}{2}\left(\frac{B_\rho'^2}{B_o} - \frac{B_z''}{2}\right)\rho^2 \tag{3.2}$$

A particle with magnetic moment μ will thus experience a harmonic trap with frequencies

$$\omega_\rho = \sqrt{\mu\left(\frac{B_\rho'^2}{B_o} - \frac{B_z''}{2}\right)\Big/ m} \tag{3.3}$$

$$\omega_z = \sqrt{\mu B_z''/m}. \tag{3.4}$$

Typically, it is easier to obtain a strong transverse trapping frequency ω_ρ (by application of a strong transverse gradient B_ρ' and/or reduction of B_o) than it is to obtain a strong axial frequency ω_z. With the exception of those produced by atom chips [75, 76, 77], IP magnetic

[4]By "tunable" we mean natural magnetic fields produced by the currents in the electromagnets of the trap.

traps formed by hand-wound current carrying wires only achieve axial field curvatures of $B_z'' \sim 100\,\mathrm{G/cm}$ [69] due to space constraints from accommodating large MOT beams and/or resistive heating-limited current densities. As this axial curvature yields a trapping frequency of $\sim 2\pi \times 10\,\mathrm{Hz}$, we can expect a $1\,\mu$K cloud of $|F=1, m_F=-1\rangle$ ^{87}Rb atoms to have a size of roughly $\sim 100\,\mu$m.

The comparison of this size to typical strongly-coupled optical cavity lengths ($50 - 200\,\mu$m) shows this field curvature to be inadequate by running afoul of the fourth stated criterion. Atom chips can produce IP field profiles with axial curvatures in excess of $10^6\,\mathrm{G/cm^2}$, but only in the close proximity ($\sim 100\,\mu$m) of the surface (violating the second criterion). Miniaturizing the current-carrying wires is a very effective method of increasing the field curvature. This is evident by considering that the magnetic field curvature from an electromagnet scales as I/d^3, where I is the total current in the wire(s) and d is the characteristic length scale of the system[5].

More precisely, the desired field is produced by two coaxial loops (of radius R, carrying current I) in the Helmholtz configuration, separated by a distance $2d$. At the trap center (located halfway between the two coils) the axial magnetic field is given by

$$\begin{aligned} B_z(z) &= \left(2\mu_o I \frac{R^2}{(R^2+d^2)^{3/2}}\right) + \frac{1}{2}\left(6\mu_o I \frac{R^2(4d^2-R^2)}{(R^2+d^2)^{7/2}}\right) z^2 + O(z^4) && (3.5)\\ &= B_o + \frac{1}{2}\left(3B_o \frac{4d^2-R^2}{(R^2+d^2)^2}\right) z^2 && (3.6)\\ &= B_o + \frac{1}{2} B_z'' z^2. && (3.7) \end{aligned}$$

A [d,R] contour plot of B_z'' (Figure 3.2(a)) shows the impressive gains promised by miniaturization, where electromagnets constructed on the mm-scale of the cavity mirrors yield field curvature/current ratios of $10^2\,\mathrm{G/cm^2/A}$, as compared to the $\approx 1\,\mathrm{G/cm^2/A}$ provided by inch-scale traps.

With the goal of $100\times$ improvement in curvature and a corresponding factor of 1/10 reduction in cloud size, an arrangement of current-carrying wires is sought which achieves a benchmark of $B_z'' = 10^4\,\mathrm{G/cm^2}$. Again consulting Figure 3.2, we find that $\sim 100\,\mathrm{Amps}$

[5]When developing this design in 2002, we considered employing atom chips for this work but came to the conclusion that adding this extra layer of complexity added too many unknowns to this first generation implementation. Tom Purdy, an alumnus of this experiment, is now leading exactly such a second generation project with multiple(!) high-finesse cavities on a microchip.

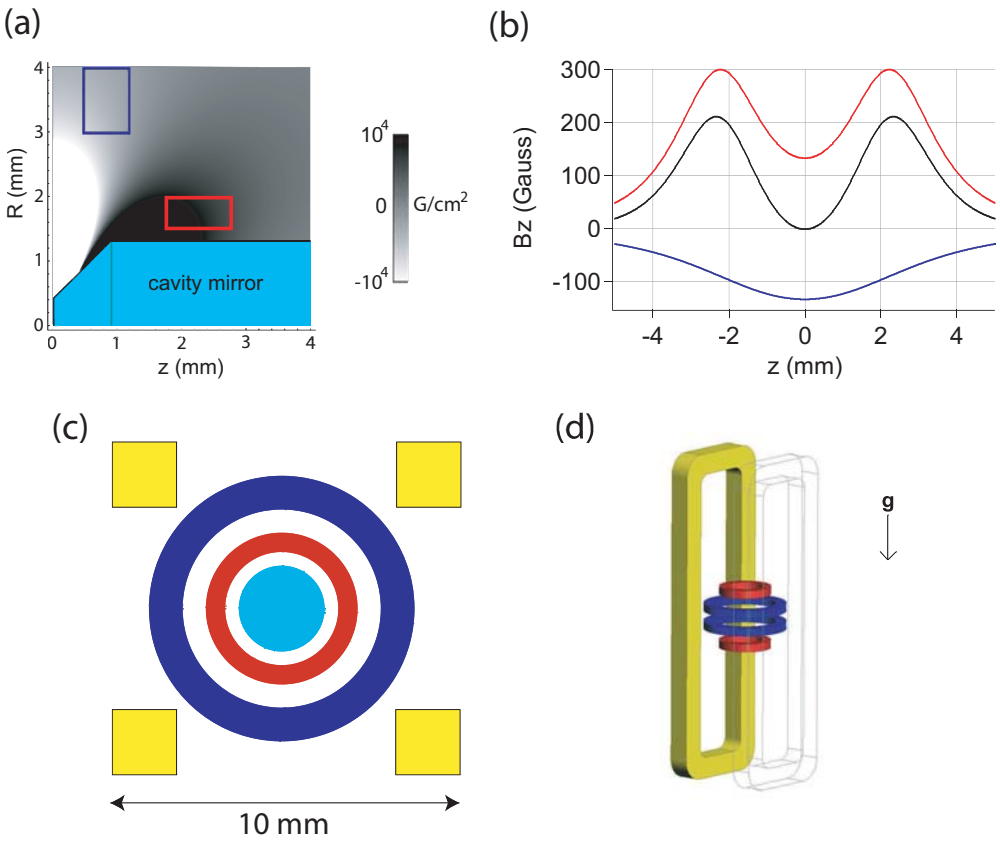

Figure 3.2: Considerations for the placement of the curvature and anti-bias coils. (a) A cavity mirrors (OD = 2.5 mm) is overlaid on a contour plot of B_z'' induced at the origin of the graph if a 10 Amp loop of current is placed at an axial distance z and a radius R. The final placement of the 5-turn curvature coils and 4-turn anti-bias coils are shown with their boundaries, represented by red and blue, respectively. (b) Axial field plots for the curvature and anti-bias coils each running 10 Amps of current, with the additive nature of the anti-bias curvature evident from the combined field (black). (c) On-axis view of the cavity/millitrap system. Shown in yellow are the gradient bars, which provide the transverse gradient B_ρ'. (d) Another view of the millitrap, with gravity oriented properly. For clarity the cavity has been omitted and the nearest gradient coil is shown as transparent.

need to be delivered to a cross-section of $< 1\,\mathrm{mm}^2$. Delivering such high current densities is a formidable technical challenge. Employing multiple turns of wire can reduce the problem of delivering large currents into a vacuum chamber, but then electrical insulation between the wires must be used. With or without the use of electrical insulation, resistive heating is of paramount concern. Room temperature copper has a resistivity of $16.8\,\mathrm{n}\Omega\cdot\mathrm{m}$ [78], so envisioning a $R = 2\,\mathrm{mm}$ loop of room temperature copper with a cross section of $0.5\,\mathrm{mm}^2$ gives a resistance of $4.2 \times 10^{-4}\,\Omega$hms. Delivering 100 A of total current to this loop will thus generate 4.2 W in the loop alone. This is a very significant amount of power to dissipate, especially in the presence of electrical insulation between multiple turns and the close proximity to a highly-sensitive high-finesse cavity!

Altogether, the considerations in the section resulted in the design presented in Figure 3.2, which shows the coils in context with the 2.5 mm OD cavity. The curvature coils are situated to maximize curvature while still leaving 0.25 mm clearance to the 2.5 mm OD cavity mirrors. The anti-bias coils, which run current in the opposite direction as the curvature coils, are placed to control not only the overall bias field at the origin but also to contribute curvature. As depicted, the curvature coils and anti-bias coils will contribute $100\,\mathrm{G/cm^2/A}$ and $33\,\mathrm{G/cm^2/A}$. The axial field profiles of these coils are given in Figure 3.2(b). Finally, the "gradient" bars (so named because they produce B'_ρ) are packed in with $4\,\mathrm{mm}^2$ cross-section, and provide a gradient of $2.5\,\mathrm{G/cm/A}$.

3.2 The Millitrap

As touched on in the preceding section, delivering the necessary current densities presents a significant engineering challenge. In addition to satisfying the design criteria already outlined, the system must also conform to the following technical criteria:

A. Accommodate at least $100\,\mathrm{A/mm}^2$ of total current density

B. Limit delivery current to $< 20\,\mathrm{A}$

C. Electrically insulate coils from themselves, each other, and the mounting system

D. Minimize and dissipate resistive heating such that the temperature of the trap does

not change significantly during operation

The second criterion is due to the difficulty in accommodating large ($< 20\,\mathrm{A}$) currents in an ultra-high vacuum system, as well as the desire to use smaller power supplies. Satisfying **A** and **B** clearly necessitates multiple turns of wire per coil, and thus the challenge becomes the general satisfaction of criteria **C** and **D**.

Copper is, of course, the most commonly employed electrical conductor, yet initial attempts using copper wire failed due to overheating issues. This was invariably caused by the fact that typical electrical insulating materials (e.g. Kapton® polymide film) are also thermally insulating, thereby making it very difficult to satisfy criterion **D**.

Ultimately, the best solution proved to be the utilization of aluminum as the current carrier. The primary virtue of aluminum for this application is its ability to be *anodized* (a process described in the next section), by which a microns-thick layer of aluminum-oxide (Al_2O_3) is grown on the surface. This electrically insulating layer is not a thermal insulating, primarily due to its relatively high thermal conductivity ($\sim 100\times$ that of Kapton®) and small thickness. Anodized aluminum films thus provide a nearly ideal conductor to wrap multiple times into a small cross section, with electrical insulation between layers and nearly all of the area filled with conducting material.

The resistivity of room temperature aluminum is $26.5\,\mathrm{n}\Omega\cdot\mathrm{m}$, generating an unacceptable 6.6 Watts of steady-state power for the desired 100 A total current. This problem is ameliorated by operating the system at a lower temperature. Aluminum at liquid nitrogen temperatures has a resistivity of just $2.5\,n\Omega\cdot\mathrm{m}$ [79], potentially offering a factor of ten reduction in power generation. Utilizing the latent heat of vaporization of liquid nitrogen is also advantageous to efficiently dissipate the residual Joule heating.

It is important to note that cryogenic operation of the system is no panacea. The millitrap system ultimately required 200 liters of liquid nitrogen for every $8-10$ hours of operation, and the temperature cycling caused many headaches and aborted data runs, especially after the integration and operation of the high-finesse optical cavity, described in chapter 6.

3.2.1 Curvature and Anti-bias Coil Construction

Manufacturing the aluminum coils and adequately dealing with the heating issues proved a very time-consuming, low-yield process, most strongly limited by the fragility of the thin aluminium foil which makes up the coils. There were four major stages of construction, each with their own approximate success-to-failure ratio: anodizing and cleaning (1:2), mandrel-winding and silver epoxying (1:3), baking and mandrel-removal (1:3), installation into mount (1:20). Each stage will be discussed herein, but the main point is that the "hand-wound" construction of the primary current-carrying wires was a tenuous, fragile process in which each aluminum strip had a very remote chance of survival.

Not even included in this dismal mortality spectrum is the initial cutting of the coil, accomplished with a precision shear (courtesy of the UC Berkeley Physics Machine Shop). The coils were cut into a "zig-zag" shape, such as the representation of a curvature coil in Figure 3.3. It was important to "deburr" the strip edges after being cut on the shear, as residual jagged edges were often the cause of electrical shorts after the strip was wound upon itself. Polishing the strips with fine 1500 grit sandpaper and machine oil before anodizing greatly diminished the chances of electrical problems down the line.

Figure 3.3: A curvature coil strip.

The next stage involved anodizing this aluminum strip, a process also carried out in the Physics Machine Shop. Anodizing such flimsy items in the industrial anodizing tank made for an incongruous sight relative to the large pieces the shop usually dealt with, but after some trial and error a "high" yield procedure was developed. To begin, the cut strips were first rinsed in deionized water and then held in a 15% nitric acid bath for approximately a minute. The strips were then suspended in the diluted 15% H_2SO_4 bath and the electrochemical anodization process commenced. The system was run at ~ 20 Volts

for only 30 minutes, just half of the typical anodization time for industrial parts. This shortened part of the procedure was a balance between the need for a sufficiently thick layer of the Al_20_3 ceramic surface and the increasingly brittle nature of the same. We found that wires which underwent the entire hour of oxide growth had a much higher chance of breaking during the anodizing or winding process. In contrast, wires anodized for less than 25 minutes were far more likely to have electrical shorts upon winding. Thus, the balance was struck at 30 minutes. After removal from the acid bath, the anodization layer was sealed with a ten minute bath in a warm nickel acetate solution (0.5% nickel acetate, 0.5% boric acid), and then rinsed again in deionized water. The anodized wire was electrically tested with a simple voltmeter acting in resistance mode. The sharp probe ends were touched along the surface, and if the coil did not exhibit "infinite" resistance everywhere along its surface, it was discarded. The $\approx$ 50% yield for this process came primarily from coils periodically breaking during the oxide growth stage or the subsequent cleaning/handling process[6].

After the anodizing process, the strip must be wound upon itself. To cohere the multi-turn coil, an adhesive agent is required. EPO-TEK manufactures a silver-based epoxy (H20E) which is acceptable for UHV conditions, and has the added benefit of being thermally conductive. We were initially concerned about the edge shorts being electrically connected by the epoxy, but we never observed any significant shorting between layers by this alone. The coils were wound upon Teflon® mandrels, which were constructed on a lathe to match the desired dimensions of the resultant coil. The use of Teflon® proved an absolute necessity, as it was the only common construction material to which the silver epoxy did not adhere. The anodization and Teflon® mandrel coil winding is depicted in Figure 3.4.

After removal from the mandrel the bent current lead, which is now on the interior winding, is wrapped over the assembly so that the input and output current leads run parallel from the exterior winding, depicted in Figure 3.5.

As mentioned previously, the probability of survival for the mandrel winding/removal

[6]This process followed the standard cleaning procedure for parts which would be introduced to the UHV chamber: a brief bath in the ultrasonic cleaner with deionized water and Simple Green®, then deionized water alone, then acetone, and finally methanol.

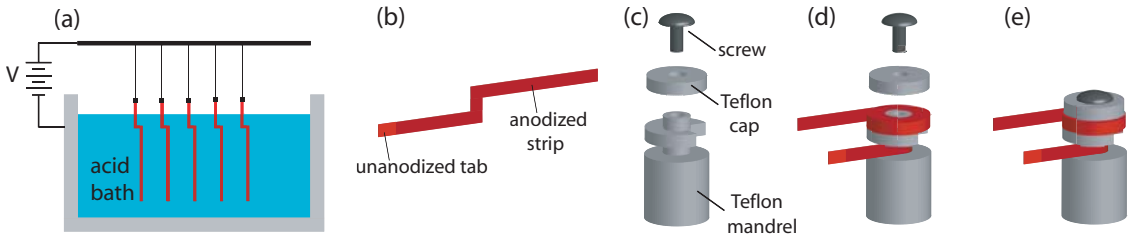

Figure 3.4: Curvature coil construction. (a) As described in text, the aluminum strips are anodized in a sulfuric acid bath, leaving a small tab of unanodized aluminum material which made electrical contact with the strip. (b) After anodization, the function of the "zig-zag" shape is evident when it must be wound around (c) the Teflon® mandrel. The mandrel is cut with a notch into which the wire corners are inserted. (d) The long anodized end of the wire is then wound about the spindle of the mandrel, interspersing silver epoxy throughout and in-between each layer. (e) After winding, the tension in the coil is maintained by taping the leads to the mandrel assembly (not shown), and the mandrel assembly is held together by the Teflon® cap and the steel screw. The entire mandrel-coil assembly is then baked on a hot plate at 150°C for an hour, setting the epoxy. As the epoxy does not adhere to the Teflon®, the intact coil can then be removed and the mandrel is reused for the next coil winding.

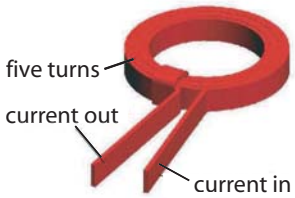

Figure 3.5: A wound curvature coil, with current in/out leads.

stage of the process was approximately 1/3 apiece, with the main mortality vector in both cases being the stress upon the zig-zag portions of the coil which are under heavy tension. Tears at the corner were especially common, and if the coils did not appear perfect upon inspection under a bright-field microscope, they were discarded. Figure 3.6 shows a sample of curvature and anti-bias coils which did not survive the process.

The final and most crucial stage was the insertion of the coils into the mounting structure. The mount itself was a significant engineering challenge, and the construction diagrams for the crucial pieces for this structure are presented in Appendix D. The first,

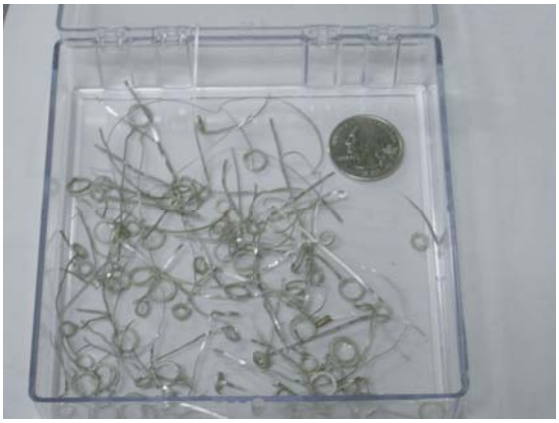

Figure 3.6: A mass grave of millitrap coils which did not survive the construction process. A U.S. quarter is included for size reference.

and perhaps most critical, mounting piece is the "faceplate" which houses the curvature and anti-bias coils. A diagram of the faceplate (with curvature coils and anti-bias coils incorporated) is presented in Figure 3.7.

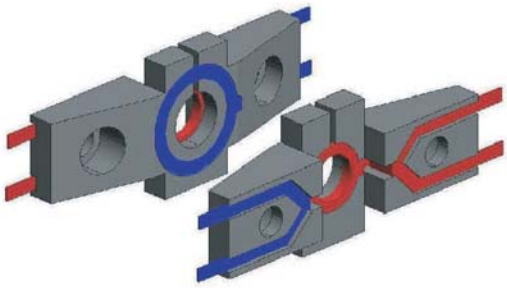

Figure 3.7: The faceplates, including incorporation of curvature coils (red) and anti-bias coils (blue).

The faceplate serves two main purposes: to hold the coils in their proper locations and to conduct away the heat generated by the coils during operation. The faceplates were constructed out of aluminum and subsequently anodized to themselves to prevent electrical shorts to the edges of the coils. The channels on the back of the faceplate allowed the current lead attachments to be made far from the coils themselves, as well as maintaining good thermal contact with the cold mount along their extent. The vertical

slice at the top of the faceplate prevented eddy currents from developing about the central aperture (which ultimately surrounded the cavity mirrors). The coils were inserted into place, with liberal amounts of silver epoxy, and again baked at 150°C to set the adhesive. This entire process was the most delicate of the entire assembly because of the relative violence inflicted upon the coils to get them properly inserted into the faceplates. The coil leads are under severe stress throughout assembly, and the extruding leads must endure one final violent procedure. In order to make a clean electrical connection to the coils with no contact resistance, the anodized layer of the extruding coil must be scraped off. If the leads break at any point then the coil must be removed and the faceplate scraped clean before attempting to insert another coil.

Further, the inserted coils must pass electrical tests showing that they are fully operational. A resistance drop of $\sim 15 - 20\%$ (compared to the unwound aluminum strip) would imply a full shorting of one of the coil's turns. Any coil with a $> 5\%$ resistance drop was deemed unacceptable. The coil must also be electrically isolated from the faceplate, and any perceived electrical contact also disqualified the coil and necessitated removal. After successful insertion of both curvature and anti-bias coils, the completed faceplate was again cleaned for UHV and awaited integration with the rest of the mount.

3.2.2 Gradient Coil Construction

Compared to the curvature and anti-bias coil construction, the gradient coils were far more robust. The aluminum strips used were 0.010" thick, and less prone to snapping. The coils consisted of 9 turns of wire, and the winding procedure was similar to that of the curvature and anti-bias coils.

Unlike the curvature/anti-bias coil assemblies, which are held in place by silver epoxy, the gradient coils were *not* epoxied throughout each layer but only on the edges which ultimately extrude from the trap mount. Mechanical pressure alone held the coils in place, as they were sandwiched between three mounting elements (described in the next subsection).

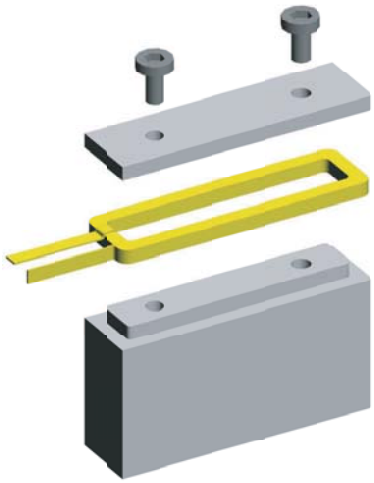

Figure 3.8: Diagram of gradient coil construction. Coil winding around the Teflon® mandrels is similar to Figure 3.4, though epoxy is only applied at the corners (see text).

3.2.3 Full Mount Assembly

The completed faceplates were affixed to anodized aluminum center pieces, constructed with center channels to allow future integration with the optical cavity. The same center pieces then had to allow the gradient coils to be incorporated into the assembly. The gradient coils were slid over the sides of the two center pieces, as shown in Figure 3.9. The picture of the central assembly also shows the current lead attachments on the sides of the center pieces. These elements were basically a custom copper lug structure which allowed electrical connection to the curvature and anti-bias leads without (a) electrical connection to the center mount or (b) any mechanical strain upon the coils when the assembly was integrated into the main chamber. The insulating material in this structure was Vespel®, a polymide material which is easily machinable and acceptable for UHV conditions. The main RF antenna for millitrap evaporation is wound around the curvature/anti-bias attachment lugs after the electrical leads have been secured.

The assembly was finally completed as the center pieces and gradient coils were fixed into place by tightening (through clearance holes) the pieces between the main copper base and the top plates (both presented in Appendix D). A critical feature of the copper base

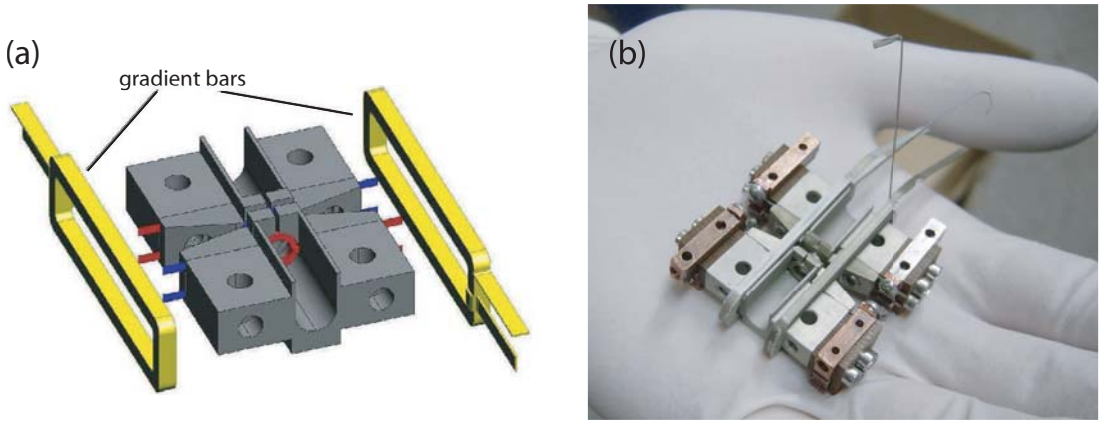

Figure 3.9: The Central Mount Assembly. (a) The faceplates are affixed to the center mount (see Appendix B) pieces, and the gradient bars are slid around the mount. (b) A photo of the assembled mount in the author's hand. Note the extra structures on the side of the center piece; these are the attachment structure pieces for the curvature and anti-bias current leads.

was a closed channel for the heat exchanging liquid nitrogen flow, as shown in Figure 3.10.

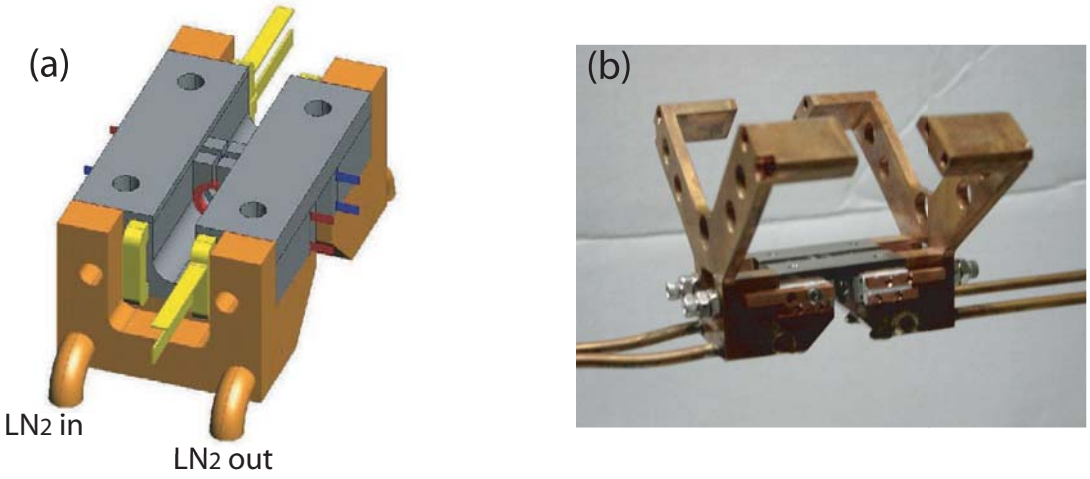

Figure 3.10: The full millitrap assembly. (a) The copper mount, with closed liquid nitrogen lines shown, is the final piece into which the millitrap is secured. Not shown are the winged structure which allows the copper mount itself to be affixed to the vacuum chamber. (b) A photo of the full millitrap assembly, with the mounting wings clearly seen.

Not shown in the diagram in Figure 3.10(a) are the "wings" which allow the mount

to be attached to the chamber, as well as accept the optical cavity assembly (described in chapter 6). A photograph of the actual assembly is shown in Figure 3.10(b).

3.2.4 Integration of the Millitrap with the Main Chamber

The winged assembly in Figure 3.10(b) is designed to mate with the mounting brackets which are seen on the inner edges of the 8" chamber in Figure 2.1. The copper wings are slightly thermally insulated by the use of Macor® spacers, though the 4-40 stainless steel threaded stock which fastens the millitrap assembly into place on these brackets does compromise this thermal insulation.

Once the millitrap was fastened into the chamber it had to be connected to the liquid nitrogen cooling line. After our group's negative experience with in-vacuum liquid connectors [63], we chose to silver solder the fluid connections on the millitrap. This nerve-wracking procedure necessitated the immense skill of the late Armando Baeza, who brought the oxy-acetelene torch down into the basement lab and made the solder connections within two inches of the millitrap while hovering precariously over the optical table. The results speak for themselves, however, as the fluid line has never exhibited any leaks despite the daily operation at an internal LN_2 pressures of 100's of psi.

After the fluid solder joints were completed and the system passed the leak test, the twelve electrical connections were made. The intra-vacuum current carriers were 10AWG (0.102 in. OD) Kapton®-coated rouond copper wires. This heavy gauge was necessary because these wires carried in excess of 10 Amps in vacuum with no heat sinking between the vacuum feedthrough and the millitrap. With twelve thick wires and two $\frac{1}{8}$" copper tubes snaking through the same 2.75" opening and a small vacuum chamber, it was a non-trivial task to position the system where neither the MOT nor imaging optical paths were obscured. A picture of the vacuum chamber, millitrap, and connections is shown in Figure 3.11.

3.3 Operation of Millitrap

As should be evident from the involved manufacturing procedure, the millitrap was incredibly delicate and, once installed, a one-of-a-kind device. This fact was not lost

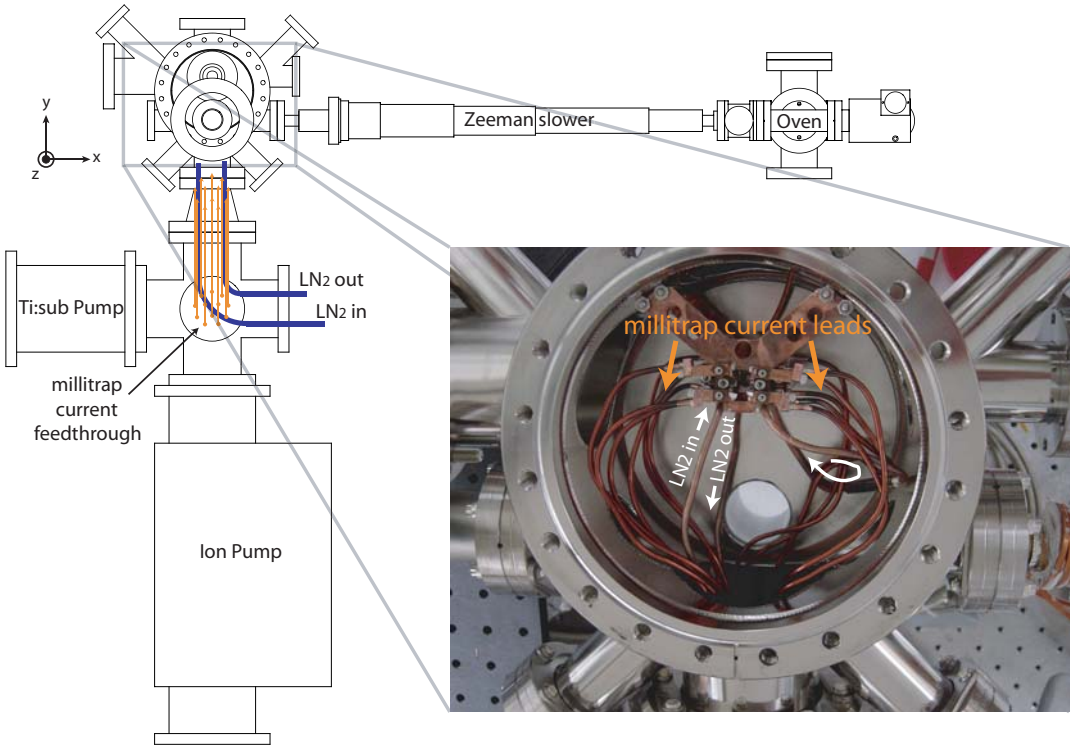

Figure 3.11: The millitrap integration into the vacuum system. The drawing shows how the current and liquid nitrogen are delivered into the vacuum chamber, and finally to the millitrap. The photo shows the central chamber assembly, with the twelve millitrap current leads attached to the millitrap, itself affixed to the interior chamber via the brackets seen in Figure 2.1. The closed-loop liquid nitrogen flow enters one half of the copper mount, out and into the second half, and finally out on the return line to be expelled from the vacuum chamber. (The output flow was actually then recycled into the Ti:sub shroud, which is not represented in this sketch.) The various leads shown must avoid obscuring optical access to the MOT region and the imaging axis of the millitrap, giving the "spaghetti" appearance. While admittedly inelegant, these wires were also employed as anchors for the RF antennae used for quadrupole trap evaporation (not shown).

on its operators, and great care was taken to protect the millitrap from any possible operational damage. The strain-relieved electrical connections all but guaranteed that the millitrap could not be damaged in the vacuum wiring process, though it did periodically develop electrical shorts when closing the chamber due to compression and contact of the current delivery wires. Our greatest concern was the overheating and subsequent damage of the millimeter trap from excessive Joule heating. To prevent this, Tom Purdy

constructed an interlock system utilizing a Keithley Digital Integra Series 2701 Multimeter Data Acquisition System. With connections at the input measuring the voltage across and current through each coil, the Keithley measurement cycle monitored each of these twelve channels at least once per second. If any of the coil voltages or currents exceeded the prescribed set points, as would occur if the coils were heating up, then the interlock would trip and the electrically circuits were switched open. This system completely disallowed any room temperature operation of the trap above $\sim$ 2 Amps, and ensured that the millitrap coils would survive any liquid nitrogen flow interruption or accidental operation errors.

To provide the most flexibility in operating the millitrap, separate electrically-floating power supplies were used for each coil. Also included in the electrical setup were a set of CLC inductor-capacitor filters, though the values for the filters depended on the desired operation of the trap (DC traps vs. AC traps). Electrical characterization of the millitrap following the vacuum bakeout revealed several undesired low-resistance (several Ohm) connections between different coils, indicating electrical connections through the common mounting structure. These inter-coil connections should have no effect since independent supplies are used for each coil. The possible presence of undesired intra-coil connections, e.g. connections between turns on the multiple-turn coils, was tested by measuring parameters of magnetic traps formed with varying currents in each of the curvature, anti-bias, and gradient coils. No clear evidence for such flaws was obtained.

At least 150 psi of input pressure on the liquid nitrogen line was required to operate the trap at normal experimental currents. During this operation, Table 3.3 summarizes the observed performance of the coils (as well as the relevant dimensions). Following a bakeout of the millitrap at a temperature of 250°C, lifetimes of over 100 s were ultimately observed for atoms trapped in the millitrap, definitively demonstrating the vacuum compatibility of all materials used in its construction.

3.4 Atom Delivery to Millitrap

In the subsequent Section, we explore the possible millitrap field configurations, but the atom delivery to these trapping potentials remains nearly identical for all of the exper-

Coil	I.D.	O.D.	Thickness	Width	Cross-sec.	No. turns	$\dot{Q}$ @ 10 A
curvature	3 mm	4 mm	0.006 in.	1 mm	0.5 mm^2	5	2 Watts
anti-bias	6 mm	8 mm	0.008 in.	0.75 mm	0.75 mm^2	4	2 Watts
gradient	N/A	N/A	0.008 in.	2 mm	4 mm^2	9	10 Watts

Table 3.1: Parameters for aluminum coil windings.

iments described in this thesis. As outlined in Section 2.5, approximately 5×10^9 atoms are collected in the MOT, and subsequently 2×10^9 atoms (in the $|F = 1, m_F = -1\rangle$ manifold) are trapped in a spherical quadrupole trap. The magnetically-trapped atoms are transported 1.75" toward the millitrap. At this position both external quadrupole coils are running full current (see Table 2.5.2, forming a quadrupolar field $\vec{B}$ = {(104 G/cm)x, (158 G/cm)y, -(262 G/cm)z}. The atoms are then cooled via forced RF evaporation to 15 μK, reducing the size of the cloud to 400 μm, before transporting them the remaining distance to the center of the millitrap. This pre-cooling is crucial because the anti-bias coils in the IP trap allow only a 1 mm gap through which the atoms are threaded. A diagram of this process, including the size and phase space density of the cloud, is presented in Figure 3.12.

3.5 Spectrum of Millitrap Magnetic Trapping Potentials

The versatility of the millitrap is evidenced by the large number of trapping configurations it is capable of producing. This section presents a subset of these more traditional magnetic trapping configurations, and the subsequent chapter discusses an entirely different kind of magnetic trapping potential produced by the millitrap.

3.5.1 Spherical Quadrupole Trap

Two coaxial circular coils, running current in the anti-Helmholtz configuration, will always produce a field zero somewhere along their common z-axis. Because there are four coaxial coils in the millitrap, this opens up three possible spherical quadrupole implementations: curvature/curvature, anti-bias/anti-bias, and curvature/anti-bias. Utilizing

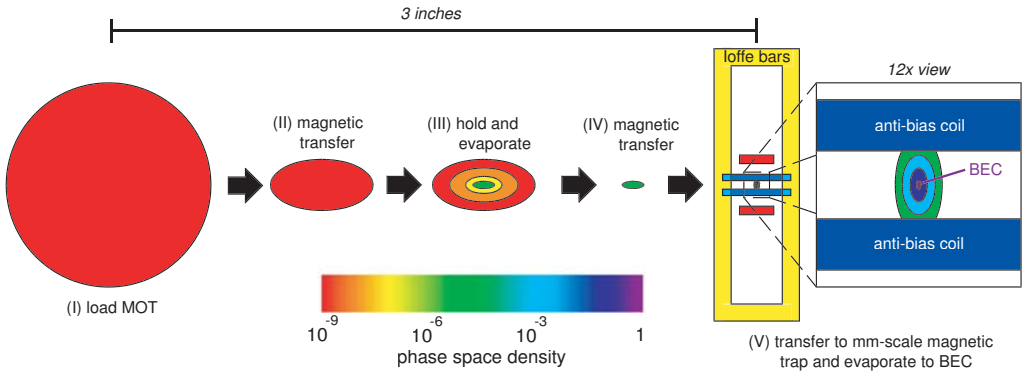

Figure 3.12: Sketch of experimental sequence for BEC in the millitrap (Ioffe-Pritchard configuration). (I) Atoms are loaded into the MOT and subsequently trapped in a spherical quadrupole trap. (II) The atoms are then transferred 1.75 inches towards the mm-scale IP trap and (III) evaporated to a phase space density of $\Gamma \sim 10^{-5}$. (IV) The cloud is magnetically transferred into the IP trap and (V) captured by a curvature coil and an anti-bias coil in a spherical quadrupole trap. The full millitrap is then turned on and the atoms are confined in the IP field with a 2 G bias field. The cloud is then further evaporated, forming a pure BEC of 1 million atoms.

the curvature/anti-bias quadrupole trap is advantageous if an Ioffe-Pritchard trap will be employed later in the experimental sequence, as the coil currents will already be running in the correct directions for this configuration. The curvature/curvature spherical quadrupole boasts the highest gradient/current ratio at 13.8 G/cm/A, but suffers from large off-axis inhomogeneities due to the geometry of the coils. The anti-bias/anti-bias spherical quadrupole is the "best" spherical quadrupole in that it can be displaced over a large distance with a transverse bias field with minimal distortion of the trap; its gradient/current ratio is 6.6 G/cm/A. This advantageous feature makes possible the delivery of Bose-condensed atoms to the high-finesse optical cavity (as presented in chapter 6), and is also the basis for the Time-Orbiting Potential trap presented later in this section.

3.5.2 Ioffe-Pritchard Trap

The Ioffe-Pritchard (IP) trap is the magnetic field configuration for which the millitrap was designed, and a number of results from our initial investigations were published in Ref. [54]. Some the main results include (a) the demonstration of $N > 10^6$ atom BECs in an IP field with the expected large curvatures ($B_z'' = 7800\,\mathrm{G/cm^2}$ at 10.5 Amps), (b) the

associated wide spectrum of trapping geometries with control of the transverse trapping frequencies, and (c) a wide range of tilt angles with respect to the z-axis.

One unexpected feature of this strong IP trap was a remarkably high efficiency of RF evaporation. This efficiency can be quantified by comparing the factor gained in phase space density Γ through the evaporative cooling loss of a given factor in atom number N, obtaining, e.g. a figure of merit $f = -d\ln\Gamma/d\ln N$, with Γ and N parameterized along some evaporation trajectory. Typical figures of merit cited in the literature for evaporation from IP traps are $f = 2$ to $f = 3$ [80, 81]. In our mm-scale IP trap, a factor of over 10^5 in phase space density is efficiently gained by evaporative cooling to the Bose-Einstein condensation transition temperature with an overall figure of merit of $f = 4.5$. The distinct advantage of this large figure-of-merit is seen in Figure 3.13, where BEC transition is reached with an order of magnitude higher atom number than would have been achieved in typical traps.

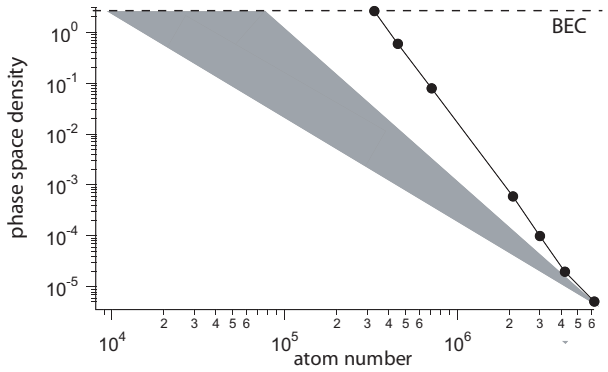

Figure 3.13: Typical phase space trajectory in the millitrap (Ioffe-Pritchard configuration). Shown for reference in grey is the domain of more typical magnetic trapping implementations (see text).

To account for this high efficiency, we note that the IP trap, aside from being strongly confining and thus compressing atomic clouds to high collision rates, is also nearly isotropic. We suspect that the condition of near isotropy improves the efficiency of evaporative cooling relative to that in the typically-used anisotropic traps since high-energy atoms produced collisionally in the gas can easily escape the center of the cloud in *any direction*, and thereby reach the trap boundary established by the applied RF radiation. In contrast, in a cigar-shaped cloud with high aspect ratio, the large axial collisional depth can prevent

the escape of all high-energy atoms except those traveling nearly purely in the radial direction. Further, we note that high evaporation efficiency is obtained in our trap in spite of the vertical orientation of the axial direction. In contrast, IP traps with weaker axial confinement are rarely oriented in this manner so as to avoid the onset of lower dimensional evaporation due to gravitational sag [81, 82].

3.5.3 Time-Orbiting Potential Trap

While the Ioffe-Pritchard trap is operated with steady DC currents in its constituent coils, the first experimental observation of dilute gas BEC [83] occurred in an AC trap known as a Time-Orbiting Potential (TOP) trap [20, 84]. For our system, a spherical quadrupole trap is produced by the anti-bias coil pair and biased by a *rotating* field of $\mathbf{B}_r = B_r\,(0, \cos\omega_r t, \sin\omega_r t)$. The rotating field is produced by the curvature coils and the gradient coils, both running current in the Helmholtz configuration. The resultant field is given by

$$\mathbf{B} = \left(B'x, B'y + B_r\cos\omega_r t, -2B'z + B_r\sin\omega_r t\right)\,. \tag{3.8}$$

If ω_r is much greater than the motional timescales of the atoms, then taking the time-average of the field is appropriate. We are also concerned with regions about the origin, which makes the product $|B'r/B_r| \ll 1$. To find the time-averaged field, we look to the magnitude of $\mathbf{B}$ to lowest order in $|B'r/B_r|$:

$$\begin{aligned}\langle|\mathbf{B}|\rangle_t &= \langle\sqrt{B'^2x^2 + (B'y + B_r\cos\omega_r t)^2 + (-2B'z + B_r\sin\omega_r t)^2}\rangle_t \\ &\approx B_r + \frac{B'^2}{4B_r}\left(2x^2 + y^2 + 4z^2\right)\,.\end{aligned} \tag{3.9}$$

This harmonic trap has a $\sqrt{2} : 1 : 2$ aspect ratio[7].

To produce a TOP trap in the millitrap, we had to rewire the coils such that a quadrupole field was produced by the anti-bias coils (operating in anti-Helmholtz configuration) and the orbiting fields described above enacted by the gradient coils and curvature coils (both operating in an Helmholtz configuration). The atoms were brought into the millitrap region and transferred to an anti-bias/anti-bias quadrupole trap, formed 1 mm from

[7] In contrast, an orbiting field in the transverse plane has a $1 : 1 : 2\sqrt{2}$ aspect ratio.

the center axis[8]. Typical operating conditions for the millitrap-produced TOP field were $B' = 36\,\mathrm{G/cm}$, with an orbiting frequency of $\omega_r = 2\pi \times 5\,\mathrm{kHz}$ loaded at $B_r = 8.6\,\mathrm{G}$. After initial "circle of death" evaporation in this trap, the orbiting field was lowered to the final value of $B_r = 6.3\,\mathrm{G}$, where the trapping frequencies were $(\omega_x, \omega_y, \omega_z) = 2\pi \times (72, 51, 102)\,\mathrm{Hz}$. Here the cloud underwent forced RF evaporation to quantum degeneracy, and nearly pure BECs of $> 40,000$ atoms were observed.

[8]This off-axis move is made to avoid the cavity which, at the time we implemented this trap, was obscuring the center axis. To form this trap outside the cavity center a transverse bias field along the y-axis is applied, provided by wires wrapped around the 4.5" "cavity structure" flange in Figure 2.1, forming a "push coil" capable of displacing the $B' = 36\,\mathrm{G/cm}$ quadrupole trap many millimeters.

Chapter 4

Bose-Einstein Condensation in a Circular Geometry

This chapter discusses quantum degenerate gases in a circular waveguide; the work in this chapter was presented in the publication:

- *S. Gupta, K. W. Murch, K. L. Moore, T. P. Purdy, and D. M. Stamper-Kurn, Bose-Einstein condensation in a circular waveguide, Phys. Rev. Lett.* ***95****, 143201 (2005). Included in Appendix G.*

As discussed in the preceding chapter, the primary difference between the millitrap and its larger counterparts are the comparatively large field curvatures arising from the millimeter length scales of the electromagnets. Beyond the described advantages for Ioffe-Pritchard traps, these field curvatures can be exploited in other trapping geometries as well. Specifically, we consider how to utilize the coaxial curvature and anti-bias coils to create a balanced, circular magnetic waveguide for ultracold atoms.

4.1 The Magnetic Quadrupole Ring

To explain the origin of the magnetic quadrupole ring (Q-ring), we look back to the Ioffe-Pritchard field in Equation (3.1) and envision eliminating the transverse gradient field $B'_\rho \to 0$. $\mathbf{B}_c$ now has a local field *saddle point* at the origin, and the field decreases for

$z = 0$, $\rho \gtrsim 0$ according to

$$\mathbf{B}_c = B_o\hat{z} + \frac{B_z''}{2}\left[\left(z^2 - \frac{\rho^2}{2}\right)\hat{z} - z\rho\hat{\rho}\right] . \tag{4.1}$$

This field $\mathbf{B}_c$ vanishes in the $x - y$ plane at a radius of $\rho_o = 2\sqrt{B_o/B_z''}$. While the magnitude of the field expands linearly from this radius, the quadrupolar field differs from that of the spherical quadrupole considered in chapter 2. The magnitude of the gradient can be shown to be $B' = \sqrt{B_o B_z''}$, but it is the form of the field which distinguishes it from the spherical quadrupole. More precisely, about a point at $(z = 0, \rho = \rho_o)$, it is the case that

$$\begin{aligned} \frac{\partial \mathbf{B}_c}{\partial z}\cdot\hat{z} = 0 \quad &, \quad \frac{\partial \mathbf{B}_c}{\partial \rho}\cdot\hat{\rho} = 0 \\ \frac{\partial \mathbf{B}_c}{\partial \rho}\cdot\hat{z} = -B' \quad &, \quad \frac{\partial \mathbf{B}_c}{\partial z}\cdot\hat{\rho} = -B' , \end{aligned} \tag{4.2}$$

and $\partial\mathbf{B}_c/\partial\theta = 0$ trivially from cylindrical symmetry. This should be contrasted with the spherical quadrupole field, which has a field profile of $\mathbf{B}_{SQ} = B'_{SQ}(x, y, -2z)$. Graphically, the Q-ring and its field lines are depicted in Figure 4.1.

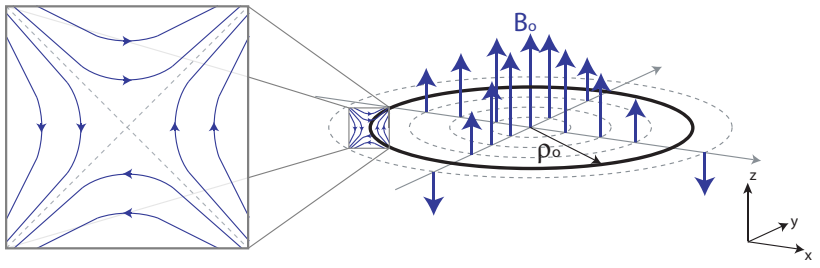

Figure 4.1: Quadrupolar Ring Diagram.

Assuming the z-axis is aligned with the direction of the gravitational acceleration g, the locus of field zeros will be a local magnetic field minimum if $B' > |mg/\mu|$. Thus, in its ideal form, the Q-ring is a perfectly flat and circular magnetic quadrupole trap.

4.2 Corrections to the Cylindrically Symmetric Q-ring

Of course, ideal cylindrical symmetry is difficult to achieve. In this section, we explore scenarios where this symmetry is broken in both controlled and uncontrolled manners. The

consequences of a departure from a perfectly flat ring are significant for ultracold atoms because of the minuscule energy scales involved. Thus, we consider field modifications from various perturbative corrections, as well as the energetic modification for a particle, of magnetic moment μ, confined in the waveguide.

4.2.1 Bias Fields

Suppose a uniform bias field $\mathbf{B}_s = B_s\hat{s}$ is applied to the Q-ring field in Equation (4.1), where $\hat{s}$ is an arbitrary unit vector. We immediately see that z-component of $\mathbf{B}_s$ is merely absorbed into an offset of the bias field of $\mathbf{B}_c$, i.e. $B_o \to B_o + \mathbf{B}_s \cdot \hat{z}$. This changes the radius ρ_o but maintains the cylindrical symmetry which gives the circular locus of field zeros.

Therefore, we need only consider bias fields in the x-y plane of the ring, with two relevant parameters being the magnitude B_s and the angle θ_s off the heretofore arbitrary x-axis. The field of the Q-ring thus becomes:

$$\mathbf{B}_c = B_o\hat{z} + \frac{B_z''}{2}\left(z^2 - \frac{\rho^2}{2}\right)\hat{z} + \left[B_s\cos(\theta-\theta_s) - z\rho\right]\hat{\rho} - B_s\sin(\theta-\theta_s)\hat{\theta}\,. \tag{4.3}$$

Some further algebra reveals that the field near the unperturbed ring behaves as

$$\mathbf{B}_c = -B'\rho\hat{z} + \left[B_s\cos(\theta-\theta_s) - B'z\right]\hat{\rho} - B_s\sin(\theta-\theta_s)\hat{\theta}\,. \tag{4.4}$$

Unlike the perfect ring field of Equation (4.1), this field vanishes at only two points $-$ $(B_s/B', 0, \theta_s)$ and $(-B_s/B', 0, \theta_s + \pi)$ $-$ in (z, ρ, θ) coordinates. This tilts and stretches the ring in the $z - \theta_s$ plane by an angle $\phi_{tilt} = \tan^{-1}\left(\frac{B_s}{2B_o}\right)$. This deformation does *not* correspond to a pure rotation, such as would result from just tilting the entire trapping assembly. The circular field has been deformed to maintain the ρ_o circular projection on the $x - y$ plane (depicted in Figure 4.2).

The modification to the potential around the ring is two-fold. First, a particle will experience a magnetic contribution to the energy as $\mu B_s|\sin(\theta-\theta_s)|$. Second, the tipping of the ring will cause a gravitational contribution to the energy shift if the field minimum at θ is lifted/lowered off $z = 0$. Together, the potential felt by a magnetic particle in the ring would, to lowest order, be given by

$$U(z,\theta) = mgz + \mu\sqrt{\left[B_s\cos(\theta-\theta_s) - B'z\right]^2 + B_s^2\sin^2(\theta-\theta_s)}\,. \tag{4.5}$$

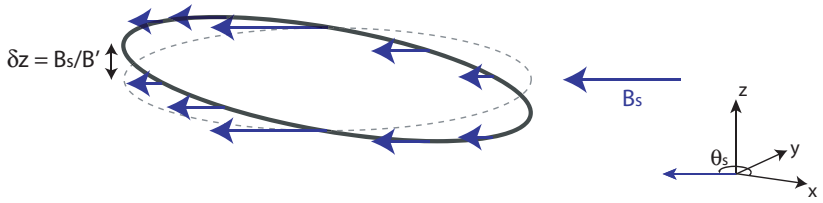

Figure 4.2: Q-ring under transverse bias field.

As previously stated, it must be the case that $B_z'' \gg |mg/\mu|$ to effect magnetic trapping against gravity. This condition guarantees that the potential energy gained by the vertical displacement at θ_s, $\Delta U_{grav} = mg(B_s/B')$, is less than the magnetic potential energy at $\theta_s \pm \pi/2$, $\Delta U_{mag} = \mu B_s$. This is best seen in a contour plot of Equation (4.5) on z and θ, shown in Figure 4.3:

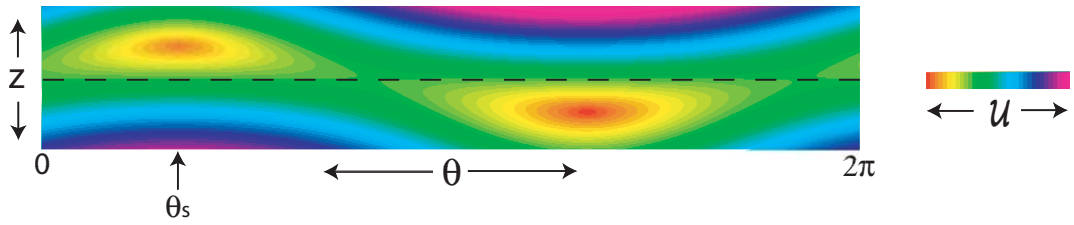

Figure 4.3: Gravi-magnetic potential contour plot.

As expected, $\theta_s + \pi$ is the energetic minimum of the ring, vertically displaced below the ring. A second local energy minimum occurs at θ_s, but displaced *above* the unperturbed $z = 0$ ring by B_s/B'. Finally, we are interested in the energetic variation of the potential around the ring, $\mathcal{U}(\theta)$, which is defined to be the minimal value of the potential at a given cylindrical angle θ. This is most readily obtained by setting the derivative of (4.5) with respect to z to zero and solving, but some care must be taken. The magnetic potential energy must be everywhere positive for a magnetically-trappable particle which remains adiabatic in the ring. With this consideration, $U(\theta)$ can be shown to have the form

$$U(\theta) = \mu B_s \left[\left(\sqrt{1 + f_2^2} + f_2 \right) |\sin(\theta - \theta_s)| + f_1 \cos(\theta - \theta_s) \right] , \tag{4.6}$$

where $f_1 \equiv mg/\mu B'$ and $f_2 \equiv mg/\sqrt{(\mu B')^2 + (mg)^2}$. The presence of the *absolute value* of $\sin(\theta - \theta_s)$ is of course representative of the fact that the magnetic potential energy is manifestly positive about the ring. That this potential contains high-order harmonics (all even, as a matter of fact) has important implications for the motion of propagating atoms, a detailed consideration of which may be found in our paper on betatron resonances [53].

4.2.2 Gravity

Even in the absence of external bias fields, gravity can play a role if the symmetry axis of the electromagnetic coils is not aligned with the gravitational acceleration, $\mathbf{g}$. If the coil axis is kept as the z-axis, then the $\mathbf{g}$ can be given as $\mathbf{g} = -g(\cos\phi, \sin\phi\cos\theta_g, \sin\phi\sin\theta_g)$, where ϕ is the angle between $\mathbf{g}$ and $\hat{z}$, and θ_g is angle formed between the $x-y$ projection of $\mathbf{g}$ and the $x-y$ plane. The potential variation around the ring can then be written as

$$U(z, \rho, \theta) = \mu B' \sqrt{z^2 + (\rho - \rho_o)^2} + mgz\cos\phi + mg\rho\sin\phi\cos(\theta - \theta_g)\,, \tag{4.7}$$

At a given θ, this equation is trivially minimized with $z = 0$, $\rho = \rho_o$. The energetic variations about the waveguide path, however, can vary substantially

$$U(\theta) = mg\rho_o \sin\phi\cos(\theta - \theta_g)\,, \tag{4.8}$$

with $\phi \to \pi/2$ and a sizeable ρ_o being the most obvious scenario. Unlike Equation (4.6), Equation (4.8) has only a first-order harmonic term in θ. This fact disallows any re-balancing of a gravitationally misaligned Q-ring using only an external bias field. Rather, a combination of bias and curvature fields is needed.

4.2.3 Inhomogeneous Fields

Moving beyond simple bias fields, an arbitrary inhomogeneous vector field $\mathbf{B}_{ext}(x, y, z)$ may be applied to the ring. As a simple bias field already added a non-trivial $|\sin\theta|$ modification to the potential energy variations about the ring, we can expect sizable inhomogeneous external fields to further complicate the energetic structure of the ring. A severe case of this is depicted in Figure 4.4:

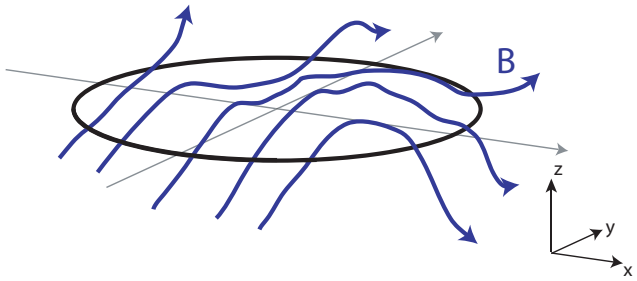

Figure 4.4: The Q-ring in the presence of inhomogeneous magnetic fields.

We may consider these fields generally in a fourier expansion about the locus of the unperturbed ring as

$$\mathbf{B}(\theta) = \sum_{l=0}^{\infty} \mathbf{B}_l \sin(l\theta - \theta_l)\,. \tag{4.9}$$

This is not immediately useful, as the fields may expand, stretch, and displace the shape of the ring. Further, the field moments $\mathbf{B}_l$ and phases ϕ_l are unknown, as is their relationship to the relevant magnetic ring quantities, B_o, B', B''_z. This does suggest, however, that we might similarly examine the deformation of the ring and the potential function about the ring minima in harmonic terms:

$$\mathbf{r}_{ring} \to \sum_{l=0}^{\infty} \left(\delta z_l \sin(l\theta - \phi_{z,l})\hat{z} + \delta\rho_l \sin(l\theta - \phi_{\rho,l})\hat{\rho}\right) \tag{4.10a}$$

$$U(\theta) \to \sum_{l=0}^{\infty} \frac{U_l}{2}\left(1 + \sin(l\theta - \phi_l)\right), \tag{4.10b}$$

where the energetic moments are measured off the $U = 0$ flat ring. The magnitude of the δz_l, $\delta\rho_l$, and U_l moments can be related back to the various orders of spatial derivatives of $\mathbf{B}_{ext}(x, y, z)$, but ultimately the central meaning of Equation (4.10) lies in the relation of the higher-order harmonic structure of the ring to the field inhomogeneities. As noted in Subsection 4.2.1, these harmonics are important for the motion of atomic beams about the ring, with the connection explored extensively in Ref. [53].

4.3 Loading Atoms into the Q-Ring

The first observation of the Q-ring came as a bit of a surprise, although it was accomplished in precisely the manner discussed in Section 4.1. Atoms were trapped in the Ioffe-Pritchard configuration and the gradient current controlling B'_ρ was progressively reduced to zero. As this was carried out, the atoms were pulled from the IP trap center and began filling in the Q-ring.

This is hardly the ideal manner to load atoms into the Q-ring, and while the atoms were delivered in a manner identical to that discussed in the previous chapter, the best "handshaking" between the external quadrupole trap and the Q-ring was to heavily bias the Q-ring along $-\hat{y}$, the entry axis for the atoms coming from the loading region. The atoms are transferred to the tilted Q-ring just as they were to the millitrap spherical quadrupole trap, a procedure which is depicted in Figure 4.5. More quantitatively, 2.5×10^7 atoms, pre-cooled to $60\,\mu$K were confined in the $200\,$G/cm field from the external quadrupole transfer coils. Within 1 second, the spherical quadrupole field was converted to a tilted Q-ring trap produced with $B''_z = 5300\,\mathrm{G/cm^2}$, $B_o = 22\,$G, and a side field of magnitude $B_s = 9.2\,$G. This process left 2×10^7 atoms trapped in the tilted Q-ring.

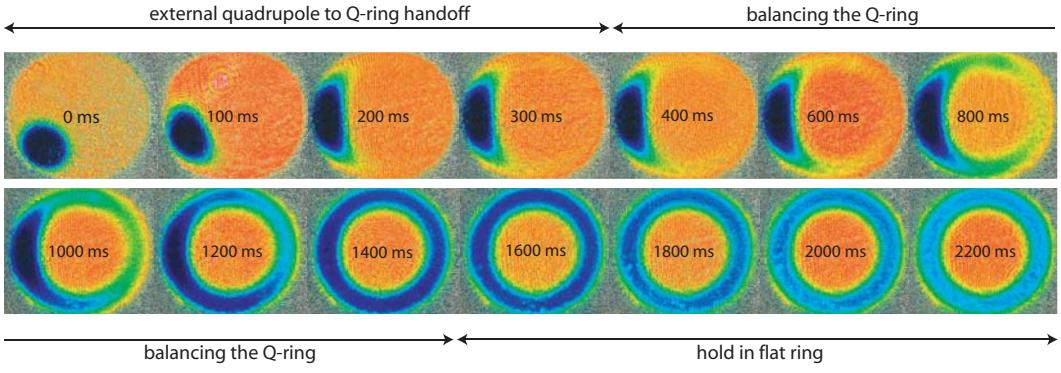

Figure 4.5: Time sequence of loading atoms into the Q-ring. In the first 500 ms, the atoms bound in the external quadrupole coils are aligned with the left edge of the Q-ring. The millitrap current is engaged (in a 9 G tilted Q-ring setting) as the external quadrupole trap is ramped off. Reorienting the Q-ring is then accomplished by bias field shifts, and in the case shown the ring is slowly balanced over the course of 1 second. In the balanced ring, the Majorana loss rate is increased (see text) and the population fades at an accelerated pace.

The bias field which tips the ring may itself be extinguished to balance the Q-ring, a sequence also shown in Figure 4.5. As the atoms fill the flattened Q-ring, a noticeable increase in the loss rate is observed. The origin of this increase, of course, comes from the fact that the Q-ring is an unbiased magnetic trap, susceptible to the same Majorana spin-flip losses which plague spherical quadrupole traps. We note here that the normal experimental operation only made use of the first 500 ms of Figure 4.5, i.e. the *Q-ring* was never actually flattened in practice. A method to bias the Q-ring and maintain the circular structure is discussed later, and this technique was employed directly in the tilted Q-ring which suffers less from Majorana losses for reasons which we will now explore.

4.4 Majorana Losses in the Q-Ring

Majorana losses are a well-known phenomenon in ultracold atomic physics precluding the use of DC current spherical quadrupole traps to achieve BEC [21]. The central idea is contained in a recognition of the fact that a magnetically-trapped spin state $|F = 1, m_F = -1\rangle$ is Larmor precessing in its *local* magnetic field at a rate $\omega_L = \frac{1}{2}\mu_B|\mathbf{B}(x, y, z)|$. Near the center of a spherical quadrupole trap the field vanishes, which means that the Larmor precession frequency of atoms near the origin can be quite small. To remain adiabatic and in a trappable state, the time rate of change of atomic orientiation must be substantially less than ω_L. In the case at hand of a spin in a magnetic field, this can be expressed as

$$\frac{\partial}{\partial t}\frac{|\hat{\mu}\cdot\mathbf{B}|}{|\mu|\,|\mathbf{B}|} \ll \frac{\mu|\mathbf{B}|}{\hbar}\,. \tag{4.11}$$

If this condition is violated then the system is open to "spin flips," in that the particles will have non-zero amplitude to be in other spin states which are untrapped. To estimate the amount of loss that a system of thermal atoms would experience in a spherical quadrupole trap of gradient B', we look to the critical radius r_c at which the two expressions in Equation 4.11 are equal:

$$\frac{v}{r_c} = \frac{\mu_B B' r_c}{\hbar}\,, \tag{4.12}$$

where v is the velocity of the atom. Within factors of unity, we can say that for a thermal gas of average velocity $v \approx \sqrt{k_B T/m}$ the critical radius is

$$r_c \approx \sqrt{\frac{\hbar}{\mu B'}\sqrt{\frac{2k_B T}{m}}}\,. \tag{4.13}$$

We also note that the thermal cloud occupies a volume of $V \approx \pi(k_B T/\mu_B B')^3$. Together these elements translate to a Majorana loss rate Γ_M by considering the thermal flux of atoms through the surface boundary of $A_c = 4\pi r_c^2$, which can be shown to be

$$\begin{aligned}\Gamma_M &\approx \frac{A_c}{V}\sqrt{\frac{2k_B T}{m}} \\ &\approx 6\frac{\hbar}{m}\left(\frac{\mu_B B'}{k_B T}\right)^2\,.\end{aligned} \tag{4.14}$$

If we extend this analysis to the Q-ring, we recognize that the critical radius r_c does not change, but instead of enclosing an ellipsoid it bounds a torus of radius ρ_o. Thus, the surface boundary is given by $A_c = 2\pi\rho_o r_c$, the volume becomes $V = 2\pi^2\rho_o(k_B T/2\mu B')^2$, and the Majorana loss rate is

$$\Gamma_M \approx \frac{\hbar^{1/2}}{\pi m^{3/4}}\frac{(\mu B')^{3/2}}{(k_B T)^{5/4}}\,. \tag{4.15}$$

The absence of any ρ dependence is initially surprising, but is merely a reflection of the fact that in a torus the surface area to volume ratio is constant with radius.

Regarding specifically our Q-ring, we attempted to quantify these losses at various Q-ring tilts. For a ring of $B_o = 22\,\mathrm{G}$, $B_z'' = 5300\,\mathrm{G/cm^2}$, a variable bias field B_s along the y-axis was applied and the atom loss rate for a $T = 60\,\mu\mathrm{K}$ cloud measured, shown in Figure 4.6.

For these experimental values, the expression in Equation (4.15) would predict a loss rate of $6\,/\mathrm{s}$, far in excess of the maximal $0.3\,/\mathrm{s}$. This is almost certainly due to residual fields, perhaps even sizeable inhomogeneous fields, which mitigate some of the Majorana damage that the flat ring prediction of Equation (4.15) would predict. This foreshadows a result presented later in this chapter for the energetic variations in the ring, but whatever the cause the Q-ring, like its spherical quadrupole counterpart, is incapable of accommodating a quantum degenerate sample. We now turn to a method which will eliminate these losses in the ring, facilitating Bose condensation in the ring.

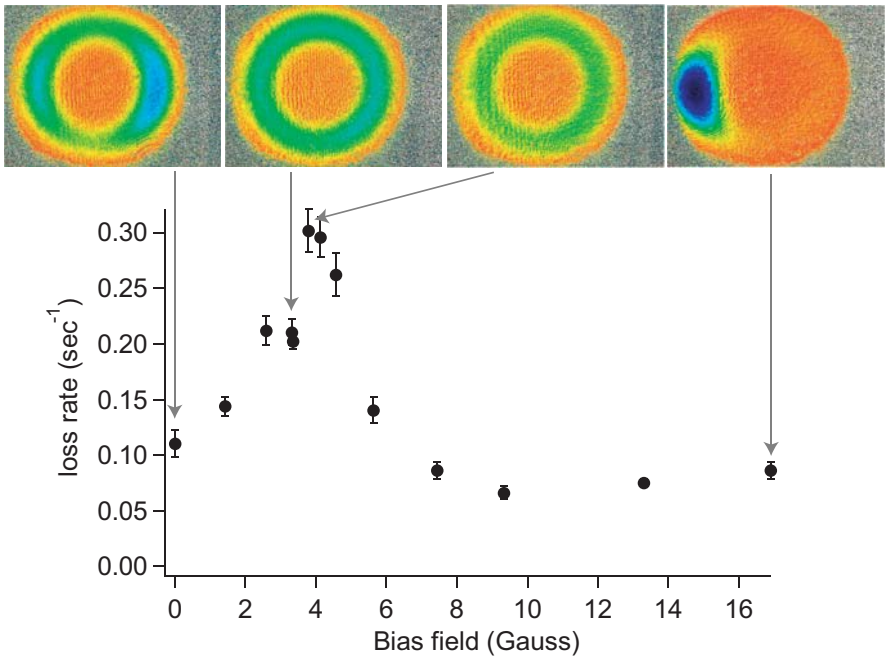

Figure 4.6: Variation of Majorana loss rate with Q-ring tip. The Majorana loss rate is measured as function of bias field, showing the increased loss rate in the balanced configuration versus tipped configuration. Absorption images are associated with the observed loss rates in the data series. With this method, we were able to diagnose not only the Q-ring but the permanent magnetic field inside our vacuum chamber to be $\approx -3.7\,\mathrm{G}\hat{y}$.

4.5 The Time-Orbiting Ring Trap

Just as the Majorana losses from a spherical quadrupole trap can be eliminated by the orbiting field of the TOP trap, we look to orbiting fields to reduce the deleterious effect of the field zero. To make the Q-ring equivalent of a TOP trap, we employ a Time-Orbiting Ring Trap (TORT) [85] which consists of the following field

$$\mathbf{B}_r = B_r\big(\cos(\omega_r t), \sin(\omega_r t), 0\big)\,, \tag{4.16}$$

and is most readily accomplished by the application of an oscillating axial bias field $\mathbf{B}_{r,1} = B_r(\cos\omega_r t, 0, 0)$ and spherical quadrupole field $\mathbf{B}_{r,2} = \frac{B_r}{\rho_o}\sin\omega_r t\,(-z, \rho, 0)$, all expressed in (z, ρ, θ) coordinates. This field must be added to the arbitrarily biased Q-ring field in

Equation (4.3). In this case, the field about the unperturbed ring is

$$\mathbf{B}_c = \left(B_r \cos\omega_r t - B'\rho\right)\hat{z} + \left(B_r \sin\omega_r t + B_s \cos(\theta-\theta_s) - B'z\right)\hat{\rho} - B_s \sin(\theta-\theta_s)\hat{\theta}\,. \quad (4.17)$$

As in Section 3.5.3, we take the time-averaged field to second-order in $|B'r/B_r|$ about the minimal azimuthal path and obtain the field magnitude

$$|\mathbf{B}_c| = B_{eff} + \frac{B'^2}{2B_{eff}}\left(1 - \frac{1}{2}\frac{B_r^2}{B_{eff}^2}\right)\left(\rho^2 + z^2\right)\,, \quad (4.18)$$

where $B_{eff} = \sqrt{B_r^2 + B_s^2 \sin^2(\theta-\theta_s)}$. It is worth noting that the base transverse trapping frequency from this field profile, $\omega_T = \sqrt{\frac{\mu}{m}\frac{B'^2}{2B_r}}$, is everywhere reduced by the application of B_s except at $\theta - \theta_s = 0,\, \pi$ where it is unchanged.

If we consider a ring which is also tipped slightly ($\phi \ll 1$) at angle θ_g with respect to gravity, then to lowest order the potential about the ring can be shown to be

$$U(\theta) = \mu\sqrt{B_r^2 + B_s^2 \sin(\theta-\theta_s)} + mgh\cos(\theta-\theta_g) + mg\frac{B_s}{B'}\cos(\theta-\theta_s)\,, \quad (4.19)$$

where $h = \rho_o \sin\phi$, the height of the tilt in the ring. It is worth noting here that the rotating field B_r can, in the appropriate limit, "smooth out" the absolute value asymmetry of the $B_s|\sin(\theta-\theta_s)|$ which doomed the balancing of the Q-ring in Equation (4.6). For $B_r \gg B_s$, the TORT may be completely flattened against slight gravitational misalignments with only energetic variations of $\mu\left(\frac{B_s}{2B_r}\right)B_s|\sin(\theta-\theta_s)|$, a significant improvement over the $B_s|\sin(\theta-\theta_s)|$ of the Q-ring.

4.6 Topping Off the Q-ring

The time-varying fields needed to convert our Q ring to the TORT traps were obtained by suitably modulating the currents in the four coils used to generate the Q-ring potential. A rotating field frequency of 5 kHz was found to yield the best conditions, easily satisfying the requirement to be much larger than the transverse motional frequencies (< 100 Hz) and also much smaller than the Larmor precession frequency (> 3 MHz). To first switch on the TORT, a rotating field magnitude of $B_{rot} = 18$ G was used.

As shown in Figure 4.7, the trap lifetime was dramatically increased by application of the TORT trap. In the first few seconds after switching on the TORT, we observed a

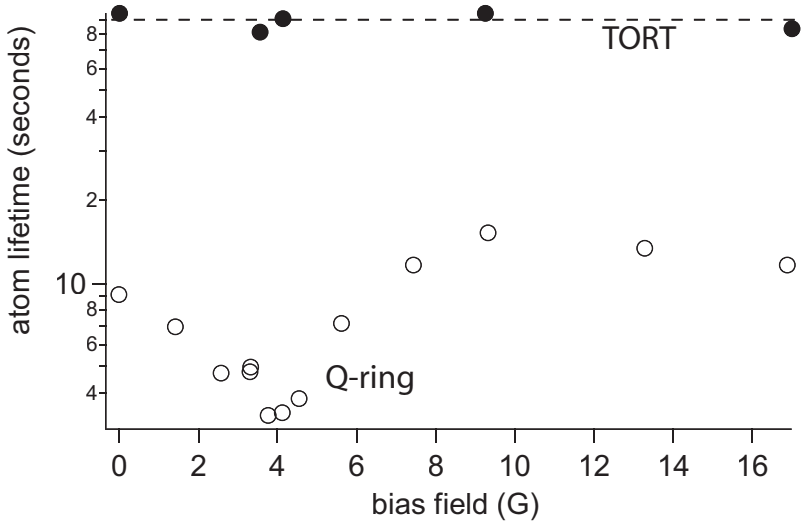

Figure 4.7: Elimination of Majorana losses in the TORT. The Q-ring loss rate data from Figure 4.6 (closed circles) are compared to the long lifetime in the TORT (solid circles). The TORT exhibits a vacuum limited lifetime of 90 seconds, irrespective of the orientation of the ring.

fast loss of atoms and a simultaneous drop in their temperature. We ascribe this loss and cooling to the evaporation of atoms from the trapped cloud to the finite depth of the trap. (This was affectionately referred to as the "torus of death.") As the temperature dropped, the evaporation rate diminished and the lifetime of trapped atoms became vacuum limited at 90 s, a value observed both for balanced and for tilted TORT traps.

4.7 BEC in the TORT

The long lifetime in the biased TORT makes possible the evaporation of the atoms to quantum degeneracy. Applying a $B_s \sim 9\,\mathrm{G}$ bias field the TORT is "tipped" and the potential is given by that in Equation (4.19). To proceed to the BEC phase transition, we begin by utilizing the finite depth of the TORT as torus of death evaporation was applied by ramping down the rotating field strength B_{rot} over 40 s to 4.8 G. The oscillation frequencies in this trap were measured as $2\pi \times (87, 74.5, 35)$Hz, with the transverse asymmetry a consequence of the applied bias field. In the second stage, RF evaporation was applied for

20 s, yielding clouds of up to 6×10^5 atoms at the Bose-Einstein condensation temperature, and pure BECs of up to 3×10^5 atoms.

A natural goal would be the Bose condensation in not just the tipped TORT but the fully balanced TORT. To get an idea of the prospects of accomplishing this in our current configuration, we can estimate the transition temperature with the current experimental values of $N\sim3\times10^5$ atoms, $\omega_T=2\pi\times85\,\mathrm{Hz}$, and $\rho_o=1.25\,\mathrm{mm}$. BEC occurs for the phase space density $\Gamma=N\lambda_{dB}^3/V\sim1$, so with the thermal volume of the ring given by

$$\begin{aligned} V &= (2\pi\rho_o)\times\left(\pi\sigma_T^2\right) \\ &= 2\pi^2\rho_o\left(\frac{k_BT}{m\omega_T^2}\right). \end{aligned} \tag{4.20}$$

With the thermal deBroglie wavelength $\lambda_{dB}=\sqrt{2\pi\hbar^2/mk_BT}$, we obtain the critical temperature (within factors of unity)

$$T_c=\frac{1}{k_B}\left[N^2\left(\frac{\hbar^2}{m\rho^2}\right)(\hbar\omega_T)^2\right]^{1/5}\approx40nK\,. \tag{4.21}$$

This is a very small temperature indeed, but hardly out of the realm of possibility when the transition temperatures for most BEC experiments are in the 100's of nK. A crucial distinction must be made, however, between comparing this temperature and that of harmonic traps. In previous sections of this chapter, we have discussed the energetic variations around the ring. The formula in Equation (4.21) relies on a perfectly flat ring, and this is unlikely to be the case. Surely we can tolerate potential variations no more than the transition temperature of the flat ring, which translate to a ring balanced to $500\,\mu$G around the circumference. This is a *very* flat ring and, as we will see, it is much flatter than our current implementation is capable of producing.

4.8 Motion in the Circular Waveguide

With the prospect of condensing the atoms in the current incarnation of the TORT looking grim, we "settled" on launching the atoms into motion about the circular waveguide. Our successful implementation of this led to the oft-used phrase *The Ultracold Atom Storage Ring*, somewhat in homage to the experts in experimental particle physics who have been studying the motion of particles in circular waveguides for over 65 years [86].

Using the motion of the atoms to probe the energetic structure of the ring led to even more connections to accelerator physics than we initially suspected, and is a prerequisite for any interferometry scheme to be implemented in the ring. In this Section, the basic elements of motion in the circular waveguide are explored, while the more detailed information about the atom beam motion is discussed in the subsequent chapter and Refs. [53, 55].

4.8.1 Azimuthal Oscillatory Motion

After condensing the atoms in the $B_s = 9\,\mathrm{G}$ biased TORT, the bias field may be shifted in magnitude and/or orientation. If the bias field is shifted slowly with respect to the atomic motion set by the trapping frequencies, then the cloud remains adiabatic and follows the ground state of the shifting trap minimum. If the bias field is reoriented rapidly, then the atoms will experience a net azimuthal force given by $-\frac{1}{\rho}\frac{\partial U}{\partial \theta}$ and be accelerated by the potential gradient. Assuming that the force is uniform across the spatial extent of the ensemble[1], the stationary atom cloud becomes a propagating atom beam which undergoes motion about the ring according to the potential $U(\theta, t)$.

In a simple case, we can consider rapidly, i.e. on a timescale faster than the $2\pi/\omega_\theta = 29\,\mathrm{ms}$, changing B_s from $9\,\mathrm{G}$ in the $-\hat{y}$-direction to $B_s = 9\,\mathrm{G}$ in the $\hat{x}$-direction. The atom cloud thus looks like a displaced oscillator in the modified $U(\theta)$, and the atoms will oscillate about the new minimum as shown in Figure 4.8(a).

In the presence of stray fields and gravitational misalignment, it is much easier to create an unbalanced biased ring than a flat, balanced ring. Oscillatory motion about a potential minimum in the ring is thus the norm and, insofar as motional oscillations of this sort are not terribly useful, much trial and error was required to *avoid* this scenario and set the atoms into unterminated propagation. Using the "shifted minimum" which accelerates the atoms was quite useful however, and made possible the following subsection which explores the range of motion where the atom beam propagates freely about the ring.

[1]The validity of this assumption will be discussed in chapter 5.

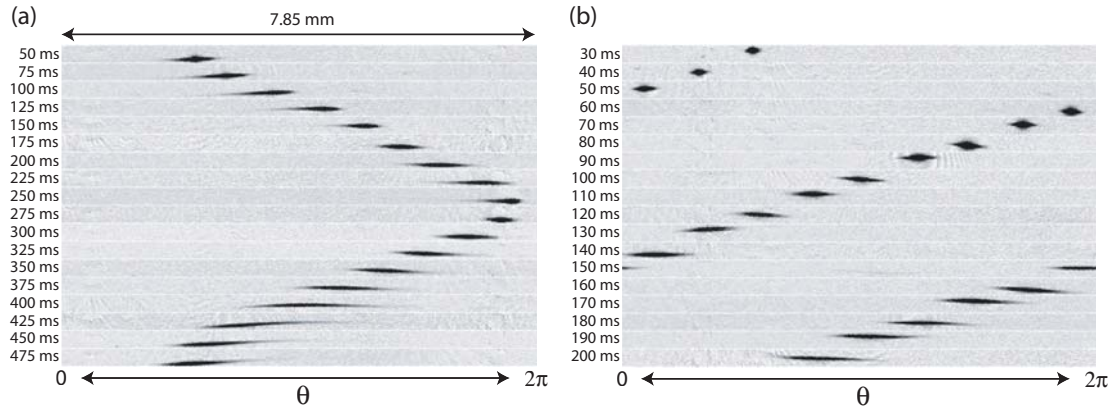

Figure 4.8: Atomic beam motion in the waveguide. (a) Shown is the time sequence of an unsuccessful launch sequence. Absorption images are collected after 2 ms time-of-flight release from the waveguide potential, and then post-processed to show an annular strip from $1.10\,\mathrm{mm} < \rho < 1.35\,\mathrm{mm}$. The atoms are not accelerated enough to overcome the residual variations in $U(\theta)$. (b) A better acceleration and balancing of the TORT allows a successful launch of the atoms into unterminated motion about the ring. The trap settings for the launch herein were $B_{rot} = 12.6\,\mathrm{G}$ ($\omega_T \simeq 2\pi \times 50\,\mathrm{Hz}$), $B_o = 20\,\mathrm{G}$, $B_z''|_{z=0} = 5300\,\mathrm{G/cm^2}$, $\rho_o = 1.25\,\mathrm{mm}$, with a final angular (linear) velocity of $2\pi \times 6.4\,\mathrm{rad/s}$ ($50.6\,\mathrm{mm/s}$).

4.8.2 Unterminated Motion in the Waveguide

Guided by the amplitude and velocity of the oscillatory motion described in the preceding subsection, we discovered a "launching" regime whereby unterminated motion about the waveguide was possible. Optimal settings were accomplished by reorienting the sideways bias field B_s, inducing the trapped atoms to accelerate toward the newly positioned tilted TORT trap minimum (advanced by an azimuthal angle of about $\theta = \pi/4$) while simultaneously reducing the magnitude of B_s to $B_s \sim 0$. Much trial and error was required, but a narrow window of final transverse bias fields B_s allowed a ring balanced enough such that the kinetic energy imparted during the acceleration stage overcame the residual potential variations in the flattened ring.

The final value of B_{rot} was a free parameter from $4.8 - 13\,\mathrm{G}$, allowing a range of possible transverse trapping frequencies $\omega_T \simeq 2\pi \times (50 - 90)\,\mathrm{Hz}$ and maximum potential height of $k_B \times (40 - 100)\,\mu\mathrm{K}$ for the waveguide. Under successful launches, the atoms were allowed to propagate freely around the guide for various guiding times before being

observed by absorption imaging. Final angular velocities were possible over a range of $\Omega \simeq 2\pi \times (6 - 19)\,\mathrm{Hz}$. A time sequence of an $\Omega = 11\,\mathrm{Hz}$ launch is shown in Figure 4.8(b).

4.8.3 Diagnosing the Azimuthal Potential Variations

The next chapter discusses in detail the atomic beam in this free propagation state, but for the purposes here we can consider the unterminated motion categorically good from the perspective of making the Ultracold Atom Storage ring useful for applications such as Sagnac interferometry. While obtaining a relatively flat ring was a requirement to inject atoms into unterminated motion, the motion of the atoms about the ring can be used to balance the azimuthal potential even further. We can infer $U(\theta)$ by measuring the azimuthal variations in the kinetic energy of a beam propagating in the static ring potential. For this, we measured the center-of-mass position of the cloud vs. propagation time, and determined the velocity and energy from differences in this position vs. time. Figure 4.9 shows, for slight variations in a bias field along the y-axis, the measured kinetic energy as a function of azimuthal position.

Assuming the kinetic energy variations are due primarily to longitudinal potential energy variations, Figure 4.9(b) shows the "flattest" waveguide potential we were able to make. The data may be fit to the presumed azimuthal potential in Equation (4.19), shown as the solid curve in Figure 4.9(b). Further efforts were unsuccessful at reducing the potential energy variations below that shown, and thereby $5\,\mu\mathrm{K}$ was taken as the "flattest" achievable ring. This is much higher than the tilted TORT BEC transition temperature of $\sim 100\,\mathrm{nK}$, and higher still than the full-ring transition temperature of $T_c \sim 40\,\mathrm{nK}$. With two orders of magnitude in ring flatness to bridge, we abandoned hope of condensing atoms into the full ring, leaving this task to the very capable next generation of experimentalists[2].

4.8.4 Expansion of the Atomic Beam

When the beam is released from the azimuthal confinement, the atoms will expand longitudinally as the mean field energy is rapidly converted into kinetic energy. This behavior is discussed in more detail in the following chapter, but briefly we may consider

[2]Tony Öttl, Ryan Olf, and Ed Marti are already hard at work.

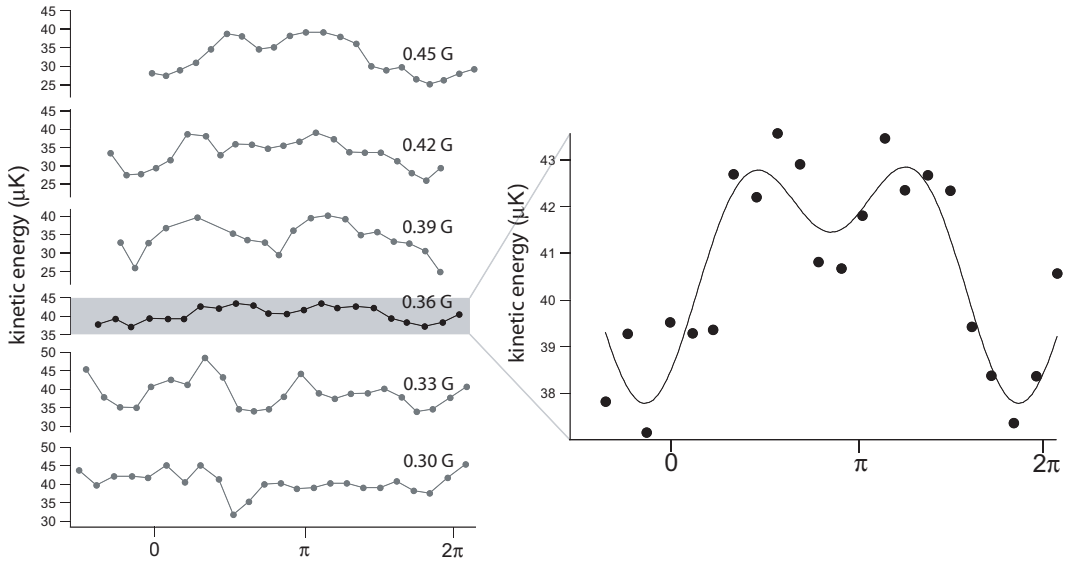

Figure 4.9: Azimuthal energy map of the circular waveguide as measured by atomic beam motion. (a) The tilt of the waveguide is controlled by a bias field along the y-axis, and the optimal setting of $B_y = 0.36\,\mathrm{G}$ is seen in the small variations of the kinetic energy of the beam as it orbits the ring. (b) A magnification of the $B_y = 0.36\,\mathrm{G}$ potential map shows that the kinetic energy, and thereby $U(\theta)$, exhibits at least $5\,\mu\mathrm{K}$ of variation around the ring.

that the energy per particle in the Thomas-Fermi approximation is $E/N = \frac{5}{7}\mu$ [20]. This will be converted to a velocity spread across the cloud of $\sigma_v = \sqrt{\frac{10\mu}{7m}}$. In the trap described herein, the chemical potential for 3×10^5 atoms is $\mu = \hbar \times 2\pi \times 860\,\mathrm{Hz}$, yielding a predicted rms longitudinal velocity spread of $1.7\,\mathrm{mm/s}$.

This is expansion can be observed and quantified as the atom beam propagates around the ring, essentially providing unlimited time-of-flight until the atom beam begins to wrap around itself. Figure 4.10 shows the expanding beam after successive orbits around the ring, and the observed expansion rate of $1.8\,\mathrm{mm/s}$ is in good agreement with the expected value.

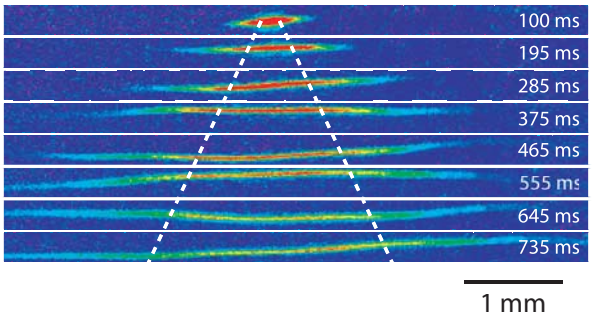

Figure 4.10: Mean-field driven expansion into the waveguide. As discussed in text, the mean-field energy released upon cessation of the longitudinal trap results in a 1.8 mm/s rms velocity width of the beam. Images shown were captured after successive laps around the ring at angular velocity $\Omega = 2\pi \times 11\,\mathrm{Hz}$. Dotted lines follow the uniformly expanding rms width.

4.9 Prospects for Sagnac Interferometry

One of the most exciting potential applications of the circular atom waveguide would be its use as a sensitive rotation sensor. The use of atom interferometry for a gyroscopic measurement has already proven a short-term sensitivity better than the best ring laser gyroscopes [87]. The principle of operation is based on the Sagnac effect [88], where an interferometric signal based on splitting a wave into counter-propagating beams which traverse a beam path that encloses an area A. The beams recombine and the relative phase is measured. If this measurement is conducted in a rotating frame Ω, then the effective path length is increased (decreased) for the beam traveling in the same (opposite) direction as the rotation. The relative phase between the waves at recombination is

$$\delta\phi = \frac{8\pi\Omega A}{\lambda v}\,. \tag{4.22}$$

This was derived for light, but is valid for matter waves of $\lambda = h/p$, which gives the matter Sagnac phase shift to be

$$\delta\phi = \frac{4m\Omega A}{\hbar}\,. \tag{4.23}$$

The sensitive atom gyroscope of Kasevich et al. [87] was implemented in free space. As ultracold atom techniques have become more refined, the use of atom waveguides to engineer an area-enclosing beam path has garnered much interest and experimental investigation

in recent years [89, 90, 91].

Achieving Sagnac interferometry in the circular waveguide described in this chapter is an attractive experimental avenue, especially due to the possibility of employing optical atom beamsplitters (discussed in the next section) which are useful in this context because of the sub-recoil velocities associated with Bose condensates. To get an idea of the potential sensitivity of a Sagnac interferometer in this storage ring, we note that the phase sensitivity will be limited by the atomic shot noise, $\sqrt{N}$. Given the $N = 3\times10^5$ atoms in the ring and the ~ 100 ms orbiting time, our waveguide could potentially have a measurement sensitivity of $\Delta\Omega = \hbar/4mA\sqrt{N} \sim 10^{-8}$ rad/s from a 1 s long (i.e. 10 lap) measurement. While this figure is nearly 20 times that of existing atom-based gyroscopes [87], improvements such as launching the atoms at higher velocities, increasing the TORT radius, and increasing the atom number may ultimately yield a useful, compact sensing device.

4.10 Bi-directional Propagation in the Circular Waveguide

Any interferometric measurement scheme, with either light or material particles, follows a basic structure: source(s) → beamsplitter → phase accumulation → beamsplitter recombination[3] → intensity detection. For viable Sagnac interferometry with atoms in the circular waveguide, all these elements must be demonstrated. With the 3×10^5 atom BEC as the "source," the next step is establishing an atomic beamsplitter in the ring. Ideally, the beamsplitter should take the at rest $|p=0\rangle$ atomic population and coherently transfer all of the atoms into a superposition of opposing momentum states $(|p=+p'\rangle \pm |p=-p'\rangle)/\sqrt{2}$.[4] The atoms would then propagate about the ring, pass each other on the opposite side, and then recombine at the beamsplitter location. The identical beamsplitting action is reapplied, and the phase-sensitive interference signal is read out.

[3] To effect the recombination step a "reflection" is sometimes required. With atoms, this typically is accomplished by a π-pulse (as compared to the $\pi/2$-pulse which serves as the 50/50 beamsplitter).

[4] For atoms confined to the ring, this may be recast in terms of orbital angular momentum states $|L=0\rangle \rightarrow (|L=+m\rho_o^2\Omega\rangle \pm |L=-m\rho_o^2\Omega\rangle)/\sqrt{2}$.

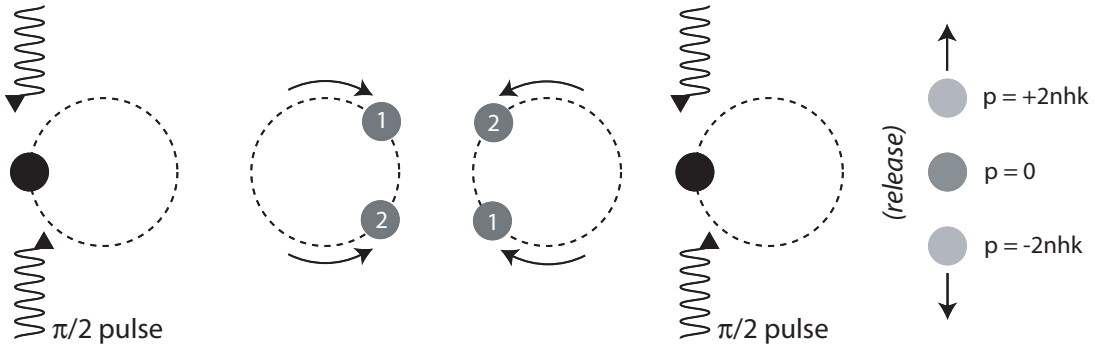

Figure 4.11: Diagram of possible Sagnac interferometry in scheme in a circular waveguide. Counter-propagating optical beams coherently transfer atoms into opposing orbits about the waveguide. The atom pulses (labeled "1" and "2") pass each other on the opposite side and recombine at the origin. The optical beamsplitters are reapplied and the accrued phase difference may be read out, for example, in atomic population differences.

4.10.1 Coherent Atomic Beamsplitters via Light Scattering

Previous attempts to accomplish magnetic beamsplitting, under even more favorable circumstances, proved problematic due to uncontrolled beam filamentation [58, 92]. We look instead to the well-established technique of momentum transfer via light scattering to act as the necessary beamsplitting element, and its proposed use in the circular waveguide is depicted in Figure 4.11. At MIT during the 1980's, fundamental light scattering experiments were conducted which demonstrated Bragg scattering of atoms [93] and Kapitza-Dirac scattering of atoms [94] with off-resonant laser light. The former technique has been used extensively in recent years with Bose condensates [95], both as a spectroscopic tool [96] and as a means of momentum transfer . Bragg scattering could work in this context by overlapping two co-propagating laser beams with a small, coherent frequency difference and then intersecting two such dual-frequency beams at the atoms [97].

A variant of Kapitza-Dirac scattering is a simpler means of doing this. The multiple pulses of light mimic the frequency structure of Bragg scattering beams to give efficient momentum transfer to $|\pm p\rangle$ momentum states, and it has been used in recent interferometry experiments with ultracold atoms in a manner similar to that presented here [98, 99]. In its original presentation, KD scattering was introduced as the deflection of electrons

from a standing wave of light [100]. In the modern context of KD scattering, atoms are diffracted by a standing wave of off-resonant light for a time τ, with the restriction that $\tau \ll 1/\omega_{rec}$ to guarantee that atomic motion is negligible relative to the wavelength of the scattering light. This is the Raman-Nath approximation, and allows the kinetic energy term in the Hamiltonian to be neglected.

To explore this regime to the desired task at hand, we follow the derivation of Ref. [101]. We begin by envisioning an ensemble of atoms illuminated with a laser field of wavevector k, atomic transition detuning $\delta = \omega - \omega_a$, polarization $\hat{\epsilon}$, and magnitude $\mathcal{E}_o$. The field is perfectly retroreflected to yield a standing wave field:

$$\begin{aligned} \mathbf{E}(z,t) &= \mathcal{E}_o \sin(kx - \omega t)\hat{\epsilon} + \mathcal{E}_o \sin(kx + \omega t)\hat{\epsilon} \\ &= 2\mathcal{E}_o \sin(kx)\cos(\omega t)\hat{\epsilon}\,. \end{aligned} \tag{4.24}$$

The field has a single-photon Rabi frequency of $\Omega_R = e\mathcal{E}_o\hat{\epsilon}\cdot\langle e|\mathbf{r}|g\rangle/\hbar$ between the ground state $|g\rangle$ and a single, dominant excited state $|e\rangle$. Finally, the laser field is envisioned to have an envelope of $f(t)$, which sets the time τ that the laser field is "on" by $\tau = \int f^2(t)\,dt$. Assuming the far-detuning limit $|\delta| \gg \Gamma$, where Γ is the linewidth of the $|e\rangle \rightarrow |g\rangle$ transition, the interaction Hamiltonian can then be written [101]:

$$U(z,t) = \frac{\hbar\Omega_R^2}{2\delta}(1 + \cos 2kx) f^2(t)\,. \tag{4.25}$$

Under the validity of the Raman-Nath approximation, an initial "at rest" atomic wavefunction $|g, p = 0\rangle$ will evolve to a final atomic wavefunction $|\psi\rangle$ of

$$\begin{aligned} |\psi\rangle &= |g,0\rangle \exp\left(-\frac{i}{\hbar}\int U(z,t)\,dt\right) \\ &= |g,0\rangle \exp\left[-i\frac{\Omega_R^2}{2\delta}\tau(1+\cos 2kz)\right]\,. \end{aligned} \tag{4.26}$$

The presence of the $\cos 2kz$ term in the exponential relates this expression to the well-known Bessel functions of the first order [102], defined by $e^{i\alpha\cos\beta} = \sum_{j=-\infty}^{\infty} i^n J_n(\alpha) e^{in\alpha}$. Thus, Equation (4.26) becomes

$$|\psi\rangle = e^{-i\frac{\Omega_R^2}{2\delta}\tau} \sum_{j=-\infty}^{\infty} i^n J_n\left(\frac{\Omega_R^2\tau}{2\delta}\right)\left[e^{i2nkz}|g,0\rangle\right]\,. \tag{4.27}$$

Noting that $e^{iqx}|p\rangle = |p + \hbar q\rangle$, Equation (4.27) becomes

$$|\psi\rangle = e^{-i\frac{\Omega_R^2}{2\delta}\tau} \sum_{j=-\infty}^{\infty} i^n J_n\left(\frac{\Omega_R^2\tau}{2\delta}\right)|g, 2n\hbar k\rangle\,, \tag{4.28}$$

and the utility of this system becomes evident. After the Kapitza-Dirac scattering "event," the formerly at rest atomic wavefunction $|g, 0\rangle$ is now in a superposition of final momentum states $|g, 2n\hbar k\rangle$ with probability amplitude $J_n^2\left(\frac{\Omega_R^2\tau}{2\delta}\right)$. This does not immediately have the desired beamsplitting character, but does phase coherently populate opposing momentum states.

More advanced techniques, exploiting the relative phase accumulation $e^{i2n^2\hbar k^2 t/m}$ of each populated momentum state under free evolution, can even effect near unity transfer of atomic ensembles to specific opposing momentum states, i.e. $|g, 0\rangle \rightarrow (|g, 2n\hbar k\rangle + i|g, -2n\hbar k\rangle)/\sqrt{2}$, exactly the desired beamsplitter functionality [98, 103]. With a reliable KD beamsplitter, the Sagnac experiment in the ring could be carried out just as depicted in Figure 4.11.

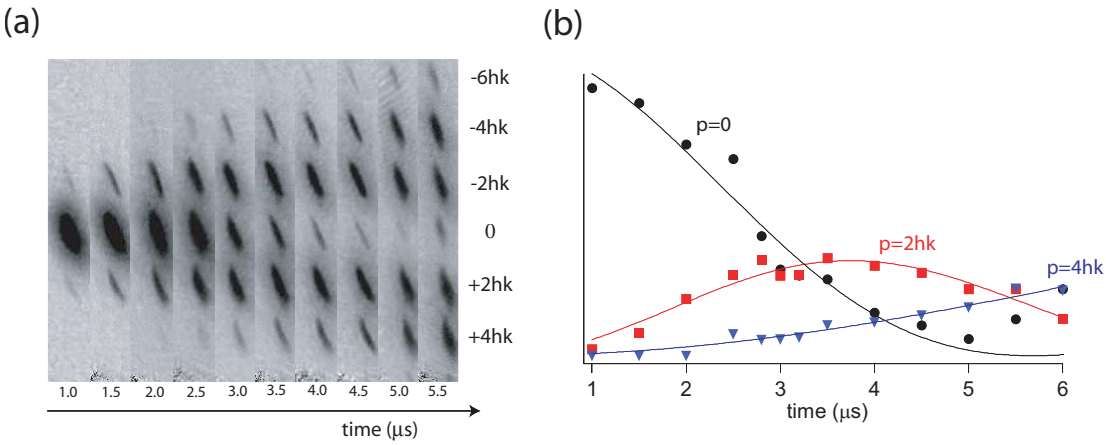

Figure 4.12: Kapitza-Dirac Scattering in the Ring. The KD pulse (a) As described in text, probabilities of populating the nth momentum order is $J_n^2\left(\frac{\Omega_R^2\tau}{2\delta}\right)$. 30 ms TOF imaging shows the scattering into higher momentum orders as the KD pulse time is increased. (The skewed appearance of the clouds is due to imperfect alignment of the KD beam with the trapping axes.) (b) Number counting of spatially separated momentum populations agrees well with the expected Bessel functions (solid curves).

4.10.2 Kapitza-Dirac Scattering in the Ring

We begin by demonstrating "normal" KD scattering, accomplished by illuminating the trapped atoms and then observing the populations of the separated wavepackets. Figure 4.12 shows the expected Bessel function population of momentum orders under time-of-flight imaging.

With the demonstrated ability to populate high-order momentum states, we attempted to send wavepackets in opposing directions about the ring. The balancing act is a fine one indeed, as the recoil energy for the first and second orders are $E_{2\hbar k} = 710\,\text{nK}$ and $2.85\,\mu\text{K}$, respectively, both less than the $5\,\mu\text{K}$ azimuthal energy profile measured in Figure 4.9. For this reason, the BEC needs to originate at the top of this potential curve before the KD pulse outcouples the momentum states to crest over the potential maxima.

Figure 4.13 shows a time-sequence of bidirectional propagation, as multiple momentum orders are set into motion. The technique successfully established bidirectional propagating in all but the $\pm 2\hbar k$ pulses, with the $4\hbar k$ exhibiting the highest contrast (and only visible full orbit recombination). Ultimately, the observation was compromised by the numerous momentum states occupying the ring, the spread of the wavepackets over the relatively long orbiting times, and perhaps collisions. The latter factor is difficult to quantify as it is not known if the pulses are in the same transverse state (i.e. ground state vs. oscillating coherent state). If 10^5 atoms at $\pm 2\hbar k$ pulses *were* to collide while in the transverse ground state after a half orbit, the collisional rate would be of the order 200 Hz. This would predict approximately 4 collisions per atom on a single pass, which would bring both beams to an effective halt in the 5μK ring. As considered, he collisional probability per pass is independent of velocity, and the fact that the $4\hbar k$ pulses pass each either renders this analysis moot or speaks a transverse excitation which vastly reduces this collision rate.

It should be clear from Figures 4.12 and 4.14 that "normal" KD scattering does not at all act as the desired beamsplitting element because of the inability to split the population into specific $\pm 2n\hbar k$ momentum orders with high efficiency. Wu *et al.* [103] report a modified KD scattering technique which can, in principle, transfer nearly the entire $p = 0$ population to a specific $p = \pm 2n\hbar k$ order with very high efficiency[5]. We attempted to

[5]Ref. [103] reports maximum theoretical fidelities of 99.99% for $n = 1$, 99.1% for $n = 2$, 96.6% for $n = 3$,

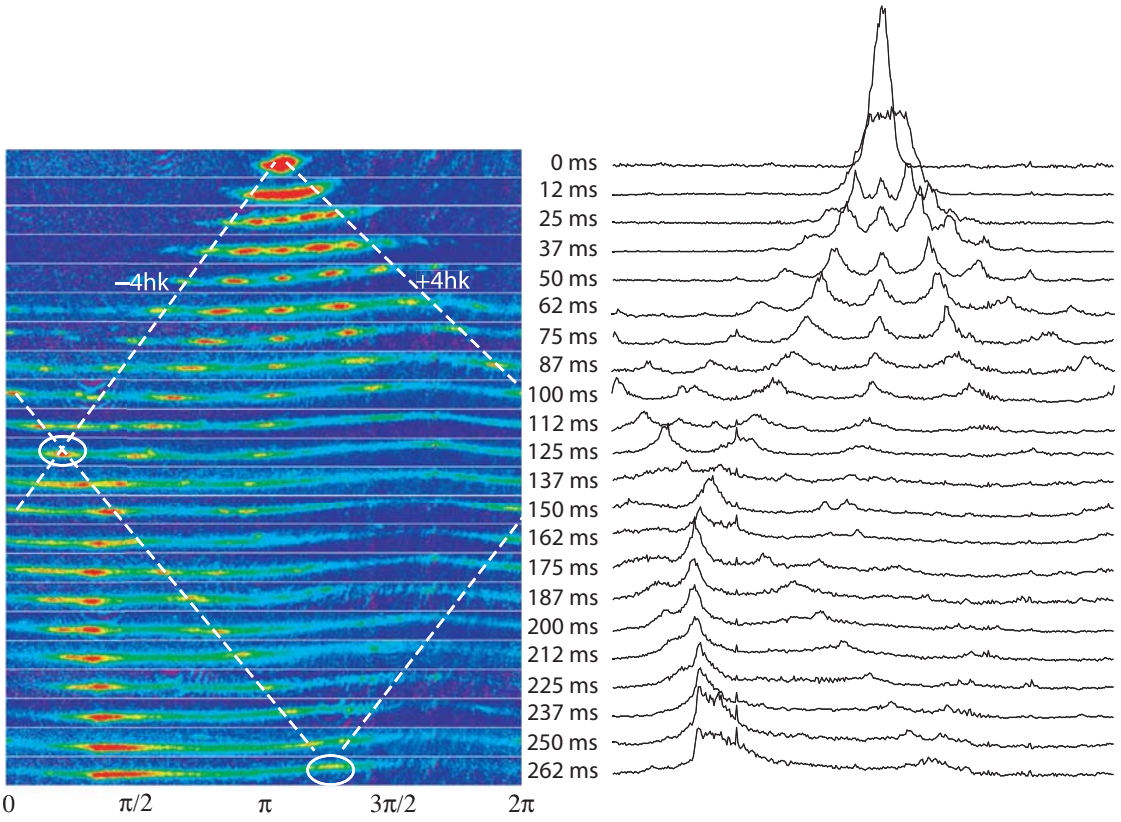

Figure 4.13: Bidirectional propagation in the ring via Kapitza-Dirac scattering. After a KD pulse which populates numerous momentum orders, we may observe their motion about the ring. All momentum orders $n \geq 2$ had enough kinetic energy to overcome the potential variations $U(\theta)$. The dotted lines guide the eye with the $\pm 4\hbar k$ pulses which can be seen crossing on the "far side" at $t = 125\,\text{ms}$ and finally recombining near the origin. That the pulses did not meet up *at* the origin implies some small net velocity at the start of the launch. Note the apparent potential valley from $\frac{3\pi}{2} \lesssim \theta \lesssim \pi$ and the potential maximum at $\theta \approx \frac{\pi}{2}$, exactly the azimuthal potential structure seen in Figure 4.9.

implement this technique, which is basically a two-pulse KD sequence with four parameters, the Rabi frequency Ω_R, the first pulse time τ_1, a wait time τ_w, and a second pulse time τ_2. The principle which allows this is a multipath interference effect between the amplitudes $C_n = \frac{1}{\sqrt{2}}(c_n + c_{-n})$, where c_n is the amplitude of the momentum state $|p = 2n\hbar k\rangle$. Ideally, the pulse sequence inverts the population between the zero-momentum state and some non-zero momentum order n', i.e. $C_0 = 1, C_{n\neq 0} = 0 \rightarrow C_{n'} = 1, C_{n\neq n'} = 0$. The Raman-Nath

and 91.7% for $n = 4$

regime equations discussed earlier, coupled with the free evolution phases $e^{-i2n^2\hbar k^2 t/m}$ allow a large enough parameter space such that proper values of Ω_R, τ_1, τ_w, and τ_2 yield mostly constructive interference for the $C_{n'}$ and destructive interference for $C_{n\neq n'}$.

In practice, while this prescription did not yield the optimal efficiencies, it was efficacious in vastly improving the momentum transfer to specific diffraction orders. Figure 4.14 shows images of this procedure enacted for the first- and second-orders.

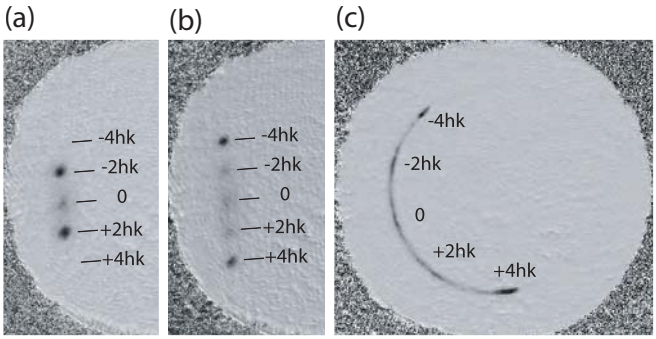

Figure 4.14: Resonant Kapitza-Dirac scattering into specific momentum modes. Using two pulse techniques [103], majority populations are driven into (a) $\pm 2\hbar k$ and (b) $\pm 4\hbar k$, as seen in 25 ms time-of-flight. (c) The same pulse in (b) is applied and atoms are allowed to propagate in the ring with enough energy to overcome the azimuthal potential variations. The sizeable remainder of 0 and $\pm 2\hbar k$ populations, as well as the unbalanced $\pm 4\hbar k$ populations, is typical for these experiments and shows the limitations of the resonant transfer in this implementation.

Unfortunately, the multiple pulse method did not prove to be robust in our experiments, as wide variances in transfer efficiency were observed shot-to-shot. Other techniques were attempted such as modulating the intensity KD pulse at the $n = 2$ Bragg resonance, but we observed similarly sporadic and inefficient experimental results. The fact that the initial beamsplitter was unreliable gave little hope that we would be able to demonstrate the second recombining pulse necessary for a Sagnac interferometer in this first iteration of the ultracold atom storage ring. We look forward to advances on this front in other more experiments in circular waveguides, perhaps even the second generation of this particular implementation.

Chapter 5

Diagnosis of a Guided Atom Laser Pulse

This chapter explores the derivation and implementation of a new tomographic technique to ascertain the state of a freely-propagating atomic ensemble; the work in this chapter was presented in the publication:

- *K. L. Moore, S. Gupta, K. W. Murch, and D. M. Stamper-Kurn, Probing the quantum state of a guided atom laser pulse, Phys. Rev. Lett.* ***97****, 180401 (2006). Included in Appendix H.*

Upon observation of the unterminated motion the atom beam launched into the circular waveguide, the following question immediately came to mind: "Is it still a BEC?" For reasons that will be discussed in this chapter, the query itself is ill-posed. Nevertheless, this was the most commonly asked question upon presentation of the ultracold atom storage ring, even to the community of experts working in the field of quantum degenerate atomic systems. The curiosity underlying this problematic question does represent a valid concern, and this chapter will address how to ask and answer the correct formulation of this concern. The answer is of paramount importance if this system is to be viable for atom interferometry, as all contributions to the evolution of the atomic phase under propagation in the circular waveguide must be accounted for.

5.1 Initial Conditions

The central question of this chapter is depicted in Figure 5.1. Succinctly stated, we want to know the quantum state of the atom laser beam as it propagates around the circular waveguide.

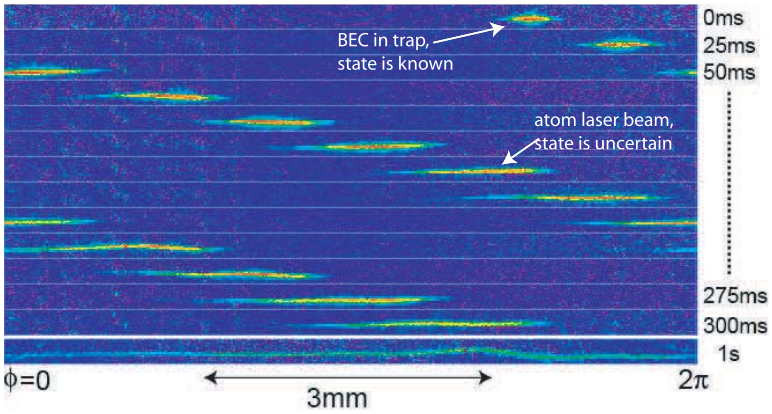

Figure 5.1: Expanding guided atom laser beam

With the general Thomas-Fermi solution for static traps, we input our particular experimental parameters (summarized in Table 5.1) and proclaim with confidence the initial state of the beam. To begin to understand the subsequent state of the system, we first examine the "launch" sequence. This was described briefly in the preceding chapter, but given the known effects of the bias field on the TORT field, we may guess the form of the longitudinal potential $U(\theta)$ experienced by the beam to be

$$U(\theta,t) = \begin{cases} \frac{1}{2}m\omega_\theta^2\left(\rho_o\theta\right)^2 & t<0 \\ \frac{m\rho_o\Omega\theta}{2}\left(\frac{t}{30\,ms}\right) & 0\le t<30\,ms \\ \frac{m\rho_o\Omega\theta}{2}\left(\frac{60\,ms-t}{30\,ms}\right) & 30\,ms<t\le 60\,ms \\ 0 & 60\,ms\le t\,. \end{cases} \tag{5.1}$$

This equation is obtained by a knowledge of the endpoints of the motion, i.e. the initial azimuthal trapping potential ($\frac{1}{2}m\omega_\theta^2(\rho_o^2\theta)^2$) and the final angular velocity (Ω). Any θ dependence beyond the linear terms in the $0 \le t \le 60\,\text{ms}$ would add or subtract to the

m	: Atomic mass of Rb-87	$1.44 \times 10^{-25}\,\mathrm{kg}$
N	: Number of atoms	3×10^5
ρ_o	: Circular trap radius	$1.25\,\mathrm{mm}$
$(\omega_z, \omega_\rho, \omega_\phi)$	: Trapping frequencies (pre-launch)	$2\pi \times (85, 85, 6)\,\mathrm{Hz}$
(ω_T, ω_ϕ)	: Trapping frequencies (post-launch)	$2\pi \times (85, 0)\,\mathrm{Hz}$
a_T	: Transverse oscillator length, $\sqrt{m/2\hbar\omega_T}$	$0.82\,\mu\mathrm{m}$
Ω	: Mean angular velocity of beam.....	*depends on launch*

Table 5.1: Guided atom laser beam parameters.

observed rms momentum width σ_P, which is already fully accounted for by the conversion of the mean-field energy of the cloud into longitudinal kinetic energy. This said, the exact effect of the launching sequence upon the beam is uncertain, and while we can propose models for the evolution from the trapped state into the freely-propagating guided beam state, we must independently verify the state of the beam after the launch and during free propagation.

5.2 Free Evolution in the Circular Waveguide

As the longitudinal potential is "turned off" by balancing the magnetic storage ring, the desired final state is an atomic beam propagating azimuthally while in the ground state of the transverse potential $\frac{1}{2}m\omega_T^2((\rho - \rho_o)^2 + z^2)$. As the mean field energy is converted into kinetic energy on a timescale of $\sim 10\,\mathrm{ms}$ [104], it would seem logical to guess that the transverse state of the beam would evolve to the ground state on the same timescale.

We tested this hypothesis by imaging the beam after variable propagation times in the ring under a relatively slow launch of $\Omega = 2\pi \times 6.3\,\mathrm{Hz}$. The slow launch part is important because, as noted in Table 5.1, the oscillator length is $a_T = 0.82\mu\mathrm{m}$, well below the resolution of our imaging system ($1.8\mu\mathrm{m}$ per pixel at a magnification of 3.7). Thus, time-of-flight imaging must be employed. Of course, for a propagating beam the atoms will not simply drop vertically under gravity, but retain a horizontal velocity of $\rho_o\Omega$. This will carry them to the edges of the 3 mm inner diameter (ID) imaging aperture in a time $\frac{1}{\rho_o\Omega}\sqrt{(ID/2)^2 - \rho_o^2}$ ($= 16.7\,\mathrm{ms}$, in this case). With 15 ms TOF, the rms width of the ground

state oscillator length is 6.6 μm, a size scale our imaging system can resolve. To be sure we are imaging the central width of the beam in the same location (with same magnification, etc.), the rms widths are measured after each period of orbit $T = 2\pi/\Omega = 158$ ms (presented in Figure 5.2).

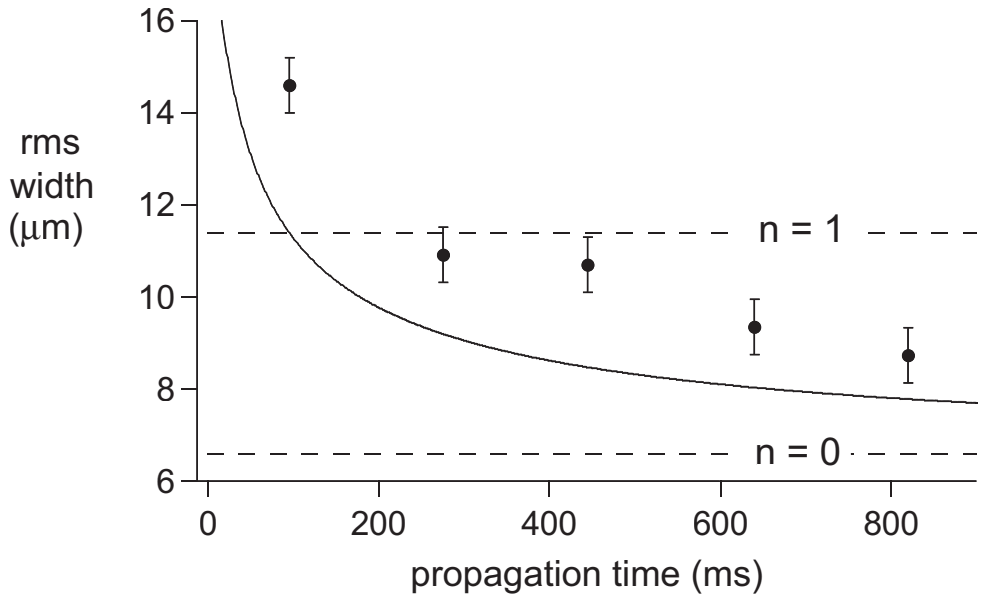

Figure 5.2: Observed transverse widths for atoms pulses after 15 ms TOF. Atoms were launched at very low angular velocity, $\Omega = 2\pi \times 6.3$ Hz. The ground state oscillator length and the first excited state oscillator length (after 15 ms time of flight) are set for reference. The single error bar represents the typical statistical uncertainty in the time-of-flight measurement. Solid line is a 1D model for the transverse width, given experimental parameters.

These data clearly contradict our initial guess of a ~ 10 ms decay to the ground state oscillator length, with the characteristic timescale at least an order of magnitude longer than expected. To account for this discrepancy, we developed a 1-dimensional model for the evolution of the interacting atoms as they freely expanded into the waveguide, roughly following the treatment of Salasnich *et al.* [105]. The prediction of this model is compared to the observed data in Figure 5.2, and while the correspondence between the simplified model and the observed transverse widths is hardly perfect, it is perhaps not terrible for the simplicity of the model. That both the model and the data approach the ground state oscillator length on the same timescale ($\sim$ 100's of ms) indicate that the atomic beam in

the waveguide does appear one-dimensional, with the decay to the transverse ground state oscillator length merely limited by mean-field repulsion. This result gives strong evidence that theoretical considerations of the longitudinal state of the beam, which will occupy the remainder of this chapter, need not consider the transverse state of the beam beyond the predicted values extrapolated from the model. We now focus our efforts solely on the longitudinal state of the beam, a rather involved topic which will consume the rest of this chapter.

5.3 A Note on Coordinates

It will be convenient to treat the system in the rest frame of the propagating atom beam. As the beam is rotating with respect to the lab frame, this may cause some confusion in regards to coordinate systems. To clarify this, we present Figure 5.3 to define the rotating beam coordinates relative to the stationary lab frame. Similarly, Table 5.3 summarizes the coordinate conventions.

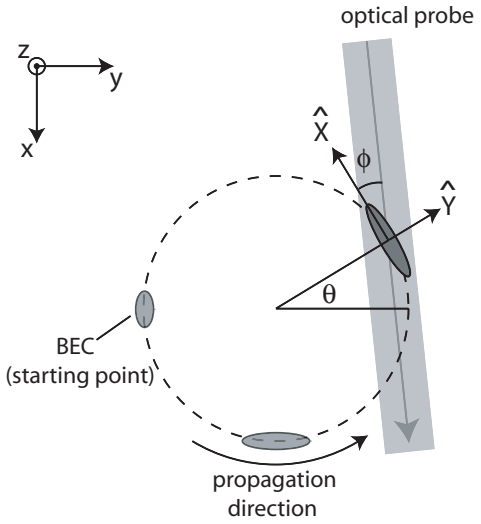

Figure 5.3: Coordinate Axes for the Rotating Atom Beam.

Included is the presence of an optical probe which may illuminate the beam at any position θ in the ring. The relevant coordinate for the optical probe will be the relative

x, y, z : Cartesian coordinates in lab frame, defined (as in chapter 1)
θ : Angular position in ring, measured off y-axis (as in chapter 4)
$\hat{X}$: Propagating axis of the atom beam
X : Longitudinal position, $\rho_o\theta$
σ_X : rms longitudinal width
P : Longitudinal momentum, $\rho_o\Omega$
σ_P : rms momentum width ($= m \times 1.8\,\mu$m/ms)
$\hat{Y}$: Transverse axis of the atom beam
ϕ : Orientation of optical probe relative to the propagating axis of the beam

Table 5.2: Guided atom laser beam coordinate definitions.

angle ϕ between the wavevector of the probe and the longitudinal axis of the beam, $\hat{X}$. These are not to be confused with the stationary axes x, y, z and θ defined in previous chapters.

The remainder of the chapter is concerned with dynamics of the longitudinal coordinate, and the phase space formalism introduced in the next section will be applied to the canonical coordinates X and P, as defined in Table 5.3. As we will show, the system will be characterized entirely by the variables X, σ_X, P, σ_P, and ϕ.

5.4 Phase space Density and the Wigner function

As non-equilibrium systems, particle beams are best understood in the context of a phase space density function $f(\mathbf{r}, \mathbf{p}, t)$ which describes the distribution of particles in phase space with $\int f(\mathbf{r}, \mathbf{p}, t)\, d\mathbf{r}\, d\mathbf{p} = N$, the total number of particles . The evolution of the system is then given by the equation of motion:

$$\left(\frac{\partial}{\partial t} + \frac{\mathbf{p}}{m} \cdot \frac{\partial}{\partial \mathbf{r}} - \frac{\partial U(\mathbf{r}, t)}{\partial \mathbf{r}} \cdot \frac{\partial}{\partial \mathbf{p}}\right) f(\mathbf{r}, \mathbf{p}, t) = \left(\frac{\partial f}{\partial t}\right)_{coll}, \tag{5.2}$$

where $U(\mathbf{r}, t)$ is the potential energy function and $(\partial f/\partial t)_{coll}$ describes the effect of collisions; for dilute gases where binary collisions are dominant, one obtains the Boltzmann transport equation [106]. A wide variety of systems may be understood in this context, spanning an immense energy range from astrophysical phenomena [107] to high-energy beams of charged particles [108] and finally down to the lowest energy scales known to

man, ultracold molecular beams [109, 53]. Full knowledge of the phase space density function and its time evolution completely characterizes a particle beam.

The notion of a phase space density function is predicated upon the assumption that a particle may have a well-defined position and momentum, a supposition which strictly has no validity in the context of quantum mechanics. The phase space picture in quantum mechanics may be recovered through the Wigner quasi-probability distribution [110], and as we have a particle beam which originated from a quantum degenerate source governed by a many-body wavefunction such a treatment would seem appropriate. Proceeding, the single-particle Wigner function is defined relative to a pure quantum state $|\psi\rangle$ as:

$$\mathcal{W}(\mathbf{r},\mathbf{p}) = \frac{1}{2\pi}\int e^{-i\mathbf{p}\cdot\mathbf{a}/\hbar}\psi^*\left(\mathbf{r}-\frac{\mathbf{a}}{2}\right)\psi\left(\mathbf{r}+\frac{\mathbf{a}}{2}\right)d^3\mathbf{a}\,. \tag{5.3}$$

$\mathcal{W}(\mathbf{r},\mathbf{p})$ is the equivalent of the classical phase space density function as $\int \mathcal{W}(\mathbf{r},\mathbf{p})\,d^3\mathbf{p} = |\psi(\mathbf{r})|^2$ and $\int \mathcal{W}(\mathbf{r},\mathbf{p})\,d^3\mathbf{r} = |\widetilde{\psi}(\mathbf{p})|^2$, where $\widetilde{\psi}(\mathbf{p}) = \left(\frac{1}{2\pi\hbar}\right)^{3/2}\int \psi(\mathbf{r})\exp\left(-i\mathbf{p}\cdot\mathbf{r}/\hbar\right)\,d^3\mathbf{r}$ is the momentum-space wavefunction. While the case of a BEC opens the possibility that many particles could occupy the same wavefunction, usually a phase space description is concerned with many particles, perhaps with a statistical mixture of quantum states. All the information about the state of a quantum system is contained in the density matrix $\hat{\rho}$, and the density operator relates to the Wigner function through the equation

$$\mathcal{W}(\mathbf{r},\mathbf{p}) = \frac{1}{2\pi}\int e^{-i\mathbf{p}\cdot\mathbf{a}/\hbar}\left\langle \mathbf{r}-\frac{\mathbf{a}}{2}\right|\hat{\rho}\left|\mathbf{r}+\frac{\mathbf{a}}{2}\right\rangle d\mathbf{a}\,. \tag{5.4}$$

For a free-particle system in the absence of inter-particle interactions the equation of motion for the Wigner function, i.e. the quantum mechanically correct equivalent to the classical Equation (5.2), is given by [111, 112]:

$$\left(\frac{\partial}{\partial t}+\frac{\mathbf{p}}{m}\cdot\frac{\partial}{\partial\mathbf{r}}\right)\mathcal{W}(\mathbf{r},\mathbf{p},t) = \sum_{j=0}^{\infty}\frac{(\hbar/2i)^{2j}}{(2j+1)!}\frac{\partial^{2j+1}U(\mathbf{r},t)}{\partial\mathbf{r}^{2j+1}}\cdot\frac{\partial^{2j+1}\mathcal{W}}{\partial\mathbf{p}^{2j+1}} \tag{5.5}$$

For potentials with no spatial dependence beyond second-order, Equation (5.5) is identical to Equation (5.2), though the Wigner function famously allows $\mathcal{W}(\mathbf{r},\mathbf{p}) < 0$ for certain regions of phase space which may arise from non-classical interference terms. For a system with $U = 0$, the time evolution dictated by Equation (5.5) may be written simply as:

$$\mathcal{W}(\mathbf{r},\mathbf{p},t) = \mathcal{W}\left(\mathbf{r}-\frac{\mathbf{p}t}{m},\mathbf{p},0\right)\,. \tag{5.6}$$

This "shearing" associated with free evolution in phase space introduces an important component of the phase space picture, namely the correlation between position and momentum. Without delving into the details which are more carefully considered elsewhere [113, 114], we can identify the first-order correlation term as $\langle (r_j - \langle r_j \rangle)(p_j - \langle p_j \rangle) \rangle$ on any component of $\mathbf{r}$. If this is non-zero, then the position and momentum of the phase space distribution are not statistically independent (to first order). Under Equation (5.6), this correlation term becomes non-zero for all $t > 0$.

With this architecture in hand we may hypothesize about the evolution of the longitudinal state of the atomic ensemble, with the accuracy of the guess to be checked against the phase space probe developed in the latter part of this chapter. In this vein, three different regimes present themselves. First, there is the condensate regime where the distribution is spread out in X but tightly distributed about $P = 0$. The second regime occurs after the confining potential is extinguished and the mean field energy is converted into kinetic energy. In phase space, this process looks like a vertical shear, driving a strong correlation between position and momentum. The third regime is that of free evolution, as dictated by Equation (5.2). In this regime, the mean field energy is negligible and the beam is freely expanding in the flat waveguide. These three processes are depicted in Figure 5.4.

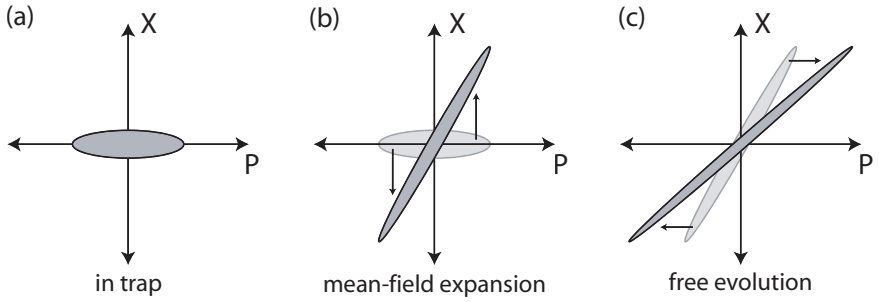

Figure 5.4: Hypothesized phase space evolution. Shown are the three regimes of phase space evolution arising from the launch in Equation (5.1).

With this picture in mind, and our notion of phase space and the Wigner function as the appropriate framework to describe the quantum state of a particle beam, we look for a probe which can ascertain the form of the phase space distribution. The final state can then be described in this context, and since we are considering a system of many particles, the

notion of phase space density remains a useful construction. The distribution of particles will occupy an effective "area" $\mathcal{A}$ in phase space, and this area will be some greater-than-unity multiple of $\hbar$. The ratio of the number of particles to the phase space area of the Wigner distribution yields the phase space density Γ, and under the free evolution both are conserved conserved. As $\Gamma = N$ for a $T = 0$ Bose condensate, we look for a similarly macroscopic phase space density of the propagating beam. We may also borrow a useful notion from particle beams at the other end of the energy spectrum, namely *emittance*. Emittance is employed somewhat in a statement of ignorance of the true phase space area of a beam, but bounds the system by an ellipsoid inside of which the true phase space area must lie [108]. Thus emittance serves as an upper bound on the phase space area, subsequently giving a lower bound on the phase space density.

In this spirit, we posit further that the phase space description of the ultracold atom beam in the circular waveguide can be reasonably described (or at least bounded) by a Gaussian phase space distribution. As the longitudinal width (σ_X) is measurable at all times by absorption imaging and the momentum width (σ_P) is obtained through successive absorption images. An absolute upper bound on the phase space area is obtained by the product $\mathcal{A}_{max} = \sigma_X \sigma_P$. We may be initially comforted by inserting some experimental values into this formula; after just a half revolution in the waveguide the rms longitudinal width was measured to be $\sigma_X = 120\,\mu$m, implying a phase space area of $\mathcal{A} = 310\hbar$. For 3×10^5 atoms, this yields a phase space density of $\Gamma \approx 1000$. This is surely evidence of macroscopic occupation of quantum states, but is a far cry from the presumed initial condition of $\Gamma = N$. Examining Figure 5.4(b) and (c) immediately show that the mere product of the observed σ_X and σ_P could be overestimating the true phase space area in the presence of a strong $X - P$ correlation. Indeed, after both mean field expansion and free evolution we have every reason to believe that there exists a very strong correlation between position and momentum. Taking this into consideration, we may write down a provisional Wigner function for the beam:

$$\mathcal{W}(X,P) = \frac{\exp\left[-\frac{1}{2(1-\eta^2)}\left(\frac{X^2}{\sigma_X^2} - 2\eta\frac{XP}{\sigma_X\sigma_P} + \frac{P^2}{\sigma_P^2}\right)\right]}{2\pi\sigma_X\sigma_P\sqrt{1-\eta^2}}, \tag{5.7}$$

where $\eta = \langle XP\rangle/\sigma_X\sigma_P$ is the correlation parameter in the center-of-mass frame of the

beam. The actual phase space area of such a beam is smaller than the aforementioned estimate by a factor $\mathcal{A}/\mathcal{A}_{max} = \sqrt{1-\eta^2}$. Put another way, for proper characterization of a beam with position-momentum correlations one must distinguish between a spatially inhomogeneous momentum width σ_P, which may be dominated by a coherent velocity chirp across the length of the beam, and a "homogeneous" width $\mathcal{A}/\sigma_X$.

While Equation (5.7) is not purported to be an *exact* description of the state, there are numerous reasons to posit this function (not the least of which is its simplicity for the ensuing calculations). Even after many months of launching beams derived from a BEC into motion about the ring, we observed no "smoking gun" which consistently distinguished the distribution as an expanding Thomas-Fermi profile (see Equation (**??**)) versus a Gaussian profile. At the very least, this can again be thought of only as an upper bound on the true phase space distribution, constraining the emittance of the beam.

5.5 Tomographic Imaging of the Wigner Function

In the preceding chapters, *absorption imaging* yielded $x-y$ projections of the three-dimensional spatial density distribution of an atomic population, $n(x,y,z)$, via attenuation of a known light intensity function $I_o(x,y)$ as

$$I(x,y) = I_o(x,y)\exp\left(-\int n(x,y,z)\,\sigma\,dz\right), \tag{5.8}$$

where $I(x,y)$ is the transmitted intensity and σ is the absorption cross section [**?**]. Such imaging is of course impossible for the two-dimensional Wigner distribution $\mathcal{W}(X,P)$, as it is not a function on real space. Spatial images do yield some information about the phase space distribution, however, as the 1D spatial density distribution $n(x)$ is related to the Wigner function of N particles by

$$n(X) = N\int \mathcal{W}(X,P)\,dP. \tag{5.9}$$

This projection has given, at the very least, a spatial bound on the phase space area, but the single line integral of the Wigner function is insufficient to "image" the full two-dimensional distribution $\mathcal{W}(X,P)$.

Tomography is the method by which a two-dimensional function is fully imaged with line integrals such as that in Equation (5.9). The technique relies on a mathematical symmetry between a line integral of a function and a line integral of its fourier transform, formally known as the *Projection-Slice Theorem* [115]. Suppose $f(u,v)$ is an unknown two-dimensional function; its full fourier transform is given by

$$F(k_u,k_v) = \frac{1}{2\pi}\int_{-\infty}^{\infty}\int_{-\infty}^{\infty} f(u,v)e^{-ik_u u}\,e^{-ik_v v}\,du\,dv. \tag{5.10}$$

We now consider a line integral on the y-axis

$$s(u) = \int_{-\infty}^{\infty} f(u,v)dv, \tag{5.11}$$

and its one-dimensional fourier transform

$$S(k_u) = \sqrt{\frac{1}{2\pi}}\int_{-\infty}^{\infty} s(u)e^{-ik_u u}\,du. \tag{5.12}$$

Combining Equations 5.11 and 5.12, we obtain the relation

$$\begin{aligned} S(k_u) &= \sqrt{\frac{1}{2\pi}}\int_{-\infty}^{\infty}\left[\int_{-\infty}^{\infty} f(u,v)dv\right]e^{-ik_u u}\,du \\ &= \int_{-\infty}^{\infty}\int_{-\infty}^{\infty} f(u,v)e^{-ik_u u}\,du\,dv \\ &= \sqrt{2\pi}\,F(k_u,0). \end{aligned} \tag{5.13}$$

The meaning of this relation is that the fourier transform $S(k_u)$ of a projection $s(u)$ of the source function $f(u,v)$ is proportional to a "slice" of the 2D fourier transform $F(k_u,0)$. This procedure can be generalized to any line integral on $f(u,v)$ in a rotated coordinate system ($\tilde{u} = u\cos\vartheta + v\sin\vartheta$, $\tilde{v} = -u\sin\vartheta + v\cos\vartheta$), allowing an infinite set of projections $s(\tilde{u}) = \int_{-\infty}^{\infty} f(u,v)\,d\tilde{v}$ from $0 \le \vartheta < \pi$ to construct the full fourier transform $F(k_u,k_v)$. Applying the inverse transform yields a "reconstruction" of the desired distribution $f(u,v)$, so named because the original function was not directly imaged (as in the case of absorption imaging), but rather inferred from a set of projections $s(\tilde{u})$. A visual representation of this process is shown in Figure 5.5.

The two-dimensional function of interest for a propagating beam is of course the Wigner quasi-probability distribution. We thus seek a probe which yields a signal dependent on the generalized line integral

$$w(\widetilde{X}) = \int_{-\infty}^{\infty} \mathcal{W}(X,P)\,d\widetilde{P}\,. \tag{5.14}$$

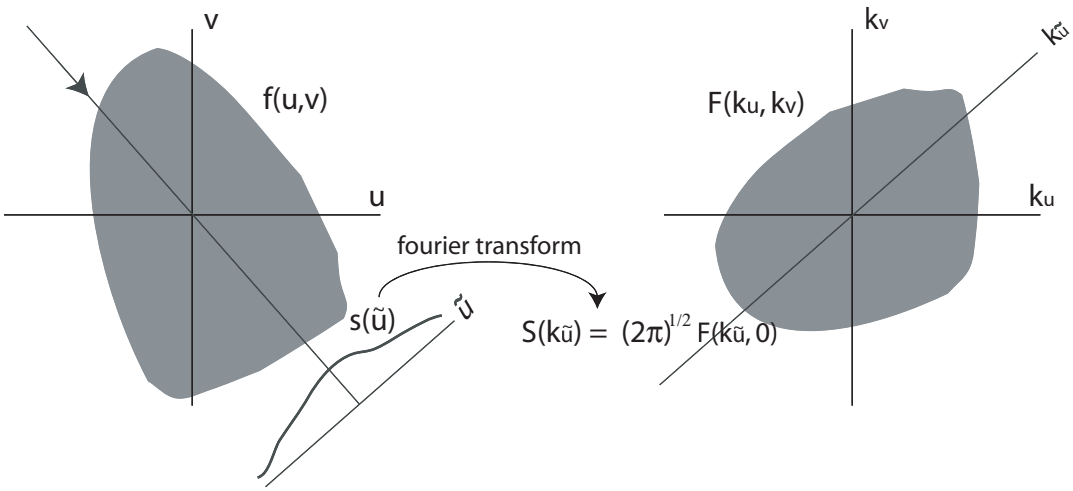

Figure 5.5: The Projection-slice theorem. Fourier transforms of line integrals in coordinate space correspond to slices in fourier space. A set of line integral projections thus clarifies the full fourier transform $F(k_u, k_v)$, and thereby the desired source function $f(u, v)$.

Obtaining the spatial probability distribution $w(X) = \int_{-\infty}^{\infty} \mathcal{W}(X, P)\, dP$ is typically straightforward, but obtaining projections for $\vartheta \neq 0$ is not. Finding and applying a probe capable of resolving a sufficient set of projections $w(\widetilde{X})$ to reconstruct the Wigner function $\mathcal{W}(X, P)$ occupies the remaining sections of this chapter, though we close this section by considering what tomography of the Gaussian Wigner function in Equation (5.7) would look like.

As depicted in Figure 5.6, simple spatial and momentum projections of Gaussian distributions such as that in Equation (5.7) cannot distinguish between correlated and uncorrelated distributions. Because of the functional simplicity of the Wigner function, the off-axis projections can be fully characterized by their rms Gaussian widths. Plotting these widths in Figure 5.6(b) shows that the correlation parameter is revealed in the full set of tomographic projections. The shaded region highlights the limits of allowing free propagation to carry out tomography. It is surely the case that information about σ_X, σ_P, and η can be obtained by absorption imaging after variable times of free propagation. This is tomography, of a sort, with assistance of Equation (5.6), which can be shown to yield

$$\sigma_X^2(t) = \left(\sigma_X^2(0) + \frac{\sigma_P^2}{m^2} t^2\right) + 2\left(\frac{\sigma_P t}{m}\right)\eta\,. \tag{5.15}$$

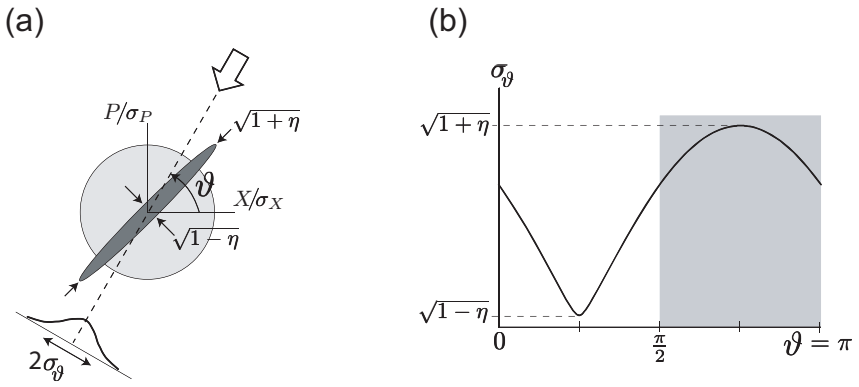

Figure 5.6: Probing a Gaussian Wigner function. (a) Off-axis projections are needed to access the true phase space density. The system is fully characterized by three parameters, σ_X, σ_P, and $\eta = \langle XP \rangle / \sigma_X \sigma_P$. (b) Plot of observed projection widths σ_ϑ show the virtues of tomography, with the widths directly measuring the correlation parameter η. Most desired is the region from $0 < \vartheta < \pi/2$, as the projection along the narrowed axis provides a much more accurate measure of η. The shaded region from $\pi/2 < \vartheta < \pi$ is the region accessible to "time of flight tomography," and fails as an accurate measure of η because for a highly-correlated system $\eta \to 1$.

According to this equation, making a large number of measurements of $|\psi(X,t)|^2$ for $0 < t < \infty$, would allow all three parameters to be extracted. There is a practical problem, however, namely that η is a number very close to unity and is thereby a weak fitting parameter. Ideally one would obtain the set of projections $0 < \vartheta < \pi/2$ as, the minimum value of σ_ϑ at $\vartheta = \pi/4$ gives a normalized width of $\sqrt{1-\eta}$. This is the "most sensitive" angle from which to probe, and is inaccessible to time-of-flight techniques because of the time asymmetry arising from the mean-field expansion, i.e. Equation (5.6) is only valid for $t > 0$. For an arbitrary distribution, projections at all angles $0 \leq \vartheta < \pi$ must of course be obtained to accurately reconstruct the distribution, but for the Gaussian distribution of Equation (5.7) only time-of-flight measurements of σ_X, σ_P, and a single projection along the narrowed axis are required to bound the phase space area.

5.6 Superradiance - A Signature of Coherence

One of the more dramatic signatures of Bose condensation in dilute gases involves the phenomenon known as "superradiance," first elucidated in the seminal work of Robert Dicke in 1954 [116]. Dicke's treatment does not necessitate a Bose-condensed sample, but the topic has seen a substantial revival in interest due to the dramatic superradiant behavior of BECs under certain experimental conditions. The crucial connection between BECs and superradiance is "coherence," and insofar as a BEC represents a macroscopic, many-particle wavefunction with a spatial extent significantly larger than the wavelength of resonant light, the superradiant properties of an ensemble are intimately related with the state of the system.

The details must be omitted here[1], but three factors collude to make superradiant scattering in BECs truly remarkable. The first factor of superradiance is the notion of "end-fire" modes, which come about for a collection of particles which are distributed inhomogeneously in space such that the ensemble is elongated in one direction (say, $\hat{z}$) relative to the remaining two. In this instance, final modes $\mathbf{k}_f = \pm|\mathbf{k}_o|\hat{X}$ which are emitted along the long axis are preferred from the bosonic stimulation (or the effective "bosonic" stimulation in the thermal or even fermionic gases [120]). Bose condensates, especially those confined in the aforementioned optical dipole and Ioffe-Pritchard traps, usually have an elongated axis and thereby strongly scatter along these directions. The second factor which make BECs ideal superradiance testbeds is the "global" coherence of the ensemble atoms, a consequence of the macroscopic occupation of a single quantum state. This will be explored in greater detail in the following section, but simply stated the phase coherence across the spatial extent of the ensemble allows an additive "phased antennae" effect which can cause constructive interference for some output modes and destructive interference for others. The third factor is purely a consequence of the nature of dilute atomic gas BECs, namely that the critical temperatures occur well below the recoil energy $\hbar^2|\mathbf{q}|^2/2m$ associated with the scattering even. This means that the scattered atoms will, under free propagation, separate from the atoms at rest. Counting the number of scattered atoms gives another method, besides the sometimes technically difficult photon detection

[1] We refer the reader to the Refs. [117, 118, 119] for more complete treatments.

of scattered light, to quantify the superradiant scattering rate.

5.7 Superradiance in the Ring

Enacting superradiant light scattering in the ultracold atom storage ring proved to be relatively simple in implementation. We began these experiments with the $\sim 3\times10^5$ atoms in a decompressed $(\omega_T, \omega_\phi) = 2\pi \times (85, 6)\,\mathrm{Hz}$ trap (as compared to the $\omega_\theta = 2\pi \times 35\,\mathrm{Hz}$ trap in the preceding chapter. The atoms were illuminated both in the trap and after the launch, approximately along the $\hat{x}$ direction with laser light $-560\,\mathrm{MHz}$ detuned from the $|^2S_{1/2}, F = 1\rangle \rightarrow |^2P_{3/2}F = 0\rangle$ transition. The light was circularly-polarized, implying that the phase of the TORT field (and therby the orientation of the atomic spins) should be irrelevant for determining the scattering rate[2]. Typical laser intensities were $10\,\mathrm{mW/cm^2}$, yielding single particle Rayleigh scattering rates of $400\,\mathrm{s^{-1}}$, and pulses were of duration $> 50\,\mu\mathrm{s}$ to ensure that we were not in the Kaptiza-Dirac regime (see Section 4.10.2).

After launching the atoms into motion about the ring, we illuminated the atom beam at various incidence angles ϕ and observed the characteristic superradiance effect of elongated Bose condensates, collective scattering out the end-fire mode. As the momentum dispersion of the beam ($\sigma_P = m \times 1.8\,\mathrm{mm/s}$) is nearly an order of magnitude less than the momentum imparted from a superradiant scattering event $2\hbar k = m \times 12.3\,\mathrm{mm/s}$, free propagation in the ring will separate the scattered atoms from the unscattered atoms. This is depicted in Figure 5.7.

Quantifying the superradiant scattering rate has been accomplished previously [117] by direct photocounting of the scattered photons. Despite numerous attempts, we were unable to measure the scattered photons in this system. This is likely due to the small number of scattered photons as well as the "orientation problem," in that at best we would be able to observe the superradiated photons at only a specific angle because the orientation of the superradiating axis is constantly rotating. As shown in Figure 5.7(d), we may quantify the number of superradiant scattering events by counting not photons but recoiling atoms. This most easily done by measuring the longitudinal center of mass,

[2]This was explicitly verified by synchronizing the superradiant light pulse to the TORT fields and varying the phase. As expected, no significant variation of the scattering rate with TORT phase was observed.

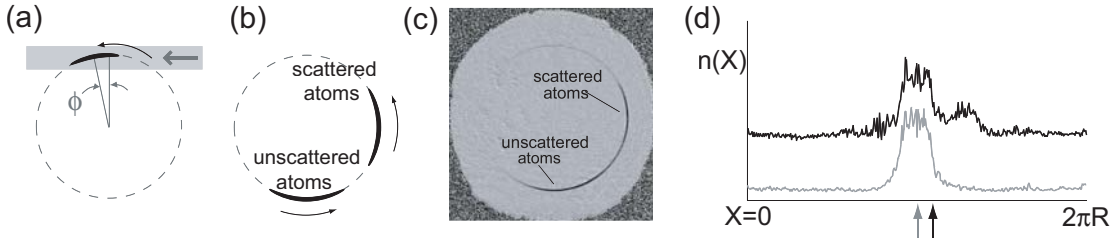

Figure 5.7: Superradiance of the atom pulse propagating in the circular waveguide. (a) Pump light illuminates the freely propagating atom beam at angle ϕ relative to the mean angular position, and (b) scattered atoms separate from the original pulse and can be distinguished from unscattered atoms. (c) Raw image of an atomic beam that has undergone superradiance. The contrast on the image cannot immediately make out Azimuthal density distributions $n(X)$ in the ring 160 ms after illumination are shown for beams that have (black) or have not (grey) undergone superradiant light scattering. The shifted center of mass (indicated by arrows) quantifies the total superradiant scattering rate.

$X_{c.m.}$, given by

$$X_{c.m.} = \frac{\int X\, n(X)\, dX}{\int n(X)\, dX} = \frac{N_{sc}}{N_{tot}} \left(\frac{2\hbar k}{m} t \right) , \tag{5.16}$$

where N_{sc} is the number of scattered atoms and N_{tot} is the total number of atoms. N_{sc} is of course a measure of the superradiant scattering rate, but to be useful we must remain in the "small-signal gain" regime [117] where the number of scattered atoms is still small relative to the unscattered atoms. If the superradiant "gain" exceeds the "loss" (which will be discussed extensively in subsequent sections), N_{sc} will increase exponentially and a center-of-mass measurement can be related to the exponential rate.

Using this method, we examined the angular dependence of the outcoupled fraction $f_{sc} = N_{sc}/N_{tot}$ for a given laser pulse of $150\,\mu$s duration and launch of $\Omega = 2\pi \times 9.1\,$Hz, shown in Figure 5.8:

This graph is, strictly speaking, a measurement of gain *minus* loss, so it is not immediately unclear from these data whether the gain, the loss, or both are responsible for the spike in N_{sc} around $\phi = 0$. The contributing factors [117] would not seem to account for the large variation of the overall superradiant gain, so we proceed by attempting to isolate the loss process. As we will see, the mechanism responsible for the angular variation of the superradiant scattering rate in Figure 5.8 is intimately related to the Wigner function of the atomic beam. This fact will be used to provide the desired phase space probe.

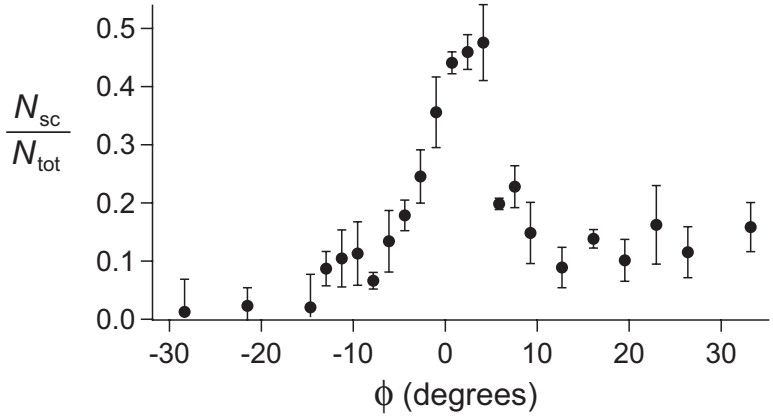

Figure 5.8: Angular dependence of superradiance. The propagating cloud was illuminated at various angles with a single optical pulse of intensity $10\,\mathrm{mW/cm^2}$, detuning $-560\,\mathrm{MHz}$ from the $F = 1 \rightarrow F' = 0$ transition, and duration $150\,\mu\mathrm{s}$. The superradiant population is counted via the center of mass measurements technique in Equation (5.16). These data do not distinguish between the angular dependence of the superradiant gain vs. loss, but do show the dramatic dependence of one or both of these quantities with angle.

5.8 Superradiant Pump-Probe Spectroscopy

Superradiant pump-probe spectroscopy (SPPS) was introduced by Yoshikawa *et al.* [121], and at its core utilizes the "wavefunction overlap" inherent in the superradiant scattering rate to probe the quantum mechanical character of a system. As noted in the preceding section, a BEC is an ideal source for superradiance. Thermal systems would not immediately seem a good source for superradiance given lack of large-scale coherence, but the particles comprising a gas of atoms at temperature T do have a thermal deBroglie wavelength of $\lambda_{dB} = \sqrt{2\pi\hbar^2/mk_BT}$. This sets the "size" of the single-particle wavepackets, as Gaussian wavefunctions with the momentum-space form $\phi(\mathbf{p}) = \exp\left(-\mathbf{p}^2/2mk_BT\right)$.

We humbly rename the technique of Yoshikawa *et al.* as *monochromatic* SPPS, for reasons that will become apparent. In monochromatic SPPS, an initial coherence in a gas is established by initiating superradiant Rayleigh scattering with a laser beam of wavevector $\mathbf{k}_o$ (the "pump" beam). The elongated geometry of the atom beam strongly favors scattering out the endfire mode[3] $\mathbf{k}_f = |\mathbf{k}_o|\hat{X}$, the effect of which is to convert all atomic

[3]This could be either or both $\pm\hat{X}$, with the preference depending on the orientation of the input mode $\mathbf{k}_o$ [122].

wavepackets in the system as $\psi_i(\mathbf{r}) \rightarrow (\alpha + \beta e^{i\mathbf{q}_1\cdot\mathbf{r}})\psi_i(\mathbf{r})$, where $\mathbf{q}_1 = \mathbf{k}_f - \mathbf{k}_o$. The hallmark of superradiance is the exponential growth of $|\beta|^2$ due to corresponding increase in the visibility of the $2\pi/|\mathbf{q}_1|$ density modulation, though this superposition state could be created via other processes, e.g. Bragg scattering.

The system is then allowed to evolve for a time τ, after which the *same* laser beam of wavevector $\mathbf{k}_o$ (now the "probe" beam) illuminates the system and superradiant light scattering is recommenced. That the identical wavevector is utilized for the pump and probe motivates the preface of *monochromatic* SPPS. The scattering rate Γ_{SR} of this pump pulse off the modulated density profile is proportional to square of the phase matching integral

$$\Gamma_{SR} \propto \int d\Omega(\mathbf{k}_f) \left| \int e^{-i(\mathbf{k}_f - \mathbf{k}_o)\cdot\mathbf{r}} \psi^*_{sc}(\mathbf{r},\tau)\psi(\mathbf{r},\tau)\, d^3\mathbf{r} \right|^2 , \tag{5.17}$$

where

$$\psi_{sc}(\mathbf{r},\tau) = \psi\left(\mathbf{r} - \frac{\hbar\mathbf{q}_1}{m}\tau, \tau\right) e^{i\mathbf{q}_1\cdot\mathbf{r}}\, e^{-i\frac{\hbar|\mathbf{q}_1|^2}{2m}\tau} , \tag{5.18}$$

and $\psi(\mathbf{r},\tau)$ is the atomic wavefunction.

End-fire superradiance is still preferred, meaning $\mathbf{k}_f = |\mathbf{k}_o|\hat{X}$ and we find that the superradiant scattering rate is just given by

$$\Gamma_{SR} \propto \left| \int \psi^*\left(\mathbf{r} - \frac{\hbar\mathbf{q}_1}{m}\tau, \tau\right) \psi(\mathbf{r},\tau)\, d^3\mathbf{r} \right|^2 , \tag{5.19}$$

If $\sigma_P \ll \hbar\mathbf{q}_q$, then the argument of Equation 5.19 is just $G^{(1)}\left(\frac{\hbar\mathbf{q}_1}{m}\tau\right)$, the first-order spatial correlation function. The scattering rate thus decreases in time from the increasing *non*-overlap of the initial and scattered atomic wavefunctions. A Gaussian form for the atomic wavefunction will give

$$\Gamma_{SR} \propto \exp\left(-\frac{t^2}{\tau_c^2}\right) , \tag{5.20}$$

where $\tau_c = m/\sqrt{2}|\mathbf{q}_1|\sigma_P$ is the $1/e$ coherence time, and σ_P is the rms momentum width. Yoshikawa *et al.* measured the coherence time for both a thermal gas and partially condensed cloud below T_c, showing a strong divergence in τ_c for the condensate component.

For the purposes herein, we may consider utilizing monochromatic SPPS on the atom beam in the circular waveguide along the elongated propagation axis with a laser beam of wavevector $k_o = \frac{2\pi}{780nm}$. End-fire superradiance will strongly favor backscattering, so

$\mathbf{q}_1 = -2k_o\hat{X}$. The longitudinal momentum dispersion is $\sigma_P = m \times 1.8\,\mathrm{mm/s}$, so the coherence time with the SPPS scheme should be $\tau_c = 24\,\mu\mathrm{s}$.

As we explore in the next sections, carrying out this experiment showed that the coherence time was nearly two orders of magnitude longer than the prediction from monochromatic SPPS! We now introduce *bichromatic* SPPS to explain this dramatic discrepancy.

5.9 Bichromatic Superradiant Pump-Probe Spectroscopy

Motivated by the fact that the guided atom beam is rotating around the circular waveguide, we must reconsider a crucial assumption in the initial consideration of SPPS, namely that the incident laser beam is stationary in time. More generally, the probe pulse may have a different wavevector from the pump laser beam. This may come about from two distinct laser sources of differing color or, more relevantly for the experiments described herein, from a single pump-probe laser source of wavevector $\mathbf{k}_o$ illuminating an atom beam propagating at a rotation rate Ω in the circular atom waveguide. In this case the second probe pulse comes a time τ after the initial pump pulse, the long axis of the atom laser beam will have rotated by an angle $\Omega\tau$. Both possibilities are illustrated in Figure 5.9.

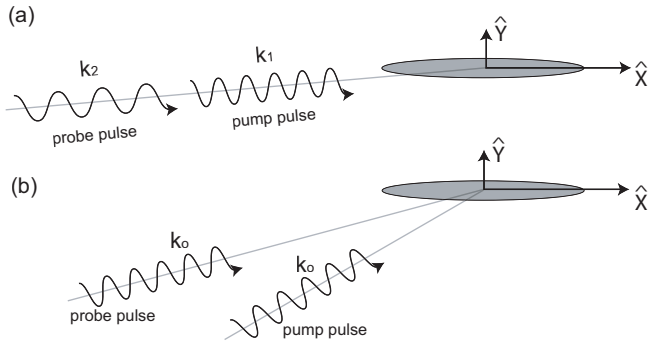

Figure 5.9: Two possible scenarios for bichromatic superradiance pump-probe spectroscopy: (a) The wavevectors of the pump and probe differ, or (b) the incidence angle of the pump and probe differ.

Returning to Equations (5.17) and (5.18), we can retain the necessary generality by

letting $\mathbf{q}_1 = \mathbf{k}_f - \mathbf{k}_1$, the recoil wavevector for the pump pulse, and $\mathbf{q}_2 = \mathbf{k}_f - \mathbf{k}_2$, the recoil wavevector for the probe pulse, differ. As $\hbar\mathbf{q}_1$ exceeds σ_P by a factor of ~ 7, we can also assume the time evolution of the original wavefunction to be negligible on the timescale of τ,[4] meaning $\psi(\mathbf{r}, \tau) \to \psi(\mathbf{r})$. Under the validity of this assumption, the superradiant scattering rate thus becomes

$$\Gamma_{SR} \propto \left| \int e^{i(\mathbf{q}_2 - \mathbf{q}_1)\cdot\mathbf{r}} \psi^* \left(\mathbf{r} - \frac{\hbar\mathbf{q}_1}{m}\tau \right) \psi(\mathbf{r})\, d^3\mathbf{r} \right|^2 , \tag{5.21}$$

Introducing $\mathbf{b} \equiv \hbar\mathbf{q}_1\tau/2m$ and $\Delta\mathbf{q} = \mathbf{q}_2 - \mathbf{q}_1$, we obtain

$$\Gamma_{SR} \propto \left| \int e^{i\Delta\mathbf{q}\cdot(\mathbf{r}-\mathbf{b})}\, \psi^*(\mathbf{r}-\mathbf{b})\, \psi(\mathbf{r}+\mathbf{b})\, d^3\mathbf{r} \right|^2 . \tag{5.22}$$

This equation may be informed further by the inclusion of the momentum-space wavefunction $\widetilde{\psi}(\mathbf{p}) = \left(\frac{1}{2\pi\hbar}\right)^{3/2} \int \psi(\mathbf{r}) \exp\left(-i\mathbf{p}\cdot\mathbf{r}/\hbar\right)\, d^3\mathbf{r}$:

$$\begin{aligned} \Gamma_{SR} \quad \propto \quad & \left| \int e^{i\Delta\mathbf{q}\cdot(\mathbf{r}-\mathbf{b})} \left[\left(\frac{1}{2\pi\hbar} \right)^{3/2} \int \widetilde{\psi}(\mathbf{p}_1) e^{i\mathbf{p}_1\cdot(\mathbf{r}-\mathbf{b})/\hbar}\, d^3\mathbf{p}_1 \right] \right. \\ & \left. \times \left[\left(\frac{1}{2\pi\hbar} \right)^{3/2} \int \widetilde{\psi}(\mathbf{p}_2) e^{i\mathbf{p}_2\cdot(\mathbf{r}+\mathbf{b})/\hbar}\, d^3\mathbf{p}_2 \right]\, d^3\mathbf{r} \right|^2 . \end{aligned} \tag{5.23}$$

Further, we define $\mathbf{p} = (\mathbf{p}_1 + \mathbf{p}_2)/2$ and $\mathbf{p}' = \mathbf{p}_2 - \mathbf{p}_1$. With some algebra, we obtain

$$\Gamma_{SR} \propto \left| \int e^{i\Delta\mathbf{q}\cdot(\mathbf{r}-\mathbf{b})}\, e^{2i\mathbf{p}\cdot\mathbf{b}/\hbar} \left[\int e^{i\mathbf{p}'\cdot\mathbf{r}/\hbar}\, \widetilde{\psi}^* \left(\mathbf{p} - \frac{\mathbf{p}'}{2} \right)\, \widetilde{\psi} \left(\mathbf{p} + \frac{\mathbf{p}'}{2} \right)\, d^3\mathbf{p}' \right]\, d^3\mathbf{p}\, d^3\mathbf{r} \right|^2 . \tag{5.24}$$

The argument inside the brackets is of course the Wigner function $\mathcal{W}(\mathbf{r}, \mathbf{p})$, yielding

$$\Gamma_{SR} \propto \left| \iint e^{i\Delta\mathbf{q}\cdot(\mathbf{r}-\mathbf{b})}\, e^{2i\mathbf{p}\cdot\mathbf{b}/\hbar}\, \mathcal{W}(\mathbf{r}, \mathbf{p})\, d^3\mathbf{p}\, d^3\mathbf{r} \right|^2 . \tag{5.25}$$

This equation may appear obscure, but one final change of variables illustrates its meaning. We perform an extended canonical transformation to generalized coordinates, i.e. scaling the position and momentum variables by some r_o and p_o, respectively:

$$\tilde{\mathbf{r}} = \cos\vartheta \frac{\mathbf{r}}{r_o} + \sin\vartheta \frac{\mathbf{p}}{p_o} , \tag{5.26a}$$

$$\tilde{\mathbf{p}} = -\sin\vartheta \frac{\mathbf{r}}{r_o} + \cos\vartheta \frac{\mathbf{p}}{p_o} . \tag{5.26b}$$

[4] A full treatment would merely keep the time dependence $\psi(\mathbf{r}, t)$ and the final results would be largely unaffected (though somewhat obscured).

This substitution takes Equation (5.25) to

$$\Gamma_{SR} \propto \left| \iint e^{i(\Delta\mathbf{q} r_o \cos\vartheta + (2p_o\mathbf{b}/\hbar)\sin\vartheta)\cdot\tilde{\mathbf{r}}}\, e^{i(-\Delta\mathbf{q} r_o \sin\vartheta + (2p_o\mathbf{b}/\hbar)\cos\vartheta)\cdot\tilde{\mathbf{p}}}\, \mathcal{W}(\mathbf{r},\mathbf{p})\; d^3\widetilde{\mathbf{p}}\, d^3\tilde{\mathbf{r}} \right|^2 , \tag{5.27}$$

which has not manifestly improved the situation upon first glance. Recall, however, that $\Delta\mathbf{q} = (\mathbf{q}_2 - \mathbf{q}_1)$ is a parameter under an experimentalist's control in bichromatic SPPS. For instance, it is possible to tune $\mathbf{q}_2$ such that the following condition is satisfied:

$$\Delta\mathbf{q} r_o \cos\vartheta + \frac{2p_o\mathbf{b}}{\hbar}\sin\vartheta = 0\,. \tag{5.28}$$

For this to be valid $\Delta\mathbf{q}$ and $\mathbf{b}$ must be collinear (with respective magnitudes Δq and b). This collinear criterion specifies that $\mathbf{q}_2$, while its magnitude may vary, must be collinear with $\mathbf{q}_1$. This puts a strong restriction on experimental implementations of bichromatic SPPS, indeed such a strong restriction that the implementation in a rotating frame would seem severely hindered. This issue will be revisited, but for now we proceed on the assumption that this criterion can be satisfied.

The phase space angle ϑ is then set by

$$\begin{aligned} \vartheta &= \tan^{-1}\left(\frac{\hbar\Delta q\, r_o}{2p_o b}\right) \\ &= \tan^{-1}\left(\frac{m\Delta q\, r_o}{p_o q_1 \tau}\right) . \end{aligned} \tag{5.29}$$

In this regime, Equation (5.27) becomes

$$\Gamma_{SR} \propto \left| \int e^{i[-\Delta\mathbf{q} r_o \sin\vartheta + (p_o\mathbf{q}_1\tau/m)\cos\vartheta]\cdot\tilde{\mathbf{p}}} \left(\int \mathcal{W}(\mathbf{r},\mathbf{p})\; d^3\tilde{\mathbf{r}} \right) d^3\tilde{\mathbf{p}} \right|^2 . \tag{5.30}$$

Finally, we note that as $\Delta\mathbf{q}$ and $\mathbf{q}_1$ are collinear, we have picked out this axis as "preferred" in that the integrations of $\mathcal{W}(\mathbf{r},\mathbf{p})$ on the two orthogonal axes contribute nothing to the signal. This may be seen through the recognition that the canonical commutation relation $[r_i, p_j] = i\hbar\delta_{ij}$ enforces the separability of the Wigner function in cartesian coordinates

$$\mathcal{W}(\mathbf{r},\mathbf{p}) = \mathcal{W}(r_1,p_1)\,\mathcal{W}(r_2,p_2)\,\mathcal{W}(r_3,p_3)\,, \tag{5.31}$$

with each obeying $\int\int \mathcal{W}(r_i,p_i)\, dr_i dp_i = 1$. Thus, without loss of generality, we may take axis common to $\mathbf{q}_1$ and $\Delta\mathbf{q}$ to define the r_1-axis and integrate out the remaining

dimensions. With this, we obtain

$$\Gamma_{SR} \propto \left| \int e^{i[-\Delta q r_o \sin\vartheta + (p_o q_1 \tau/m)\cos\vartheta]\tilde{p}} \left(\int \mathcal{W}\left(r_1, p_1\right)\, d\tilde{r}_1 \right) d\tilde{p}_1 \right|^2 . \tag{5.32}$$

This equation represents the main result of bichromatic SPPS, and thereby deserves close scrutiny. First, we note that the parenthetical expression represents an off-axis projection of the Wigner function, the necessary element of tomographic phase space imaging, and thus the superradiant scattering signal now depends directly on this function. Second, we note that the remaining integral is the fourier tranform of the off-axis projection. Recalling the projection-slice theorem from Section 5.5, this corresponds to a slice in the fourier transform space of the original function $\mathcal{W}(r_1, p_1)$. Thus, with full experimental control over $\mathbf{q}_1$, $\mathbf{q}_2$, and τ, complete tomography of the six-dimensional $\mathbf{r} - \mathbf{p}$ phase space is accessible.

5.9.1 Bichromatic SPPS with Two Light Sources

The notion of "full experimental control" is obviously the rub. For $\mathbf{q}_2$ to be aligned with $\mathbf{q}_1$ and still achieve tomography, the wavelength of the second light pulse must be different from the first (again, see Figure 5.9). This is experimentally challenging and generally disadvantageous because of the fact that atoms do not Rayleigh scatter all wavelengths equally. (The consequences of differing Rayleigh scattering rates for the pump/probe pulses has not been considered in this analysis.) However, with the use of a second laser a closer examination of Equation (5.29) shows that for a single positive Δq, only $0 \leq \vartheta < \pi/2$ is accessed by mapping scattering rate signals from $0 \leq \tau < \infty$. Swapping the first and second laser pulses has the effect of sending $\Delta q \rightarrow -\Delta q$, completing the complete set of $-\pi/2 < \vartheta < \pi/2$ projection angles necessary for full tomography.

5.9.2 Bichromatic SPPS in a rotating frame

As depicted in Figure 5.9(b), an alternative mechanism to implement phase space tomography is utilizing a single probe laser and probing the Wigner function of a rotating system. This necessitates a revision of Equation (5.32) (though the result will ultimately be retained in the proper limit). In this sub-section we consider the general case of an

atomic beam rotating in a circular 1D waveguide, with the goal being a general result which can then be compared to our experimental parameters in the final section of this chapter.

We begin by considering an elongated beam such as that propagating around a circular waveguide. In the lab frame, the beam is rotating at an angular velocity Ω. We further restrict the system to the two-dimensional plane of the circular waveguide, i.e. the beam motion and pump-probe wavevectors have no z-components. Three length scales must immediately be compared, namely the rms longitudinal width of the beam, σ_X, the rms transverse width of the beam, σ_Y, and the radius of the ring, ρ_o. The following regime is specifically considered:

$$\sigma_Y \ll \sigma_X \ll \rho_o \,. \tag{5.33}$$

The first criterion makes end-fire superradiance with the output mode(s), $\mathbf{k}_f = \pm|\mathbf{k}_i|\hat{X}$, most likely. The second criterion means that the beam subtends a small angular spread $\Delta\phi \approx \sigma_X/\rho_o$, as we will the assign the average angular position to the beam.

As depicted in Figure 5.9(b), the system is illuminated with a pump-probe sequence by a single laser of wavevector k, with pulses separated by time τ. In this separation the probe pulse will have rotated by an angle $\Omega\tau$ with respect to the pump pulse's angle of incidence ϕ, measured off the x-axis. Thus, the following equations are valid:

$$\mathbf{k}_1 = k\left[\cos\phi\hat{X} + \sin\phi\hat{Y}\right] \tag{5.34a}$$

$$\mathbf{k}_2 = k\left[\cos\left(\phi+\Omega\tau\right)\hat{X} + \sin\left(\phi+\Omega\tau\right)\hat{Y}\right) \tag{5.34b}$$

$$\mathbf{k}_f = -k\hat{X} \tag{5.34c}$$

$$\begin{aligned}\mathbf{q}_1 &= \mathbf{k}_1 - \mathbf{k}_f \\ &= k\left[(1+\cos\phi)\hat{X} + \sin\phi\hat{Y}\right]\end{aligned} \tag{5.34d}$$

$$\begin{aligned}\mathbf{q}_2 &= \mathbf{k}_2 - \mathbf{k}_f \\ &\approx k\left[(1+\cos\phi-\Omega\tau\sin\phi)\hat{X} + (\sin\phi+\Omega\tau\cos\phi)\hat{Y}\right]\end{aligned} \tag{5.34e}$$

$$\Delta\mathbf{q} = \mathbf{q}_2 - \mathbf{q}_1 \tag{5.34f}$$

$$\approx k\Omega\tau\left(-\sin\phi\hat{X} + \cos\phi\hat{Y}\right)\,. \tag{5.34g}$$

Where "$\approx$" symbols are used, the assumption that $\Omega\tau \ll 1$ has been made, and as is

typically the case experimentally. These geometric constructions are depicted in Figure 5.10:

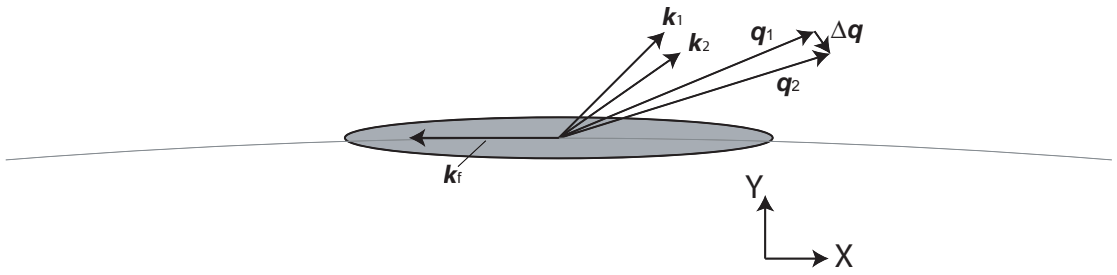

Figure 5.10: Bichromatic SPPS in a circular waveguide.

Returning to Equation (5.25), the generalized phase matching equation, we recast it in two dimensions as:

$$\Gamma_{SR} \propto \left| \iint e^{i\Delta\mathbf{q}\cdot(\mathbf{r}-\frac{\hbar\mathbf{q}_1\tau}{2m})}\, e^{i\mathbf{p}\cdot\mathbf{q}_1\tau/m}\, \mathcal{W}(\mathbf{r},\mathbf{p})\; d^2\mathbf{p}\, d^2\mathbf{r} \right|^2 . \tag{5.35}$$

This may be simplified to

$$\begin{aligned} \Gamma_{SR} \;\propto\; & \left| \iint e^{-ik\Omega\tau\sin\phi X + i\frac{k\tau}{m}(1+\cos\phi)P}\, \mathcal{W}(X,P)\, dX\, dP \right|^2 \\ & \times \left| \iint e^{-ik\Omega\tau\cos\phi Y + i\frac{k\tau}{m}\sin\phi P_Y}\, \mathcal{W}(Y,P_Y)\, dY\, dP_Y \right|^2 . \end{aligned} \tag{5.36}$$

The separability of the two axes is highly advantageous, as we desire a probe solely of the Wigner function of the X-axis and can look at the signal in two pieces, $\Gamma_{SR} \propto \Gamma_{X,SR}\Gamma_{Y,SR}$ as delineated in Equation (5.36). Further, as described in Section 5.2, the transverse state of the beam in a waveguide is dependent upon the longitudinal state of the beam. The rotating system ensures that $\mathbf{\Delta q}$ will *not* be collinear with $\mathbf{q}_1$, so we accept that attempting tomography on one axis will necessarily be "contaminated" by the (quantifiable) effect of the pump-probe sequence on the perpendicular axis or axes.

Proceeding, we look to the $X - P$ integral term in Equation (5.36), and perform the same phase space transformation as conducted in Equation (5.26):

$$\widetilde{X} = \frac{X}{\sigma_X}\cos\vartheta + \frac{P}{\sigma_P}\sin\vartheta\,, \tag{5.37a}$$

$$\widetilde{P} = -\frac{X}{\sigma_X}\sin\vartheta + \frac{P}{\sigma_P}\cos\vartheta\,. \tag{5.37b}$$

Instead of substituting arbitrary spatial and momentum scaling factors, the rms spatial and momentum widths (σ_X and σ_P) are chosen as natural normalization factors. With these, the longitudinal component of Equation (5.36) becomes

$$\begin{aligned}\Gamma_{X,SR} \;=\; &\left|\iint \exp\left[ik\tau\left(-\Omega\sigma_X\sin\phi\cos\vartheta + \frac{\sigma_P}{m}(1+\cos\phi)\sin\vartheta\right)\widetilde{X}\right]\right. \\ &\left.\times\exp\left[ik\tau\left(\Omega\sigma_X\sin\phi\sin\vartheta + \frac{\sigma_P}{m}(1+\cos\phi)\cos\vartheta\right)\widetilde{P}\right]\,\mathcal{W}(X,P)\,d\widetilde{X}d\widetilde{P}\right|^2 .\end{aligned} \tag{5.38}$$

As before, we define ϑ by the satisfaction of the following condition

$$-\Omega\sigma_X\sin\phi\cos\vartheta + \frac{\sigma_P}{m}(1+\cos\phi)\sin\vartheta = 0\,, \tag{5.39}$$

which has the solution

$$\vartheta = \tan^{-1}\left(\frac{m\Omega\sigma_X}{\sigma_P}\frac{\sin\phi}{1+\cos\phi}\right)\,, \tag{5.40}$$

or, equivalently,

$$\vartheta = \tan^{-1}\left(\frac{m\Omega\sigma_X}{\sigma_P}\tan\frac{\phi}{2}\right)\,. \tag{5.41}$$

A crucial difference exists between this rotating case and the preceding example of "linear" bichromatic SPPS, namely that this definition of ϑ has no dependence on τ. This surprising fact is a consequence of the linear-in-time angular variation of $\mathbf{q}_2$, which ultimately cancels with the linear-in-time evolution of the wavefront spacing. Instead of temporal dependence, the phase space angle ϑ is tuned most easily by a variation of ϕ, though Ω is potentially an experimental control knob as well.

Regardless of the method of varying ϑ, the X-component of the superradiant scattering rate is now given by

$$\Gamma_{X,SR} = \left|\int \exp\left[ik\tau\left(\Omega\sigma_X\sin\phi\sin\vartheta + \frac{\sigma_P}{m}(1+\cos\phi)\cos\vartheta\right)\widetilde{P}\right]\left(\int\mathcal{W}(X,P)\,d\widetilde{X}\right)d\widetilde{P}\right|^2 , \tag{5.42}$$

with the desired tomographic projection $\int\mathcal{W}(X,P)\,d\widetilde{X}$ evident in the equation. For completeness, we present the transverse component of the superradiant signal is

$$\Gamma_{Y,SR} = \left|\iint e^{-ik\Omega\tau\cos\phi Y + i\frac{k\tau}{m}\sin\phi P}\,\mathcal{W}(Y,P_Y)\,dY\,dP_Y\right|^2 , \tag{5.43}$$

with the product $\Gamma_{SR} = \Gamma_{X,SR}\Gamma_{Y,SR}$ setting the functional dependence of the superradiant signal. That ϕ sets the $X-P$ phase space angle ϑ yet also contributes to the signal through $\Gamma_{Y,SR}$ means it is incumbent upon the experimentalist to account for the effect of the transverse dimension on the predicted signal. Put another way, Γ_{SR} can only yield tomography on $\mathcal{W}(X,P)$ when the functional behavior of $\Gamma_{Y,SR}$ is fully accounted for, as otherwise the signal is polluted by the transverse contribution.

As a test case, we can imagine enacting bichromatic SPPS on the posited Wigner function in Equation (5.7). Evaluating the line integral with this distribution, we obtain

$$\int \mathcal{W}(X,P)\, d\widetilde{X} = \frac{1}{\sqrt{2\pi\,(1-\eta\sin 2\vartheta)}}\, e^{-\widetilde{P}^2/2(1-\eta\sin 2\vartheta)}\,, \tag{5.44}$$

which is a Gaussian distribution on $\widetilde{P}$ of rms width $\sqrt{1-\eta\sin 2\vartheta}$. Continuing with the evaluation of $\Gamma_{X,SR}$, we have:

$$\begin{aligned}
\Gamma_{X,SR} &= \left| \int \exp\left[ik\tau \left(\Omega\sigma_X \sin\phi \sin\vartheta + \frac{\sigma_P}{m}(1+\cos\phi)\cos\vartheta \right) \widetilde{P} \right] \left(\int \mathcal{W}(X,P)\, d\widetilde{X} \right) d\widetilde{P} \right|^2 \\
&= \left| \int e^{ik\tau\left(\Omega\sigma_X \sin\phi\sin\vartheta + \frac{\sigma_P}{m}(1+\cos\phi)\cos\vartheta\right)\widetilde{P}} \left(\frac{e^{-\widetilde{P}^2/2(1-\eta\sin 2\vartheta)}}{\sqrt{2\pi\,(1-\eta\sin 2\vartheta)}} \right) d\widetilde{P} \right|^2 \\
&= \exp\left[-\frac{m^2k^2}{\sigma_P^2} \left(\frac{1-\eta\sin 2\vartheta}{\cos^2\vartheta} \right) (1+\cos\phi)^2\, \tau^2 \right] .
\end{aligned} \tag{5.45}$$

Recognizing $|\mathbf{q}_1| = k(1+\cos\phi)$ and the parameters in the parenthetical are positive for all ϑ and ϕ, Equation (5.45) becomes simply

$$\Gamma_{X,SR} = \exp\left(-\frac{\tau^2}{\tau_c^2} \right) , \tag{5.46}$$

with τ_c defined as the e^{-1}-decay time,

$$\tau_c = \frac{m}{\sigma_P|\mathbf{q}_1|} \frac{\cos\vartheta}{\sqrt{1-\eta\sin 2\vartheta}} . \tag{5.47}$$

The maximal coherence times will occur at $\vartheta = \pi/4$, the projection along the narrowed axis, yielding

$$\tau_c\big|_{\vartheta=\pi/4} = \frac{m}{\sqrt{2}\sigma_P|\mathbf{q}_1|} \frac{1}{\sqrt{1-\eta}} , \tag{5.48}$$

which corresponds exactly to the monochromatic SPPS signal when $\eta = 0$. Thus, a measurement of the maximal coherence time yields η by

$$\eta = 1 - \left(\frac{m}{\sigma_P|\mathbf{q}_1|\tau_{c,max}} \right)^2 , \tag{5.49}$$

and the bounding phase space area is $\mathcal{A} = \mathcal{A}_{max}\sqrt{1-\eta^2}$. These two equations show that enacting SPPS in the ultracold atom storage ring should (a) result in coherence times much longer than the monochromatic SPPS result would predict and (b) provide the probe we desire to measured the phase space area $\mathcal{A}$.

As previously mentioned, the transverse component $\Gamma_{Y,SR}$ can potentially detract from this measurement of η, so a similar algebraic exercise involving Equation (5.43) can illuminate exactly this contribution to the signal. Under the same Gaussian approximation that correctly predicted the transverse ground state decay, we may envision an *uncorrelated* Gaussian Wigner function with spatial rms width σ_Y. Equation (5.45) then becomes

$$\Gamma_{Y,SR} = e^{-(k^2\Omega^2\sigma_Y^2\cos^2\phi)\,\tau^2} \times e^{-(\hbar^2k^2\sin^2\phi/m^2\sigma_Y^2)\,\tau^2} \tag{5.50}$$

$$= \exp\left(-\frac{\tau^2}{\tau_{c,Y}^2}\right). \tag{5.51}$$

where the transverse decay time $\tau_{c,Y}$ is given by

$$\tau_{c,Y} = \left(k^2\Omega^2\sigma_Y^2\cos^2\phi + \frac{\hbar^2k^2\sin^2\phi}{m^2\sigma_Y^2}\right)^{-1/2}. \tag{5.52}$$

It will depend upon the experimental parameters whether this term will "hide" the long coherence times that Equation (5.47) would afford from the longitudinal term.

5.10 Bichromatic SPPS in the Ultracold Atom Storage Ring

With a theoretical understanding of the issues involved in the bichromatic SPPS signal in a rotating reference frame, we implemented this scheme in the circular waveguide. The angular velocity was $\Omega = 2\pi \times 8.4\,\mathrm{Hz}$, and the earliest time at which the atoms will be approximately aligned with the laser beam occurs after $\approx 61\,\mathrm{ms}$ of propagation time in the ring. At this stage, the atom beam has an rms width of $\sigma_X \approx 120\,\mu\mathrm{m}$, subtending an angle of $\Delta\phi \approx 5.5^o$. This immediately highlights a problematic feature of this incarnation of bichromatic SPPS, namely that the angular spread of the beam potentially compromises the assignment of a single angle ϕ to the system. 2D models which numerically evaluate the azimuthal and transverse phase matching integrals for a curved beam give some credence to the supposition that this is not a problem for this limited extent.

Considering the light pulses themselves, the pump and probe beams were obtained with an SRS pulse generator driving an RF switch (Mini-Circuits ZFSWHZ-1-20) which, in turn, initiated and extinguished the deflection of a beam from an acousto-optic modulator. The pump and probe beams were typically $50\,\mu$s in duration, with the variable delay τ between them. In the duration of the pulses, the atomic beam will rotate by an angle 0.15^o, another effect which detracts from the ideal implementation introduced in the preceding section. In fact, this rotation and the associated rotational dephasing was likely responsible for the angular variations of Γ_{SR} in Figure 5.8, as the beam rotated by an angle 0.49^o during the $150\,\mu$s pulse time.

Experimentally, a systematic measurement of the coherence times at various angles around the ring was even more dramatic than the angular gain picture in Figure 5.8. The sum of the numerous measurements

That the peak is at an angle close, but not equal to zero, makes one suspicious of a systematic error in angular measurement. Unlike superradiance, momentum transfer from Kapitza-Dirac scattering is dependent only on the orientation of the light beams. As the superradiance beam was identical in alignment to the Kapitza-Dirac beam (minus the retroreflection), the axis of scattering seen in Figure 4.14 was the reference for 0^o. The conservative 2^o error estimate is thus based on the uncertainty on the atom beam axis, representing at least 1σ-confidence.

The very long coherence times of $\tau_c \sim 1\,$ms are immediate evidence of a highly correlated system, as they exceed the monochromatic SPPS decoherence time $m/\sigma_P|\mathbf{q}_1| = 35\,\mu$s by a factor of 40. All is not immediately clear, however, as the experimental parameters and an inversion of Equation (5.41) would predict an angle $\phi_c = 31^o$ for these large coherence times to occur, while the data would indicate $\phi_c = 4(2)^o$. This discrepancy is not understood at this time, though we suspect that it may be necessary to adapt our 1D treatment of superradiance to beams with small Fresnel number, i.e., with length greatly exceeding the Rayleigh range defined by the probe wavelength and the transverse width of the atom beam. Our method may be probing only short portions of the beam, the momentum width of which is enhanced by their small extent, rather than probing the beam as a whole.

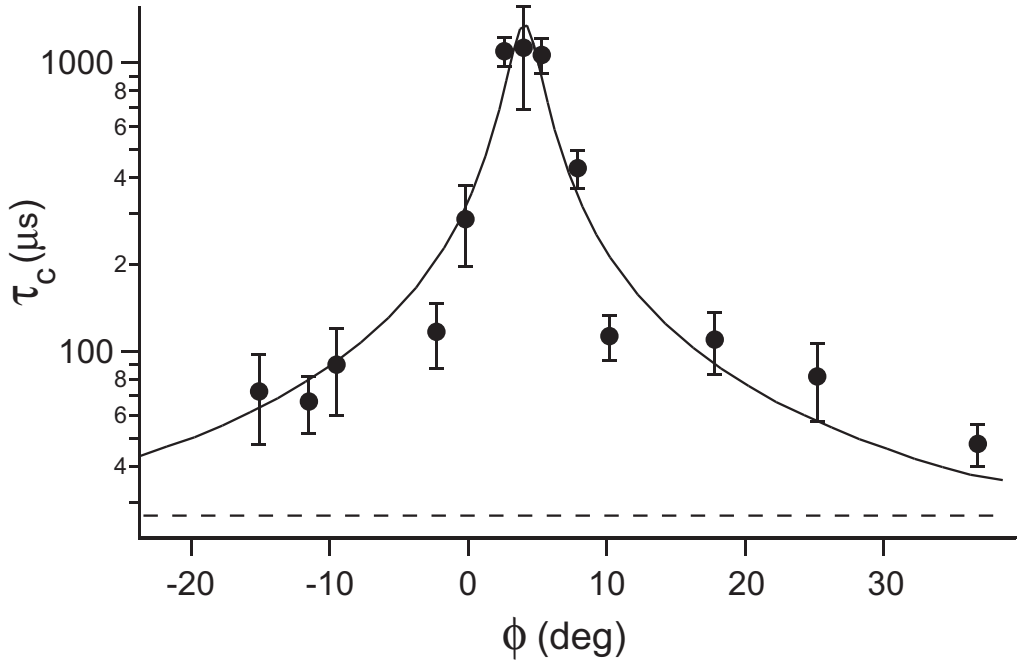

Figure 5.11: Measured coherence times are compared to theoretical predictions for a coherent Gaussian beam (solid line) and an incoherent, uncorrelated ensemble (dotted line). The theoretical curve in fact predicts the maximum coherence time at $\phi = 31^o$ (see text), but has been shifted for comparison to data.

A brief consideration of the transverse contribution to this signal shows that this may be the factor which ultimately limits the observed coherence times. Incorporating experimental values into Equation (5.52) shows the dominant transverse loss to be $\tau_{c,Y} \approx (k\Omega\sigma_Y \cos\phi)^{-1}$. Utilizing the lower bound from the 1D model of Figure 5.2, the transverse width should be $\sigma_Y \approx 2.4\sqrt{\hbar/2m\omega_Y}$. This gives a limiting transverse decay time of $\tau_{c,Y} \approx 1\,\text{ms}$, right in line with the maximum observed coherence time.

Taking the observed maximum coherence time of $\tau_c = 1.1(1)\,\text{ms}$, we infer the correlation parameter to be $\eta = 1 - \left[4.9(6) \times 10^{-4}\right]$. The atom beam is thus constrained to inhabit a phase space area of no more than $\mathcal{A} = 9(1)\hbar$.[5] The constraining Wigner distribution, inside which lies the true distribution, is plotted in Figure 5.12:

This upper bound on the phase space area is presented in lieu of a true reconstructed

[5]This is equivalent to placing a lower bound of $\mathcal{L} = (\hbar|\mathbf{q}|/m)\,\tau_c = 13(1)\,\mu\text{m}$ [123] on the longitudinal coherence length of the propagating cloud.

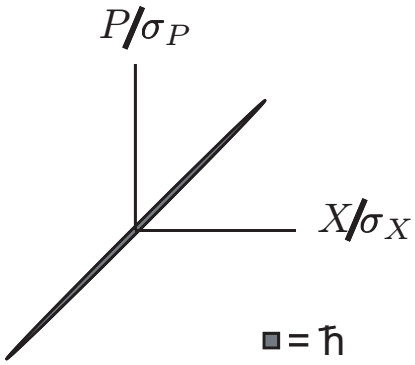

Figure 5.12: Wigner distribution implied by coherence times of 1.1 ms. The phase space area is bounded by $9\hbar$, where an area of $1\hbar$ is shown for reference. In this distribution of ≈ 9 quantum states reside 3×10^5 atoms.

Wigner distribution due to current limitations in data quality (seen in the scatter of Fig. **??**a), though a reconstruction even from the thirteen data points in Fig. **??**b would already yield a distribution of phase space area less than $9\hbar$. This small phase space area further implies a macroscopic phase space density of $N/\mathcal{A} \geq 3.3 \times 10^4$, meaning the beam is still highly degenerate and, if the transverse decay is truly limiting the measurement, possibly fully quantum generate. Thus, our observations should be construed as placing quantitative lower bounds on the coherence of the propagating atom beam while remaining consistent with its complete coherence.

Finally, we note that this effect persisted for multiple orbits about the ring. Figure 5.13 shows the maximal coherence times after 1, 2, and 3 orbits about the ring. All show the same ≈ 1 ms coherence times, implying that the macroscopic phase space occupation is not compromised even after > 300 ms of propagation time. Of particular note is the inset of Figure 5.13(c), which shows that only a small portion of the cloud is undergoing superradiance. This is because at this stage the cloud is subtending a large angular spread of XXX degrees. Because of this expansion, we were unable to make measurements for orbits of greater than three, though we observed nothing which would suggest that the quantum degeneracy is compromised at later propagation times.

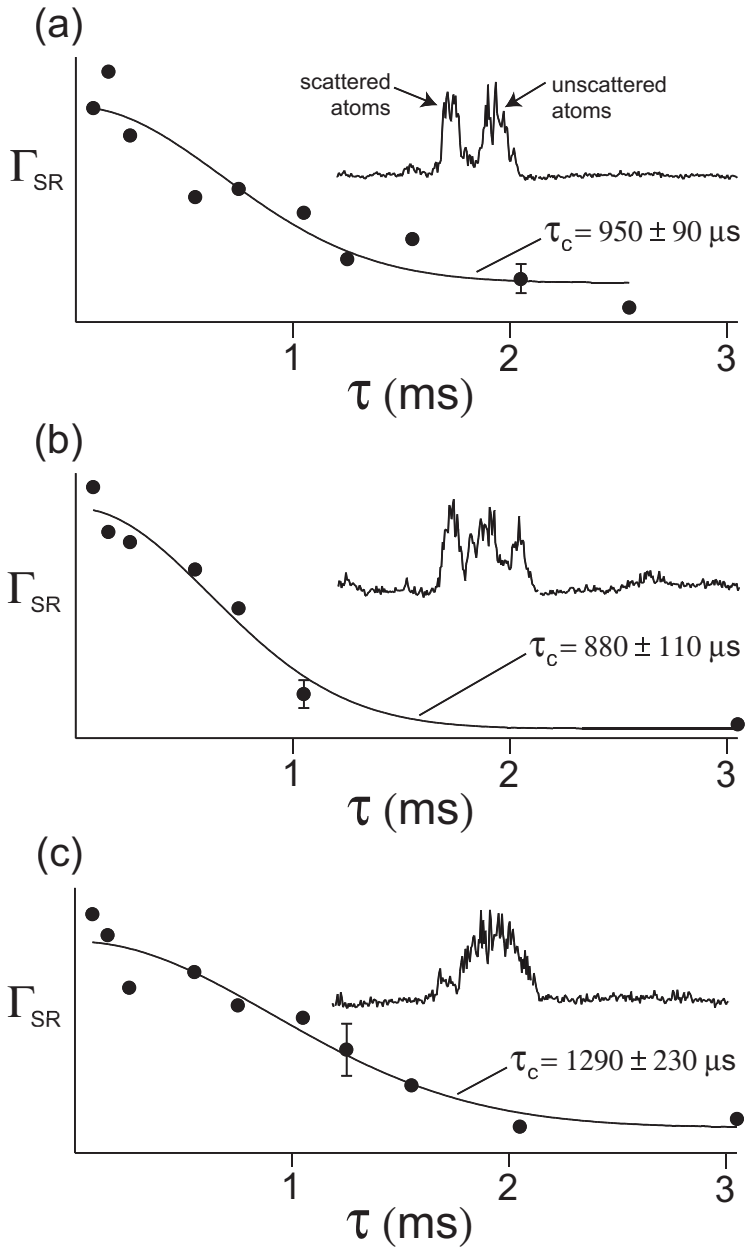

Figure 5.13: Long coherence times after multiple trips around the ring. Insets show typical density profiles $n(X)$ for the respective data series.

Chapter 6

Ultracold Ensembles in a Strongly-Coupled Cavity

This chapter expands on the introduction of cavity QED in chapter 1 and explores the physics of many atoms coupled to a strongly-coupled cavity, including the relevant experimental regime accessed by our apparatus. Akin to the description of the atom cooling elements in chapter 2, the latter part of this chapter presents the crucial experimental systems which comprise the BEC-CQED apparatus. The definitions on the following page will be utilized throughout this chapter and the following chapter as well, where the first experiments with this system are recounted.

6.1 Introduction to Cavity Quantum Electrodynamics

As noted in the introduction, cavity QED begins with the quantization of the electromagnetic field itself. One starts with the specification of boundary conditions by which classical modes of the electromagnetic field may be defined. For example, one may take two infinite planes separated by length L, where the field must vanish at the various boundaries $\big(\mathbf{E}(x,y,0) = \mathbf{E}(x,y,L) = 0\big)$. The allowable electric field can be decomposed into the allowed eigenmodes of the "cavity"

$$\mathbf{E}(\mathbf{r},t) = \sum_j \mathcal{E}_{o,j}\phi_j(x,y)\sin(k_j z)\sin(\omega_j t - \varphi)\,\hat{\varepsilon}\,, \tag{6.1}$$

where $k_j = \pi j/L$, $\omega_j = c\pi j/L$, φ is an arbitrary phase, $\hat{\varepsilon}$ is the polarization, $\mathcal{E}_{o,j}$ is the electric field amplitude, and $\phi_j(x,y)$ is the transverse mode function. We may construct an "area" for the mode from $\iint |\phi(x,y)|^2 dxdy = A_j$, and similarly a "volume" $V_j = A_j L/2$ (the 1/2 factor is from the spatial averaging of the $\sin^2 k_j z$ function). Under field quantization [124, 32], the electric field *operator* for the same physical system is expressed as

$$\hat{\mathcal{E}}_j = \sqrt{\frac{\hbar\omega_j}{2\epsilon_o V_j}} \times \sin(k_j z) \times \left(\hat{a}_j\, e^{i\omega_j t} + \hat{a}_j^\dagger\, e^{-i\omega_j t}\right), \tag{6.2}$$

where $\hat{a}_j^\dagger$ ($\hat{a}_j$) are the creation (annihilation) operators for the j^{th} mode. The coefficient $\sqrt{\frac{\hbar\omega_j}{2\epsilon_o V_j}}$ may be regarded as the electric field per photon, and the strength of the field in the cavity is thus seen to depend on $\sqrt{1/V_j}$.

The notion of cavity QED is thus seen as the enforcement of a finite (and preferably small) mode volume V_j, resulting in a sizeable electric field per photon. For example, in this work we make use of a cavity which gives a mode volume of $V_j = 8.3 \times 10^{-14}$ m^3 for $k_j = 2\pi/(780\,\text{nm})$, yielding an electric field per photon of 416 V/m. Compared to DC fields this is not particularly large, but if this AC field interacts resonantly with an electric dipole transition in an atom or molecule, the dynamic polarizability (and thereby the AC Stark shift) may be enormous. In this work, the intensity of a single intracavity photon may exceed 50 times the saturation intensity for the D2 transition in ^{87}Rb – clearly a case where a single photon interacts strongly with a quantum system.

6.1.1 Dissipation-free Cavity QED

More precisely, we look to the Hamiltonian which governs the evolution of an atom-field system, neglecting (for the time being) the role of dissipation. We consider a two-level atom with $\hbar\omega_a$ energy difference between the excited state $|e\rangle$ and the ground state $|g\rangle$. This two-level system can be expressed with the Pauli spin operators $\hat{\sigma}^+ = |e\rangle\langle g|$ and $\hat{\sigma} = |g\rangle\langle e|$. The atom is then located in the cavity, with a single cavity mode ω_c nearly resonant with the atomic transition frequency $\omega_c \approx \omega_a$.

Ignoring the external motion of the atom, the Hamiltonian for a single atom interacting

with this cavity mode may be written as [125, 126]

$$\hat{\mathcal{H}} = \frac{1}{2}\hbar\omega_a\left(\hat{\sigma}^z + 1\right) + \hbar\omega_c\hat{a}^\dagger\hat{a} + \hbar g\left(\hat{a}^\dagger\,\hat{\sigma}^- + \hat{a}\,\hat{\sigma}^+\right), \tag{6.3}$$

where $g = \sqrt{\frac{d^2\omega_c}{2\hbar\epsilon_o V_c}}$, d is the dipole matrix element between $|e\rangle$ and $|g\rangle$, and the rotating wave approximation (RWA) has been invoked to eliminate counter-rotating terms (such as $\sigma^+\hat{a}^\dagger$). It is no understatement to say that g is *the* characteristic quantity in cavity QED. This is the Rabi frequency for an atom driven by the field from a single photon, exactly the desired coherent evolution of a system with light quanta. For the $D2$ transition in ^{87}Rb and the cavity parameters for this work (which are described later in this chapter), we obtain a theoretical maximum coupling of $g_m = 2\pi \times 15.8\,\text{MHz}$.

The lowest-order excited states of Equation (6.3) have eigenfrequencies

$$\omega_+ = \frac{\omega_a + \omega_c}{2} + \sqrt{\left(\frac{\Delta_a}{2}\right)^2 + g^2} \tag{6.4a}$$

$$\omega_a = \frac{\omega_a + \omega_c}{2} - \sqrt{\left(\frac{\Delta_a}{2}\right)^2 + g^2}\,, \tag{6.4b}$$

where $\Delta_a = \omega_c - \omega_a$. The eigenstates are superpositions of the photon excitation $|g, 1\rangle$ and atomic excitation $|e, 0\rangle$, and are deemed "cavity-like" or "atom-like" in nature given their relative amplitudes for these states. For $\Delta_a < 0$, ω_+ is atom-like and ω_- is cavity-like, the converse for $\Delta_a > 0$. On resonance, the two states are even and odd superpositions of equal amplitude.

6.1.2 Dissipation-free Cavity QED with Many Atoms

Moving beyond a single atom in a cavity, we may consider N two-level atoms in the same resonator[1]. Instead of a single two-level atom hamiltonian we require a sum over all N atoms in the system

$$\hat{\mathcal{H}}_a = \frac{\hbar\omega_a}{2}\sum_{j=1}^{N}(\hat{\sigma}_j^z + 1)\,, \tag{6.5}$$

with each atom afforded its own spatial wavefunction $\psi_j(\mathbf{r})$. It will be advantageous for basic considerations of many-atom cavity QED to assume that each atom is well localized

[1]This system was explored in the seminal paper by Tavis and Cummings [127], and the system is known as the Tavis-Cummings model.

in the axial direction to $\Delta z_j \ll 2\pi c/\omega_c$ (much smaller than the photon wavelength[2]), and similarly well-localized in the transverse direction $\Delta x_j, \Delta y_j \ll w_j$ (much smaller than the transverse mode waist). This allows us to consider ignore the features of $\psi_j(\mathbf{r})$ and assign instead a position $\mathbf{r}_j$ for the j^{th} atom. We will see that this limit is born out by all of the experimental work presented in this chapter[3].

The full Hamiltonian of the system is then

$$\hat{\mathcal{H}} = \frac{\hbar\omega_a}{2}\sum_{j=1}^{N}(\hat{\sigma}_j^z + 1) + \hbar\omega_c\hat{a}^\dagger\hat{a} + \hbar\sum_{j=1}^{N} g(\mathbf{r}_j)\left(\hat{a}^\dagger\hat{\sigma}_j^- + \hat{a}\hat{\sigma}_j^+\right). \tag{6.6}$$

It is instructive to look at the matrix representation of the lowest excitation manifold of this system, where the basis states are a single intracavity photon $|0\ldots0;\,1\rangle$ and the set of states with a single excited state atom, e.g. $|0\ldots0,1,0\ldots0;\,0\rangle$:

$$\hat{\mathcal{H}} \to \hbar\begin{pmatrix} \omega_c & g(\mathbf{r}_1) & g(\mathbf{r}_2) & g(\mathbf{r}_3) & \ldots & g(\mathbf{r}_N) \\ g(\mathbf{r}_1) & \omega_a & 0 & 0 & \ldots & 0 \\ g(\mathbf{r}_2) & 0 & \omega_a & 0 & \ddots & 0 \\ g(\mathbf{r}_3) & 0 & 0 & \omega_a & \ddots & \vdots \\ \vdots & \vdots & \ddots & \ddots & \ddots & 0 \\ g(\mathbf{r}_N) & 0 & 0 & \ldots & 0 & \omega_a \end{pmatrix}. \tag{6.7}$$

This $N \times N$ Hamiltonian of course has N eigenstates, but only two of these are excited by cavity transmission[4] [129]. The eigenfrequencies of system are

$$\omega_+ = \frac{\omega_a + \omega_c}{2} + \sqrt{\left(\frac{\Delta_a}{2}\right)^2 + \sum_{j=1}^{N}|g(\mathbf{r}_j)|^2} \tag{6.8a}$$

$$\omega_- = \frac{\omega_a + \omega_c}{2} - \sqrt{\left(\frac{\Delta_a}{2}\right)^2 + \sum_{j=1}^{N}|g(\mathbf{r}_j)|^2}, \tag{6.8b}$$

where again we distinguish "cavity-like" excitations and "atom-like" excitations. Before proceeding, it is important to note that the eigenstates associated with these energy states

[2]This is also known the *Lamb-Dicke* regime.

[3]Though many interesting future experiments could be imagined where the atomic wavefunctions are delocalized over a larger spatial range [128].

[4]The remaining $N-2$ excited states are all degenerate at energy $\frac{\hbar\omega_a}{2}$, and are not excited by cavity transmission because they have zero amplitude for an intracavity photon. The presence of these states does guarantee that, when conducting the absorption imaging on the *side* of cavity as discussed in chapter 7, the atomic resonances will not be shifted.

of this Hamiltonian obey a symmetry on the atomic excitations. The action of $\sum_{j=1}^{N} \hat{\sigma}_j^+$ on the atomic ground state $|\tilde{0}\rangle = |0 \ldots 0\rangle$ results in an (unnormalized) excited state

$$\sum_{j=1}^{N} \hat{\sigma}_j^+ |0 \ldots 0\rangle = \sum_{j=1}^{N} |\delta_{1j}, \delta_{2j}, \ldots \delta_{Nj}\rangle \,, \tag{6.9}$$

where δ_{ij} is the Kronecker delta. Such excitations were elucidated by Dicke [116] as cooperative spin states, where the symmetry represents the fact that generally it will not be "known" which atom from the ensemble is excited. The first atomic excitation is thus defined

$$|\tilde{1}\rangle = \frac{1}{\sqrt{N}} \sum_{j=1}^{N} |\delta_{1j}, \delta_{2j}, \ldots \delta_{Nj}\rangle \,. \tag{6.10}$$

or, using Dicke's original "cooperation number" formalism, $|\tilde{0}\rangle = |\frac{N}{2}, -\frac{N}{2}\rangle$ and $|\tilde{1}\rangle = |\frac{N}{2}, -\frac{N}{2}+1\rangle$. This symmetric excitation has many important consequences, highlighted by the large body of work with such collective effects in atomic ensembles [130, 131, 132, 133, 134], and one need look no further than the previous chapter's discussion of superradiance to see yet another example of the importance of these collective excitations.

In Equation (6.6) we do not immediately obtain these perfectly symmetric Dicke states, as the analogous collective raising operator is rather $\sum_{j=1}^{N} g(\mathbf{r}_j)\hat{\sigma}_j^+$. Thus, the modified first atomic excited state is

$$|\tilde{1}'\rangle = \left(\frac{1}{\sum_{j=1}^{N} |g(\mathbf{r}_j)|^2} \right) \sum_{j=1}^{N} g(\mathbf{r}_j) |\delta_{1j}, \delta_{2j}, \ldots \delta_{Nj}\rangle \,, \tag{6.11}$$

where the state $|\tilde{1}\rangle$ enters only under identical coupling for all atoms. We need not invoke this limit, as it is unlikely to be the case experimentally and the energy level structure can be understood regardless. The important point is to consider excitations of the system which treat all atoms of the system symmetrically, weighted by $g(\mathbf{r})$.

It will be convenient to define g_{eff}, the effective cavity coupling per atom, as $g_{eff}^2 = \frac{1}{N}\sum_{j=1}^{N} |g(\mathbf{r}_j)|^2$. The eigenvalues in Equation (6.8) thus simplify to

$$\omega_+ = \frac{\omega_a + \omega_c}{2} + \sqrt{\left(\frac{\Delta_a}{2}\right)^2 + N g_{eff}^2} \tag{6.12a}$$

$$\omega_- = \frac{\omega_a + \omega_c}{2} - \sqrt{\left(\frac{\Delta_a}{2}\right)^2 + N g_{eff}^2} \,, \tag{6.12b}$$

Generally we may regard value of g_{eff} as dependent on "internal" and "external" factors. External factors include the spatial positions of atoms in the mode and the atomic wavefunctions (if they are relevant). As will be the case for this work, an evenly distributed of ensembles of atoms in the Lamb-Dicke limit amidst the $\sin k_p z$ standing wave mode will yield an external factor of $\frac{1}{2}$.

The internal factors include the elements which contribute to the dipole moment, e.g. the Clebsch-Gordon coefficients for a transition driven with by polarized light. Again considering an example relevant for this work, we look to driving a collection of $|F = 1, m_F = -1\rangle$ ^{87}Rb atoms on the $D2$ transition. By convention, the cavity coupling is expressed as the maximum coupling for the $\langle J|e\mathbf{r}|J'\rangle$ dipole transition, and then the hyperfine matrix elements for the transitions are given by the Clebsch-Gordon coefficients for the transitions [135]. We may consider probing the these atoms with either σ^+, π, or σ^- light. The respective squared coefficients for $D2$ transitions from this manifold are summarized in the inset of Figure 6.1.

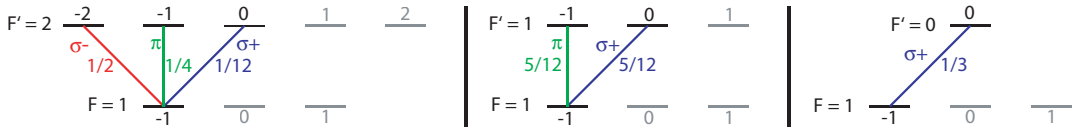

Figure 6.1: (a) Relevant Clebsch-Gordon spectrum for $D2$ transitions of $|F = 1, m_F = -1\rangle$ atoms. Squared values connect σ^- (red), π (green), and σ^+ (blue) transitions to the $F' = 2, 1, 0$ excited state manifolds.

As will be the case in the far-detuned limit described in the subsequent section, the atom-cavity detuning Δ_a can be large enough to render the excited-state hyperfine energy splitting negligible. In this case, the direct quadrature sum of the Clebsch-Gordon coefficients for the appropriate transition gives the modified g^2 coupling. For example, for the maximum coupling for a σ^+ polarized probe on the $D2$ transition from the

$|F = 1, m_F = -1\rangle$ is given by

$$\begin{aligned} g_o^2 &= g_m^2 \sum_{k=-1}^{+1} |c_{1,-1;1+k,-1+k}|^2 \\ &= g_m^2 \left(\frac{1}{12} + \frac{5}{12} + \frac{1}{3} \right) \\ &= \frac{5}{6} g_m^2 \,. \end{aligned} \tag{6.13}$$

This represents the maximum *attainable* coupling from the $|F = 1, m_F = -1\rangle$ state. With a few notable exceptions outlined in the chapter 7, this is taken as the new cavity coupling standard for the system, with $g_o = 2\pi \times 14.4\,\mathrm{MHz}$. Thus, the effective cavity coupling is given by

$$\begin{aligned} g_{eff}^2 &= (external) \times (internal) \times g_m^2 \\ &= \frac{1}{2} g_o^2 \,, \end{aligned} \tag{6.14}$$

the value of which was memorized at $g_{eff}^2 = (2\pi)^2 \times 104\,\mathrm{MHz}^2$ because of its ubiquity in practice.

6.1.3 The Far-Detuned Limit ($\sqrt{N} g_o \ll |\Delta_a|$)

The "resonant regime," where $|\Delta_a| < g_o$ has been explored by a number of experimental groups [37, 43, 136]. In this limit, the eigenenergies in Equation (6.12) become simply $\omega_\pm = \omega \pm \sqrt{N} g_{eff}$. For small atom number, this may also be regarded as the "absorptive" regime because the excitation probability per atom can be sizeable. In a particularly nice experiment, McKeever *et al.* [137] measured directly one, two, three, and four cesium atoms in a strongly coupled cavity by the $\sqrt{N}$ dependence of the eigenfrequencies.

For the work presented in this document, we consider instead the "far detuned limit," where $\sqrt{N} g_o \ll |\Delta_a|$ (Figure 6.2). Here, the excitations are *decidedly* cavity-like and atom-like in character, as shown. The eigenvalues take on a very different character from the resonant regime:

$$\widetilde{\omega}_c = \omega_c + \Delta_N \tag{6.15a}$$

$$\widetilde{\omega}_a = \omega_a - \Delta_N \,, \tag{6.15b}$$

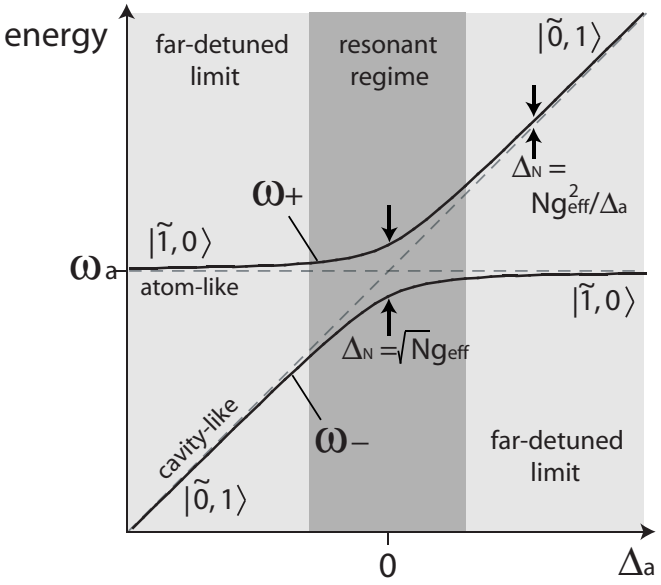

Figure 6.2: Energy level avoided crossing in the many-atom cavity system, highlighting the distinction between the resonant regime and the far-detuned limit.

where $\Delta_N \equiv \frac{Ng_{eff}^2}{\Delta_a}$. This shift is linear with the atom number, and the "per-atom" shift is given by g_{eff}^2/Δ_a, simply the far-detuned AC Stark shift associated with atoms interacting with the single cavity photon. The sketch of the level structure for $|\Delta_a| \gg \sqrt{N}\, g_o$ with $\Delta_a > 0$ is shown in Figure 6.3.

As depicted in the Figure, this system will be probed by laser light which is detuned from the bare cavity resonance by $\Delta_c = \omega_p - \omega_c$. The system will be in resonance when $\Delta_c = \Delta_N$, resulting in full transmission of the probe. In driving the cavity off resonance $\Delta_c \neq \Delta_N$, the transmission is suppressed and the probe light will reflect off the cavity. While the level structure depicted in Figure 6.3 is indisputably simple, as in the case of single atom CQED even simple level structures can bring surprises. Life gets interesting when both the dissipation mechanisms and the role of the probe field are considered, which respectively are the subjects of the following two sections.

It should be noted that while we have only considered the first manifold in the Tavis-Cummings model [127], this is as far as we need to go even in the case of many photon excitations in the cavity. If $\bar{n} \ll N$, as will be the case in this work, the excitation proba-

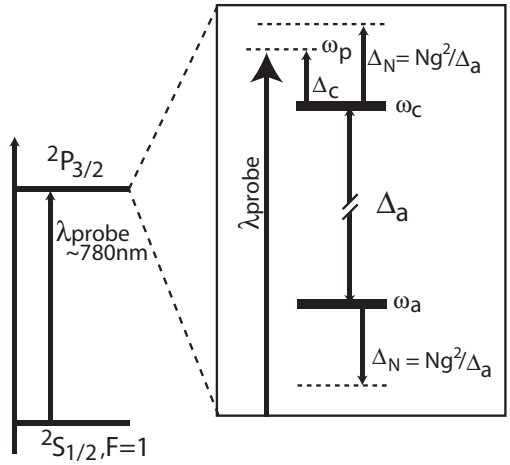

Figure 6.3: Dispersive energy level structure. This is a "blue" cavity, in that the cavity resonance is of higher frequency than the atomic transition. The cavity shift Δ_N is thereby also positive, shifting the atom-cavity resonance.

bility per atom is always small and the higher manifolds are irrelevant [129]. The largest intracavity photon number was $\bar{n} \sim 20$, compared to typical atom numbers measured in the 10's of thousands.

6.2 Dissipation

The crucial role of dissipation in a realistic cavity QED system has been ignored thus far, and to proceed we must now account for the system losses. The process of spontaneous emission is familiar, taking the atomic excitation $|\tilde{1}', 0\rangle \rightarrow |\tilde{0}, 0\rangle$ at a rate γ. For the $D2$ transition in ^{87}Rb, the atomic field decay rate is $\gamma = 2\pi \times 2.99\,\mathrm{MHz}$ [135]. As for the cavity decay, if the mirrors are realistic reflectors with combined transmission and scattering losses of rate κ, the amplitude of the excited state $|\tilde{0}, 1\rangle$ will decay as $\exp(-\kappa t)$ to the ground state $|0, \tilde{0}\rangle$. As κ is the half-linewidth of the cavity, it also sets the cavity transmission. For a monochromatic probe, the transfer function of the (empty) cavity is $(1 + \Delta_c^2/\kappa^2)^{-1}$.

Detailed models involving master equations for a driven atom-cavity system in the presence of dissipation may be found elsewhere [138], but the coherent evolution rate

g_o should be surely be stacked up against the decay rates κ and γ.[5] This leads to the identification of some dimensionless quantities which characterize cavity QED systems. The single atom cooperativity $C_1 = g_o^2/2\kappa\gamma$ can be thought of as the square of a Q-factor, where in this case the "oscillator" is the coherent oscillation of energy between the atom and the cavity photon at frequency $2g_o$. The critical atom number is defined as $n_a = 2\kappa\gamma/g_o^2 = 1/C_1$, which quantifies the number of intracavity atoms required to significantly alter the optical response of the system. The critical photon number is $n_p = \gamma^2/2g_o^2$, which quantifies the number of intracavity photons which saturate the atomic system. The regime of "strongly-coupled" cavity QED can be identified as the situation where $(n_a,\, n_p) \ll 1$, i.e. a high-Q oscillator with single atoms and single photons.

We now move past the basic theoretical considerations of many-atom cavity QED and on to the practical considerations in implementing such a system.

6.3 The BEC-CQED System

In this section, we describe the integrated elements of the full system BEC-CQED apparatus as it functions in this capacity. The subsystems can roughly be compartmentalized into the cavity system itself, the cavity stabilization system, the cold atom delivery, and the finally the probing/detection system.

6.3.1 The Cavity

The cavity decay rate κ is related to the separation and reflection/transmission properties of the mirrors. Following Hood *et al.*, each mirror is characterized by intrinsic transmission $\mathcal{T}$ and loss $\mathcal{L}$ coefficients, which relate the cavity finesse $\mathcal{F}$ as

$$\mathcal{F} = \frac{2\pi}{all\,losses} = \frac{\pi}{\mathcal{T} + \mathcal{L}}\,. \tag{6.16}$$

For the REO mirrors used in this work, Deep Gupta measured $\mathcal{T} = 1.6\,\text{ppm}$ and $\mathcal{L} = 3.8\,\text{ppm}$, translating to an expected finesse of $\mathcal{F} = 580,000$. At room temperature, the cavity itself has a length of $192.3\,\mu\text{m}$. During experimental operation, the cavity length *lengthens* to $194\,\mu\text{m}$ from the radiative thermal coupling between the cavity mount and

[5] They are normally expressed together as (g_o, γ, κ), with values of $2\pi \times (14.4, 2.99, 0.66)$ for our system.

k_p	: Cavity probe wavevector	$2\pi/780\,\text{nm}$
L_{RT}	: Cavity length (lN_2 off)	$192.3\,\mu\text{m}$
L	: Cavity length (lN_2 on)	$194\,\mu\text{m}$
R	: Radius of curvature	$5\,\text{cm}$
w_p	: TEM_{00} mode waist for 780 nm	$23.4\,\mu\text{m}$
V_m	: Mode volume $\left(\pi w_p^2 L/4\right)$	$8.27\times10^4\,\mu\text{m}^3$
ν_{fsr}	: Free spectral range	$780\,\text{GHz}$
$\mathcal{T}$	: Mirror transmission @ 780 nm	$1.6\,\text{ppm}$
$\mathcal{L}$	: Total mirror losses @ 780 nm	$3.8\,\text{ppm}$
$\mathcal{F}$	: Cavity finesse @ 780 nm	584,000
$\mathcal{F}_t$	: Cavity finesse @ 850 nm	38,000 (avg)
g_o	: Maximum cavity coupling	$2\pi\times14.0\,\text{MHz}$
κ	: Cavity loss rate	$2\pi\times0.66\,\text{MHz}$
γ	: Spontaneous emission rate	$2\pi\times2.99\,\text{MHz}$
n_a	: Critical atom number $(1/C_1)$	0.019
n_p	: Critical photon number $(\gamma^2/2g_o^2)$	0.018
C_1	: Single-atom cooperativity $(g_o^2/2\kappa\gamma)$	51.4
C	: Collective atomic cooperativity $(Ng_{eff}^2/2\kappa\gamma)$	$\lesssim 2.5\times10^6$

Table 6.1: Cavity QED Parameters

the liquid-nitrogen cooled millitrap mount[6]. During these experimental conditions,the free spectral range is $\nu_{fsr} = 780\,\text{GHz}$ ($\Delta\lambda_{fsr} = 1.5\,\text{nm}$). The full cavity linewidth 2κ may be measured by a simple cavity ringdown measurement which measures the $1/e$ decay time of light transmission as the cavity is swept rapidly across resonance (i.e. $\frac{d}{dt}\Delta_c \gg \kappa^2$). Repeated ringdown measurements have consistently shown a $1/e$ time of $\sim 120\,\text{ns}$, implying $\kappa = 2\pi\times0.66\,\text{MHz}$. As the usual definition of the finesse [139] is the ratio of the free spectral range to the full cavity linewidth. As κ is the *half*-linewidth, we have $\mathcal{F} = \pi\nu_{fsr}/\kappa = 5.9\times10^5$, right in line with the theoretical value. The topic of probing and detection will be revisited later in this chapter, but it is important to note that while the intracavity photons are lost at a rate 2κ they are not necessarily emitted towards the detector (presumably placed on one side of the cavity). For a cavity with identical mirrors, the probability that an intracavity photon decay will result in a detectable photon is $\mathcal{T}/2(\mathcal{T}+\mathcal{L}) = 0.15$.

[6]That the cavity length increases seems counterintuitive, but between the small thermal mass and the fact that the glass cavity structure "sees" almost no solid angle that is *not* the cold millitrap surface $\sim 0.25\,\text{mm}$ away, it is no surprise that the cavity mirrors cool to a temperature lower than their bulk copper support structure (described later). The cavity length did fluctuate some during data runs, leading to many annoying stoppages as the cavity length wandered beyond the dynamic range of the tuning PZT, requiring re-locking at the next free spectral range.

Table 6.1 summarizes the relevant cavity QED parameters for our system. We may compare our system to some other notable many-atom CQED implementations, which typically look to the *many-atom* cooperativity as an important figure of merit for ensemble-based protocols for [140, 141, 142, 131]. It is strictly defined as [138]

$$\begin{aligned} C &\equiv \frac{1}{2\kappa\gamma}\sum_{j=1}^{N}|g(\mathbf{r}_j)|^2 \\ &= N\frac{g_{eff}^2}{2\kappa\gamma} = NC_1\,. \end{aligned} \tag{6.17}$$

For the system described in chapter 7, we were able to place up to $N = 10^5$ atoms inside the cavity described in this section, and with the $\frac{1}{2}$ spatial averaging factor this gives a collective atomic cooperativity of $C = Ng_o^2/4\kappa\gamma = 2.5 \times 10^6$. Comparing this with two recent experiments by Sauer *et al.* ($C = 5.4 \times 10^3$, in a strongly-coupled system [49]) and Tuchman *et al.* ($C = 1.2 \times 10^4$, in a weakly-coupled system [56]), we have achieved the largest collective cooperativity ever reported, two orders of magnitude over the previous state of the art.

Lost perhaps, in the usual discussion of optical properties and cavity QED parameters, is the sizeable mechanical infrastructure upon which such a cavity rests. That our cavity must integrate with the two chapters worth of architecture already described makes the cavity infrastructure worth a close look.

6.3.2 The Cavity Mount

A small but very important element of the cavity system is the "payload" piece which rests at the end of the second mass and holds the cavity. This mount is actually two pieces designed to mate the cavity with the millitrap. To accomplish this, the mirror faces must be spatially separated so that they may bridge the faceplates (see chapter 3), and then returned to their original 192.3 μm separation. Figure 6.4 shows the pieces upon which the cavity mirrors rest. The threaded bolt allows the two interlocking copper pieces to be spread apart while remaining a single unit. During installation into the main chamber, the mirror faces are spread apart by ~ 1 cm. The cavity is then positioned into the central channel of the millitrap center piece. After the cavity mirrors are in their proper $x - y$

positions, the pieces are contracted so that the cavity mirrors have threaded the faceplate apertures. The goal was that the cavity mirrors never touch the millitrap in spite of the very narrow clearances, although during installation and a handful of times since[7] this occurred without any detrimental effects. When this happens, the 3D translation stage (described in the next section) is just used to walk the cavity back into place.

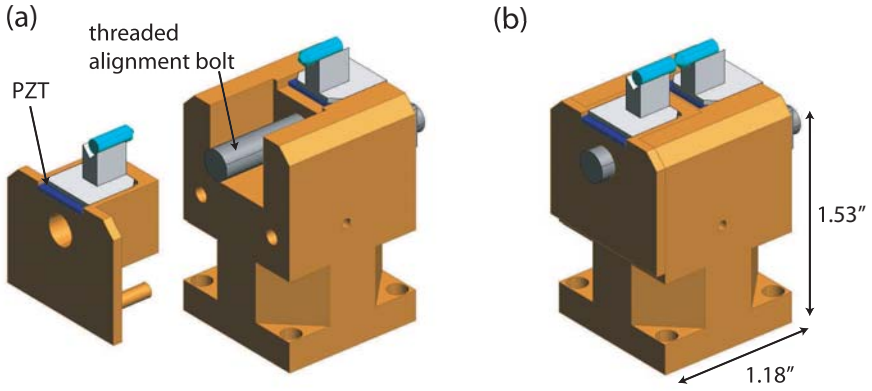

Figure 6.4: The retractable cavity mount. (a) The two cavity mount pieces (a) separated and (b) mated. The threaded alignment bolt ($1/4 - 20$ stainless steel hex cap) allows the linear travel which separates the cavity mirrors for both integration with the millitrap (its essential function) and cleaning (its very handy incidental function).

6.3.3 Cavity Stabilization

Implicit in the theoretical treatment of the cavity resonance is that the cavity has well-defined resonances. To accomplish this, the cavity must be "locked" to a specific frequency, meaning that the mirror separation L must be set to high precision. The system requirements are substantial, as one considers what level of length stabilization is required. The cavity frequency must be stabilized much tighter than its linewidth 2κ, and the cavity resonance itself is probed at roughly $\lambda_p = 780\,\text{nm}$, or $\omega_p = 2\pi \times 3.8 \times 10^{15}\,\text{Hz}$. This is ≈ 490 times the free spectral range $\nu_{fsr} = \frac{c}{2L} = 7.8 \times 10^{11}\,\text{Hz}$. From this, the

[7] The 4.2 magnitude earthquake on March 1st, 2007 which crashed the cavity was a notable instance.

length change ΔL which will shift the cavity by a single linewidth may be shown to be

$$\begin{aligned} \Delta L &\approx \frac{\lambda\kappa}{4\pi\nu_{fsr}} \\ &\approx \frac{\lambda}{2\mathcal{F}} \\ &\approx 0.7\text{pm}\,, \end{aligned} \tag{6.18}$$

where the finesse enters from $\mathcal{F} = \kappa/2\pi\nu_{fsr}$. Within its bandwidth the lock must stabilize the cavity length to much less than this level, putting the required length accuracy into the 10^{-13} m range. This is an incredibly small length, but the sensitivity of the cavity itself makes this possible.

The cavity stabilization takes two forms, a passive vibration isolation system and an active locking component. The passive system is designed to eliminate high frequency > 10 kHz mechanical vibrations, and follows similar systems used in scanning tunneling microscopes (STMs) [143]. The principle is merely one of spring-mass filtering, where the sensitive element (the cavity) is coupled to the environment (the chamber/laboratory) through interspersed "springs" and masses. Generally, large masses and springs of low spring constant K are desirable, although the very low-K springs used in modern STM systems were inappropriate because they would allow the cavity a range of motion which could crash the mirrors into the millitrap. We utilized instead Viton®, a UHV compatible rubber, as the intermediary "spring" element upon which the cavity mount pieces rest. The mounting masses were 0.5 kg and 2.9 kg, and their shape was designed to simultaneously rest on the 3D translation stage (Thermionics EC-1.39-2, which controls the positioning of the cavity), and fit into the main UHV chamber to mate with the millitrap. The full vibration isolation system is shown in Figure D, and the design drawings are presented in Appendix D.

Initial design estimates for the two mechanical resonant frequencies were $f_1 \approx 200$ Hz and $f_2 \approx 1000$ Hz, commensurate with Deep Gupta's measurements of the cavity resonances to be $f_1 \lesssim 70$ Hz and $f_2 \sim 800$ Hz. After the second resonance, the displacement transfer function falls off as $1/f^4$, strongly suppressing the high frequencies which would plague the cavity system.

To eliminate the low-frequency vibrations, piezo-electric transducers (PZTs) are em-

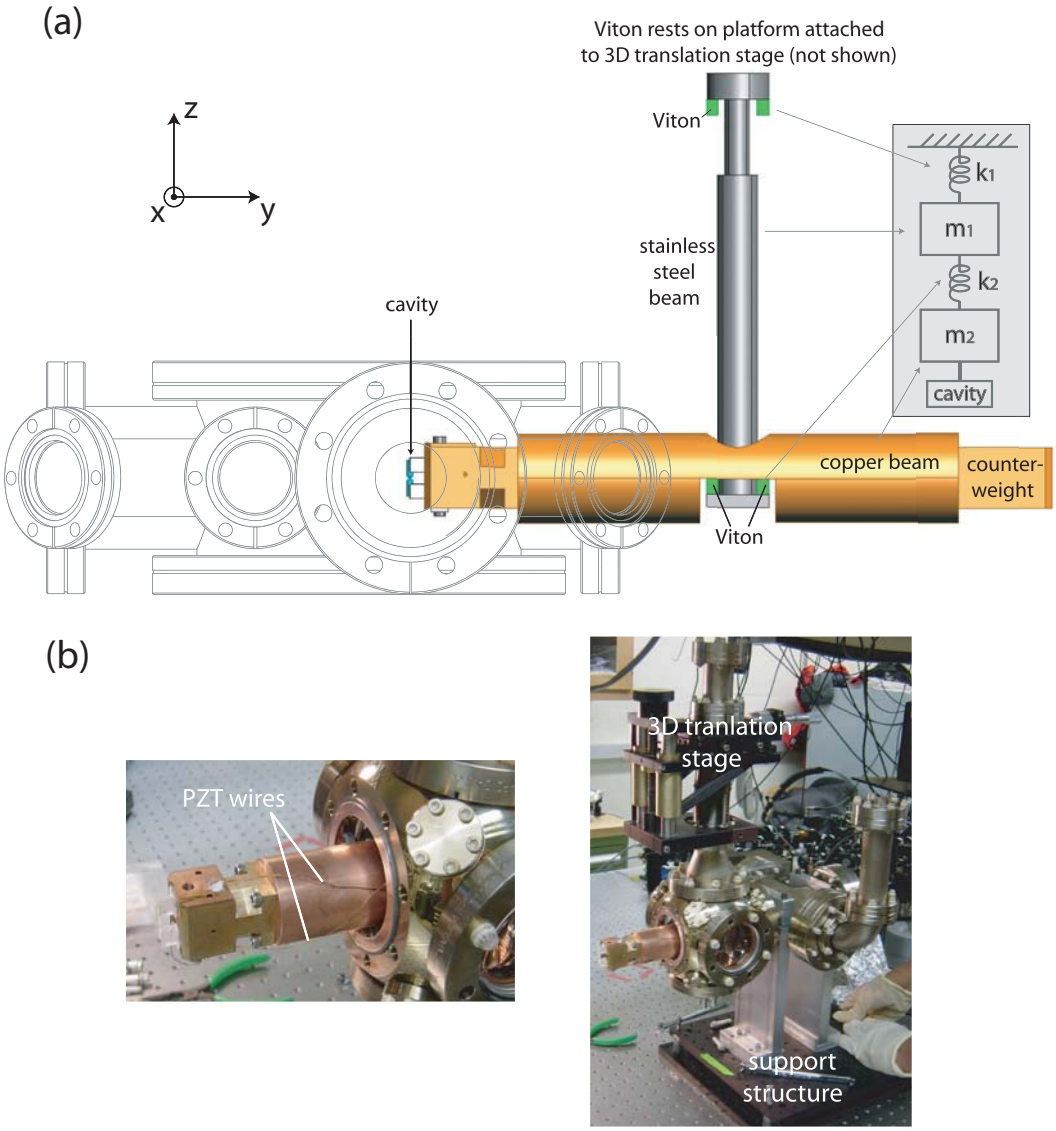

Figure 6.5: The cavity mounting structure. (a) The passive vibration isolation system is seen in context. The T-shaped structure is designed to mate with the main chamber, yet allow 3D positioning of the entire mounting system. The steel beam rests on a platform attached to a 3D translation stage which allows fine adjustments of the entire assembly. The Viton® pieces serve as the "springs" and the steel/copper beams are the "masses" in an idealized coupled oscillator system, diagrammed on the inset. The cavity payload is seen in its final position inside the main chamber. (b) The photos show the cavity prior to installation in the chamber, with critical elements labeled.

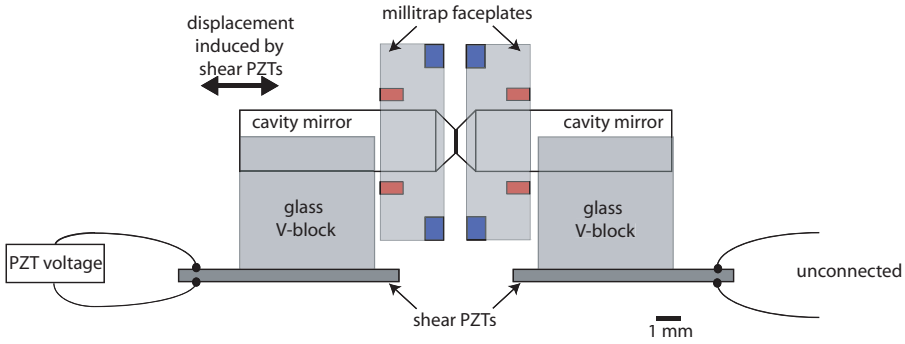

Figure 6.6: The cavity-PZT system. Shown are the elements of the cavity mounting platform, including the shear PZTs which control the cavity length. Both mirrors rest on PZT elements, a redundancy which both ensures identical height off the platforms/cavities and provides a backup in case the wired PZT element was to malfunction.

ployed to actively stabilize the cavity length. The cavity mirrors rest on glass[8] V-blocks, which are in turn epoxied to the PZT elements. This assembly is depicted in Figure 6.6. The maximum voltage on the PZTs is $\sim 500\,\mathrm{V}$, and the voltage was kept to $< 450\,\mathrm{V}$. This limited the range of the cavity PZT tuning to just greater than one free spectral range. The bandwidth of this active locking was limited by these PZTs, as the feedback had to be cutoff at $\lesssim 1\,\mathrm{kHz}$ to avoid uncontrolled resonances in the ceramic material.

Stabilizing the cavity requires no less than three independent servo controls, as shown in Figure 6.7. The "length standard" in the system was the *transfer cavity*, which is a Fabry-Perot cavity of length 30 cm, $\nu_{fsr} = 500\,\mathrm{MHz}$. The transfer cavity mirrors had radius of curvature 25 cm, and half-linewidths of $\approx 100\,\mathrm{kHz}$ at 850 nm, $\approx 30\,\mathrm{kHz}$ at 780 nm (CVI Laser TLM2-800-0-0537-0.25CC). The transfer cavity rests on Sorbothane® squares inside a stainless steel cylinder, which also rests on Sorbothane® to eliminate vibrations. The cylinder is evacuated to prevent air currents from disturbing the locks.

In practice, the sequence of locking was as follows. The 780 nm probe laser is tuned to the desired atomic detuning Δ_a. The ECDL was then frequency stabilized to the transfer cavity via Pound-Drever-Hall (PDH) locking (on transmission) after $\sim 300\,\mathrm{kHz}$ sidebands

[8]These pieces (custom manufactured by Mindrum Precision) are constructed out of glass so that they have the same coefficient of thermal expansion as the mirrors themselves, thereby reducing stresses which could cause modification of the optical properties (i.e. birefringence) of the mirrors.

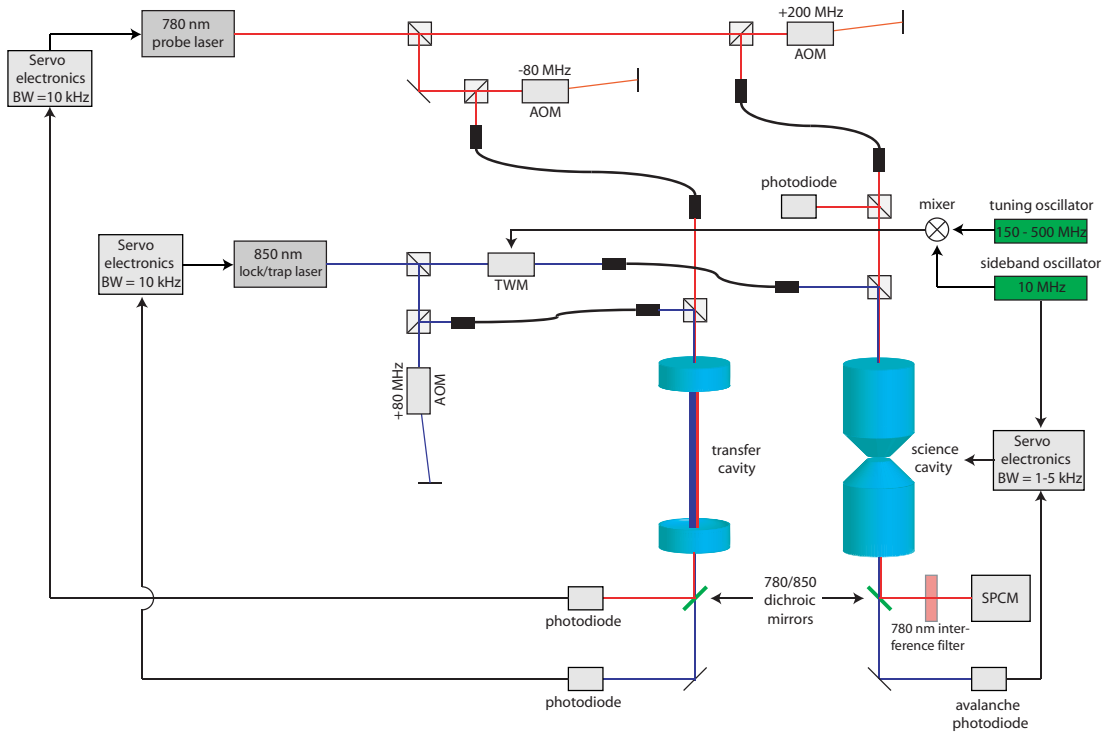

Figure 6.7: The cavity laser feedback system. The locking procedure is outlined in the text, but of special note on this diagram is special role of the two modulation frequencies on the 850 nm locking light. The $150-500$ MHz tuning oscillator allows the locked cavity to be fine-tuned by the variation of the sideband frequency, which is the "carrier" for the cavity lock. The 10 MHz secondary sidebands are the "modulation" sidebands which are mixed down to provide the PDH locking signal for the cavity.

were induced with a double-pass acousto-optic modulator. Turning to the science cavity, both the 780 nm probe and 850 nm locking light are impinged on the cavity, which is in "sweep" mode at this stage to locate the frequencies of the two lasers. The probe laser is then monitored on reflection off the cavity, and the 850 nm locking laser was monitored on transmission by an avalanche photodiode (APD). The 850 nm light was modulated with a traveling wave electro-optic modulator (TWM) with a mixed signal including the primary "tuning" sideband (of range $150-500$ MHz) and the secondary "locking" sideband ($\sim$ 10 MHz). The 850 nm laser is then tuned such that one of the primary sidebands overlaps with the stationary 780 nm probe. The 850 nm laser is then locked to the nearest lockable transverse mode of the transfer cavity. Fine tuning of the primary sidebands

overlapped the 850 nm and 780 nm beams on the science cavity, which is finally locked by PDH on transmission to the APD with the secondary 10 MHz sidebands.

It is important to note here that, while locked, the cavity *always* has some level of 850 nm locking light inside. The probe can be engaged/extinguished at will, but we found that the locking light cannot drop below 100 nW at the APD without losing the cavity lock. The AC Stark shift of this red-detuned light is irrelevant, but higher intracavity powers can be significant enough to confine the atoms in the standing wave potential of the locking light. This feature of a controlled optical trap functionality is a hallmark of the subsequent chapter. Thus, the phrase "locking light" and "trapping light" were interchangeable while operating the system.

6.3.4 Cavity Probing and Light Detection

Actually coupling light into and measuring the light emitted from the cavity immediately bring in issues related to the quantum efficiency of a measurement. Consider, for example, that light is impinged on one side of the symmetric cavity with a detector placed on the other side. If the detector registers a "click," what has been learned about the state of the photon field inside the cavity? In practice the detector will register a certain photon count rate Γ_{meas}, and again the question is posed: what has been learned about the state of the photon field inside the cavity? All detectors will have "dark counts" which have nothing to do with the cavity at all. Furthermore, the cavity is twice as likely to scatter an intracavity photon as transmit it, and with a photodetector on only one side of the symmetric cavity the information gathered is reduced by another factor of two. Accounting for all of these effects is a budgeting of efficiencies and noise, and it is crucial to be very precise about these factors when making claims about measurements of a quantum system.

There are three main factors determining the efficiency of the measurements made herein. First, the cavity efficiency η_{cav} for the two-sided cavity (with one-sided detection) is given by $\eta_{cav} = \mathcal{T}/(2\mathcal{T} + 2\mathcal{L}) = 0.15$. Second, there will be losses on the optical path to the detector, and in this case the dichroic (CVI Laser LWP-45-RU720-TU850-PW-1008-C) and 780 nm interference filter (Intor 780/10/58-2R) which distill the probe

light from the 850 nm cavity locking light and background light contribute $\eta_{filt} = 0.74$. Finally, there is the efficiency of the detector itself. The Perkin-Elmer SPCM-AQR-13 single-photon counting module (SPCM) has a measured quantum efficiency at 780 nm of $\eta_{det} = 0.45$. These efficiencies are of course multiplicative, so the *maximum* total efficiency is $\eta = \eta_{cav}\,\eta_{filt}\,\eta_{det} = 0.05$.

We must also recognize the role played by background counts. The "dark counts" on the detector are an ever-present signal, and represent the absolute noise floor for any quantum optical measurement. The quoted dark count for the SPCM is 250 /s, but on the optical table [9] the measured dark count was $\Gamma_{d.c.} = 250 - 500$ /s. A second contribution to the background counts is the leakage of the 850 nm locking light. The dichroic mirror and interference filter prevent the typically ~ 100 nW of locking light emitted from the cavity from reaching the SPCM, which itself has a quoted detector efficiency at 850 nm of $\eta'_{det} \approx 0.45$. The SPCM background counting rate from the locking light leakage was typically $\Gamma_{850} = \eta'_{det}\Gamma_{leak} = 2 \times 10^4$ /s; in later implementations not treated in this thesis, these 850 nm leakage counts were eliminated below the dark count rate by use of a second dichroic mirror.

Thus, we have the full budget for the measured count rate Γ_{meas} with the equation

$$\Gamma_{meas} = (\eta_{det}\,\eta_{filt}\,\eta_{cav}) \times (2\kappa\bar{n}) + \Gamma_{850} + \Gamma_{d.c.}\,. \tag{6.19}$$

The conversion of measured count rate Γ_{meas} to the average intracavity photon number is thus

$$\bar{n} = 2.41\left(\frac{\Gamma_{meas}}{MHz}\right) - 0.05\,. \tag{6.20}$$

A graphical representation of the detection parameters is represented in Figure 6.8.

6.3.5 Atom Delivery to the Cavity

In terms of slowing, cooling, and delivering atoms to the millitrap region, the principles of operation are ultimately the same as described in previous chapters. While the system was designed to employ an Ioffe-Pritchard trap for ultracold atoms inside the cavity, we found we were unable to efficiently load atoms from the external quadrupole trap into IP

[9] With the rubber cap provided with the unit in place, the quoted dark count was approximately the specified 250 /s.

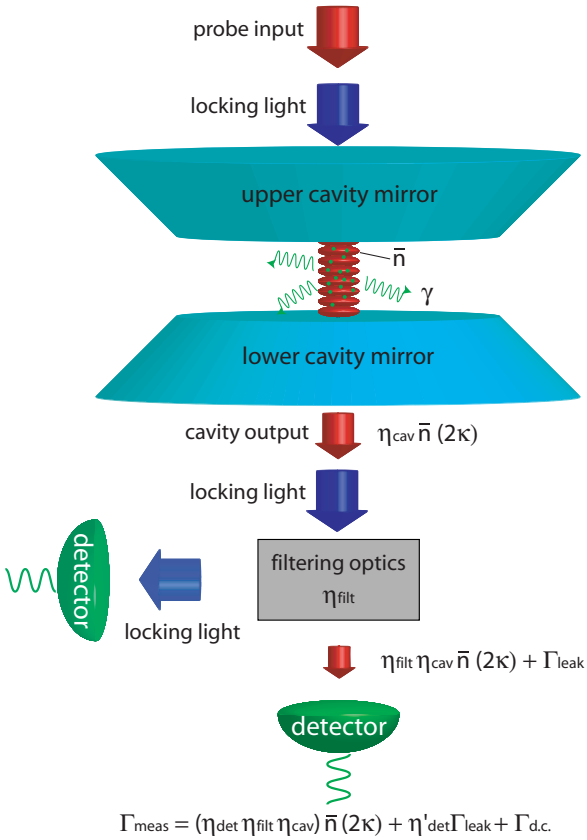

Figure 6.8: Many-atom cavity QED in the practice. N atoms are distributed over the cavity mode while 850 nm locking and 780 nm probe light are impinged on the cavity. (Note that there are in fact ~ 500 anti-nodes, and not the handful shown here for clarity.) The probe light establishes an average photon number of $\bar{n}$ inside the cavity, which decay at a rate 2κ from the cavity. The probability that this decay correlates to a photon emission toward the detector is η_c, and after factoring in the losses due to the filtering optics, the quantum efficiency of the detector,and the 850 nm leakage, we obtain a conversion formula (Equation (6.19)) for measured count rate to $\bar{n}$, the photonic state of the cavity.

trap in the presence of the cavity. The difficulty came about because the IP trap had to be biased with a transverse field to hold atoms the atoms outside the cavity, and as described in Ref. [54] this lowers the trap IP trap depth substantially for large deviations from the trap center. While we were able to load atoms into this shallowed trap, the transfer efficiency was so compromised that achieving runaway evaporative cooling became impossible.

As outlined in Section 3.5.3, 40,000 atom BECs were produced in a TOP trap 1 mm from the trap center. At $T \lesssim 1\,\mu$K, the atoms can be easily transported into the cavity

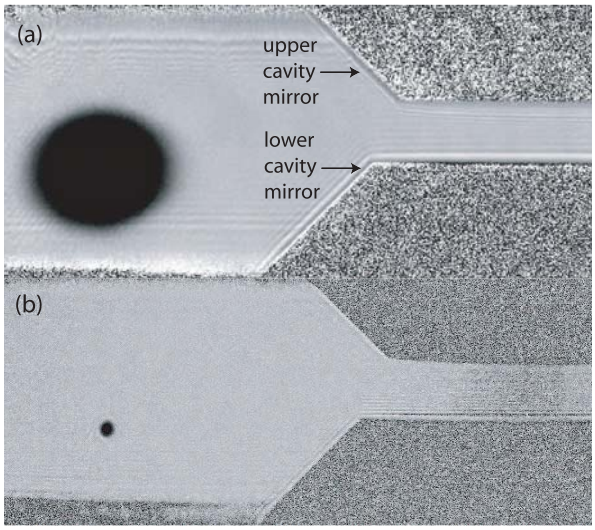

Figure 6.9: BEC in the TOP trap. (a) Atoms in the TOP trap before RF evaporation. Seen on the right are the shadows of the cavity mirrors. (b) After RF evaporation, a nearly pure condensate of 4×10^4 atoms is seen under 11 ms time of flight.

separation by displacing the position of the TOP center with bias field. One outstanding question prior to the delivery of cold atoms to the cavity was the lifetime of trapped atoms between the mirrors. While we certainly hoped it would be the same as the vacuum-limited lifetime outside the cavity, the outgassing properties of dielectric-coated mirrors was a large unknown and it didn't seem beyond the realm of possibility that the atoms would experience greater losses inside the narrow cavity due to increased background collisions. We directly compared the "inside" and "outside" lifetimes by holding a 1μK cloud in and out of the cavity, and measuring the atom decay from identical traps. Thankfully, we found that the lifetime inside the cavity (in the absence of probe light) slightly *surpassed* that outside the cavity region, though the improvement was not very significant.

6.4 Data Processing and Real-Time Detection

The output of the SPCM is an experimentalist's dream, a 5 V TTL pulse of width 30 ns. The dead time is ~ 70 ns, meaning only fluxes of $< 10^7$/s were allowed on a single SPCM. From Equation (6.20), this limits the intracavity photon number for the 780 nm

probe light to $\bar{n} \approx 20$.

We typically examined the SPCM data stream in two ways. For detailed processing, data was collected with a GageScope® digital oscilloscope which was operated with a dedicated[10] computer to collect the data. The duration of the data stream depended on the sampling rate of the oscilloscope, but it was typically operated at a sampling rate of 10 mega-samples-per-second (MSPS), which gave a 256 ms time window. For sensitive detection we would employ 50 MSPS, but there was little point in going any higher because the SPCM saturation count rate was 10 mega-counts-per-second (Mc/s). The data were stored in a dated file which required ~ 5 MB of disk space. Over the year and half of cavity operation, many data analysis routines (using Igor® software) have been developed to churn through these files to extract the information from the data stream. The workhorse was Deep Gupta's conversion program which converted the huge 5 MB analog Gagescope® files to a more manageable digital signal. These allowed very detailed analyses of the stream, though not yet in real time. This "post-processing" of the digital TTL output is non-ideal for experiments which need to discern the state of the system upon probing to trigger some other element, but is wonderful for hitting the "go" button for repeated experiments, going to Strada for a coffee, and returning to a set of data which the data analysis routines can batch through.

While it seems a perverse irony to take this beautiful (and pricey!) single photon counter and derive an analog signal from it, this is exactly the functionality that is needed to make the output of the device experimentally useful. Luckily, one gets to "have his cake and eat it too," as the signal from the SPCM may be split into two channels with only slight distortion of the $5\,V$, 30 ns square pulses[11] which are designed to be 50 Ohm-terminated. The first split channel inputs to the GageScope® (with an inline 50 Ohm terminator), the second to a device constructed to convert the count rate to an analog voltage (with a high-impedance input). Commercial count-rate-to-voltage converters (CRVCs) are available, but are typically designed for high count rates. To convert the cavity signal (which can

[10] This computer's processor was also heavily dedicated towards daily music consumption (KLM), cricket scores (Deep), and scouring Craigslist for $1,000 cello bows (Kater).

[11] The distortion typically took the form of a "ringing," where the pulse was presumably reflected on the BNC cable line and resulted in ~ 3 pulses of decaying amplitude. Both the GageScope® and the CRVC could be tuned to disregard these after-events.

be as low as 1000 counts/sec) to an analog voltage which is tailored to the SPCM output, we designed a CRVC circuit with a tunable bandwidth from $1 - 250$kHz with just $2\,\mu$s of dead time per cycle. Figure 6.10 describes the timing diagram, and Figure 6.11 shows the details of the electronic elements.

The CRVC thus allows the use of the SPCM as both a highly sensitive photodiode and a digital photon counter. The analog output of the CRVC is input to an Agilent digital oscilliscope, allowing sensitive triggering of the cavity flux to within the inverse of the CRVC bandwidth. With this element, we obtain a real-time monitor of the cavity transmission, and thereby the state of the atoms in the cavity mode. As described in the following chapter, many experiments relied on this functionality to initialize the system.

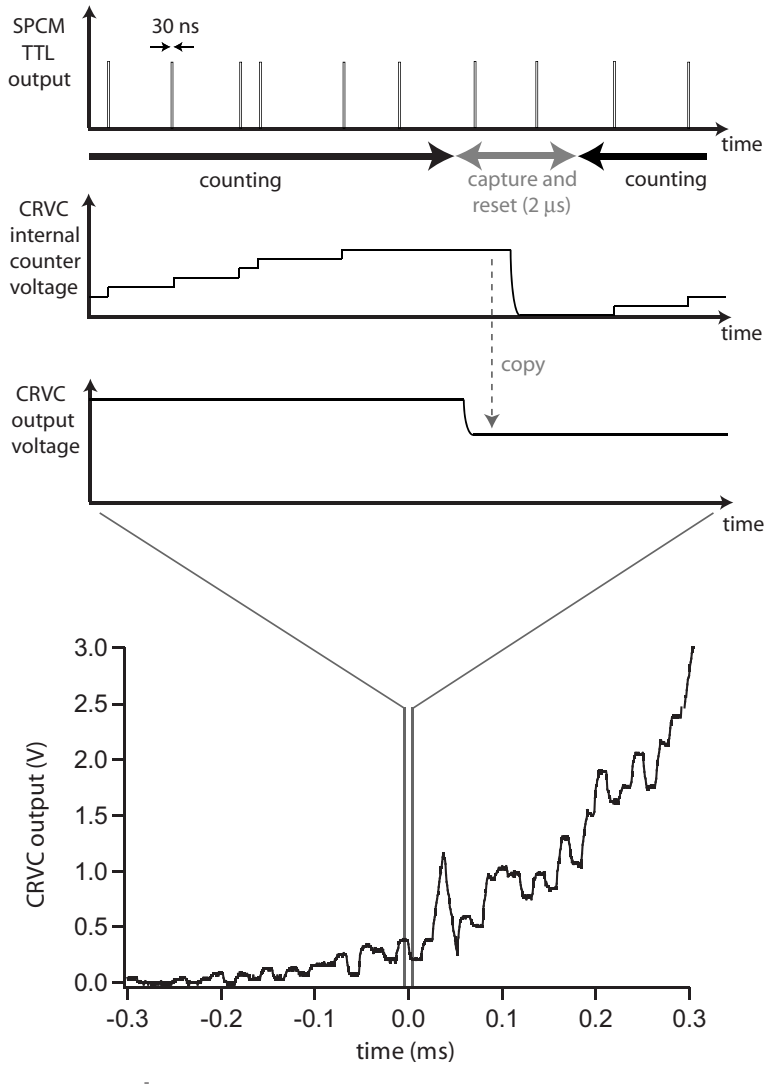

Figure 6.10: The count-rate-to-voltage converter (CRVC) timing diagram. The upper trace shows the SPCM output as 30 ns TTL pulses, which are input to the CRVC circuit which increments the counter during the "capture" time. The clock cycle has 2 μs dead time, during which the count number is "copied" to the output value of the CRVC, the counter is subsequently cleared, and finally the count for the next clock cycle begins from zero. The bottom trace shows what the output of the CRVC looks like as the cavity comes into resonance in the presence of a probe, and many experiments described in the following chapter are initialized by this rising edge harkening the arrival of the cavity resonance condition.

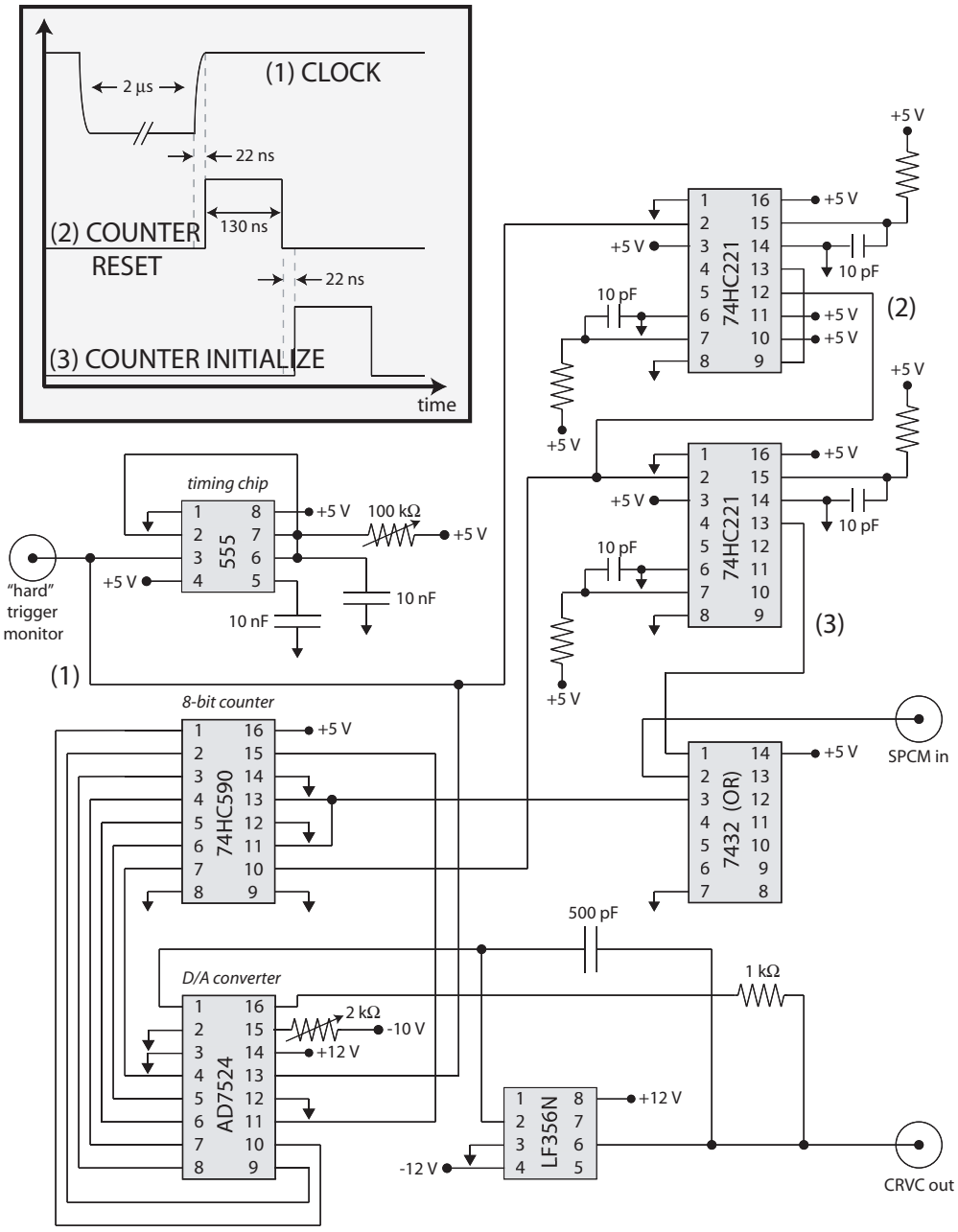

Figure 6.11: Count-rate-to-voltage converter circuit diagram.

Chapter 7

First Experiments with the BEC-CQED System

While its operators harbored no illusions about the substantial technical complexity of this experiment, we were somewhat surprised by the downright finicky nature of the apparatus. This could have been foreseen from the increased infrastructure (added to the already substantial complexity of the apparatus described in chapters 2 and 3), but we soon found the sensitivity of the locking chain described in Figure **??** to be the largest impediment to forward progress. Operating the system required much longer start-up time than the pure millitrap work, and for many months ~ 2 all-nighters per week became the norm as the system appeared to retain lock for longer stretches of time if the *clock* time was single digits, followed by A.M. While many missteps were made and many confused debates were conducted in the wee hours of the morning, at the time of this writing the system appears very well understood (as evidenced by the two papers referenced above). While the definitive word on the new physics which will be borne out of BEC-CQED system awaits documentation in other theses, this chapter follows (somewhat chronologically) the critical experiments which allowed us to understand the unique system we had implemented.

7.1 Atom Transits

The first step in any cavity QED experiment is the observation of atom "transits" through the cavity by the change in the cavity transmission. The atoms will ultimately be precisely delivered to the cavity mode, but to begin the cavity mode must be located. The cavity was thereby tuned to resonance and we blindly moved the atoms through the cavity while monitoring the cavity transmission. After some trial and error in the transverse positioning of the atom trajectory, the signal shown in Figure 7.1 was observed.

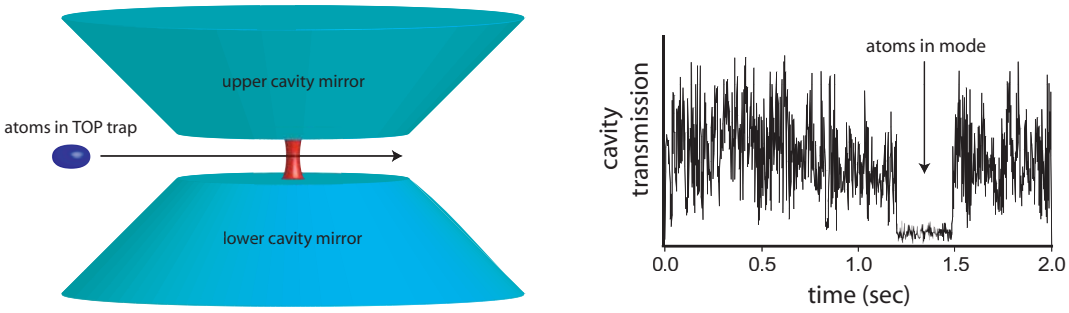

Figure 7.1: Observation of controlled atom transits. As shown in the sketch on the left, the TOP-trapped atoms are brought through the cavity mode. As seen in the cavity transmission, the presence of the atoms in the mode shifts the resonance away. After the atoms have left the mode, the transmission returns to its previous level.

With this signal in hand, the precise spatial position of the cavity mode could be determined via cavity transmission alone. Ultimately we would gain another method by which to "see" the mode, but this must await a later section.

7.2 Probing the Shifted Cavity

As reliably transferring ultracold atomic clouds (initially bound in the TOP trap) into the cavity mode became commonplace, a new language began to emerge as we dutifully recorded "uptick times," searched far and wide for the "the line," and dreamt lofty goals of publishing a PRL entitled simply "Quantum Upticks." While obscure to outside observers, these phenomena became familiar to us as our first window in the dynamics of the many-

atom cavity system, and surely deserve a detailed exploration here.

7.2.1 Upticks

As seen in the atom transit graph of Figure 7.1, the cavity is rapidly shifted out of resonance as atoms are introduced to the cavity mode. The hard edge which is seen as the cavity comes back into resonance, however, is caused in this case by the fact that the atoms are removed from the cavity mode as quickly as they arrived while the cloud follows a constant velocity trajectory.

Far more interesting is the case where the atoms are placed in the cavity mode and are removed from the system through other mechanisms. We defer a detailed discussion of the loss induced by the cavity probe (both off- and on-resonance) [144], but at the very least the number loss due to background gas collisions is omni-present. As these losses take the atom number in the mode $N \rightarrow 0$, the cavity shift $\Delta_N = \frac{Ng_{eff}^2}{\Delta_a}$ will be tuned back to $\Delta_N = 0$. For the experimentalist monitoring the transmission of the cavity with probe tuned to the unshifted cavity resonance ($\Delta_c = 0$), the CRVC output will resemble the data stream presented in Figure 7.2(b).

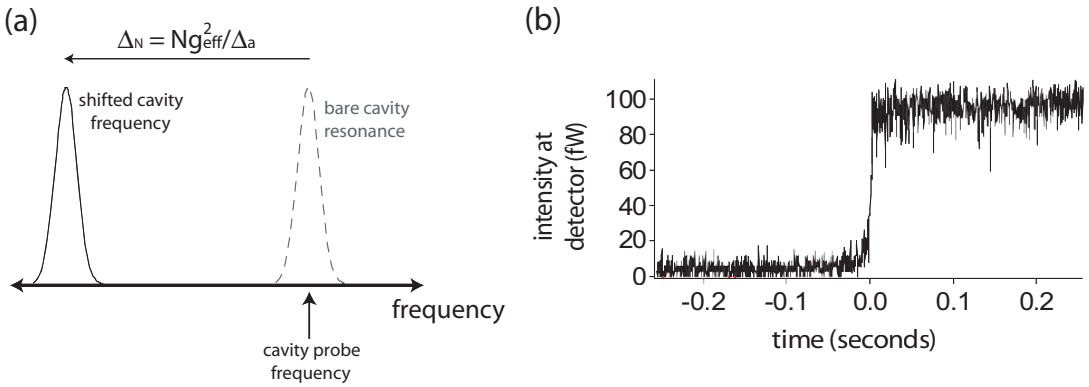

Figure 7.2: Upticks (a) Frequency-space picture of the uptick process. Atoms are loaded into the cavity ODT, shifting the cavity from resonance by $\Delta_N = Ng_{eff}^2/\Delta_a$. Light resonant with the empty cavity is impinged upon the system, but is reflected due to the Δ_N shift. As the atoms are depleted from the trap, the cavity is brought back into resonance, finally sparking full transmission as seen in (b).

The time delay between the initiation of the probe and the moment at which the cavity

transmission spikes back to its "empty cavity" level is known as the uptick time. With a weak probe ($\Gamma_{meas} = 10^5$ /s, $\bar{n} = 0.24$), uptick times of > 40 seconds were observed. Shortened uptick times spoke to either poor atom number population (which could be confirmed by absorption imaging) or an increased atom loss rate. The increased atom loss rate could speak to higher chamber pressure or, far more likely, some light-induced losses from the action of the probe. There are some important subtleties for off-resonance probe losses which will be revisited later in this chapter.

7.2.2 The Stationary Probe

Measuring the cavity shift Δ_N of course involves tuning the probe away from the bare cavity resonance. Two types of experiments which explore the cavity shift are possible, both with their own virtues. The first is the "stationary probe," which is closely related to the uptick measurements and is depicted in Figure 7.3.

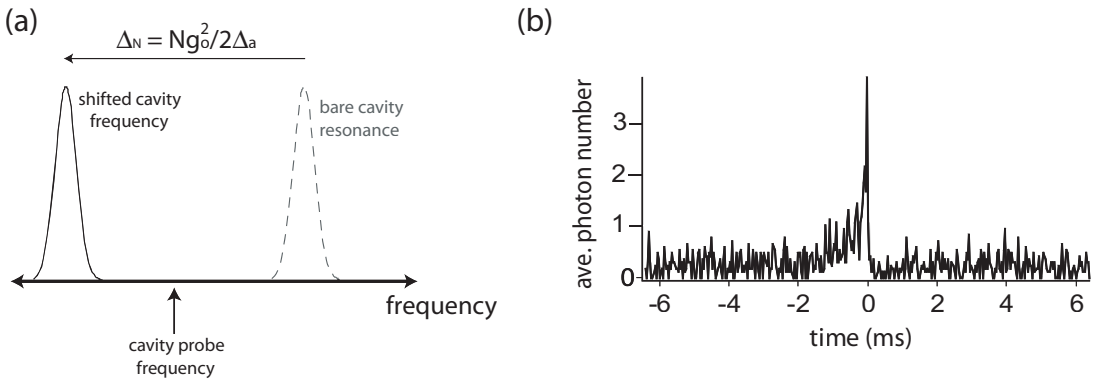

Figure 7.3: Cavity Line Transits with Stationary Probe. (a) Similar to the uptick process, the cavity is shifted by the presence of the atoms, but the probe is now tuned between the shifted cavity and the bare cavity. (b) As the atoms are depleted the cavity is brought into resonance for a brief time, and then tuned away from resonance as the system returns to the empty cavity resonance. The atomic detuning in this case was $\Delta_a = -2\pi \times 300\,\text{GHz}$.

For these stationary probe experiments, the cavity probe is detuned from the bare cavity resonance by $\Delta_c = \omega_p - \omega_c$. With N intracavity atoms in the dispersive limit, the cavity shift is $\Delta_N = Ng_{eff}^2/\Delta_a$ and is presumably greater than Δ_c. As atoms are lost from the system, Δ_N will steadily be reduced until it approaches and equals Δ_c. Up to

this point, the probe light which was incident upon the cavity was mostly reflected as the lorentzian lineshape dictates the transmission to be $(1 + \frac{(\Delta_c - \Delta_N)^2}{\kappa^2})^{-1}$ off-resonance. As $\Delta_c \approx \Delta_N$ within κ, the transmission spikes as the resonance condition is met and the intracavity light field is built up. The presence of $\lambda_p \approx 780\,\text{nm}$ light in the cavity causes heating which accelerates the atom loss [144]. This will rapidly take the system from $\Delta_N > \Delta_c$ to $\Delta_N < \Delta_c$, and the observation at the photodetector will be a "line" which represents the photons which passed through the cavity for the brief time when $\Delta_N \approx \Delta_c$.

As the value of Δ_c is set by the experimentalist, the arrival of the line is in fact a measurement of the atom number from $N = \frac{\Delta_a \Delta_c}{g_{eff}^2}$ (on resonance). This hypothesis may be tested by triggering an absorption image on the arrival of the line, and the linear correlation between the cavity shift and the number count in Figure 7.4(b) not only confirms the theory but also provides an independent measurement of g_{eff}^2. For the data shown in Figure 7.4(b), the data confirm the expected value of $g_{eff}^2 = \frac{1}{2} \times \frac{5}{6} \times (2\pi \times 15.6\,\text{MHz})$. The $\frac{1}{2}$ factor is of course from spatial averaging, the 15.6 MHz conforms to the expected value of the cavity coupling from the knowledge of the mode volume, and the $\frac{5}{6}$ factor arises from the σ^+ polarization of the probe light.

7.2.3 The Chirped Probe

The second method of probing the cavity shift involves operating the probe in "sweep" mode, where the cavity detuning Δ_c is swept linearly in time across Δ_N. This situation is perhaps more controlled than the passive line transits of the stationary probe, as in the sweep experiments the probe level and sweep rate are determined by the experimentalist. In particular, the probe power can be reduced to such a level that the traversal of the line (and corresponding dose of optical power) hardly influences the atom number after sweeping through resonance, yielding a "non-destructive" probe of the atom number. The relation of this non-destructive nature to the topic of quantum non-demoltion (QND) measurements will be discussed in a subsequent section, but for the purposes of this discussion the technique may be thought of as an alternative measurement of the atom number akin to phase-contrast imaging [21] in its weak effect on the atom population. The sweeping method is depicted in Figure 7.5.

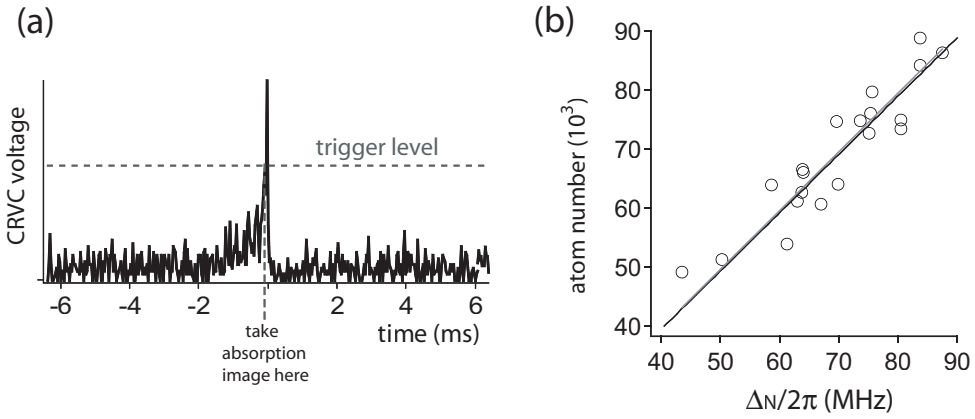

Figure 7.4: Cavity line shift as a number measurement. (a) The CRVC output is set to trigger an absorption image at a certain count rate corresponding to $\Delta_c \approx \Delta_N$. (b) The absorption images provide an independent measurement of the atom number, and for a set of such experiments with $\Delta_a = 2\pi \times (100\text{GHz})$ the number count from the triggered absorption images are plotted against the Δ_N. There is not one but two lines through the data, with the black line representing the slope predicted by the expected $g_{eff}^2 = \frac{1}{2} \times \frac{5}{6} \times g_m^2 = (2\pi)^2 \times 104\text{MHz}^2$ and the grey line the least squares fit to the data (with a constrained zero crossing). The fit gives the measured value of g_{eff}^2 to be $(2\pi)^2 \times 99\text{MHz}^2$, 5% off the expected value. The noise on the absorption imaging measurements were at least at this level due to poor image quality from light diffraction off the mirror edges, so this should be interpreted as a confirmation of our hypothesis within the experimental precision.

7.3 FORT in the Cavity

While the primary function of the 850 nm laser is to lock the cavity length, it boasts a second and remarkably useful function: that of a Far-Off-Resonance optical Trap (FORT) [145]. The advantages of optical trapping in a cavity are many, but perhaps none as much as the "state independent" nature of the trapping [41]. Optical trapping opens the possibility of probing ensemble spin dynamics with the cavity, a scenario which is precluded by a magnetic trap and explored later in this chapter.

The theory behind optical trapping is explored in great detail elsewhere [20, 63, 146, 147]. The AC Stark shift of the ground state for a far-detuned π-polarized beam of intensity

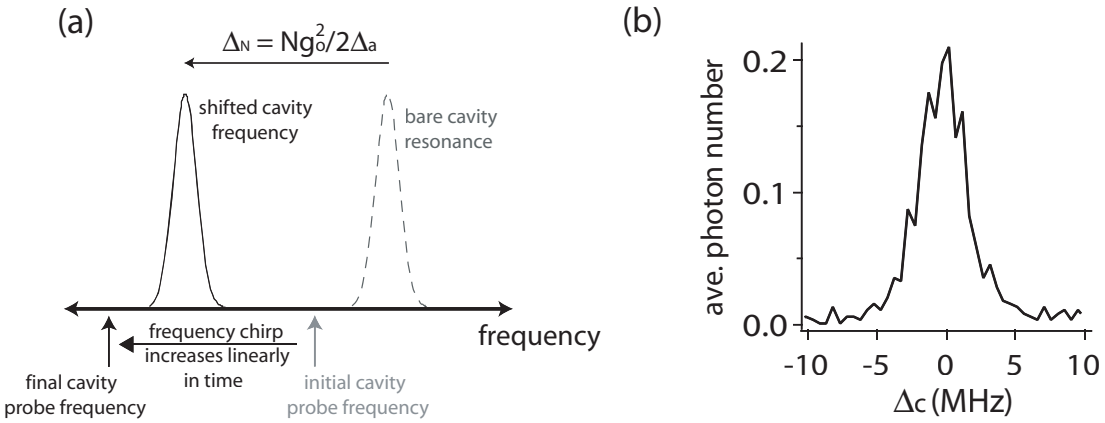

Figure 7.5: Sweeping the probe over the shifted cavity resonance. (a) Unlike the passive process of Figure 7.3, the probe is chirped in time such that it sweeps across the shifted cavity resonance. (b) A

I incident upon a ^{87}Rb atom is given by

$$\Delta E_g = \frac{\hbar\gamma^2}{8}\frac{I}{I_{sat}}\left(\frac{1}{3}\frac{1}{\delta_{D1}} + \frac{2}{3}\frac{1}{\delta_{D2}}\right), \tag{7.1}$$

where $I_{sat} = 1.4\,\mathrm{mW/cm^2}$, δ_{D1} and δ_{D2} are the detunings of the beam from the $D1$ and $D2$ lines (the $\frac{1}{3}$ and $\frac{2}{3}$ factors are from the Clebsch-Gordon coefficients for the transitions).

The optical power inside the cavity P_c is discerned from the output power P_{out} by $P_c = \mathcal{F}_t P_{out}/\eta_t$, where η_t is the efficiency budget for the 850 nm light $\eta_t = \frac{1}{2}\times\frac{0.66}{\times}0.8 = 0.26$, where the factors were the balanced cavity, the dichroic mirrors, and the interference filter, respectively. The maximum AC stark shift in the cavity is thus given by

$$\Delta E_g = -k_B \times 65 \times \left(\frac{P_{out}}{nW}\right) nK\,. \tag{7.2}$$

As the mode structure inside the cavity is of the form $|\phi(\mathbf{r})|^2 \propto \sin^2(k_t z)\, e^{-\rho^2/w_t^2}$, the conversion to the trapping frequencies of the wells of the optical potential is given by:

$$\omega_z = 2\pi \times 4.1 \times 10^3 \times \sqrt{\frac{P_{out}}{nW}}\; Hz \tag{7.3}$$

$$\omega\rho = 2\pi \times 32.5 \times \sqrt{\frac{P_{out}}{nW}}\; Hz\,. \tag{7.4}$$

While these conversions come from the theoretical equations, they were ultimately confirmed experimentally.

This is not the first standing wave FORT inside a cavity to trap cold atoms [41], but it is the first instance where atoms are controllably delivered *pre-cooled* to an intracavity FORT. Loading the atoms into the FORT was complicated by the fact that the intracavity optical power couldn't be arbitrarily lowered without losing the cavity lock. The lowest level which we would maintain lock was effected an AC Stark shift of $\Delta E_g \sim -k_B \times 100\,\mathrm{nK}$, well below the $4E_{rec} = k_B \times 710\,\mathrm{nK}$ level at which the FORT cannot support bound states, so its effect can be ignored other than a modification of the effective mass. The $1\,\mu$K level is approximately the temperature of atoms which will be placed into the cavity region from the TOP trap. While the "sky's the limit" on the largest Stark shift possible, other detrimental effects enter in such as increased three-body losses and enhanced heating from the ODT power fluctuations.

Loading the atoms was optimized through a sequence which lowered the FORT to $\sim 1\,\mu$K, aligned the TOP-trapped atoms with the cavity mode, and then terminated the magnetic trap and, over the course of $\approx 1\,\mathrm{ms}$, increased the FORT depth to $6\,\mu$K. While some atoms were lost in the transfer process, the loading was $> 25\%$ efficient. The loading process is depicted in Figure 7.6(a), including an image of $\sim 10^5$ atoms trapped in the FORT.

As the $6\,\mu$K trap was typical, it is instructive to consider some thermodynamic quantities of interest. With similarly typical loading conditions, we can consider placing $100,000$ atoms evenly distributed over 300 sites, meaning each lattice site holds approximately 300 atoms. Finally, observed temperatures[1] consistently showed $\sim 0.8\,\mu$K temperatures for the optically trapped atoms. Table 7.3 summarizes relevant energetic and thermodynamic quantities.

A few facts stand out from Table 7.3. First, the ground state energy of the axial trap is $\frac{1}{2}\hbar\omega_z \approx 1\,\mu$K, almost exactly the observed temperature. Thus, the atoms will primarily be found in the axial ground state and are thermally distributed amongst the transverse harmonic states. Second, the evaporation parameter $\eta = U_o/k_BT = 6$ is very

[1] These were measured in the brief time of flight imaging available when the cavity FORT is extinguished and the atoms fall under gravity. With less than $100\,\mu$m to fall before the majority of the cloud is obscured by the lower cavity mirror, no more than 4 ms of free fall time was available. Temperatures were estimated from the growth of the transverse width, though the data were rather noisy due to the diffraction of imaging light off mirror edge.

k_t : Cavity FORT wavevector	$2\pi/850\,\mathrm{nm}$
w_t : TEM_{00} mode waist for 850 nm	$24.4\,\mu\mathrm{m}$
N_s : Atom number per site	~ 300
U_o : Trap depth	$5\,\mu\mathrm{K}$
T : Temperature	$0.8\,\mu\mathrm{K}$
η : Evaporation parameter, $\frac{U_o}{k_B T}$	6
ω_z : Axial trapping frequency, $k_t\sqrt{\frac{2U_o}{m}}$	$2\pi \times 40\,\mathrm{kHz}$
ω_ρ : Transverse trapping frequency, $\frac{2}{w_t}\sqrt{\frac{U_o}{m}}$	$2\pi \times 310\,\mathrm{Hz}$
σ_z : Axial width (rms), $\sqrt{\frac{2\hbar}{m\omega_z}}$	70 nm
σ_ρ : Transverse width (rms), $\frac{1}{\omega_\rho}\sqrt{\frac{k_B T}{m}}$	$12\,\mu\mathrm{m}$
n : Density, $N_s/\sigma_z\sigma_\rho^2$	$3 \times 10^{13}\,\mathrm{cm}^{-3}$
g : Interaction strength, $\frac{4\pi n\hbar^2 a_s}{m}$	$2\pi \times 210\,\mathrm{Hz}$
T_c : BEC transition temperature, $\approx \hbar\bar{\omega}N_s^{1/3}/k_B$	$0.5\,\mu\mathrm{K}$
Γ_c : Collision rate, $n(8\pi a_s^2)\sqrt{\frac{k_B T}{m}}$	500 Hz
Γ_t : Tunneling rate, $\approx \omega_z e^{-\lambda_p\sqrt{2m(U_o-\hbar\omega_z)}/2\hbar}$	0.02 Hz
η_{LD} : Lamb-Dicke parameter, $k_p\sigma_z$	0.28

Table 7.1: Optical lattice parameters

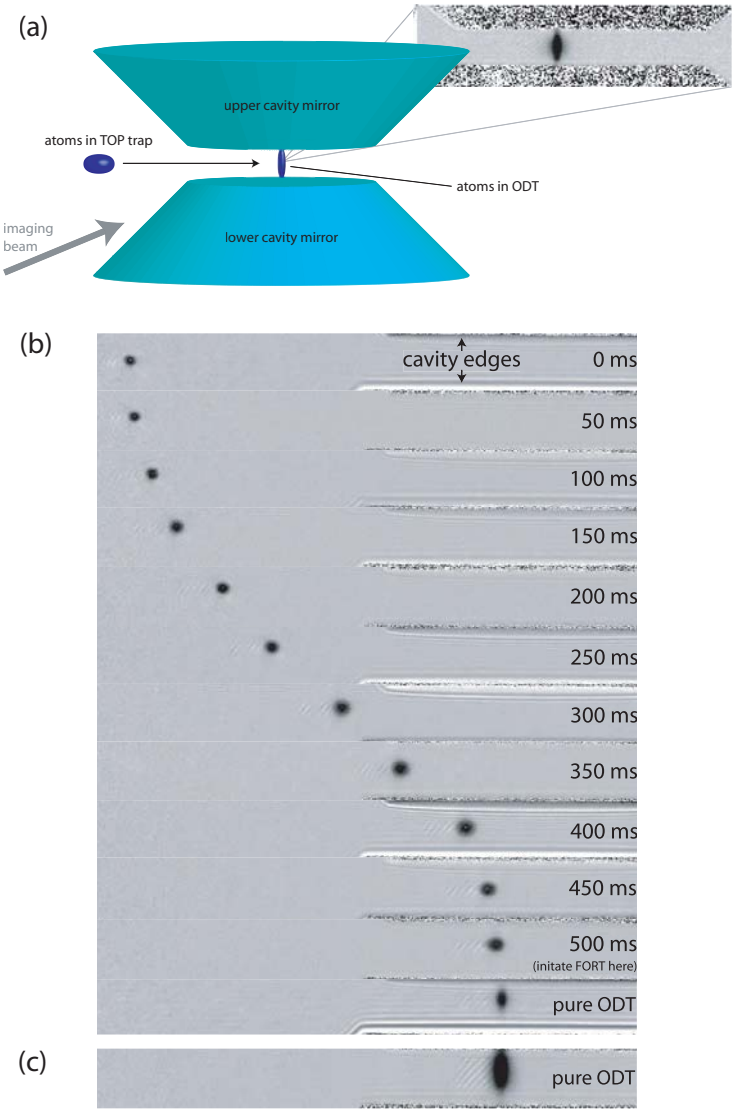

Figure 7.6: Loading atoms into the cavity FORT. (a) Diagram shows the transfer of atoms from outside to inside the cavity, with the imaging axis shown. (b) In-trap images of a condensate being loaded into the ODT of the cavity. The TOP minimum is smoothly shifted from outside the cavity to inside over 500 ms, and then finally loaded into the ODT as described in the text. (c) A much larger ODT population in the cavity FORT is seen by the loading of a 1μK thermal cloud.

noteworthy, as typically during forced rf evaporation towards BEC this parameter is held at ≈ 10. Finally, that the ratio of $T/T_c = 1.6$ is so close to 1 raises the possibility of Bose condensation in each lattice site. As $T_c \propto U_o^{1/2} \times N_s^{1/3}$, modest enhancements could

readily bring the transition temperature to 1 μK. The trap depth was particularly easy to increase, but even we operated the system with $U_o > 20\,\mu$K (nominally, $T/T_c = 1.1$) we did not observe any signature of condensation. Further improvements are well within the realm of possibility, and this remains a subject surely worth further investigation.

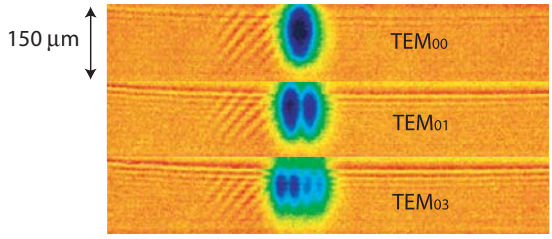

Figure 7.7: Ultracold atoms as intracavity power meters. The cavity is locked to different transverse modes of the 850 nm locking/trapping light, and the atoms are loaded from the TOP as in Figure 7.6. The higher order TEM modes show the characteristic Hermite polynomial shape, with a slight bias in population on the loading side.

While this apparatus was designed to magnetically confine atoms in the cavity mode, utilizing the FORT to confine the atoms has proven to be the most useful experimental avenue. One reason for this is the fact that each well of the standing wave potential is in the regime where the Lamb-Dicke parameter $\eta_{LD} = k_p\sigma_z = 0.28$ for the 6 μK FORT. The "Lamb-Dicke regime" is the case where $\eta_{LD} < 1$, and in the context of cavity QED this implies that each site in the optical lattice has a well-defined cavity coupling. The value of each well coupling is easily calculated by the beat note between the 850 nm trapping light and the 780 nm probe light. The coupling is thus approximately periodic over 4.7 μm, or ~ 11 lattice sites, which is depicted in Figure 7.8.

7.4 Splitting the Cavity Shift with Atomic Polarization

It is likely to be the case that the TOP-to-ODT transfer will retain the entire population in the $|F = 1, m_F = \pm 1\rangle$ state. With this known atomic polarization, we may verify the effect of light polarization on the cavity shift. In the dispersive limit, the hyperfine energy splittings are irrelevant and a look at the Clebsch-Gordon coefficients (presented in Figure 6.1) for the D2 transitions shows how the polarization will affect the line splitting.

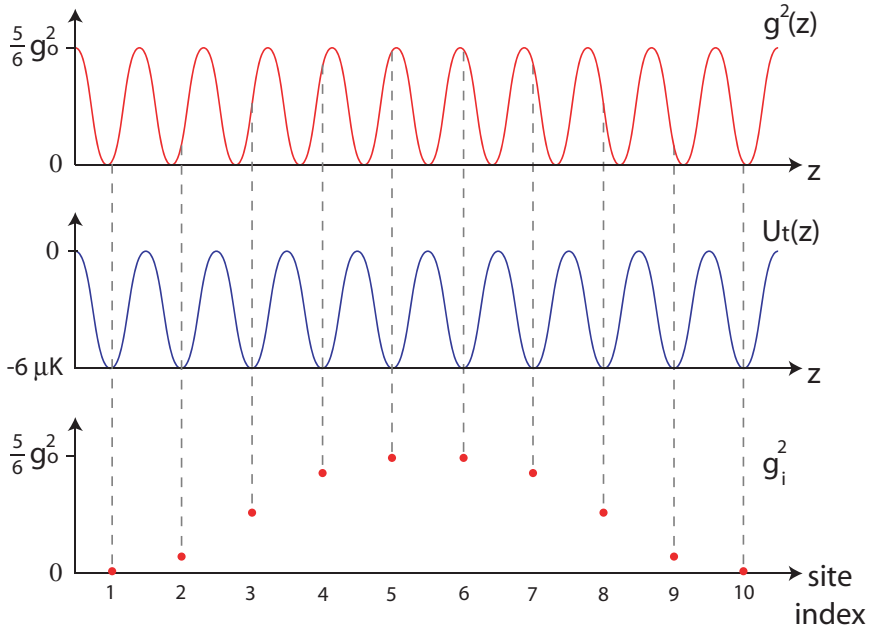

Figure 7.8: The axial variation of the cavity coupling $g^2(z)$ (red) is compared with the axial variation of the optical trap potential $U_t(z)$. Atoms are confined to the minima of $U_t(z)$, and for atoms well-localized in these minima each well will have a specific value of g_i^2 as shown.

The sum of the squared coefficients for each transition gives the coefficient on the cavity shift, i.e. $\Delta_N \rightarrow \left(\frac{5}{6}\right)\frac{Ng^2}{\Delta_a}$ in the case of σ^+ polarization and $\Delta_N \rightarrow \left(\frac{1}{2}\right)\frac{Ng^2}{\Delta_a}$ in the case of σ^- polarization.

Presented in Figure 7.9 is a stationary probe trace for the system with a linearly polarized probe, which of course consists of equal parts σ^+ and σ^-. *Two* lines are seen as two different values of the atom number satisfy the σ^+ resonance condition ($\Delta_c = \frac{5}{6}\frac{N_+ g_o^2}{2\Delta_a}$) and the σ^- resonance condition ($\Delta_c = \frac{1}{2}\frac{N_- g_o^2}{2\Delta_a}$). The σ^- is seen first, as its resonance occurs with 1.5× the atom number of the σ^+ resonance. This line splitting may be used to verify the polarization character of the probe, which may differ from the "on-the-table" polarization due to cavity birefringence (though we did not observe this). The fact that the σ^+ trace in Figure 7.9 shows only one discernable line is compelling evidence that other spin states remain unpopulated in the transfer to the cavity FORT, but *definitive* experimental evidence for this must await a later section.

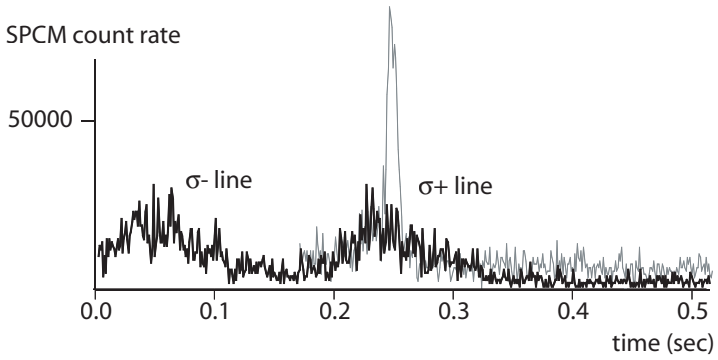

Figure 7.9: Line Splitting with a linearly polarized probe for $\Delta_a = 2\pi \times (-80\text{GHz})$, $\Delta_c = 2\pi \times (-5\text{MHz})$. Shown are stationary probe traces for a σ^+ polarized probe (grey) and a linearly polarized probe (black). The distinctly different widths and heights actually portended recent work cavity heating [144] and nonlinear optics [148].

7.5 Hybrid Trap

One novel functionality of the apparatus came when the atoms confined in the TOP trap were overlapped with the cavity mode while intracavity locking/trapping light was also engaged at a level sufficient to trap the atoms. We came to call this dual trapping scenario the "hybrid trap," and while it is not immediately interesting as a testbed for many-atom cavity QED, it is instructive to consider the dynamics of the hybrid trap. It also highlights the atomic polarization sensitivity of the cavity, which leads to the introduction of a new data analysis technique explored in the subsequent section.

In the hybrid trap the majority of the atoms are confined entirely in the TOP (very weakly coupled to the cavity), but a fraction of the atoms are confined by both the TOP and FORT (strongly coupled to the cavity). There is no motional dissipation, so this conservative system assures that the populations will be exhanging particles at a rate at roughly the transverse trapping frequency of the TOP trap. This situation is depicted in Figure 7.10(a).

Investigating this system with a stationary detuned probe shows this system to behave quite differently than the lines observed for atoms in the FORT. As seen in Figure 7.10(b), the line is much longer in duration and heavily asymmetric on the "outgoing" side (when atom loss is tuning the cavity shift *away* from resonance). This asymmetric line may be

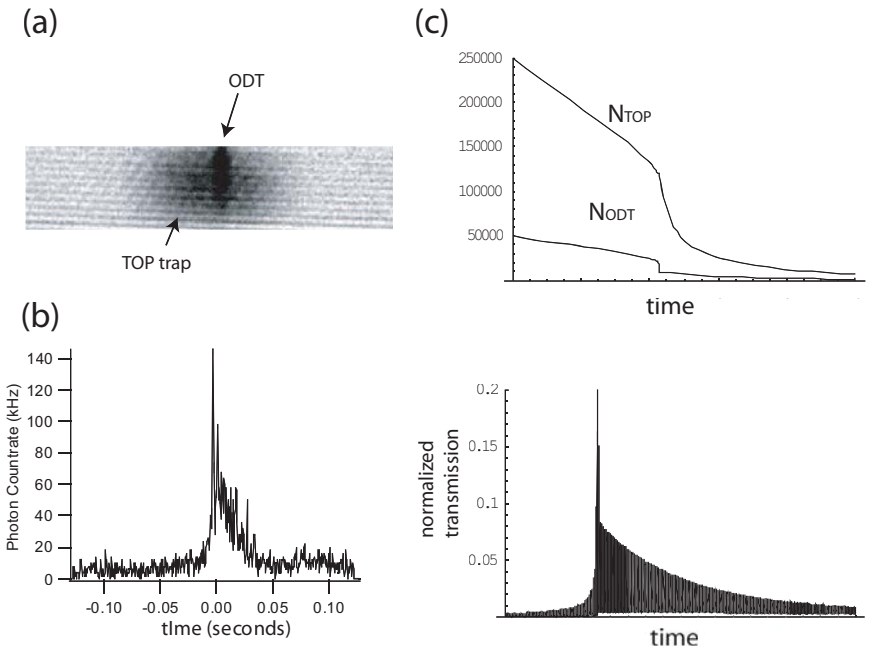

Figure 7.10: The hybrid trap. (a) Absorption image of the hybrid trap, with both TOP trapped atoms and ODT trapped atoms. (b) Stationary probe at a detuning of $\Delta_a = 2\pi \times (-5.7\text{GHz})$ shows a line biased to the "outgoing" side. (c) Numerical models described in text account for the TOP and ODT populations (N_a and N_2, respectively) in time. (d) The same model (at high bandwidth $\gg \omega_r$) shows the cavity transmission to qualitatively match the observed output, with a heavy modulation at ω_r.

understood in the context of a simple two population model involving N_1 (the atoms in the cavity) and N_2 (the atoms outside the cavity but still bound by the TOP trap). Both populations suffer a homogeneous loss rate λ_H from background losses. The populations exchange particles at a rate $\sim \omega$ (the transverse TOP trapping frequency) and the nominal ratio of the populations is $f = \frac{N_2(t=0)}{N_1(t=0)}$ (this will depend on a number of factors including trap volume, temperature, cavity mode size, FORT intensity, etc.). Finally, the population N_1 is susceptible to loss due to the intracavity photons, given by a per-atom loss rate of $\alpha/(1 + \frac{(\Delta_c - \Delta_N)^2}{\kappa^2})$. α is a coefficient predicted by cavity heating models (see the last section of this chapter), and the Lorentzian lineshape of the cavity quantifies the number of intracavity photons for a constant input flux[2]. Finally, the action of the TOP field

[2]Recent investigations presented in Ref. [144] show that this should in fact be the Voigt profile, a convolution of the Lorentzian cavity lineshape and a Gaussian probe. Incorporating this into the present analysis would not give qualitatively different results, and qualitative features are all this model is expected

must be considered. Under a probe circularly-polarized along the cavity axis, the orbiting TOP field orients the $|F = 1, m_F = -1\rangle$ atoms along (effectively σ^+ polarization) and against (effectively σ^- polarization) the cavity axis, yielding respective squared couplings of $\frac{1}{2}\frac{g_o^2}{2}$ and $\frac{5}{6}\frac{g_o^2}{2}$. This implies that the cavity shift is oscillating at the TOP frequency as $\Delta_N = \frac{N_1 g_o^2}{2\Delta_a}\left(\frac{2}{3} + \frac{1}{6}\sin\omega_r t\right)$.

With this we can construct a first-order model of the hybrid trap lineshape under a stationary probe. The coupled differential equations for this simple model are:

$$\dot{N}_1 = -\Gamma_H N_1 + \omega\left(fN_2 - N_1\right) - \alpha\left(1 + \frac{\left(\Delta_c - \frac{N_1 g_o^2}{2\Delta_a}\left(\frac{2}{3} + \frac{1}{6}\sin\omega_r t\right)\right)^2}{\kappa^2}\right)^{-1} N_1 \tag{7.5a}$$

$$\dot{N}_2 = -\Gamma_H N_2 - \omega\left(fN_2 - N_1\right) \tag{7.5b}$$

which are numerically integrated in and displayed in Figure 7.10(c). The cavity output is proportional to $\left[1 + \left(\Delta_c - \frac{N_1 g_o^2}{2\Delta_a}\left(\frac{2}{3} + \frac{1}{6}\sin\omega_r t\right)\right)^2 / \kappa^2\right]^{-1}$ and is the observed quantity at the photodetector. The cavity transmission for the numerically integrated equations in Equations 7.5a and 7.5b are shown in 7.10(d) with the same asymmetric lineshape seen in the data. Briefly stated, the reservoir of N_2 atoms streaming into N_1 provides a source term on Δ_N, which is otherwise a monotonically decreasing quantity. This was initially thought to be a situation of negative feedback where, for a time, the source term $\omega f N_2$ was balanced by the losses. This would not hold N_1 constant, as N_2 is obviously decreasing as well, but the line would be "stretched" until the N_2 reservoir is so depleted that the N_1 loss rate returns to $\approx \lambda_H$. In the presence of the fast TOP frequency ω_r this picture is muddied further, and the hybrid line is perhaps better thought of as merely a complex interplay between the reservoir N_2, the inhomogeneous cavity losses on N_1, and the now oscillating Δ_N.

One upshot of this complex system is the fact that the line is now 30 ms long as opposed to 1 ms, the overall signal for a hybrid line is substantially greater than that of the FORT line from sheer photon counts. In particular, the harmonic drive ω_r on the cavity coupling should be evident in the data stream, and by taking the fourier power spectrum of the raw SPCM data stream associated with the hybrid line shown in Figure 7.10(b), we obtain the graph in Figure 7.11 with a prominent and familiar frequency component.

to provide.

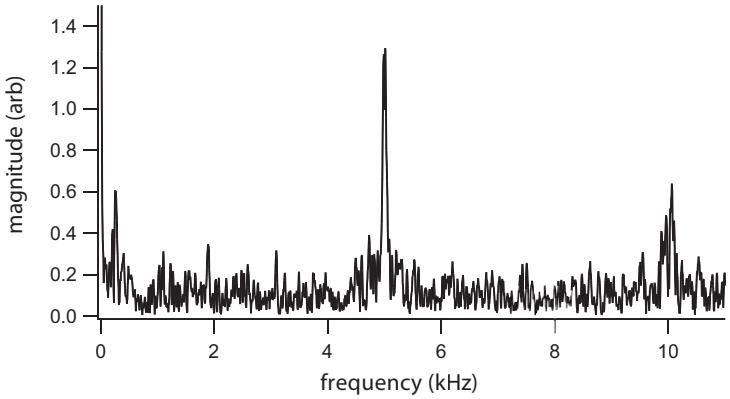

Figure 7.11: Fourier transform power spectrum of a hybrid line. The 5 kHz TOP frequency is picked up as a modulation on the cavity shift. (The power spectrum is obtained by taking the fourier transform of the SPCM data stream.)

7.6 Cavity Fourier Transform Spectroscopy

At this stage, Figure 7.11 is merely a measurement of the (already known) TOP frequency, but this "cavity fourier transform spectroscopy" on the internal state of the atoms will prove itself even more useful when considering the far more interesting cases of Larmor precession. It can also be employed in the case of collective atomic motion, as a coordinated reorganization of the N atoms in the cavity can take the cavity shift from $\Delta_N = \frac{5}{6}Ng_o^2$ for the atoms all located at $\lambda = 780\,\text{nm}$ cavity anti-nodes, $\Delta_N = 0$ for the atoms all located at $\lambda = 780\,\text{nm}$ cavity nodes.

The concept of cavity fourier transform spectroscopy also relates to the correlation function of the cavity transmission, which has been the preferred method for measuring photon anti-bunching [42] and even counting statistics of atom lasers (as measured by a strongly-coupled cavity) [50]. The first-order correlation function is defined as $G^{(1)}(\tau) \equiv \int_{-\infty}^{\infty} dt\, f^*(t) f(t+\tau)$. In this case, $f(t)$ is the TTL output of the SPCM, which was of course the source of the fourier transform power spectrum shown in Figure 7.11. A few lines of algebra yields the connection of the correlation function to the fourier transform spectrum.

$$
\begin{aligned}
G^{(1)}(\tau) &= \int_{-\infty}^{\infty} dt\, f^*(t) f(t+\tau) \\
&= \int_{-\infty}^{\infty} dt \left(\int_{-\infty}^{\infty} d\omega\, F^*(\omega) e^{-i\omega t} \right) \left(\int_{-\infty}^{\infty} d\omega'\, F(\omega') e^{i\omega'(t+\tau)} \right) \\
&= \int_{-\infty}^{\infty} d\omega \int_{-\infty}^{\infty} d\omega'\, F^*(\omega) F(\omega') e^{i\omega'\tau} \int_{-\infty}^{\infty} dt\, e^{i(\omega'-\omega)t} \\
&= \int_{-\infty}^{\infty} d\omega \int_{-\infty}^{\infty} d\omega'\, F^*(\omega) F(\omega') e^{i\omega'\tau} \delta(\omega-\omega') \\
&= \int_{-\infty}^{\infty} d\omega\, |F(\omega)|^2 e^{i\omega\tau}\,, \qquad (7.6)
\end{aligned}
$$

which is of course just the inverse fourier transform of the square of the fourier transform of $f(t)$. Thus, all the information in the fourier transform power spectrum is accessible via the correlation techniques of Refs. [42, 50], and vice versa.

7.7 Sub-"Shot Noise" Number Counting

That a measurement of the cavity resonance directly relates to a measurement of the atom number immediately invites the question as to how precisely the ensemble population could be determined. If we presuppose the ideal initial condition of a coherent state of number and phase for the ensemble[3], then Poissonian statistics are expected and the atom number uncertainty is given by $\Delta N = \sqrt{N}$. Using the previously-described "non-destructive" probe to initialize the system at $N = 24,000$ atoms, we found that we could trigger on and then measure the atom number to a precision of $\Delta N = 95$ atoms. This is well below the predicted "shot noise" value of $\Delta N = 155$ atoms. As this method appears akin to spin squeezing techniques [150], it is instructive to consider whether such cavity transmission measurements achieve a Heisenberg-limited determination of the atom number.

For the following reasons, we claim that this method does *not* represent number squeezing of the atom population, and the arguments herein apply to any other quantum variable (e.g. position, momentum, or spin) to which the atom-cavity system is sensitive.

[3]There is no *a priori* reason to expect the system to be in a coherent state of number and phase, but this serves as the "ideal" initial state in the absence of more advanced preparation techniques [149].

First, we note that the measurement made was not directly measuring the atom number, but instead $\sum_i N_i g_i^2$, where i indexes the respective wells of the optical trap. As previously noted, g_i^2 can varies from 0 to $\frac{5}{6}g_o^2$ depending on the overlap of the 850 nm trapping potential with the 780 nm probe. Second, it is conceivable that instead of squeezing the atom number N that perhaps we are projecting the system into a subset of atom distributions which satisfy $\Delta_N = \sum_i N_i g_i^2/\Delta_a$. While this is not an obviously a useful subset of states, it is composed of two quantum variables – number and position – which could be squeezed. Again we must assert that no squeezing has occurred because neither the atomic populations in the wells, nor the atoms which comprise them, have an *a priori* phase coherence. Thus, even if the atomic population were measured to a precision of one atom, the absence of either initial phase correlations or *in situ* mechanisms to establish phase correlations in the system preclude the possibility that we have yet accomplished any Heisenberg-limited measurement. The presence of cavity heating terms could further doom the prospects of cavity-enhanced Heisenberg-limited measurements; a discussion of these deleterious effects can be found in Ref. [144].

Appendix A

Design for the Main Chamber

This appendix includes the engineering schematics for the main vacuum chamber.

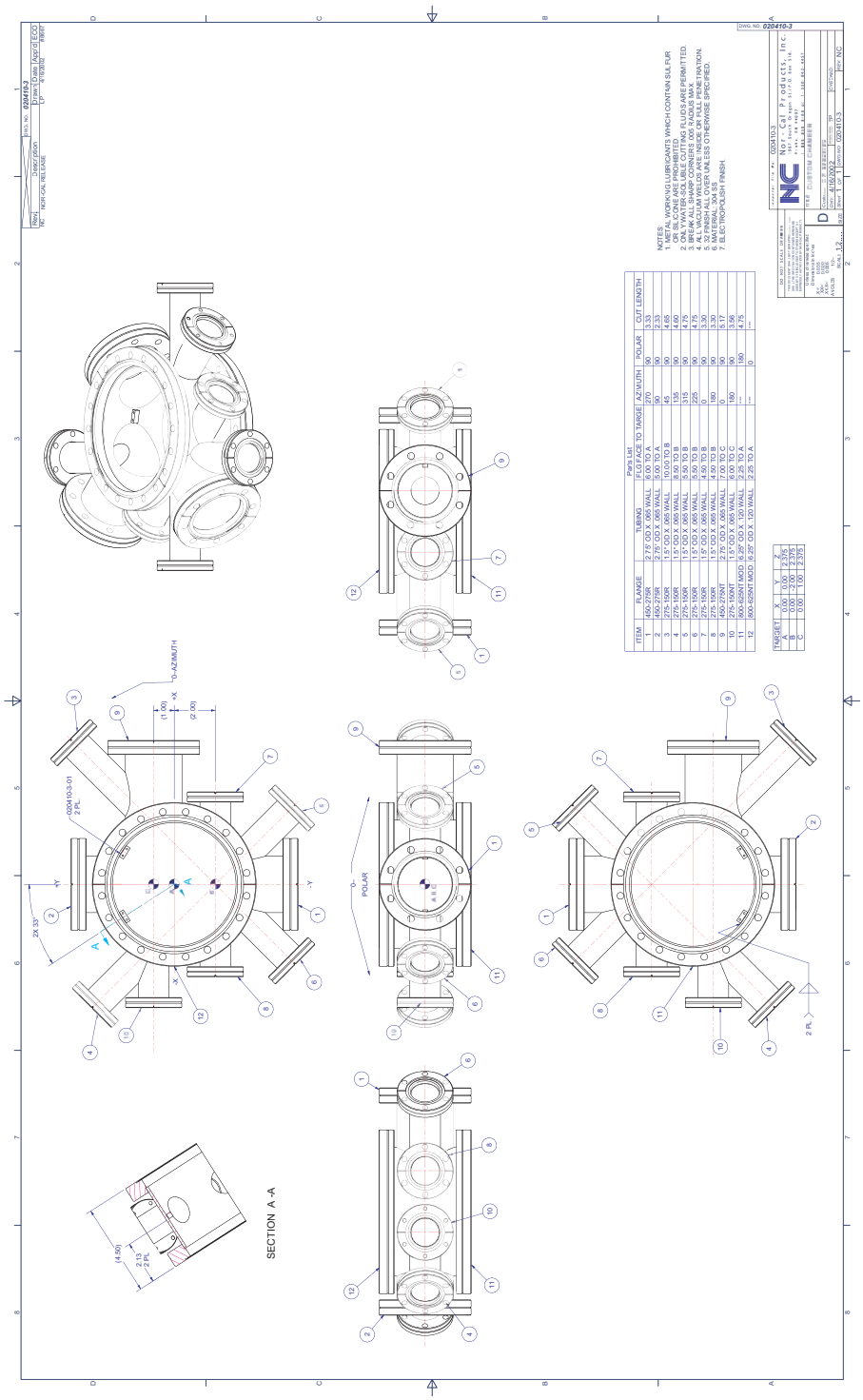

Figure A.1: The main chamber. Drawing generated by Nor-Cal USA.

Appendix B

Designs for the Magnetic Transfer System

This appendix includes the engineering schematics for the magnetic transfer system, including the reentrant bucket, the coil dimensions and layouts, and the mounting bracket.

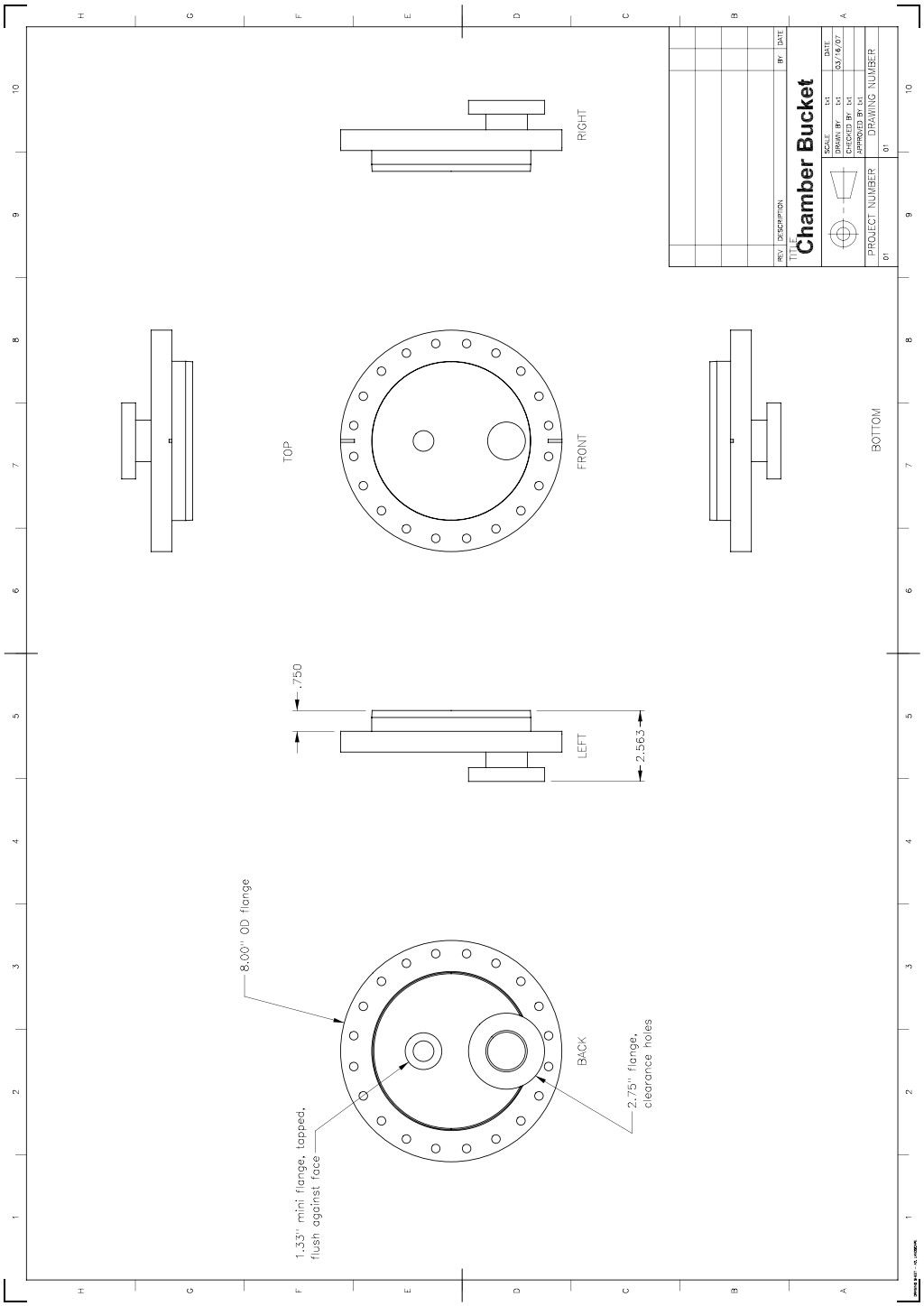

Figure B.1: The reentrant bucket.

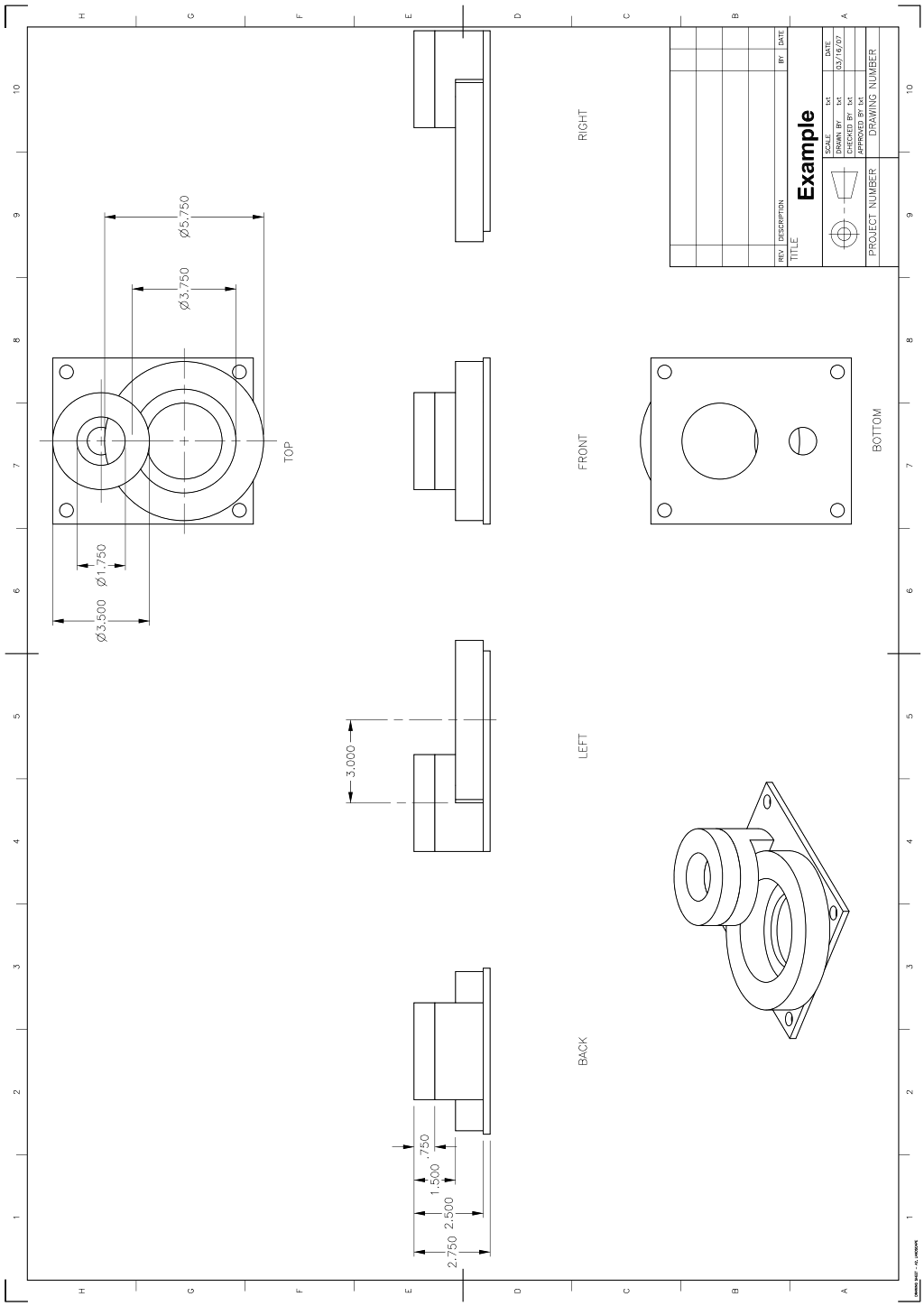

Figure B.2: The magnetic transfer coils.

Appendix C

Designs for the Millitap

This appendix includes the engineering schematics for the millitrap mount pieces.

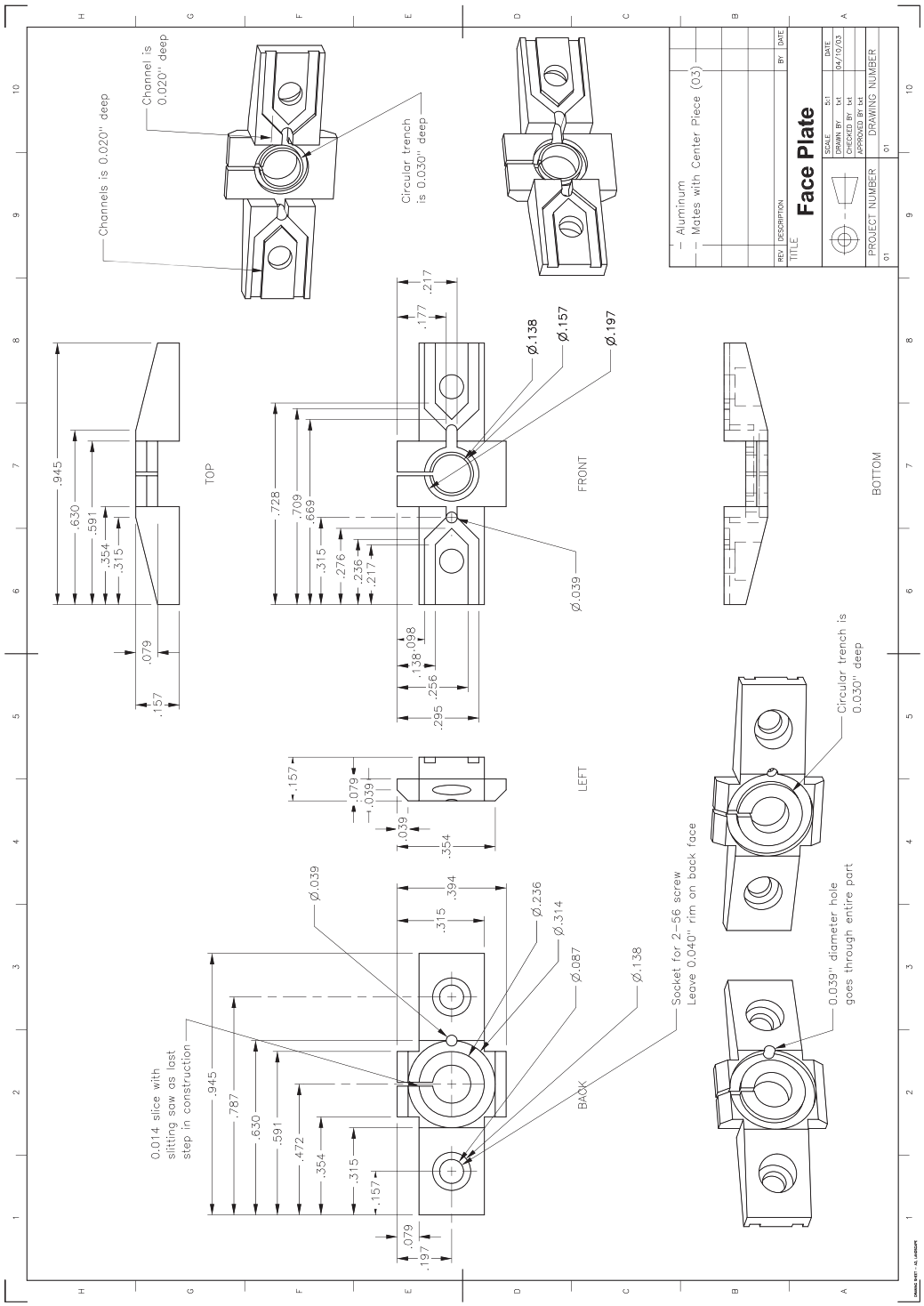

Figure C.1: The mounting plate for the millitrap curvature and anti-bias coils.

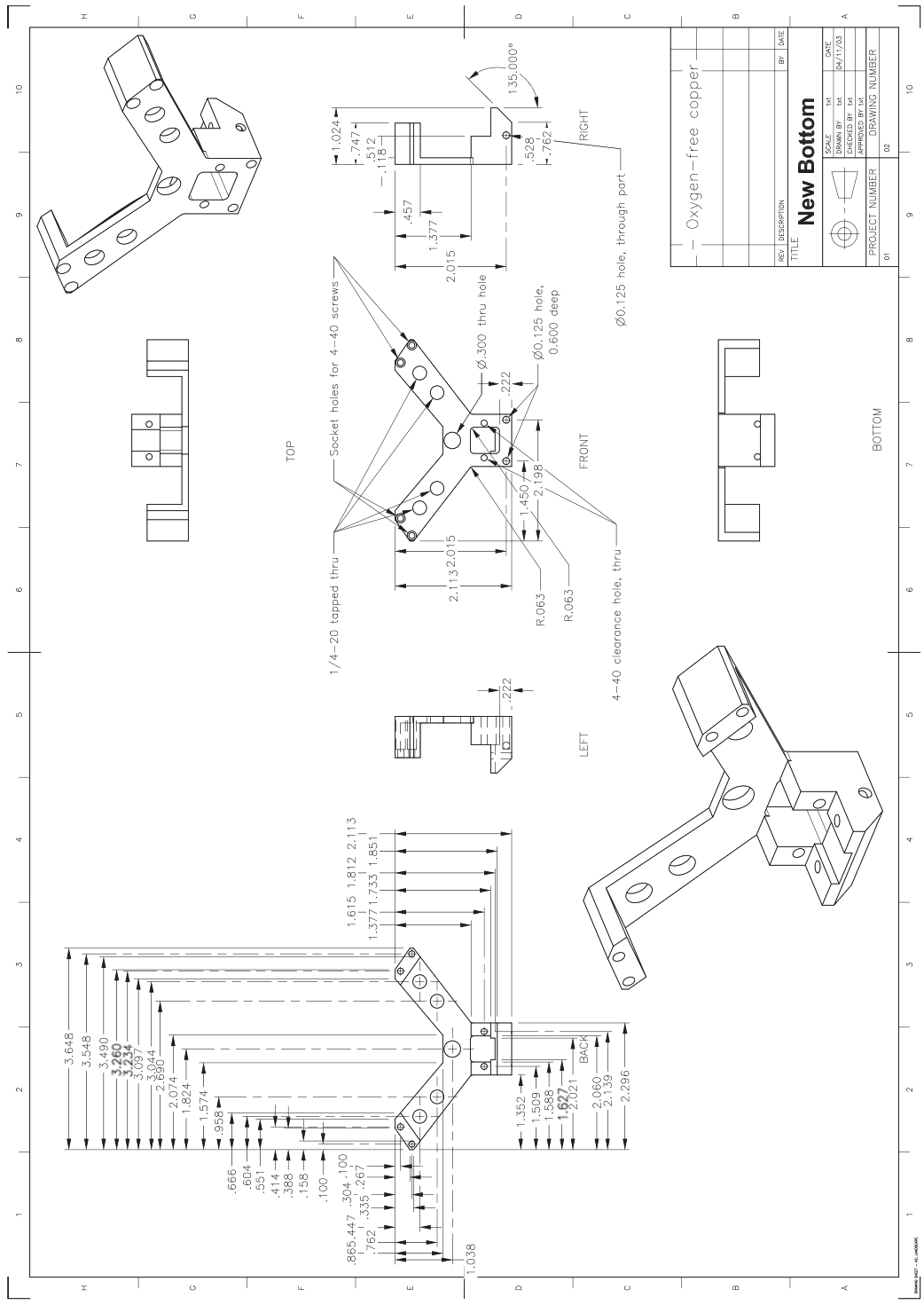

Figure C.2: The critical millitrap mounting piece. The winged structure mates with the main chamber (see Appendix A), and the bottom holes are plugged such that a closed path is made for liquid nitrogen circulation.

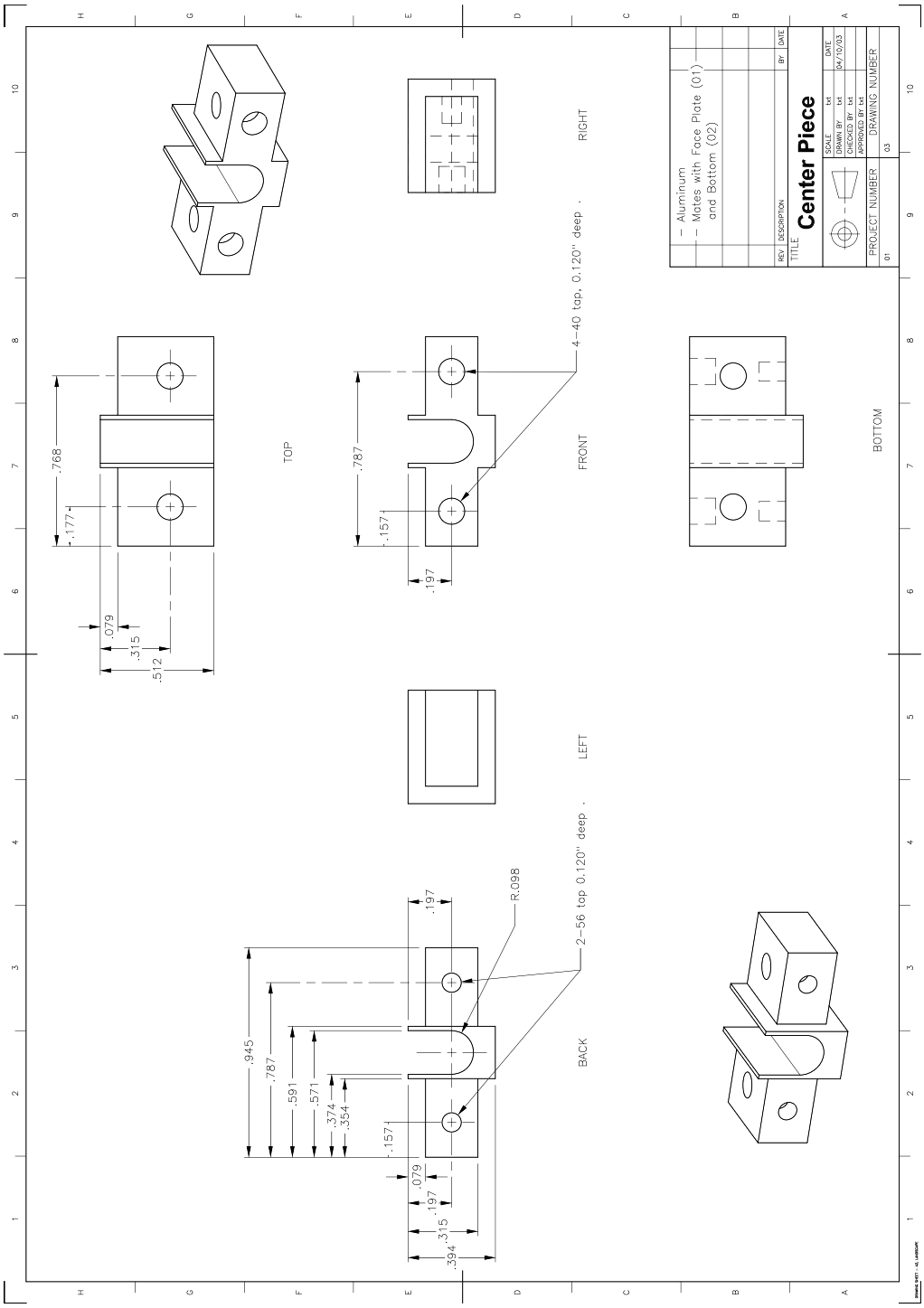

Figure C.3: The center piece, constructed out of aluminum and subsequently anodized.

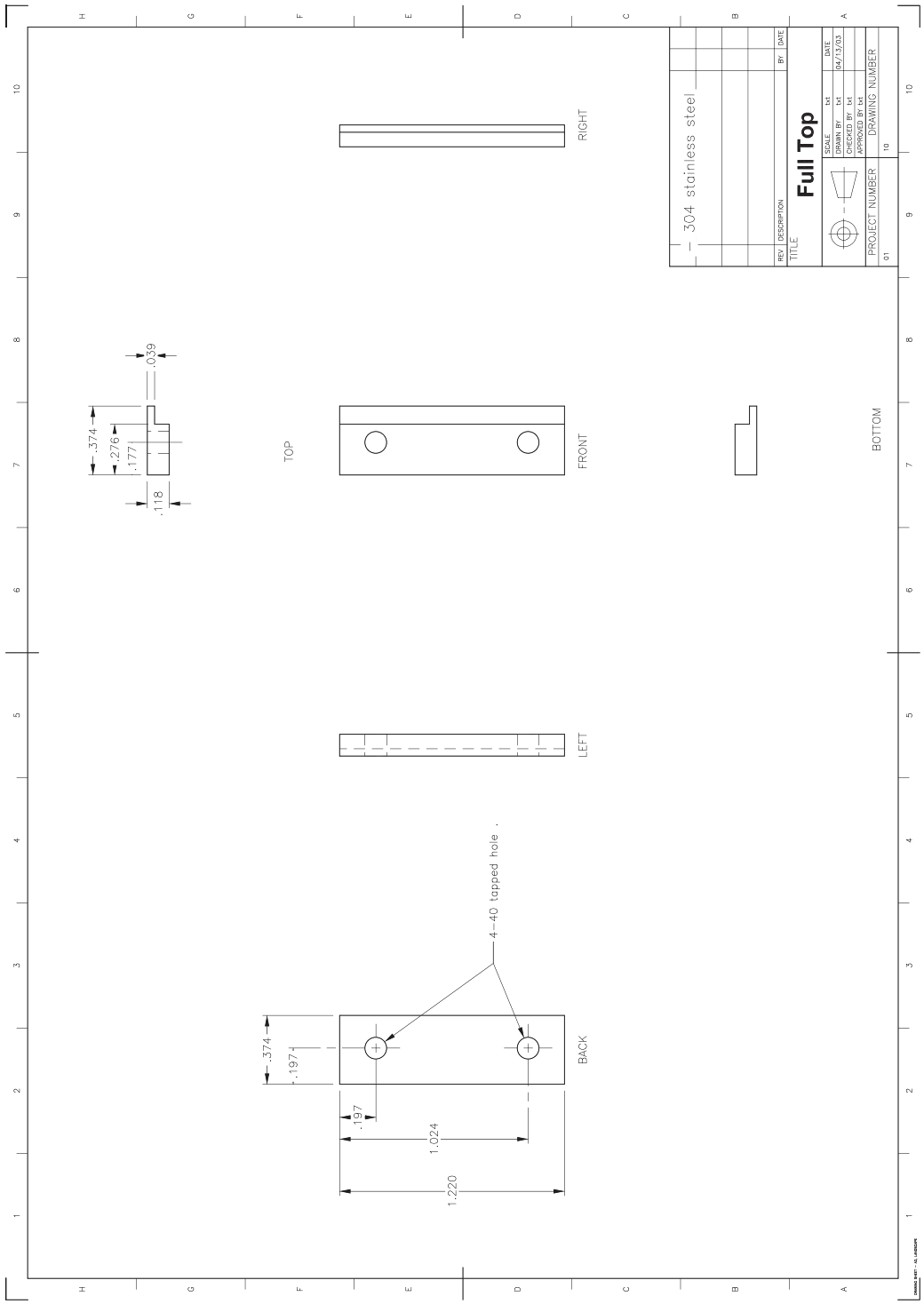

Figure C.4: The millitrap top bracket.

Appendix D

Designs for the Cavity Mounting Structure

This appendix includes the engineering schematics for the cavity mounting system.

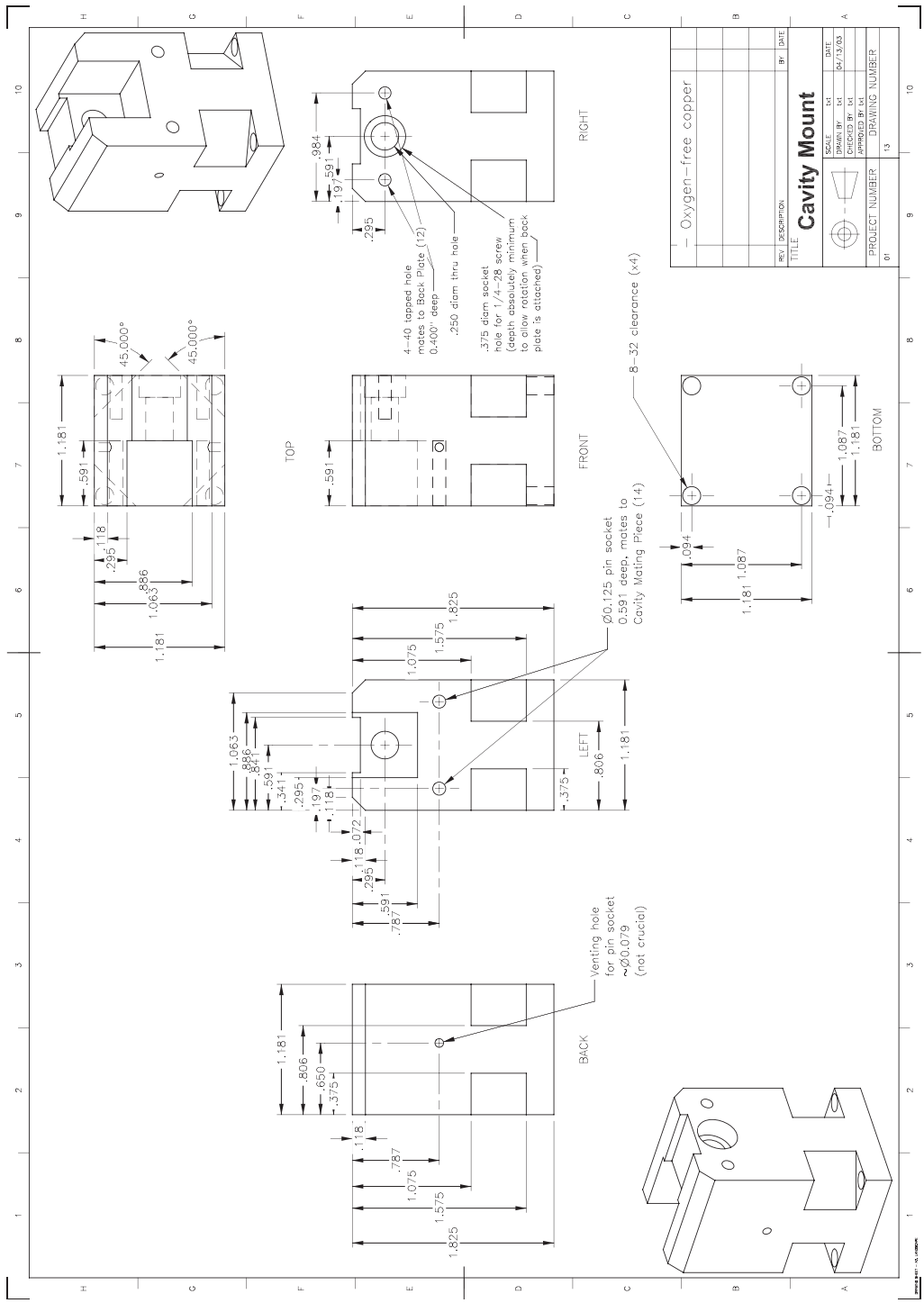

Figure D.1: The cavity mount.

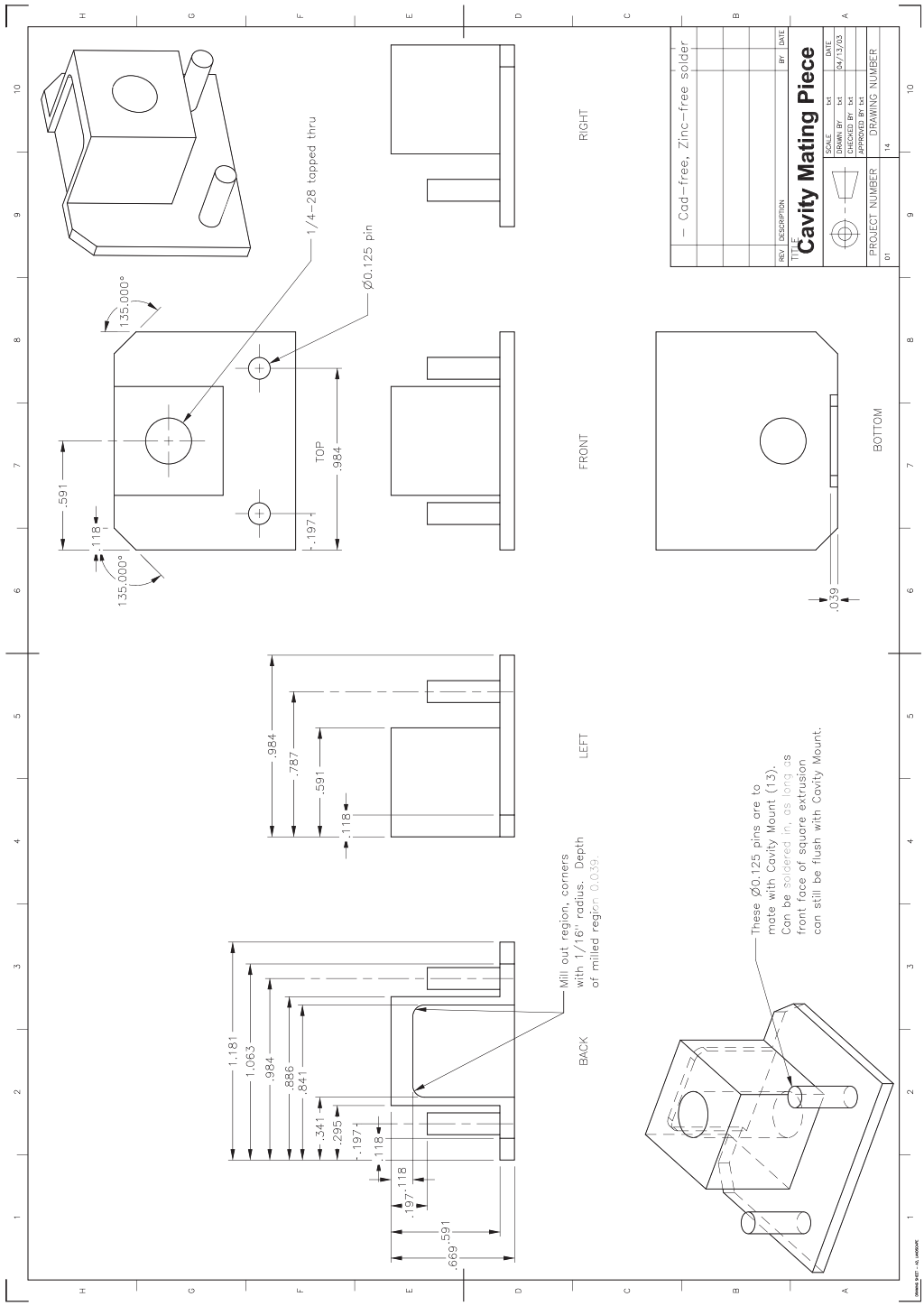

Figure D.2: The cavity mount mating piece, second mirror goes on here.

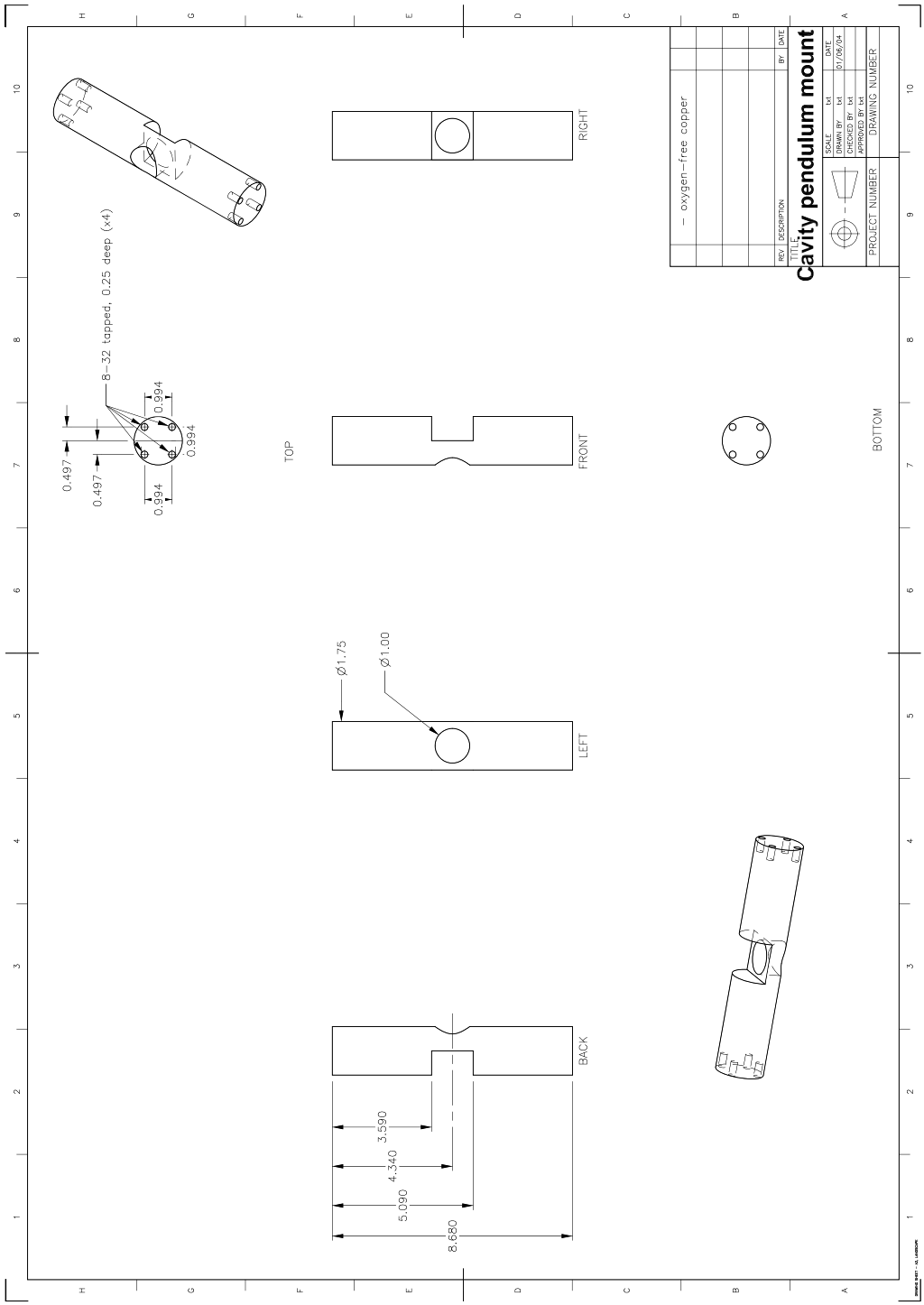

Figure D.3: The pendulum center piece.

Appendix E

Collimated, single-pass atom source from a pulsed alkali metal dispenser for laser-cooling experiments

This appendix includes the following paper:

- *K. L. Moore, T. P. Purdy, K. W. Murch, S. Leslie, S. Gupta, and D. M. Stamper-Kurn, "Collimated, single-pass atom source from a pulsed alkali metal dispenser for laser-cooling experiments," Rev. Sci. Instruments* ***76****, 023106 (2005)*

Collimated, single-pass atom source from a pulsed alkali metal dispenser for laser-cooling experiments

Kevin L. Moore,[a] Thomas P. Purdy, Kater W. Murch, Sabrina Leslie, Subhadeep Gupta, and Dan M. Stamper-Kurn
University of California, 366 LeConte Hall, Berkeley, California 94720

(Received 10 September 2004; accepted 9 November 2004; published online 10 January 2005)

We have developed an improved scheme for loading atoms into a magneto-optical trap (MOT) from a directed rubidium alkali metal dispenser in $<10^{-10}$ Torr ultrahigh vacuum conditions. A current-driven dispenser was surrounded with a cold absorbing "shroud" held at $\leqslant 0$ °C, pumping rubidium atoms not directed into the MOT. This nearly eliminates background atoms and reduces the detrimental rise in pressure normally associated with these devices. The system can be well-described as a current-controlled, rapidly switched, two-temperature thermal beam, and was used to load a MOT with 3×10^8 atoms. © *2005 American Institute of Physics.*
[DOI: 10.1063/1.1841852]

I. INTRODUCTION

The first step in the construction of an atomic physics experiment is obtaining an appropriate source of atoms. *Directed* sources of atoms have a long and storied history.[1] A thermal beam of atoms is easily obtained from an oven or other gas source, though this inevitably involves a differential pumping scheme, a $1/r^2$ decrease in atom flux with distance between the oven and the collection region, a mechanical shutter to quench the beam, and direct handling of a purified sample of the atom of interest. A Zeeman slower[2] can improve the flux of laser-cooled atoms from an oven, but suffers from the same drawbacks as an oven as well as the added complications of the magnetic design and the slowing beams. A multiply loaded magneto-optical trap (MOT) initially loaded from a vapor cell is a widely-used source for cold atom experiments,[3] but has the drawback of increased optical, electronic, and vacuum infrastructure. Light-induced atomic desorption (LIAD),[4] while not a collimated beam source, is an elegant technique which has recently been improved to yield very fast MOT loading rates.[5]

Alkali metal dispensers,[6] or "getters," have emerged as a useful alternative to these sources,[7,8] requiring only a modest electric current (<10 A) for their operation. The driving current rapidly heats the dispenser causing a reduction reaction, inducing the cm-scale devices to release an atomic vapor (rubidium, in our case) with a rapid turn-off time. The emitted atoms are quite hot, as the dispensers reach temperatures of 800 °C or more for typical current pulses.[7,8] The fraction of atoms capable of being captured by a typical MOT is quite small ($\approx10^{-5}$) due to the large temperatures reached, but the efficacy of the dispensers for direct loading is salvaged both by the large atom flux and their ability to be placed close to the MOT. Alkali metal dispensers are already used as sources for vapor cell MOTs (Refs. 9–11, for example), but in these cases the 800 °C atoms are cooled by the walls of the vapor cell so the loading rate into the MOT is increased.

Many ultracold atomic physics experiments demand base pressures of less than 10^{-10} Torr, particularly in the case of magnetic trapping of atoms for long periods of time. Getters have been used directly in an ultrahigh vacuum (UHV) ultracold atom experiment[12] and the atomic flux from a dispenser has been collimated to make an atom beam,[13] but to the best of the authors' knowledge no published work describes a system which attempts to control the output flux of the getter entirely in the UHV chamber.

The desire for a fast, simple, and efficient source of rubidium atoms with a minimal impact on UHV conditions led us to the development of a cold shroud for the rubidium dispenser and MOT system. The shroud acts as a pump for rubidium atoms released by the dispenser that are either (a) not directed towards the MOT, (b) of the wrong isotope, or (c) moving too quickly to be captured by the MOT. The dispenser-shroud system thus acts as a fast, compact, collimated atomic beam source with a minimized impact on UHV conditions.

This article discusses the performance of the getter-shroud system as well as the efficiency of loading atoms into a MOT from the direct flux of a dispenser. Importantly, our measurements characterizing the loading rate and equilibrium populations of a MOT indicate that direct loading of atoms from a getter is strikingly ineffective. In contrast, our measurements indicate that a secondary, lower temperature atomic source was also formed, contingent on operation of the getter, which was much more effective at loading a MOT at UHV conditions. Future getter-loaded, UHV experiments can be designed to make use of this tempered source in a more controlled manner.

II. EXPERIMENT

Our experiments are carried out in a stainless steel UHV chamber pumped to below 10^{-10} Torr (see Fig. 1). This

[a]Electronic mail: klmoore@socrates.berkeley.edu

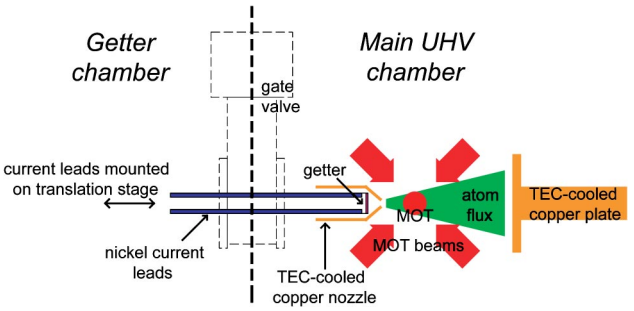

FIG. 1. (Color online) Essential elements of the getter and cold shroud system. The getter is brought within 1.2 in. of the MOT center, and with a driving current greater than 2.7 A it releases a hot rubidium vapor. When cold, the copper nozzle that surrounds the getter absorbs nearly all of the emitted rubidium atoms that are not directed through the open aperture towards the MOT. The MOT is loaded from the resultant atomic beam exiting the nozzle. The vast majority of emitted atoms are moving too quickly to be captured by the MOT, but are absorbed by the cold copper plate on the right. The shroud is comprised of the copper nozzle, the copper plate, and surrounding mechanical structure.

chamber is divided between a main chamber and a secondary "getter chamber," designed so as to allow defective or depleted getters to be replaced without exposure of the main UHV chamber to atmosphere. The getter is spot-welded to nickel rods and mounted on a hollow linear feedthrough[14] which provides six inches of travel. The current feedthrough also has a hollow interior (0.4 in. i.d. tube) and a 1.33 in. mini-flange port which accepts an electrical feedthrough to control the current through the getter. A single-rod current feedthrough is sufficient, as the return current path can be grounded to the chamber on the interior bellows of the linear motion feedthrough.

To prepare a new getter, the getter chamber is vented with dry nitrogen with the gate valve to the main chamber closed. It then takes less than 30 min to open the getter chamber, spot weld a new getter, and reseal the vacuum system. The "getter chamber" is then evacuated and undergoes a modest bakeout ($\approx$2 days), during which the dispenser is degassed as discussed by the authors of Ref. 7. We typically follow their procedure, although the alternate method advocated by Ref. 8 also provides a usable rubidium source.

When the gate valve is re-opened, pressures in the 10^{-10} Torr range are established in both the getter chamber and the main chamber. With the entry path though the gate valve clear, the dispenser can be translated to within 1.25 in. of the MOT center.

To ensure that rubidium atoms not captured by the MOT are pumped away, all line of sight from the dispenser to the room temperature UHV chamber is blocked by a nickel-plated cold copper shroud. As the shroud is cooled, the sticking probability for a rubidium atom (or any alkali metal) impacting the surface approaches unity. In theory this would protect all sensitive surfaces from the direct flux of atoms as well as preventing a room temperature background vapor of rubidium from permeating the chamber during an experiment. Figure 2 highlights the suppression of the background rubidium vapor with the cooling of the cold shroud; operating the getter while the shroud is at room temperature produces visible fluorescence throughout the chamber due to a

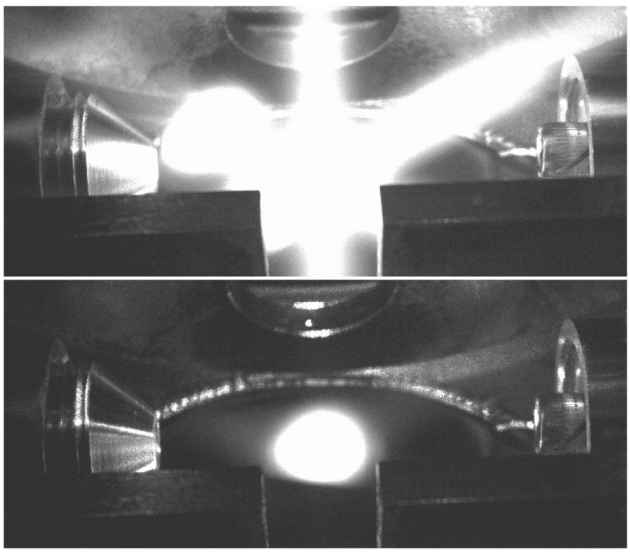

FIG. 2. Extinction of a background vapor and production of a single-pass atomic beam by low temperature shroud. The top image shows the fluorescence of the background rubidium atoms for a getter pulse of 10 A for 15 s at a shroud temperature of 21.5 °C. The bottom image is the fluorescence for an identical getter pulse and incident MOT beams, but instead the shroud is held at −30 °C. Note the sharp edges of the atom beam, as well as the disappearance of background fluorescence. In both images, the atom beam flows from left to right, consistent with the orientation of Fig. 1.

thermal rubidium vapor, while similar operation with a cold (−30 °C) shroud yields fluorescence only from a beam with line-of-sight access to the getter. The pressure spike associated with the dispenser heating, observable at 10^{-10} Torr with an ion gauge, is also reduced by nearly a factor of 2 with the cooling of the shroud, although not entirely eliminated because the dispenser and current leads outgas more than just rubidium at such high temperatures.

Atoms are collected in a MOT centered within the getter-emitted beam. The MOT is formed from 50 mW of total laser power split into four 0.75 in. diam beams, two of which are retroreflected. The quadrupole coils are placed outside the vacuum system, three inches from the center of the MOT, and are typically operated with axial field gradients of 20 G/cm. The MOT population was limited by the relatively small amount of light power per beam. The trends reported in this paper should scale directly with improvements in MOT loading.

III. RESULTS

Our pulsed atomic source should be evaluated under two criteria: first, that operating the source yields an atomic flux which is efficiently loaded into sizable MOTs, and, second, that the source can be quickly switched off to yield UHV conditions for subsequent experimentation (e.g., magnetic trapping and evaporation) of the laser-cooled atoms. We assessed the performance of our getter-shroud system under both criteria by measuring the loading rate and equilibrium population in MOTs formed either during or after the atomic source was pulsed: large MOTs formed during the getter pulse indicate efficient loading, while small MOTs formed seconds after the getter pulse indicate the desired suppression of the atomic flux when the source is turned off. Measure-

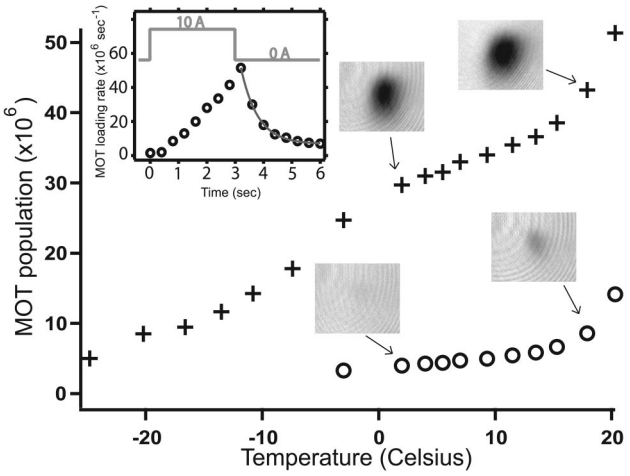

FIG. 3. MOT population as a function of shroud temperature. Crosses (+) denote a MOT loaded by a 10 A, 6 s pulse, circles (○) a MOT loaded from background atoms for 6 s with no getter pulse. Inset shows MOT loading rate as a function of time overlayed upon the current profile of a 3 s, 10 A getter pulse (the shroud temperature was 19 °C). The rapid quenching of the MOT loading rate upon cessation of the getter current has a decay time of 0.6 s.

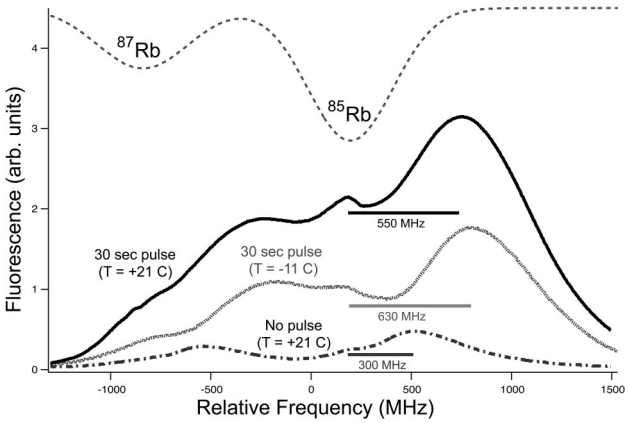

FIG. 4. Fluorescence spectra of atom flux in the MOT region. The probe laser beam was incident upon the atom flux at 45° to the center line of the the shroud nozzle. Dotted lines show absorption spectrum, inferred from an absorption signal generated in a reference rubidium vapor cell. Plotted are fluorescence curves when the shroud is at room temperature and at −11 °C, given a 30 s, 10 A current pulse to the getter. Also plotted is the background fluorescence in the MOT region with no getter pulse, clearly showing the sizable room temperature flux emitted from the room temperature shroud surface after a large layer of atoms have desorbed on the inner surface of the nozzle.

ments of MOT populations under both conditions (getter on/getter off) are shown in Fig. 3 as a function of the temperature of the shroud.

Several conclusions can be drawn from these data. First, at all temperatures of the shroud, the MOT populations formed through operating the getter are much higher than those collected from the background atomic flux, indicating that the getter-shroud system is indeed operating as a pulsed atomic beam source, as desired. Longer getter pulses make use of this high loading rate to reach equilibrium MOT populations of 3×10^8. Second, confirming the visual findings of Fig. 2, the cold shroud extinguishes the background rubidium vapor if it is operated at sufficiently low temperatures; below 0 °C, the MOTs formed from the background vapor were only barely detected by our optical absorption measurements. Further, the inset of Fig. 3 shows the rapid termination of the MOT loading rate upon extinguishing the getter current, satisfying the second stated criterion for the system.

While the getter-shroud system satisfies the stated criteria as an efficient, rapidly-switched atom source, these data exhibit some surprising features. The reason that the getter-loaded MOT depends so strongly on the shroud temperature, including an almost complete elimination of trapped atoms for the coldest temperatures, is not immediately obvious. The dispenser assembly has no mechanical contact with the shroud, meaning that the getter itself arrives at the same temperatures regardless of the temperature of the shroud. The small MOT populations for low shroud temperatures suggest that the direct atom flux from the getter is actually a rather poor source for a MOT. Our original intent was to utilize this shroud at or below −20 °C, but the reduced MOT population at lower temperatures forces a choice between rubidium background elimination and larger MOT populations. The optimum shroud temperature will likely vary for different experimental requirements.

In order to diagnose the thermal character of atoms emitted by the dispenser, a laser 45° to the atomic beam was scanned in frequency while fluorescence at the center of the MOT region was detected on a photodiode. This yields information about the velocity distribution of the emitted atoms, though the resultant spectrum is expected to be a convolution of many competing factors due to the large probe beam size (≈0.75 in. diameter), divergence of emitted atoms, optical pumping rates, and background fluorescence.

The fluorescence data (Fig. 4) show the effect of the cold shroud on the velocity distribution of the emitted atoms from a strong getter pulse (10 A, 30 s). For a shroud at room temperature the overall rubidium density in the MOT region is approximately twice that of a −11 °C shroud. At 21 °C the background rubidium vapor and the rubidium flux from the nozzle can be clearly distinguished, and the Doppler-shifted atoms show peak fluorescence at 550 MHz from the background vapor. At −11 °C, the background atoms are barely resolvable, and the Doppler-shifted atoms are now peaked at 630 MHz. Also plotted in Fig. 4 is the fluorescence curve for a room temperature (21 °C) shroud and no getter flux. In this case, the peak fluorescence in the MOT region is shifted by 300 MHz from the line center of the Doppler-broadened background rubidium spectrum. We believe this is caused by the flux of desorbing atoms from the shroud nozzle surface which acts as a directed, room-temperature background flux into the MOT region; we were only able to discern this fluorescence spectrum after an atypically large layer of rubidium had been deposited on the inner surface of the shroud nozzle.

These data explicitly demonstrates that the velocity distribution of the atomic flux through the nozzle and into the MOT region is significantly affected by the thermal state of the shroud. The strong dependence of the getter-loaded MOT population on shroud temperature in Fig. 3 is better under-

stood in this context, especially given the fact that a room temperature beam loads ≈10 times more atoms into a MOT than a 1000 K oven of the same number flux. The most likely explanation for the modification of the atom flux is that a large fraction of the atomic flux from the getter is impingent upon the cold nozzle used to collimate the remaining flux. If the surface has a substantial probability of reflecting and *thermalizing* these atoms, then a flux seemingly colder than the getter-only flux seen at −11 °C will be emitted because the emitted atoms will be a mixture of hot getter-emitted atoms and cooler reflected atoms. The thermalization of getter-emitted atoms with surrounding walls has been previously observed.[13] The sum of these two fluxes yields the reduced Doppler shift seen in the room temperature data in Fig. 4. We found that after a few weeks of normal operation of the getter the desorbing flux would then persist for several days.

IV. DISCUSSION

While the dispenser-shroud system has proven itself to be potentially useful for ultracold atomic experiments, there are some drawbacks. We tried many different avenues for continuous operation in an attempt to maximize MOT population and minimize the experiment repetition time. If the getter is pulsed too frequently (<20 s separation between 3 s, 10 A pulses) the pressure in the chamber rises to a steady state above the minimum base pressure. While we believe this to be an improvement over bare operation of a dispenser in UHV, we had hoped to reduce this repetition time further. However, even with the coldest shrouds that the TEC system could effect we were unable to execute an experimental cycle of less than 20 s.

Second, rubidium adsorbed on the shroud will be released into the UHV if the shroud is allowed to warm up. If one is to prevent this substantial gas load from interfering with in-vacuum equipment (such as ion pumps or high-finesse mirrors), the cooling of the shroud must be made fail safe. Furthermore, one would not be able to bake the shroud in UHV. Thus contamination of the UHV chamber would be correctable only by selective baking or by thoroughly cleaning the chamber. This disadvantage belies the purpose of the getter as an easily-exchanged UHV atom source.

Drawbacks aside, several improvements to our design could be made which would make the system a useful tool in many instances. First, the aperture on the nozzle could be widened to allow a larger flux into the MOT. The aperture is currently 0.25 in. in diameter and appears to "choke" the MOT at lower temperatures because the beam is only shining into a fraction of the MOT cross section. A larger aperture would increase the flux as the square of the aperture diameter, allowing the maximum getter-loaded population number to be reached in less time with a reduced impact on the pressure.

Another improvement would be the addition of a "shadow" for the getter. This would likely take the form of a metal piece which would obscure the getter slit from direct line of sight to the center of the MOT. This should drastically reduce the losses due to MOT atoms colliding with fast Rb atoms, allowing for a larger final MOT population.

Finally, given our understanding of the fluorescence spectrum in Fig. 4, one could construct a system which would utilize the secondary room temperature beam generated by the rubidium-coated surfaces of the shroud. A miniature "oven," operated in the main UHV chamber, could surround a dispenser that purposefully directs its atomic flux towards the inner walls of the oven. Atoms emitted from the getter would be tempered by the inner surface of the oven, and these thermalized atoms would then be allowed to escape through a collimated aperture to efficiently load a closely situated MOT. Cold baffles would then be placed behind the MOT to pump away the atoms which are not captured by the MOT. During experimental operation the oven could be held at or slightly above room temperature to increase atom yield and prevent a surface layer of atoms from forming. When the experimental system is not in operation the miniature oven could be heated further to release any remaining adsorbed atoms onto the cold baffles.

ACKNOWLEDGMENTS

The authors thank Stefan Schmid, Mike Grobis, and Dave Murai for their technical assistance and advice. The authors effort was sponsored by the Defense Advanced Research Projects Agency (DARPA) and Air Force Laboratory, Air Force Materiel Command, USAF, under Contract No. F30602-01-2-0524, the National Science Foundation under Grant No. 0130414, the Sloan Foundation, the David and Lucile Packard Foundation, and the University of California. K.L.M. acknowledges support from the National Science Foundation. S.G. acknowledges support from the Miller Institute for Basic Research in Science.

[1] N. F. Ramsey, *Molecular Beams*, reprint ed. (Oxford University Press, Oxford, 1997).
[2] W. D. Phillips and H. Metcalf, Phys. Rev. Lett. **48**, 596 (1982).
[3] C. J. Myatt *et al.*, Opt. Lett. **21**, 290 (1996).
[4] B. P. Anderson and M. A. Kasevich, Phys. Rev. A **64**, 023404 (2001).
[5] S. N. Atutov *et al.*, Phys. Rev. A **67**, 053401 (2003).
[6] Manufactured by SAES Getters USA Inc.
[7] J. Fortagh, A. Grossman, T. W. Hansch, and C. Zimmermann, J. Appl. Phys. **84**, 6499 (1998).
[8] U. D. Rapol, A. Wasan, and V. Natarajan, Phys. Rev. A **64**, 023402 (2001).
[9] H. J. Lewandowski, Ph.D. thesis, University of Colorado, 2002.
[10] M. R. Matthews *et al.*, Phys. Rev. Lett. **81**, 243 (1998).
[11] C. Wieman, G. Flowers, and S. Gilbert, Am. J. Phys. **63**, 317 (1995).
[12] H. Ott *et al.*, Phys. Rev. Lett. **87**, 230401 (2001).
[13] T. M. Roach and D. Henclewood, J. Vac. Sci. Technol. A **22**, 2384 (2004).
[14] Manufactured by Thermionics Vacuum Products, part number FLMH-275-50-6. Inclusion of this item is not an endorsement; we expect that devices from other manufacturers would behave in a similar fashion.

Appendix F

Bose-Einstein condensation in a mm-scale Ioffe Pritchard trap

This appendix includes the following paper:

- *K. L. Moore, T. P. Purdy, K. W. Murch, K. R. Brown, K. Dani, S. Gupta, and D. M. Stamper-Kurn, "Bose-Einstein condensation in a mm-scale Ioffe-Pritchard trap," Applied Physics B* ***82****, 533-538 (2006)*

Bose-Einstein condensation in a mm-scale Ioffe-Pritchard trap

Kevin L. Moore,* Thomas P. Purdy, Kater W. Murch, Kenneth R. Brown, Keshav Dani, Subhadeep Gupta, and Dan M. Stamper-Kurn
Department of Physics, University of California, 366 LeConte Hall #7300, Berkeley, CA 94720
(Dated: March 31, 2005)

We have constructed a mm-scale Ioffe-Pritchard trap capable of providing axial field curvature of 7800 G/cm^2 with only 10.5 Amperes of driving current. Our novel fabrication method involving electromagnetic coils formed of hard anodized aluminum strips is compatible with ultra-high vacuum conditions, as demonstrated by our using the trap to produce Bose-Einstein condensates of 10^6 ^{87}Rb atoms. The strong axial curvature gives access to a number of experimentally interesting configurations such as tightly confining prolate, nearly isotropic, and oblate spheroidal traps, as well as traps with variable tilt angles with respect to the nominal axial direction.

PACS numbers: 03.75.Nt, 32.80.Pj, 05.30.Jp

Magnetic traps have become a staple of ultracold atomic physics. As such, innovations in magnetic trapping techniques have consistently led to new experimental breakthroughs. For example, the invention of the time-orbiting-potential (TOP) trap to stem Majorana losses in spherical quadrupole traps led to the first gaseous Bose-Einstein condensates (BECs) [1]. The cloverleaf trap [2], the QUIC trap [3], and other electro- and permanent magnet configurations allowed for stable confinement of large BECs with DC fields and variable aspect ratios; these capabilities led, for example, to precise tests of mean-field theories [4], observations of quasi-condensates in reduced dimensions [5], and studies of long-lived hyperfine coherences in two-component gases [6]. The rapidly-developing magnetic-trapping technology of atom chips now provides new capabilities for manipulating ultracold atoms and studying their properties (e.g. coherence of condensates in a waveguide [7], the decay of doubly-charged vortices in a BEC [8], etc.).

A typical configuation for magnetic trapping with DC magnetic fields is the Ioffe-Pritchard (IP) trap [9]. Near the trap center — at distances small compared to the size of or distance to the magnets used to generate the trapping fields — an IP trap is characterized by three quantities: the axial bias magnetic field B_0, the radial quadrupole field gradient B'_ρ, and the axial field curvature B''_z. The magnitudes of these parameters scale as I/d, I/d^2 and I/d^3, respectively, where I is the total current carried in the wire(s) (or magnetization of ferromagnets), and d is their characteristic length scale or distance from the location of the magnetic trap center. Both because of this scaling, and because the effective radial curvature can be greatly increased by lowering the bias field B_0, the limitation to the confinement strength of an IP trap comes typically from the maximum axial curvature which can be attained.

As indicated by the I/d^3 scaling of the axial curvature, strategies for increasing the confinement of an IP trap involve both increasing the current in the coils and decreasing the characteristic size scale of the trap. Magnetic traps used in most ultracold atom experiments have been constructed on one of two different length scales. Centimeter (inch) scale traps, which provide superior optical access, utilize currents of 1000's of Amperes, typically distributed as smaller currents in each of several turns of wire. The highest currents sustainable in such traps, limited by resistive heating, restrict axial field curvatures to the neighborhood of 100 G/cm^2.

Alternatively, magnetic confinement can be provided with modest currents by reducing the field-producing wires and their distance to the ultracold atoms to microscopic sizes. This strategy has been carried out effectively with surface microtraps [10–12], resulting in versatile ultracold atomic experiments. The typical size scale for these microfabricated magnetic traps is $\sim$100 μm, and typically only 1 A of current is required to produce IP traps with field curvatures in excess of 10^4 G/cm^2 [11, 13]. Microtraps are not ideally suited for all experimental endeavors, however, as the atomic cloud is trapped $\sim$100 μm or less from the planar surface.

In this article we describe the design, construction, operation, and performance of a millimeter-scale, $\sim$10 A (or $\sim$ 100 Ampere-turns) magnetic trap which bridges the two aforementioned regimes. This "millitrap" utilizes a novel fabrication scheme which allows for the production of axial field curvatures of over 7800 G/cm^2 and is shown to be compatible with experimental requirements for the creation of large BECs. We demonstrate that this trap, owing to its high axial field curvature, allows for a wide range of trapping geometries, ranging from the typical prolate spheroidal to the more unusual oblate spheroidal configuration. Further, we describe a modification of the IP trapping fields which allows for traps with a variable tilt angle with respect to the nominal axial direction, a capability which is compatible with excitation of the "scissors mode" [14], the creation of vortices [15, 16] or other studies of superfluid flow [17, 18] in a BEC. The trap is also suitable for loading and trapping an ultracold atomic gas inside a high-finesse cavity formed by conventional mm-scale mirrors [19–21](or near other mm-scale

*Electronic address: klmoore@socrates.berkeley.edu

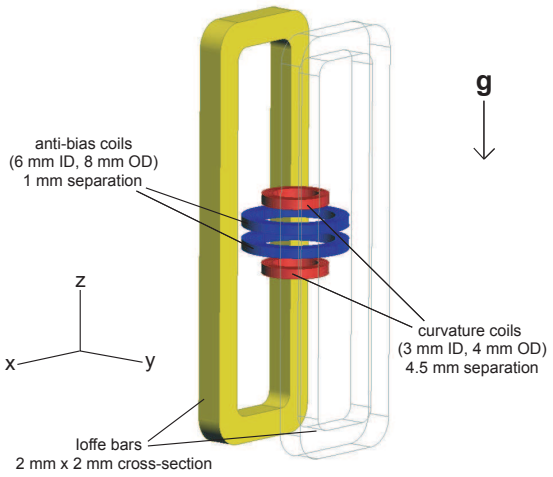

FIG. 1: Sketch of the mm-scale IP trap. The primary curvature coils (red), the anti-bias coils (blue), and the gradient coils (yellow) are depicted in this diagram as solid bodies, but are in actuality multiple turns of wire with protruding leads. For clarity the coil leads have been omitted and the nearest gradient coil is shown as transparent. *Higher resolution version of figures at http://physics.berkeley.edu/research/ultracold.*

objects).

The winding pattern of the millitrap is similar to that of inch-scale IP traps (see Figs. 1 and 2). The axial field is shaped by two pairs of coaxial coils, with parallel currents in each pair of coils but opposite currents in each of the two pairs. The small diameter coils ("curvature coils") are positioned to generate the maximum possible curvature given their diameter. The larger diameter coils ("anti-bias coils") allow for near cancelation of the large bias field produced by the curvature coils at the trap center, while their small axial separation allows for a slight increase (about 15 %) in the total axial curvature. Finally, two elongated rectangular coils ("gradient coils"), run antiparallel currents to produce a radial quadrupole field. The dimensions of various coils were chosen to maximize axial curvature while allowing for a 3 mm diameter cylindrical clearance along the trap axis (for the later accommodation of mirrors for a Fabry–Perot cavity), and a 1 mm clearance along the radial directions for the purpose of imaging. Further details on the positioning and cross sectional area of the coils are shown in Table I.

To maximize the current density while avoiding large input currents and uncontrolled magnetic fields from current leads, multi-turn coils (with total cross sections on the order of 1 mm^2) were used. The maximum current density attainable in coils fabricated by various methods is limited by the steady state temperature of the coils, due to the tendency of the coil resistance to rise with temperature. We found that, for all implementations, there is a threshold at which no more current can be added to a coil without the resistance increasing exponentially from overheating. Thus, in order to minimize resistive heating and maximize heat dissipation, it is desirous to choose a fabrication method which allows for the cross-sectional area to be efficiently packed with current carrying conductor rather than electrical (and typically thermal) insulation.

Guided by these criteria, we chose to form electromagnetic coils from multiple turns of hard-anodized pure aluminum foil strips. The assembly procedure is illustrated in Fig. 2. Shear-cut strips of aluminum foil were cleaned and then hard anodized in sulfuric acid after smoothing their jagged edges with lubricated fine grit sandpaper. The thickness of the insulating Al_2O_3 layer (on the order of microns) was controlled by varying the duration of the anodization, and chosen to be thick enough to reliably prevent current shorts between turns of the coil but thin enough to allow the coils to be wound without fracture. Coils were then wound on Teflon mandrels with a UHV-compatible, thermally-conductive epoxy applied between turns. The epoxy was set by baking the coil and mandrel at 150°C for two hours, after which the coil was removed and then tested for electrical shorts through both DC resistance measurements and AC magnetic field measurements.

The coils were then inserted into a compound mounting and heat-sinking structure and secured by epoxy (curvature and antibias coils) or by pressure (gradient coils). Portions of the mount in contact with the coils were formed from hard-anodized aluminum. Current connections to the coil were formed by removing oxide layers from the leads and then clamping them tightly between two pieces of copper. Finally, the trap and mounting structure was installed in a UHV vacuum chamber, with current connection made through polyimide-insulated copper wires to a set of 20 A vacuum current feedthroughs. The mounting structure also contains two hollow channels for circulation of liquid nitrogen. Operating the magnetic trap at liquid nitrogen temperatures lowers the resistance of the aluminum coils by a factor of four compared to that at room temperature, allowing higher current densities to be maintained. Following a bakeout of the millitrap at a temperature of 250°C, lifetimes of over 100 s were observed for atoms trapped in the millitrap, demonstrating the vacuum compatibility of all materials used in its construction.

To provide the most flexibility in operating the millitrap, separate electrically-floating power supplies were used for each coil. Also included in the electrical setup were a set of inductor-capacitor filters and an interlock system to protect the millitrap from overheating. Electrical characterization of the millitrap following the vacuum bakeout revealed several undesired low-resistance (several Ohm) connections between different coils, indicating electrical connections through the common mounting structure. These inter-coil connections should have no effect since independent supplies are used for each coil. The possible presence of undesired intra-coil connections,

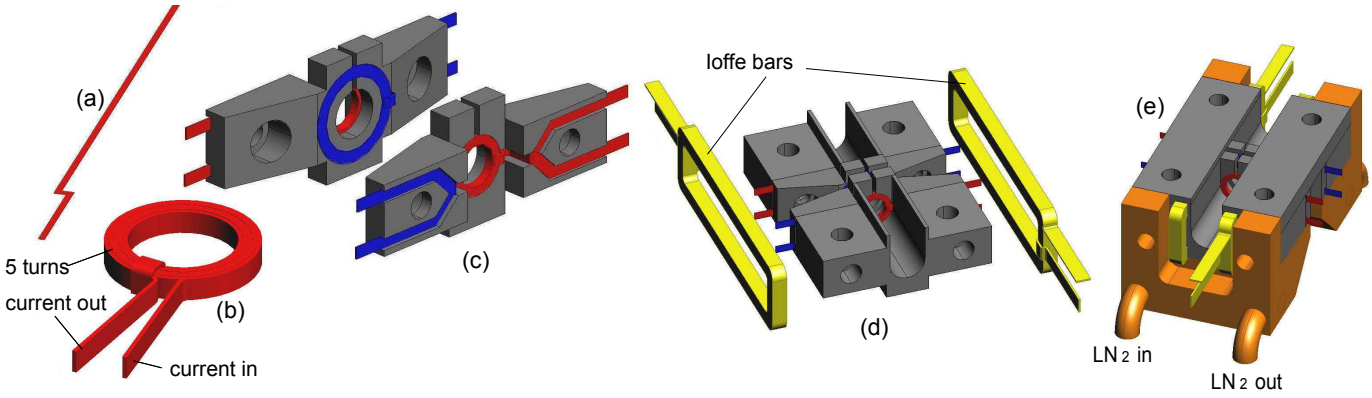

FIG. 2: Sketch of the assembly procedure and part integration. (a) Aluminum strips were cut with a z-shaped pattern to allow for the extraction of the interior current channel after the coil is wound. (b) A curvature coil with input and output current leads. (c) Curvature coils (red) and anti-bias coils (blue) were epoxied into anodized aluminum (grey) faceplates; current leads protrude from sides. (d) The faceplates were attached to an anodized aluminum mount which allows the gradient coils (yellow) to slide over the assembly. (e) A top fixture plate holds the mount in place by bolting into a copper mount (orange) below. A closed path inside the copper piece allows liquid nitrogen to be circulated.

TABLE I: Parameters for aluminum coil windings.

Coil	Inner Diam.	Outer Diam.	Foil thickness	Width	Cross-section	No. turns	Heat generated @ 10 A
curvature	3 mm	4 mm	0.006 in.	1 mm	0.5 mm^2	5	2 Watts
anti-bias	6 mm	8 mm	0.008 in.	0.75 mm	0.75 mm^2	4	2 Watts
gradient	N/A	N/A	0.008 in.	2 mm	4 mm^2	9	10 Watts

e.g. connections between turns on the multiple-turn coils, was tested by measuring parameters of magnetic traps formed with varying currents in each of the curvature, anti-bias, and gradient coils. No clear evidence for such flaws was obtained.

Cold atoms were loaded into the millitrap by optically cooling and trapping atoms in one portion of the UHV chamber, and then magnetically transporting them to the millitrap region. This multi-stage experimental procedure is depicted in Fig. 3. In a "loading region" which is displaced 3 inches horizontally from the millitrap, a 5×10^9 atom MOT was loaded from a Zeeman slowed beam of ^{87}Rb. About 2×10^9 atoms were trapped in the $|F = 1, m_F = -1\rangle$ magnetic sublevel by a spherical quadrupole magnetic trap with an axial gradient of 200 G/cm. The atoms were then transported using two sets of stationary anti-helmholtz coil pairs external to the chamber (similar to Ref. [22]), one of which is centered at the "loading region" and which is used for the initial spherical quadrupole trap and the other centered at the millitrap. As the two anti-helmholtz coil pairs overlap each other, the magnetically-trapped cloud was easily transported between the two coil centers by varying the currents in the two quadrupole coil pairs. During this transport, the atomic cloud was cooled by RF evaporation to reduce the cloud size to about 400 μm before passing the atoms through the 1 mm gap between the millitrap anti-bias coils.

Transfer of the atoms from the external-coil-based spherical quadrupole trap to the IP trap was accomplished in two stages of "handshaking." First, atoms were transferred to a spherical quadrupole trap formed by two of the six millitrap coils (a curvature coil and an opposing anti-bias coil); at 2 A running through each of these coils, a quadrupole trap with 150 G/cm axial gradient was produced, nearly matching the field strength generated by 400 A of current running through the external quadrupole coils. The spherical quadrupole trap was then suddenly (within 100 μs) replaced with the IP millitrap. This sudden quadrupole-to-IP transfer caused 25% (or less) of the atoms to be lost. RF evaporative cooling was then performed in a prolate IP trap, with trapping frequencies of $(\omega_x, \omega_y, \omega_z) = 2\pi \times (151, 138, 52)$ Hz (axes oriented as in Fig. 1), yielding atomic clouds near or below the BEC transition temperature (about 300 nK for our system). The transition temperature was reached with 2.5×10^6 atoms, and nearly pure condensates of 1×10^6 atoms produced upon further cooling.

The strongest confinement provided by the millitrap depends on whether such confinement is provided for long or for short trapping times. For example, up to about 7 A of current can be maintained in the curvature and anti-bias coils on a steady-state basis. Coils were safely operated at higher currents, up to about 11 A, although we found that after about 100 ms, the resistive heating of the coils led to increased outgassing which worsened the vacuum conditions in the millitrap region. The axial curvature provided under these conditions was mea-

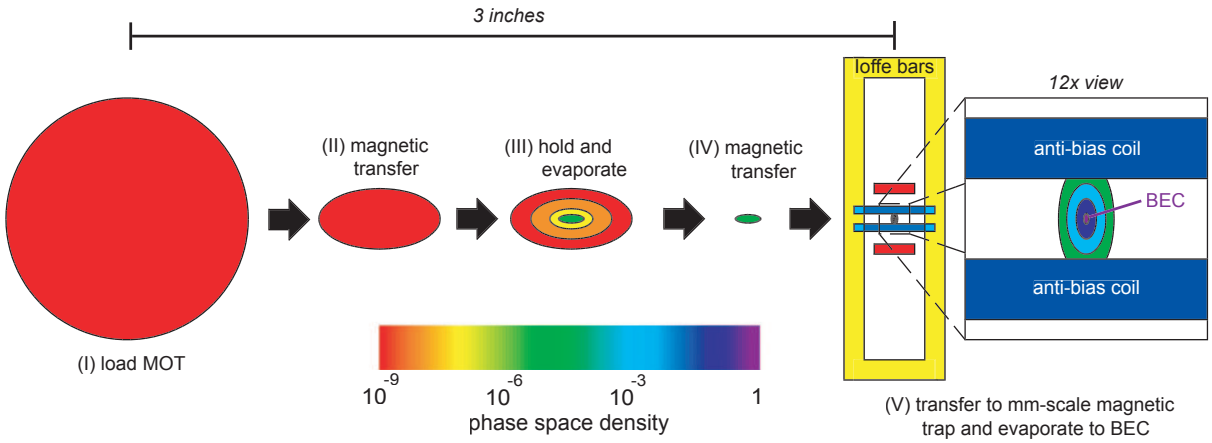

FIG. 3: Sketch of experimental sequence. (I) Atoms are loaded into the MOT and subsequently trapped in a spherical quadrupole trap. (II) The atoms are then transferred 1.75 inches towards the mm-scale IP trap and (III) evaporated to a phase space density of $\Gamma \sim 10^{-5}$. (IV) The cloud is magnetically transferred into the IP trap and (V) captured by a curvature coil and an anti-bias coil in a spherical quadrupole trap. The full millitrap is then turned on and the atoms are confined in the IP field with a 2 G bias field. The cloud is then further evaporated, forming a pure BEC of 1 million atoms.

sured in-situ using the trapped atoms as a probe, both by measuring the axial oscillation frequency of the trapped cloud, as well as by measuring the axial displacement of the cloud due to the application of a known axial field gradient. From these measurements, we determine that steady-state axial curvatures of 5300 G/cm^2 (7 A setting) and brief confinement with 7800 G/cm^2 (10.5 A setting) can be reached. Gradient coils are operated at a maximum of 11 A, yielding radial gradients of 220 G/cm.

One unexpected feature of this strong IP trap is a remarkably high efficiency of RF evaporation. This efficiency can be quantified by comparing the factor gained in phase space density Γ through the evaporative cooling loss of a given factor in atom number N, obtaining, e.g. a figure of merit $f = -d\ln\Gamma/d\ln N$, with Γ and N parameterized along some evaporation trajectory. Typical figures of merit cited in the literature for evaporation from IP traps are $f = 2$ to $f = 3$ [23, 24]. In our mm-scale IP trap, a factor of over 10^5 in phase space density is efficiently gained by evaporative cooling to the Bose-Einstein condensation transition temperature with an overall figure of merit of $f = 4.5$.

To account for this high efficiency, we note that the IP trap, aside from being strongly confining and thus compressing atomic clouds to high collision rates, is also nearly isotropic. We suspect that the condition of near isotropy improves the efficiency of evaporative cooling relative to that in the typically-used anisotropic traps since high-energy atoms produced collisionally in the gas can easily escape the center of the cloud in *any direction*, and thereby reach the trap boundary established by the applied RF radiation. In contrast, in a cigar-shaped cloud with high aspect ratio, the large axial collisional depth can prevent the escape of all high-energy atoms except those travelling nearly purely in the radial direction. Further, we note that high evaporation efficiency is obtained in our trap in spite of the vertical orientation of the axial direction; in contrast, IP traps with weaker axial confinement are rarely oriented in this manner so as to avoid the onset of lower dimensional evaporation due to gravitational sag [24, 25].

We have investigated several new features which are afforded by the large axial curvature in our trap. For instance, considering the generic magnetic field configuration of an IP trap and expanding about the minimum of the magnetic field, an effective radial curvature is obtained as $B''_\rho = {B'_\rho}^2/B_0 - B''_z/2$. The dependence of the radial trap strength on the applied bias field B_0 offers a simple means of varying the aspect ratio of the trap arbitrarily, ranging from prolate ($B''_z > B''_\rho$) to near-isotropic ($B''_z \simeq B''_\rho$) to oblate ($B''_z < B''_\rho$) geometries. While experiments using IP traps have typically employed prolate or near-isotropic geometries, the oblate geometry has been avoided since the very weak confinement afforded by such traps (limited to below the already weak axial confinement), makes it difficult to compensate for gravitational sag and stray magnetic fields. Thus, by greatly boosting the typical axial confinement strength, our trap gives more convenient access to oblate DC magnetic traps, with advantages for the study of two-dimensional [26–28] and/or rotating condensates.

Fig. 4 shows the range of trapping geometries accessed by our millitrap. After evaporatively cooling a thermal gas to a temperature of about 500 nK, the bias field B_0 was ramped to values ranging from 2 G to 18 G while holding the axial curvature at $B''_z \simeq 4000$ G/cm^2 and radial gradient at $B'_\rho = 205$ G/cm. We then displaced the cloud slightly in this new trap configuration, and recorded the harmonic motion of the trapped cloud to determine trap frequencies along three orthogonal directions. For this purpose, absorption imaging was employed along either of two imaging axes — one through

the 3 mm vertical aperture along the vertical trap axis, and the other along the horizontal $\hat{y}$ direction through the 1 mm gap between the anti-bias coils.

These measurements illustrate the breaking of radial trap symmetry in our trap due to gravity. This can be understood by considering that the atomic cloud sags under gravity to the point where the axial gradient of about 30 G/cm gives a force on atoms in the $|F = 1, m_F = -1\rangle$ equal to the gravitational force. By the condition $\vec{\nabla} \cdot \vec{B} = 0$, the presence of this axial gradient implies a radial field gradient of 15 G/cm which breaks the symmetry of the radial quadrupole field, adding to the magnetic field gradient along one direction ($\hat{y}$) while subtracting from that along the other direction ($\hat{x}$). Thus, triaxial, rather than cylindrically symmetric, traps are produced.

One motivating factor in our tailoring the aspect ratio of the IP trap is the desire to detect the presence of quantum depletion by precise measurements of collective excitation frequencies, as proposed by Stringari and Pitaevskii [29]. If one considers a fixed condensate number and axial trap strength, one finds that the largest magnitude frequency shift of the lowest collective mode would be obtained with traps that are nearly isotropic; even though higher condensate densities (and hence higher quantum depletion) are produced in prolate traps, the quadrupole modes in this case are more surface-like, rather than compressional, in character, and hence are only weakly affected by depletion effects. In our case, the broken symmetry due to effects of gravity produced, at best, nearly isotropic traps. For instance, Fig. 5 shows time-of-flight absorption images of atoms from a $\omega_x : \omega_y : \omega_z = 0.91 : 1.08 : 1.00$ trap. The familiar pronounced anisotropy of an expanding BEC is absent from such images due to the trap isotropy.

Another feature highlighted by the large axial confinement of our trap is a means to vary the orientation of the trap with respect to the nominal axial direction. This effect arises from considering the effects of displacing the radial quadrupole gradient field so that its zero-field axis no longer coincides with the axis of the curvature fields. That is, one considers the fields

$$\begin{aligned} \vec{B}_{curv} &= B_0 \hat{z} + \frac{B_z''}{2}\left[\left(z^2 - \frac{x^2+y^2}{2}\right)\hat{z} - z\,(x\hat{x} + y\hat{y})\right] \\ \vec{B}_{grad} &= B_\rho' \left[(x - x_0)\hat{x} - (y - y_0)\hat{y}\right] \end{aligned} \quad (1)$$

where (x_0, y_0) is the position of the gradient-preferred-axis in the $\hat{x}$ – $\hat{y}$ plane. This position is controlled experimentally by applying uniform radial fields to a well-aligned ($x_0 = y_0 = 0$) IP trap. Such misalignment yields both a variable displacement and variable tilt of the resulting magnetic trap, which can be understood as follows. Considering for now just the $z = 0$ plane, the location of the magnetic trap is determined by the competition between $\vec{B}_{grad}$, which tends to locate the cloud at (x_0, y_0), and the radial variation of the axial field $\vec{B}_{curv}$ which, for small displacements, exerts a radially repulsive force. The (x, y) position of the resulting field minimum varies for $z \neq 0$ due to the fact that the $\vec{B}_{curv}$ fields now acquire radial components, displacing the position of the radial-field minimum from (x_0, y_0).

To illustrate this effect, we present in Fig. 6 the tilt angles θ with respect to the $\hat{z}$ axis of the weakest trap axis in a prolate IP trap, as derived from Eqs. 1. Field parameters of $B_z'' = 2000$ G/cm^2, $B_\rho' = 180$ G/cm, and displace-

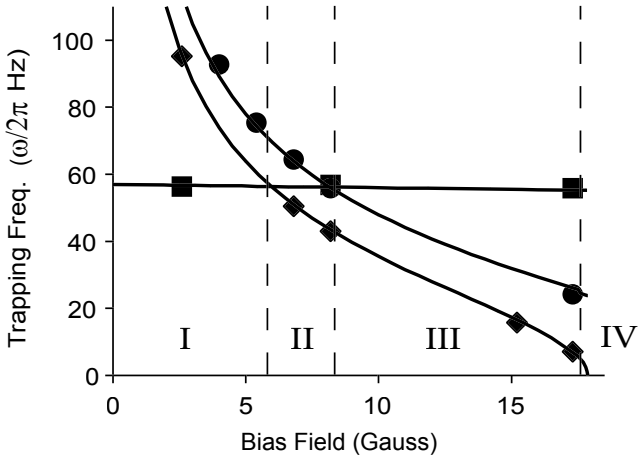

FIG. 4: Measured axial trapping frequency ω_z (squares) and transverse trapping frequencies ω_x (diamonds) and ω_y (circles) as a function of bias field, which was controlled by varying the current in the anti-bias coil pair. The solid lines are theoretical predictions for the trapping frequencies. The only free parameter in the transverse trapping frequency fit is the gradient coil contribution which was allowed to vary within its measured uncertainty. Four distinct regimes can be identified: I - the prolate spheroidal regime ("cigar"-shaped clouds), II - the nearly-isotropic regime, III - the oblate spheroidal regime ("pancake"-shaped), and IV - the unstable regime.

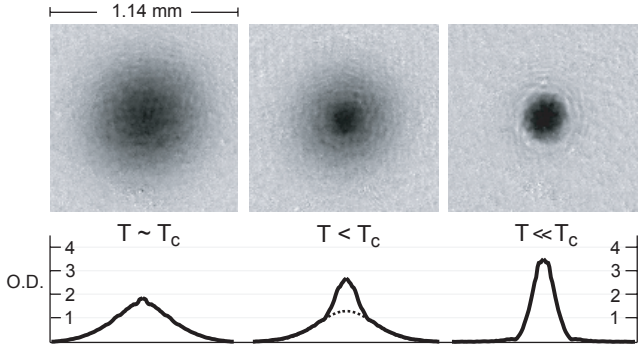

FIG. 5: Absorption images of a nearly-isotropic ultracold gas. Images show separate 36 ms time-of-flight images of a thermal cloud (1.5×10^6 atoms), bimodal distribution, and pure BEC (0.5×10^6 atoms), respectively. The trapping frequencies for this trap are $\{\omega_x, \omega_y, \omega_z\} = 2\pi \times \{52, 62, 57\}$Hz. Below the images are associated radial averages of the optical densities. The bimodal distribution (center plot) is clearly seen with the condensate rising from the Gaussian fit to the thermal wings (dotted line).

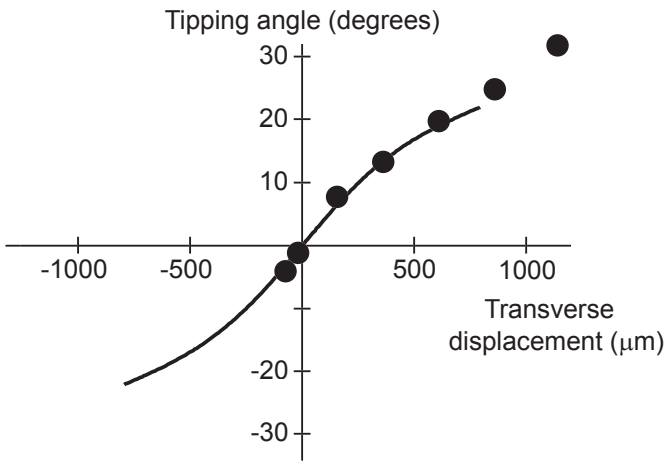

FIG. 6: Tilting atomic clouds in an IP magnetic trap. *In situ* images of tipped prolate clouds yield both the displacement (distinct from x_o) and the tipping angle (data shown as points). These data are compared with calculations (solid line) obtained from the generic IP field expressions of Eqs. 1 for the trap parameters of this experiment ($B_z'' = 2000$ G/cm^2, $B_\rho' = 180$ G/cm, and $y_0 = 0$). The theoretical curve is shown only over the range of displacements at which the IP traps (non-zero bias fields) are retained. Beyond this range, the displaced traps become filled, asymmetric spherical quadrupole traps, as presumably applies to the two data at highest displacements.

ments $y_0 = 0$ and variable x_0 are chosen to match experimental settings. The tilt angle varies over a wide range of x_0, out to a limiting displacement $x_c = 2\sqrt{B_0/B_z''}$ beyond which a non-zero-bias trap is no longer produced.

Aside from varying the tilt angle, this variation of the IP trap also changes the trap frequencies. Indeed, we observed experimentally that the "axial" trap frequency, i.e. the smallest frequency in a prolate IP trap, can be dramatically reduced in the case of a misalignment (x_0 and/or $y_0 \neq 0$). This leads to an apparent discrepancy between this trap frequency, which was determined by following the oscillatory motion of a trapped cloud, and a measurement of B_z'', as determined from measuring the upward ($\hat{z}$) displacement of the magnetic trap for a given axial field gradient, when the misalignment was large. Once external fields were applied to correct this misalignment, the measured trap frequencies and axial field curvatures were in agreement.

In conclusion, we have constructed a novel mm-scale IP magnetic trap which provides the means for tailoring magnetic potentials on length scales intermediate to the larger, inch-scale electromagnets and smaller microfabricated devices. The millimeter length scale is in some ways natural for manipulating cold atomic clouds, generating sufficiently deep and well behaved potentials over the ∼100 micron scale of typical gaseous samples. This trapping technology may thus provide a flexible means to transport ultracold clouds or construct large scale waveguides appropriate for condensate-based interferometry schemes [7, 30–32]. Further, making use of the strong axial confinement of the millitrap, we have demonstrated a wide range of trapping geometries which may enable a variety of experiments. For instance, the ability to continuously manipulate the tilt of a cigar-shaped condensate with respect to a fixed axis, simply by the application of uniform magnetic fields, provides a new all-magnetic method for imparting angular momentum to a trapped gas. Compared with laser-based excitation schemes, the utility of which is limited by the length scales of an optical focus (Rayleigh range, beam waist radius) [15], this method may allow the excitation of vortices in BECs with extremely small radial dimensions. Finally, the achievement of large BECs in the millitrap, which by design is compatible with existing technologies for high-finesse Fabry-Perot optical resonators, accomplishes a significant milestone toward the application of cavity quantum electrodynamics to magnetically trapped ultracold atoms.

We acknowledge the skillful work of Dave Murai and Armando Baeza of the UCB Physics Machine Shop in constructing and installing the mount pieces. The authors effort was sponsored by the Defense Advanced Research Projects Agency (DARPA) and Air Force Laboratory, Air Force Materiel Command, USAF, under Contract No. F30602-01-2-0524, the NSF (Grant No. 0130414), the Alfred P. Sloan and David and Lucile Packard Foundations, and the University of California. KLM acknowledges support from the National Science Foundation. SG acknowledges support from the Miller Institute for Basic Research in Science.

[1] M. H. Anderson *et al.*, Science **269**, 198 (1995).
[2] M.-O. Mewes *et al.*, Phys. Rev. Lett. **77**, 416 (1996).
[3] T. Esslinger, I. Bloch, and T. W. Hänsch, Phys. Rev. A **58**, R2664 (1998).
[4] D. M. Stamper-Kurn, H. J. Miesner, S. Inouye, M. R. Andrews, and W. Ketterle, Phys. Rev. Lett. **81**, 500 (1998).
[5] S. Dettmer *et al.*, Phys. Rev. Lett. **87**, 160406 (2001).
[6] H. J. Lewandowski, D. M. Harber, D. L. Whitaker, and E. A. Cornell, Phys. Rev. Lett. **88**, 070403 (2002).
[7] Y.-J. Wang *et al.*, preprint, ArXiV cond-mat/0407689.
[8] Y. Shin *et al.*, Phys. Rev. Lett. **93**, 160406 (2004).
[9] D. S. Durfee *et al.*, in *"Bose-Einstein condensation in atomic gases", Proceedings of the International School of Physics, Course CXL*, edited by M. Inguscio, S. Stringari, and C. E. Wieman (IOS Press, Amsterdam, 1999), pp. 67–176.
[10] R. Folman *et al.*, Phys. Rev. Lett. **84**, 4749 (2000).
[11] W. Hänsel, P. Hommelhoff, T. W. Hänsch, and J. Reichel,

Nature **413**, 498 (2001).
[12] H. Ott, J. Fortagh, G. Schlotterbeck, A. Grossmann, and C. Zimmermann, Phys. Rev. Lett. **87**, 230401 (2001).
[13] Specialized atom-chip traps have been fabricated which may give axial curvatures up to 10^8 G/cm^2 [33, 34] .
[14] O. M. Maragò *et al.*, Phys. Rev. Lett. **84**, 2056 (2000).
[15] K. W. Madison, F. Chevy, W. Wohlleben, and J. Dalibard, Phys. Rev. Lett. **84**, 806 (2000).
[16] J. R. Abo-Shaeer, C. Raman, J. M. Vogels, and W. Ketterle, Science **292**, 476 (2001).
[17] G. Hechenblaikner, E. Hodby, S. A. Hopkins, O. M. Marago, and C. J. Foot, Phys. Rev. Lett. **88**, 070406 (2002).
[18] S. Stringari, Phys. Rev. Lett. **86**, 4725 (2001).
[19] C. J. Hood, M. S. Chapman, T. W. Lynn, and H. J. Kimble, Phys. Rev. Lett. **80**, 4157 (1998).
[20] J. Ye, D. W. Vernooy, and H. J. Kimble, Phys. Rev. Lett. **83**, 4987 (1999).
[21] P. W. H. Pinske, T. Fischer, P. Maunz, and G. Rempe, Nature **404**, 365 (2000).
[22] M. Greiner, I. Bloch, T. W. Hänsch, and T. Esslinger, Phys. Rev. A **63**, 031401(R) (2001).
[23] J. Arlt *et al.*, J. Phys. B **32**, 5861 (1999).
[24] W. Ketterle and N. J. van Druten, in *Advances in Atomic, Molecular, and Optical Physics*, edited by B. Bederson and H. Walther (Academic Press, San Diego, 1996), Vol. 37, pp. 181 – 236.
[25] P. W. H. Pinkse *et al.*, Phys. Rev. A **57**, 4747 (1998).
[26] A. Gorlitz *et al.*, Phys. Rev. Lett. **87**, 130402 (2001).
[27] D. Rychtarik, B. Engeser, H.-C. Nägerl, and R. Grimm, Phys. Rev. Lett. **92**, 173003 (2004).
[28] N. L. Smith *et al.*, arXiv preprint cond-mat/0410101.
[29] L. Pitaevskii and S. Stringari, Phys. Rev. Lett. **81**, 4541 (1998).
[30] Y. Shin *et al.*, Phys. Rev. Lett. **92**, 050405 (2004).
[31] W. Hänsel, J. Reichel, P. Hommelhoff,and T. W. Hänsch, Phys. Rev. A **64**, 063607 (2001).
[32] E. Andersson *et al.*, Phys. Rev. Lett. **88**, 100401 (2002).
[33] B. Lev, Nanotechnology **15**, S556 (2004).
[34] M. Drndic *et al.*, Applied Physics Letters **72**, 2906 (1998).

Appendix G

Bose-Einstein Condensation in a Circular Waveguide

This appendix includes the following paper:

- *S. Gupta, K. W. Murch, K. L. Moore, T. P. Purdy, and D. M. Stamper-Kurn, Bose-Einstein condensation in a circular waveguide, Phys. Rev. Lett.* ***95****, 143201 (2005)*

Bose-Einstein Condensation in a Circular Waveguide

S. Gupta, K. W. Murch, K. L. Moore, T. P. Purdy, and D. M. Stamper-Kurn
Department of Physics, University of California, Berkeley, California 94720, USA
(Received 27 April 2005; published 29 September 2005)

We have produced Bose-Einstein condensates in a ring-shaped magnetic waveguide. The few-millimeter diameter, nonzero-bias ring is formed from a time-averaged quadrupole ring. Condensates that propagate around the ring make several revolutions within the time it takes for them to expand to fill the ring. The ring shape is ideally suited for studies of vorticity in a multiply connected geometry and is promising as a rotation sensor.

DOI: 10.1103/PhysRevLett.95.143201 PACS numbers: 39.20.+q, 03.75.−b, 05.30.Jp, 39.25.+k

The long range phase coherence of superfluids and superconductors, aside from leading to interesting physical effects, is also of practical importance in allowing for precise measurement devices based on quantum interference. In such devices, spatially separated paths forming a multiply connected geometry are imposed on the macroscopic quantum system. For example, a SQUID magnetometer makes use of a superconducting ring interrupted by Josephson junctions to allow continuous sensitivity to magnetic fields. A similar geometry was used in a superfluid ^{3}He gyroscope [1].

Dilute gas superfluids have now enabled novel forms of matter-wave interferometry. Precise sensors of rotation, acceleration, and other sources of quantal phases [2,3] using trapped or guided atoms have been envisioned. In particular, the sensitivity of atom-interferometric gyroscopes is proportional to the area enclosed by the closed loop around which atoms are guided [4]. Such considerations motivate the development of closed-loop atom waveguides that enclose a sizable area.

A number of multiply connected trapping geometries for cold atoms have been discussed. Optical traps using high-order Gauss-Laguerre beams were proposed [5,6], and hollow light beams were used to trap nondegenerate atoms in an array of small-radius rings [7]. Large-scale magnetic storage rings were developed for cold neutrons [8] and discussed for atomic hydrogen [9]. More recently, closed-loop magnetic waveguides were demonstrated for laser cooled atoms [10,11]. Unfortunately, these guides are characterized by large variations in the potential energy along the waveguide and by high transmission losses at points where the magnetic field vanishes.

In this Letter, we report the creation of a smooth, stable circular waveguide for ultracold atoms. A simple arrangement of coaxial electromagnetic coils was used to produce a static ring-shaped magnetic trap, which we call the quadrupole ring (Q ring), in which strong transverse confinement is provided by a two-dimensional quadrupole field. Atoms trapped in the Q ring experience large Majorana losses, but we can eliminate such losses with a time-orbiting ring trap (TORT) [12]. In this manner, stable circular waveguides with diameters ranging from 1.2 to 3 mm were produced. Finally, we report on the production of Bose-Einstein condensates (BECs) in a portion of the circular waveguide, and on the guiding of an ultracold atomic beam for several revolutions around the guide. This ring-shaped trap presents opportunities for studies of BECs that are homogeneous in one dimension and therefore of the unterminated propagation of sound waves [13] and solitons [14–16], of persistent currents [17–20], of quantum gases in low dimensions, and of matter-wave interferometry.

To explain the origin of the quadrupole ring trap, we consider a cylindrically symmetric static magnetic field $\vec{B}_c$ in a source-free region. Expanding $\vec{B}_c$ to low order about a point (taken as the origin) on the axis where the field magnitude has a local quadratic minimum, we have

$$\vec{B}_c = B_0\hat{z} + \frac{B_z''}{2}\left[\left(z^2 - \frac{x^2+y^2}{2}\right)\hat{z} - z(x\hat{x} + y\hat{y})\right], \quad (1)$$

where $B_0 > 0$ is the field magnitude at the origin, B_z'' is the

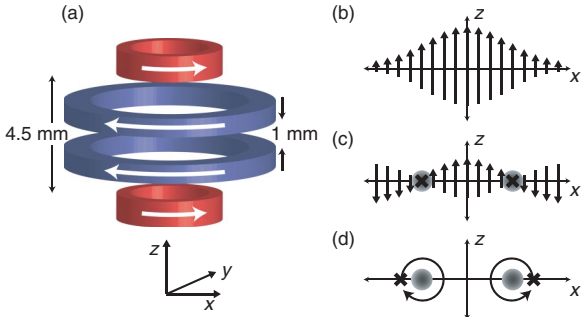

FIG. 1 (color). Forming a circular magnetic waveguide. (a) Four coaxial circular electromagnets (see [21] for details) are used to generate both the static (currents as shown) and rotating fields needed for the waveguide. Axes are indicated; gravity points along $-\hat{z}$. (b) As shown schematically, the field (arrows) from just the two outer coils (curvature coils, outer pair) points axially in the midplane between the coils, with largest fields at the axis. (c) Adding a uniform opposing bias field (using antibias coils, inner pair) produces a ring of field zeros (×) in the $\hat{x}$-$\hat{y}$ plane around which weak-field seeking atoms (shaded region) are trapped. (d) Rapidly rotating the field zeros around the trapped atoms produces the TORT.

axial field curvature, and Cartesian coordinates (x, y, z) are chosen so that z is the axial coordinate. The magnetic field magnitude falls to zero in the $\hat{x}$-$\hat{y}$ plane along a circle of radius $\rho_0 = 2\sqrt{B_0/B_z''}$ centered at the origin. This is the Q ring, a ring-shaped magnetic trap for weak-field seeking atoms. Near the field zeros, the magnetic field has the form of a transverse (radial and axial directions) two-dimensional quadrupole field with gradient $B' = \sqrt{B_0 B_z''}$. Such traps can also be obtained using different electromagnet configurations [12].

In our apparatus, the Q ring is formed using a subset of the coils (the curvature and antibias coils; see Fig. 1) used in our recently demonstrated millimeter-scale Ioffe-Pritchard magnetic trap [21]. Our work is aided, in particular, by the large axial curvatures produced in this trap and by the vertical orientation of the trap axis. These features are relevant for the operation of a Q ring in the presence of gravity, for two reasons. First, trapping atoms in the Q ring requires transverse confinement sufficient to overcome the force of gravity; this places a lower bound on the radius of the Q ring of $\rho_0 > \rho_{\min} \simeq 2mg/|\mu|B_z''$ with m the atomic mass, g the acceleration due to gravity, and μ the atomic magnetic moment. Indeed, if $\rho_{\min}$ exceeds the range over which Eq. (1) is valid, typically the distance to the field-producing coils, the formation of a Q ring may be precluded entirely. With $B_z'' = 5300$ G/cm^2 in our experiments, $\rho_{\min} = 115$ μm is much smaller than the millimeter dimensions of the electromagnets used for the trap. Second, the vertical orientation of the Q-ring axis allows cold atoms to move slowly along the nearly horizontal waveguide rather than being confined in a deep gravitational well.

Atoms can be localized to a particular portion of the Q ring by application of a uniform sideways (in the $\hat{x}$-$\hat{y}$ plane) magnetic field; e.g., a weak bias field $B_s\hat{x}$ tilts the Q ring by $\Delta z/\rho_0 = (B_s/B')/\rho_0$ about the $\hat{y}$ axis. This adjustment also adds an azimuthal field of magnitude $B_s|\sin\theta|$, splitting the Q ring into two trap minima at opposite sides of the ring, with θ being the azimuthal angle conventionally defined.

We loaded cold atoms into the Q ring using a procedure similar to previous work [21]. Briefly, about 2×10^9 ^{87}Rb atoms in the $|F = 1, m_F = -1\rangle$ hyperfine ground state were loaded into one of two adjacent spherical quadrupole magnetic traps. Using these traps, atoms were transported 3 inches from the loading region to the Q-ring trap region. During this transport, rf evaporative cooling was applied, yielding 2.5×10^7 atoms at a temperature of 60 μK in a spherical quadrupole trap with an axial field gradient of 200 G/cm. Within 1 s, we then converted the spherical quadrupole to a tilted Q-ring trap produced with $B_z'' = 5300$ G/cm^2, $B_0 = 22$ G, and a side field of magnitude $B_s = 9.2$ G. This process left 2×10^7 atoms trapped in the Q ring (Fig. 2).

The trapping lifetime of atoms in the Q ring is limited by Majorana losses. In a balanced Q ring, trapped atoms passing close to the line of zero field, which extends all around the ring, may flip their spins and be expelled from the trap. Extending the treatment by Petrich *et al.* [22] to this scenario, we estimate a Majorana loss rate of $\frac{\hbar^{1/2}}{\pi m^{3/4}} \times \frac{(\mu B')^{3/2}}{(k_B T)^{5/4}} = 6$ s^{-1} for our trap at a temperature of 60 μK. In a tilted Q ring, the zero-field region is reduced to just two points at opposite sides of the ring. Majorana losses in a tilted Q ring are thus similar to those in spherical quadrupole traps and much smaller than in a balanced Q ring. We confirmed this qualitative behavior by measuring the lifetime of trapped atoms in balanced and tilted Q-ring traps. In the balanced Q ring, the measured 0.3 s^{-1} Majorana loss rate was thrice that in a tilted Q ring, while falling far short of the predicted 6 s^{-1} loss rate, presumably due to residual azimuthal fields.

The high loss rates in the Q ring can be mended in a manner similar to the time-orbiting potential (TOP) trap by which Majorana losses in a spherical quadrupole field were overcome [22]. As proposed by Arnold [12], a TORT with nonzero bias field can be formed by displacing the ring of field zeros away from and then rapidly rotating it around the trapped atoms [Fig. 1(d)]. From Eq. (1), the Q ring can be displaced radially by application of an axial bias field, and displaced along $\hat{z}$ by a cylindrically symmetric spherical quadrupole field. The TORT provides transverse quadratic confinement with an effective field curvature of $B_{\text{eff}}'' = B'^2/2B_{\text{rot}}$, where B_{rot} is the magnitude of the rotating field seen at the trap minimum. Just as the TOP trap depth is limited by the "circle of death," the TORT trap

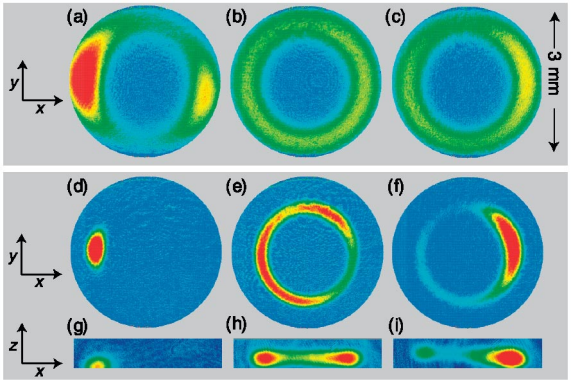

FIG. 2 (color). Atoms in a ring-shaped magnetic trap. Shown are top (a)–(f) and side (g)–(i) absorption images of ultracold ^{87}Rb clouds in either a Q ring (a)–(c) or TORT (d)–(i) with applied side field $B_s = 9.2$ (left), 0 (middle), and -2.5 G (right column), respectively, in the $\hat{x}$ direction. Images were taken 2 ms after turning off the traps. The applied field tilts the Q ring or TORT and favors atomic population in one side or another of the trap. For $B_s \sim 0$, the trap lies nearly in the horizontal plane and its azimuthal potential variation is minimized. For the Q ring, $B_0 = 22$ G; for the TORT, $B_0 = 20$ G and $B_{\text{rot}} = 17$ G; and $B_z'' = 5300$ G/cm^2 for both. The temperature of trapped atoms is 90 μK in the Q ring, and 10 μK in the TORT. Resonant absorption ranges from 0 (blue) to >80% (red).

depth is limited by a "torus of death," the locus of points at which the magnetic field is zero at some time [23]. This scheme may be applied equally to a tilted Q ring, yielding a tilted TORT and providing a stable trap in which atoms are confined to a portion of the ring. The sideways magnetic field (e.g., along $\hat{x}$) causes the magnetic potential minimum to vary azimuthally in the tilted TORT as $|\mu|\sqrt{B_{\rm rot}^2 + B_s^2 \sin^2\theta}$, while the gravitational potential is the same as that in a Q ring.

The time-varying fields needed to convert our Q ring (or tilted Q ring) traps to TORT (or tilted TORT) traps were obtained by suitably modulating the currents in the four coils used to generate the Q-ring potential. A modulation frequency of 5 kHz was chosen to be much larger than the transverse motional frequencies (< 100 Hz) and also much smaller than the Larmor frequency (> 3 MHz) at the location of the trap minimum. To first switch on the TORT, a rotating field magnitude of $B_{\rm rot} = 18$ G was used [24].

As shown in Fig. 3, the trap lifetime was dramatically increased by application of the TORT trap. In the first few seconds after switching on the TORT, we observed a fast loss of atoms and a simultaneous drop in their temperature. We ascribe this loss and cooling to the evaporation of atoms from the trapped cloud through the "torus of death." As the temperature dropped, the evaporation rate diminished and the lifetime of trapped atoms became vacuum limited at 90 s, a value observed both for balanced and for tilted TORT traps.

Given their longevity, it was possible to cool evaporatively the TORT-trapped atoms to the point of quantum degeneracy. Using a tilted TORT with $B_s \sim 9$ G, evaporation was performed in two stages. First, "torus of death" evaporation was applied by ramping down the rotating field strength $B_{\rm rot}$ over 40 s to 4.8 G. The oscillation frequencies in this trap were measured as $\omega_\perp = 2\pi \times (87, 74.5)$ Hz in the transverse and $\omega_\theta = 2\pi \times 35$ Hz in the azimuthal directions, in agreement with predictions [25]. In the second stage, rf evaporation was applied for 20 s, yielding clouds of up to 6×10^5 atoms at the Bose-Einstein condensation temperature, and pure BECs of up to 3×10^5 atoms.

Finally, to assess the suitability of the TORT as an atomic waveguide for interferometry, we launched our trapped BECs into closed-loop circular motion along the guide. This was accomplished by reorienting the sideways bias field B_s, inducing the trapped BEC to accelerate toward the newly positioned tilted TORT trap minimum (advanced by an azimuthal angle of about $\pi/4$), while simultaneously reducing the magnitude of B_s to $B_s \sim 0$ and increasing $B_{\rm rot}$ to 12.6 G to produce a well-balanced TORT trap. The TORT was then maintained at this setting, with radius $\rho_0 = 1.25$ mm ($B_0 = 20$ G, $B_z'' = 5300$ G/cm^2), and transverse trap frequencies of $\omega_\perp \simeq 2\pi \times 50$ Hz as measured at the launch point of the atoms. The atoms were allowed to propagate freely around the guide for various guiding times before being observed by absorption imaging. As shown in Fig. 4, the ultracold atomic beam propagated around the circular waveguide at an angular (linear) velocity of 40.5 rad/s (50.6 mm/s). As measured from the azimuthal extent of the atoms for different guiding times, this pulsed atom beam was characterized by an azimuthal rms velocity spread of 1.4 mm/s, equivalent to a longitudinal kinetic temperature

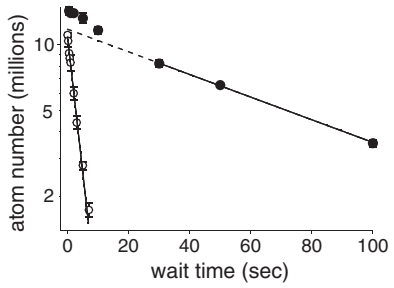

FIG. 3. Elimination of Majorana losses in the TORT. The measured number of trapped atoms in a Q ring (open circles) or TORT (solid circles) trap is shown vs residence time in the trap. Exponential fits indicate a 3 s Majorana-loss-limited lifetime in the Q ring. In the TORT, following an initial (30 s) loss of atoms due to evaporation, a vacuum limited lifetime of 90 s was observed. Settings for B_0, B_z'', and $B_{\rm rot}$ are as in Fig. 2, $B_s \sim 0$, and the initial temperature is 60 μK.

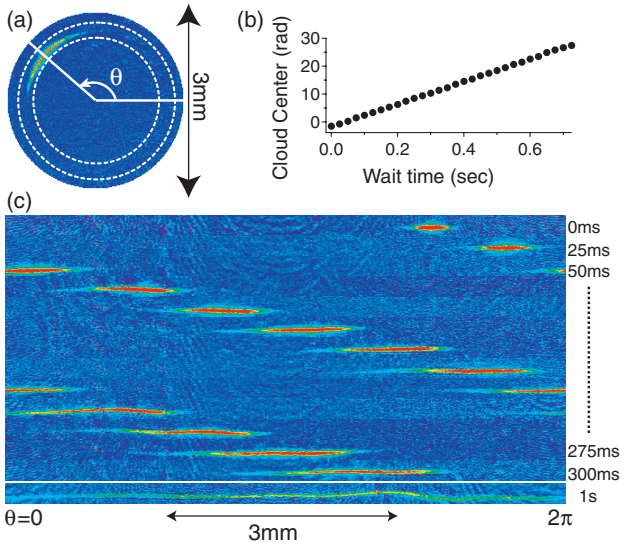

FIG. 4 (color). Circular motion of a quantum degenerate atomic beam in a waveguide. A Bose-Einstein condensate was launched into a balanced TORT and allowed to propagate. (a) Top view in-trap absorption image during the propagation. The mean azimuthal position of the BEC measured from such images is shown in (b). Annular portions (indicated by dashed circles) of top-view images taken at different guiding times are shown in (c) displayed in polar coordinates (radius vs azimuthal angle). The beam advances at an angular velocity of 40.5 rad/s while expanding due to an rms azimuthal velocity spread of 1.4 mm/s. After 1 s, the beam fills the entire guide.

of 22 nK. After about 1 s of guiding, this velocity variation caused the atomic cloud to spread throughout the waveguide, by which point the atoms had traveled $L = 51$ mm along the waveguide, encompassing an area of $A = L\rho_0/2 = 32$ mm^2. One would expect the front and back ends of the expanding BEC to interfere spatially as they overlap after 1 s of propagation in the guide. However, the fringe periodicity of ~600 nm expected for such interference is well below our imaging resolution of several μm, and we observed no such interference.

Many requisite elements for interferometric rotation sensing are still lacking in our system, including a means of in-guide coherent atomic beam splitting [26,27], bidirectional propagation, proper radial waveguiding [28], full characterization of longitudinal coherence in the beam, an assessment of the influence of the time-orbiting field on sensor precision, and atom-interferometric stability. Nevertheless, it is valuable to consider the possible sensitivity of our system if these elements are attained. As limited by atomic shot noise, rotation measurements with an uncertainty of $\Delta\Omega = (\hbar/4mA)N_0^{-1/2} \sim 1 \times 10^{-8}$ rad/s could be made from a single (1 s long) measurement, where $N_0 = 3 \times 10^5$ is the number of atoms used. While this figure is nearly 20 times that of existing atom-based gyroscopes [4], improvements such as launching the atoms at higher velocities, increasing the TORT radius, and increasing the atom number may ultimately yield a useful, compact sensing device.

Other applications of the TORT may include studies of propagation [29–31] and nonlinear dynamics [32] in atomic waveguides. In a TORT potential that is modified either by application of magnetic fields or by tilting with respect to gravity, BECs can be studied both undergoing pendular motion (terminated guide) when launched at small velocities, and undergoing circular motion (unterminated guide) at larger velocities.

Another appealing possibility is the study of BECs that fill the ring-shaped trap, rather than forming in just a portion of the ring. Such a system would allow for studies of quantized and persistent circulation [17–20], unterminated motion of solitons [14–16], and other aspects of nonlinear dynamics [33]. For this purpose, the azimuthal variation in the TORT potential must be reduced below the typical ~100 nK scale of the BEC chemical potential. From measurements of the kinetic energy of BEC's undergoing circular motion in our trap (data of Fig. 4), we estimate the TORT potential varied by as much as 5 μK. We believe this figure can be reduced greatly by using traps of smaller radius, by designing better electromagnets for both the static and the rotating fields used for the TORT, and also by controlling the orientation of the electromagnets with respect to gravity.

This work was sponsored by DARPA (Contract No. F30602-01-2-0524), the NSF (Grant No. 0130414), the David and Lucile Packard Foundation, and the University of California. K. L. M. acknowledges support from the NSF, and S. G. from the Miller Institute.

Note added.—After the submission of this paper, related work was reported by Arnold and collaborators [34].

[1] R. W. Simmonds *et al.*, Nature (London) **412**, 55 (2001).
[2] K. G. Petrosyan and L. You, Phys. Rev. A **59**, 639 (1999).
[3] Y. Lyanda-Geller and P. M. Goldbart, Phys. Rev. A **61**, 043609 (2000).
[4] T. Gustavson, A. Landragin, and M. Kasevich, Classical Quantum Gravity **17**, 2385 (2000).
[5] E. M. Wright, J. Arlt, and K. Dholakia, Phys. Rev. A **63**, 013608 (2001).
[6] B. P. Anderson, K. Dholakia, and E. M. Wright, Phys. Rev. A **67**, 033601 (2003).
[7] P. Verkerk and D. Hennequin, physics/0306155.
[8] K.-J. Kügler, K. Moritz, W. Paul, and U. Trinks, Nucl. Instrum. Methods Phys. Res. **228**, 240 (1985).
[9] D. Thompson, R. V. E. Lovelace, and D. M. Lee, J. Opt. Soc. Am. B **6**, 2227 (1989).
[10] J. A. Sauer, M. D. Barrett, and M. S. Chapman, Phys. Rev. Lett. **87**, 270401 (2001).
[11] S. Wu, W. Rooijakkers, P. Striehl, and M. Prentiss, Phys. Rev. A **70**, 013409 (2004).
[12] A. S. Arnold, J. Phys. B **37**, L29 (2004).
[13] M. R. Andrews *et al.*, Phys. Rev. Lett. **79**, 553 (1997).
[14] L. Salasnich, A. Parola, and L. Reatto, Phys. Rev. A **59**, 2990 (1999).
[15] J. Brand and W. P. Reinhardt, J. Phys. B **34**, L113 (2001).
[16] J.-P. Martikainen *et al.*, Phys. Rev. A **64**, 063602 (2001).
[17] F. Bloch, Phys. Rev. A **7**, 2187 (1973).
[18] J. Javanainen, S. M. Paik, and S. M. Yoo, Phys. Rev. A **58**, 580 (1998).
[19] M. Benakli *et al.*, Europhys. Lett. **46**, 275 (1999).
[20] E. Nugent, D. McPeake, and J. F. McCann, Phys. Rev. A **68**, 063606 (2003).
[21] K. L. Moore *et al.*, cond-mat/0504010.
[22] W. Petrich, M. H. Anderson, J. R. Ensher, and E. A. Cornell, Phys. Rev. Lett. **74**, 3352 (1995).
[23] Because of this topology, rf evaporation should be equally effective whether one approaches the Larmor frequency at the trap minimum from above or below.
[24] The magnitude of B_{rot} ranged between ~15 and 20 G during the 5 kHz modulation.
[25] The transverse asymmetry arises because of the sideways field.
[26] Y.-J. Wang *et al.*, Phys. Rev. Lett. **94**, 090405 (2005).
[27] S. Wu, E. J. Su, and M. Prentiss, cond-mat/0503130.
[28] E. Andersson *et al.*, Phys. Rev. Lett. **88**, 100401 (2002).
[29] K. Bongs *et al.*, Phys. Rev. A **63**, 031602(R) (2001).
[30] A. E. Leanhardt *et al.*, Phys. Rev. Lett. **89**, 040401 (2002).
[31] J. Fortàgh *et al.*, Appl. Phys. B **76**, 157 (2003).
[32] H. Ott *et al.*, Phys. Rev. Lett. **91**, 040402 (2003).
[33] L. J. Garay, J. R. Anglin, J. I. Cirac, and P. Zoller, Phys. Rev. Lett. **85**, 4643 (2000).
[34] A. S. Arnold, C. S. Garvie, and E. Riis, cond-mat/0506142.

Appendix H

Probing the Quantum State of a Guided Atom Laser Pulse

This appendix includes the following paper:

- *K. L. Moore, S. Gupta, K. W. Murch, and D. M. Stamper-Kurn, Probing the quantum state of a guided atom laser pulse, Phys. Rev. Lett. 97, 180401 (2006)*

Probing the Quantum State of a Guided Atom Laser Pulse

Kevin L. Moore,* Subhadeep Gupta, Kater W. Murch, and Dan M. Stamper-Kurn
Department of Physics, University of California, Berkeley, California 94720, USA
(Received 7 June 2006; published 2 November 2006)

We describe bichromatic superradiant pump-probe spectroscopy as a tomographic probe of the Wigner function of a dispersing particle beam. We employed this technique to characterize the quantum state of an ultracold atomic beam, derived from a ^{87}Rb Bose-Einstein condensate, as it propagated in a 2.5 mm diameter circular waveguide. Our measurements place an upper bound on the longitudinal phase space area occupied by the 3×10^5 atom beam of $9(1)\hbar$ and a lower bound on the coherence length of $\mathcal{L} \geq 13(1)$ μm. These results are consistent with full quantum degeneracy after multiple orbits around the waveguide.

DOI: 10.1103/PhysRevLett.97.180410 PACS numbers: 03.75.Pp, 32.80.−t, 42.50.Gy

Advances in the control of quantum degenerate gases have mirrored those of optical lasers, including the realization of high-contrast atom interferometers [1,2], nonlinear atom optics [3], and dispersion management [4,5]. Further, given single-mode waveguides [6] and other atom optical elements, the prospect of sensitive guided-atom interferometry has invited intensive experimental pursuit. Critical to realizing this prospect are methods for characterizing the coherence of a guided atom beam, akin to beam characterization in a high-energy particle accelerator.

Pulsed particle beams are naturally described by the Wigner quasiprobability distribution, defined as [7]

$$W(\mathbf{r}, \mathbf{p}) = \frac{1}{2\pi} \int e^{-i\mathbf{p}\cdot\mathbf{y}/\hbar} \left\langle \mathbf{r} - \frac{\mathbf{y}}{2} \middle| \hat{\rho} \middle| \mathbf{r} + \frac{\mathbf{y}}{2} \right\rangle d\mathbf{y}, \quad (1)$$

with $\hat{\rho}$ being the density matrix of the system. This distribution is the quantum mechanical equivalent of the classical phase space distribution. Experimentally, $W(\mathbf{r}, \mathbf{p})$ is determined tomographically by measuring its projection at various angles in phase space [8,9].

In this Letter we describe the use of bichromatic superradiant pump-probe spectroscopy (SPPS) to measure the Wigner function of an atomic beam propagating in a circular waveguide [10]. A form of such spectroscopy is applied to atoms in a circular waveguide, allowing for a measurement of the phase space density despite a significant coherent velocity chirp across the beam. Both long-range coherence and single transverse mode propagation were evident over many waveguide revolutions, implying that a guided atom laser pulse derived from a Bose-Einstein condensate remains coherent for at least 300 ms of propagation.

Superradiant light scattering from quantum degenerate gases provides striking confirmation of their long-range coherence [11,12]. An elongated cloud undergoing superradiance scatters light preferentially into "end-fire modes," leading to highly directional emission [13]. Coherence between scattered and unscattered atoms establishes a periodic grating of density or polarization which stimulates further light scattering. Once established, by superradiance or otherwise [14,15], this grating will decay or dephase on a time scale $\tau_c = m/2|\mathbf{q}|\sigma_p$ with m being the atomic mass, $\hbar\mathbf{q}$ the superradiant scattering recoil momentum, and σ_p the rms momentum spread of the unscattered atoms along the recoil direction. This can be isolated experimentally by applying superradiance in a pump-probe spectroscopic technique: after a first optical pump pulse initiates superradiance and establishes coherence in the gas, this coherence is allowed to decay freely for a time τ before a second optical pulse is applied. In Ref. [12], this technique revealed in detail the bimodal momentum distribution of a partly condensed Bose gas.

Let us consider applying such spectroscopy to a beam of N atoms in the transverse ground state of a 1D waveguide with longitudinal rms spatial and momentum widths of σ_x and σ_p, respectively. The 1D Wigner function of the beam is bounded by these widths to occupy a phase space area of $\mathcal{A}_{\max} = \sigma_x\sigma_p$. However, $\mathcal{A}_{\max}$ may represent a gross overestimate of the actual phase space area occupied by the beam. For example, assume that the beam originates from a thermally equilibrated trapped gas that was released into the waveguide. Free expansion causes the momentum and position of the beam to be strongly correlated, a feature captured by a posited Wigner function of the form

$$W(x, p) = \frac{\exp\left[-\frac{1}{2(1-\eta^2)}\left(\frac{x^2}{\sigma_x^2} - 2\eta\frac{xp}{\sigma_x\sigma_p} + \frac{p^2}{\sigma_p^2}\right)\right]}{\pi\sigma_x\sigma_p\sqrt{1-\eta^2}}, \quad (2)$$

where $\eta = \langle px\rangle/\sigma_p\sigma_x$ (Fig. 1). The actual phase space area $\mathcal{A}$ of such a beam is smaller than the aforementioned estimate by a factor $\sqrt{1-\eta^2}$. That is, for proper characterization of a beam one must distinguish between a spatially inhomogeneous momentum width σ_p, which may be dominated by a coherent velocity chirp across the length of the beam, and a "homogeneous" width $\mathcal{A}/\sigma_x$.

To access these correlations, we consider *bichromatic* SPPS in which the recoil momenta $\hbar\mathbf{q}_1$ and $\hbar\mathbf{q}_2$ imparted

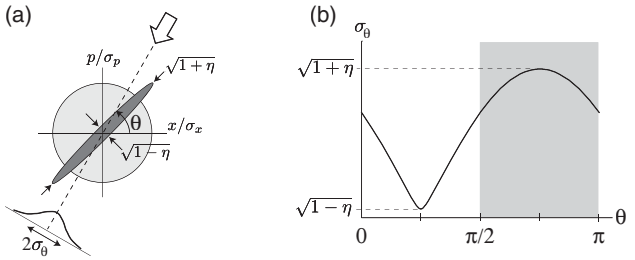

FIG. 1. Projective measurements as probes of quantum degeneracy. (a) Contours of Gaussian Wigner distributions $W(x, p)$ are shown. $W(x, p)$ is determined by its projections at all angles $0 \leq \theta < \pi$. Measurements of only the momentum and position distributions ($\theta = 0$ and $\theta = \pi/2$ projections, respectively), cannot distinguish a homogeneous (light shading) from a correlated ensemble (dark shading). (b) rms widths of distributions derived at various projection angles are shown. Time-of-flight analyses recover a limited range of projection angles (shaded), while bichromatic SPPS accesses all projection angles.

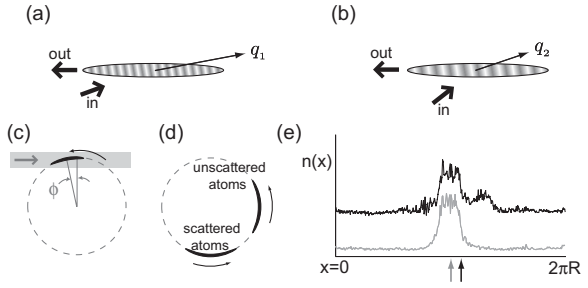

FIG. 2. Bichromatic SPPS in a circular waveguide. (a) Superradiant Rayleigh scattering of a pump pulse establishes a density modulation of wave vector $\hbar\mathbf{q}_1$ in an elongated atomic beam. (b) A coherent velocity chirp causes the modulation wave vector to decrease along the long axis. The remaining coherence is revealed by light scattering with recoil momentum $\hbar\mathbf{q}_2$ matched to the modified density grating. (c) Pump (probe) light illuminates the freely propagating atom beam at angle ϕ ($\phi + \Omega\tau$) relative to the mean angular position, and (d) scattered atoms separate from the original pulse and can be distinguished from unscattered atoms. (e) Azimuthal density distributions $n(x)$ in the ring 160 ms after illumination are shown for beams that have (black) or have not (gray) undergone superradiant light scattering. The shifted center of mass (indicated by arrows) quantifies the total superradiant scattering rate.

by superradiance are different for the pump and probe pulses, respectively (Fig. 2). These differing momenta may result experimentally from pump and probe pulses which differ in wave vector, or, as in the present experiment, which differ in their angle of incidence with respect to the long axis of the cloud. Restricting our treatment to one dimension along $\hat{x}$, the superradiant scattering rate Γ from the second (probe) light pulse [11,16] can be expressed in terms of the Wigner function of the state of the system *before* the first (pump) pulse as

$$\Gamma \propto \left| \iint e^{i(\frac{q_1\tau}{m}p + \Delta q x)} W(x, p) dx dp \right|^2, \qquad (3)$$

where $\Delta q = q_2 - q_1$ with $\hbar q_1$ and $\hbar q_2$ being the projections of the recoil momenta along the $\hat{x}$ axis, and τ is the pump-probe delay time. Performing an extended canonical transformation to generalized coordinates $\tilde{x} = (x/\sigma_x) \times \cos\theta + (p/\sigma_p)\sin\theta$ and $\tilde{p} = -(x/\sigma_x)\sin\theta + (p/\sigma_p) \times \cos\theta$, with $\tan\theta = -\frac{\Delta q m}{q_1 \tau}\frac{\sigma_x}{\sigma_p}$ we obtain

$$\Gamma \propto \left| \int e^{i(\frac{\sigma_p q_1 \tau}{m}\cos\theta - \sigma_x \Delta q \sin\theta)\tilde{p}} d\tilde{p} \int W(x, p) d\tilde{x} \right|^2. \qquad (4)$$

Monochromatic SPPS ($\Delta q = 0$) yields information only on the overall momentum distribution of the atomic system, which derives from projecting the Wigner function on the momentum axis ($\theta = 0$) [12]. In contrast, bichromatic SPPS assesses the Wigner function at a nonzero projection angle θ. In particular, tuning experimental parameters such that $\theta = \pi/4$ probes the Wigner function of Eq. (2) along the narrow axis corresponding to the linear momentum chirp across the cloud, and thereby provides a sensitive measurement of η and of the phase space density of the beam. In this case the observed coherence time is increased to $\tau_c = m/2|\mathbf{q}|\sigma_p\sqrt{1-\eta}$.

In other words, in monochromatic SPPS the reduction of the superradiant scattering rate from a linearly chirped beam comes about mainly by dephasing. The density modulation established by the pump pulse evolves at a frequency which is Doppler-shifted upward on one end and downward on the other end of the momentum-chirped beam. This causes the wave vector of the density modulation to decrease linearly with time. In bichromatic SPPS, by matching the recoil momentum of the probe pulse to the wave vector of the density grating, we recover a superradiant scattering rate which reveals the remaining homogeneous decay of motional coherence.

We now turn to our implementation of this scheme to probe a pulsed atom laser beam in a circular waveguide. This beam originated from a ^{87}Rb Bose-Einstein condensate of 3×10^5 atoms produced in a magnetic time-orbiting ring trap (TORT) [10,17], biased to yield a three-dimensional harmonic trap with trapping frequencies $(\omega_x, \omega_T) = 2\pi \times (35, 85)$ s^{-1} in the longitudinal (i.e., azimuthal in the ring) and transverse directions, respectively. These atoms were launched azimuthally by adiabatically decompressing the trap to $\omega_x = 2\pi \times 6$ s^{-1} and displacing the trap minimum to a new longitudinal position for 30 ms, accelerating the cloud to a mean orbital angular frequency $\Omega = 2\pi \times 8.4$ s^{-1} chosen to be far from any betatron resonances [17]. The TORT potential was then balanced over the next 30 ms and operated with radius $R = 1.25$ mm and ω_T as above. The launched atomic beam was allowed to propagate freely in this circular guide.

While the beam's provenance as a Bose-Einstein condensate suggests its full coherence at later times, it may also be argued that heating from trap vibrations and imperfections, collisions with background gas particles, or effects related to the quasi-1D nature of the guided atoms

[18] can indeed cause the coherence to be spoiled after sufficient propagation times. Thus, our experimental goal was to measure quantitatively the coherence of this propagating atom beam at an arbitrary time after its launch.

We made use of direct absorption imaging of the propagating atom beam to discern several properties of its evolution. Such imaging, applied along the symmetry axis of the circular waveguide, quantified the longitudinal linear density of the beam $n(x)$ [Fig. 2(c)]. From the growth of the spatial width σ_x of the beam vs propagation time, we determined the rms momentum width as $\sigma_p = m \times 1.8$ mm/s, a value within 10% of that expected due to the release of interaction energy in the launched Bose-Einstein condensate. The transverse state of the atomic beam was characterized by suddenly releasing the atom beam from the waveguide and imaging the transverse extent of the beam after variable times of flight. These observations agreed well with a mean-field model of the coherent expansion of a Bose-Einstein condensate into a tight waveguide [19], and indicated the transverse state of the beam to be the ground state of the harmonic transverse confining potential after about 150 ms of propagation. The beam can thus be treated as one-dimensional with its azimuthal state remaining unknown. Combining these observations, we obtain an upper bound on the longitudinal phase space area of $\mathcal{A}_{\max} = 310\hbar$ for the beam after a half-revolution in the guide given its $\sigma_x = 120$ μm rms width at that stage.

This constraint on $\mathcal{A}_{\max}$ was dramatically improved by application of SPPS to the propagating beam. The probe and pump pulses were both obtained from a single laser source propagating in the plane of the waveguide (to within $\pm 1°$) with a 0.4 mm beam diameter, a detuning 560 MHz below the $^2S_{1/2}, F = 1 \rightarrow {}^2P_{3/2}, F = 0$ transition, and circular polarization. Typical intensities were 10 mW/cm^2, corresponding to observed single-particle Rayleigh scattering rates of 400 s^{-1}, and pulses were typically 50 μs in duration. After application of the light pulses, the atoms were allowed to propagate in the waveguide until the scattered atoms had clearly separated from the unscattered atoms. The fraction of scattered atoms and, hence, the total superradiant scattering rate from the pump-probe sequence, was then determined from the center-of-mass of the beam ($x_{\text{c.m.}}$) in the azimuthal coordinate.

Such pump-probe spectroscopy was applied to the atom beam at different propagation times, and thus at different locations in the circular guide. As shown in Fig. 3, the measured coherence times depend strongly on the position of the beam in the guide. Letting ϕ measure the central angular position of the beam away from the point at which the pump/probe light is tangential to the guide, the superradiant response of atoms at large angles ($|\phi| \gtrsim 20°$) decays after a pump-probe delay time of around 50 μs, consistent with the coherence time discussed above for monochromatic SPPS determined by the overall momentum width of the beam. In contrast, for beam positions

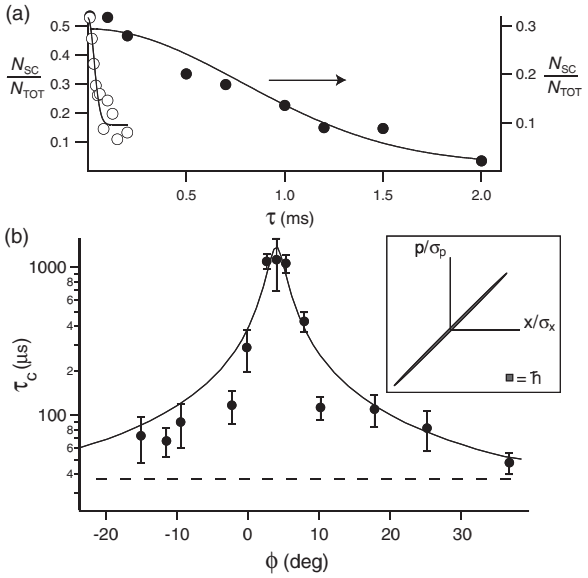

FIG. 3. Bichromatic SPPS of a quantum degenerate beam at approximately a half-revolution in the circular waveguide. (a) SPPS at $\phi = 38°$ (open circles) and $\phi = 4°$ (closed circles) gives coherence times $\tau_c = 47(8)$ μs and 1.1(1) ms, respectively, defined by the $1/e$ decay time of the superradiant signal (Gaussian fits to data are shown). (b) Measured coherence times are compared to theoretical predictions for a coherent Gaussian beam (solid line) and an incoherent, uncorrelated ensemble (dotted line). The theoretical curve in fact predicts the maximum coherence time at $\phi = 31°$ (see text), but has been shifted for comparison to data. The inset shows the Wigner distribution implied by the 1.1 ms coherence time. A phase space cell of area $\hbar$ is included for reference.

closer to $\phi = 4°$, the coherence time is dramatically increased to over 1 ms, indicating coherence in the beam beyond that implied solely by the overall momentum width. Similar coherence times were observed after one, two, and three full revolutions around the ring.

This strong geometric dependence can be understood in the context of bichromatic SPPS. During the time τ between application of the pump and probe pulses, the propagating atom beam rotates by an angle $\Omega\tau$, thereby varying the relative orientation between the incident light and the end-fire superradiant emission from the gas. Expressed in a frame corotating with the atom beam, the superradiant recoil momenta of the pump and probe beams differ by $\Delta\mathbf{q} \simeq k\Omega\tau(-\sin\phi\hat{x} + \cos\phi\hat{r})$, with $\hat{x}$ and $\hat{r}$ being unit vectors in the azimuthal and radial transverse directions, respectively, and assuming $\Omega\tau \ll 1$. Thus, the pump-probe wave vector difference Δq, which is needed for tomographic measurements of the Wigner function, is not established by varying the incident probe light; rather, Δq arises from the rotation of the atomic beam, and thereby of the wave vector of "end-fire mode" light emission, during the delay time.

We now apply the one-dimensional treatment of bichromatic SPPS to this situation by considering just the con-

tribution of longitudinal phase matching to superradiant scattering. SPPS applied to the rotating beam while at an angle ϕ probes the Wigner function of the beam at a *constant* phase space projection angle given by $\tan\theta = \frac{m\Omega\sigma_x}{\sigma_p}\frac{\sin\phi}{1+\cos\phi}$. Different projections of θ are thus obtained merely by measuring τ_c at different positions ϕ of the beam. We note that while these measurements of τ_c do not constitute a complete tomography of the Wigner function, they do allow us to reconstruct an ellipsoid which bounds the phase space occupied by the beam. Under this approximation that $W(x, p)$ is indeed Gaussian, our measurements do suffice for complete tomographic reconstruction. With better data quality, our technique could be used to reconstruct a Wigner function of a more general form.

Using experimentally measured quantities for the beam after a half-revolution in the waveguide, the condition $\tan\theta = 1$ for probing the homogeneous momentum width of the correlated atom beam is predicted to occur at $\phi_c = 31°$. This value clearly does not match the experimentally observed $\phi_c = 4(2)°$ [Fig. 3(b)]. 2D models which numerically evaluated the superradiance phase-matching integral [11] showed that the beam curvature alone did not resolve this disagreement. Rather, to account for this discrepancy, we suspect it is necessary to adapt our 1D treatment of superradiance to beams with small Fresnel number, i.e., with length greatly exceeding the Rayleigh range defined by the probe wavelength and the transverse width of the atom beam. We suspect that our method may be probing only short portions of the beam, the momentum width of which is enhanced by their small extent, rather than probing the beam as a whole.

Despite the imperfect match between the 1D theory and the experimental data, the most important prediction of bichromatic SPPS in a rotating system—long coherence times at $\phi > 0$—is clearly evident in this system. We thus assert that the observations retain their relevance as a probe of the phase space distribution of the atom beam. From the maximum coherence time of $\tau_c = 1.1(1)$ ms, we obtain an empirical value of $\eta = 1 - [4.9(6) \times 10^{-4}]$ for the aforementioned correlation parameter. The atom beam is thus constrained to inhabit a phase space area of $\mathcal{A} = 9(1)\hbar$, equivalent to placing a lower bound of $\mathcal{L} = (\hbar|\mathbf{q}|/m)\tau_c = 13(1)\ \mu$m [14] on the longitudinal coherence length of the propagating cloud.

The maximum coherence time observed is plausibly limited not by the lack of longitudinal coherence, but rather by the decay of the superradiant scattering rate $\Gamma(\tau)$ due to transverse phase matching. Assessing a 2D phase-matching integral with the transverse state being the noninteracting ground state of the transverse trapping potential, one finds an upper bound on the coherence time of $\approx(2\Omega k\sigma_T\cos\phi)^{-1} < 1200\ \mu$s, with $\sigma_T = \sqrt{\hbar/2m\omega_T}$ and ω_T being the transverse trap frequency. Thus, our observations should be construed as placing quantitative lower bounds on the coherence of the propagating atom beam while remaining consistent with its complete coherence.

This work was supported by DARPA (Contract No. F30602-01-2-0524), ARO, and the David and Lucile Packard Foundation. K. L. M. acknowledges support from NSF and S. G. from the Miller Institute.

*Electronic address: klmoore@berkeley.edu

[1] S. Gupta, K. Dieckmann, Z. Hadzibabic, and D. E. Pritchard, Phys. Rev. Lett. **89**, 140401 (2002).
[2] Y. Torii, Y. Suzuki, M. Kozuma, T. Sugiura, T. Kuga, L. Deng, and E. W. Hagley, Phys. Rev. A **61**, 041602(R) (2000).
[3] L. Deng, E. W. Hagley, J. Wen, M. Trippenbach, Y. Band, P. S. Julienne, J. E. Simsarian, K. Helmerson, S. L. Rolston, and W. D. Phillips, Nature (London) **398**, 218 (1999).
[4] B. Eiermann, P. Treutlein, Th. Anker, M. Albiez, M. Taglieber, K.-P. Marzlin, and M. K. Oberthaler, Phys. Rev. Lett. **91**, 060402 (2003).
[5] B. Eiermann, Th. Anker, M. Albiez, M. Taglieber, P. Treutlein, K.-P. Marzlin, and M. K. Oberthaler, Phys. Rev. Lett. **92**, 230401 (2004).
[6] A. E. Leanhardt, A. P. Chikkatur, D. Kielpinski, Y. Shin, T. L. Gustavson, W. Ketterle, and D. E. Pritchard, Phys. Rev. Lett. **89**, 040401 (2002).
[7] E. Wigner, Phys. Rev. **40**, 749 (1932).
[8] D. Leibfried, D. M. Meekhof, B. E. King, C. Monroe, W. M. Itano, and D. J. Wineland, Phys. Rev. Lett. **77**, 4281 (1996).
[9] C. Kurtsiefer, T. Pfau, and J. Mlynek, Nature (London) **386**, 150 (1997).
[10] S. Gupta, K. W. Murch, K. L. Moore, T. P. Purdy, and D. M. Stamper-Kurn, Phys. Rev. Lett. **95**, 143201 (2005).
[11] S. Inouye, A. P. Chikkatur, D. M. Stamper-Kurn, J. Stenger, and W. Ketterle, Science **285**, 571 (1999).
[12] Y. Yoshikawa, Y. Torii, and T. Kuga, Phys. Rev. Lett. **94**, 083602 (2005).
[13] N. E. Rehler and J. E. Eberly, Phys. Rev. A **3**, 1735 (1971).
[14] B. Saubaméa, T. W. Hijmans, S. Kulin, E. Rasel, E. Peik, M. Leduc, and C. Cohen-Tannoudji, Phys. Rev. Lett. **79**, 3146 (1997).
[15] S. Inouye, R. F. Löw, S. Gupta, T. Pfau, A. Görlitz, T. L. Gustavson, D. E. Pritchard, and W. Ketterle, Phys. Rev. Lett. **85**, 4225 (2000).
[16] J.-Y. Courtois, S. Guibal, D. R. Meacher, P. Verkerk, and G. Grynberg, Phys. Rev. Lett. **77**, 40 (1996).
[17] K. W. Murch, K. L. Moore, S. Gupta, and D. M. Stamper-Kurn, Phys. Rev. Lett. **96**, 013202 (2006).
[18] K. Bongs, S. Burger, S. Dettmer, D. Hellweg, J. Arlt, W. Ertmer, and K. Sengstock, Phys. Rev. A **63**, 031602(R) (2001).
[19] L. Salasnich, A. Parola, and L. Reatto, Phys. Rev. A **65**, 043614 (2002).

Bibliography

[1] D. M. Stamper-Kurn and W. Ketterle. Spinor condensates and light scattering from Bose-Einstein condensates. In R. Kaiser, C. Westbrook, and F. David, editors, *Coherent Matter Waves*, pages 137 – 218. Springer-Verlag, New York, 2001.

[2] W. Zhang, D. L. Zhou, M.-S. Chang, M. S. Chapman, and L. You. Dynamical Instability and Domain Formation in a Spin-1 Bose-Einstein Condensate. *Phys. Rev. Lett.*, 95(18):180403, 2005.

[3] Q. Gu, K. Bongs, and K. Sengstock. Spin waves in ferromagnetically coupled spinor Bose gases. *Phys. Rev. A*, 70(6), 2004.

[4] L. E. Sadler, J. M. Higbie, S. R. Leslie, M. Vengalattore, and D. M. Stamper-Kurn. Spontaneous symmetry breaking in a quenched ferromagnetic spinor Bose condensate. *Nature*, 443:312, 2006.

[5] A. T. Black, E. Gomez, L. D. Turner, S. Jung, and P. D. Lett. Spinor Dynamics in an Antiferromagnetic Spin-1 Condensate, 13 April 2007. arXiv:cond-mat/0704.0925.

[6] S. Richard, F. Gerbier, J. H. Thywissen, M. Hugbart, P. Bouyer, and A. Aspect. Momentum Spectroscopy of 1D Phase Fluctuations in Bose-Einstein Condensates. *Phys. Rev. Lett.*, 91:010405, 2003.

[7] T. Kinoshita, T. R. Wenger, and D. S. Weiss. Observation of a one-dimensional Tonks-Girardeau gas. *Science*, 305:1125, 2004.

[8] B. L. Tolra, K. M. O'Hara, J. H. Huckans, W. D. Phillips, S. L. Rolston, and J. V.

Porto. Observation of Reduced Three-Body Recombination in a Correlated 1D Degenerate Bose Gas. *Phys. Rev. Lett.*, 92(19):190401–4, 2004.

[9] Z. Hadzibabic, P. Krüger, M. Cheneau, B. Battelier, and J. Dalibard. Berezinskii-Kosterlitz-Thouless crossover in a trapped atomic gas. *Nature*, 441:1118, 2006.

[10] A. Griesmaier, J. Werner, S. Hensler, J Stuhler, and T. Pfau. Bose-Einstein Condensation of Chromium. *Phys. Rev. Lett.*, 94:160401, 2005.

[11] S. Giovanazzi, P. Pedri, L. Santos, A. Griesmaier, M. Fattori, T. Koch, J. Stuhler, and T. Pfau. Expansion dynamics of a dipolar Bose-Einstein Condensate. *Phys. Rev. A*, 74:013621, 2006.

[12] M. Greiner, O. Mandel, T. Esslinger, T. W. Hänsch, and I. Bloch. Quantum phase transition from a superfluid to a Mott insulator in a gas of ultracold atoms. *Nature*, 415:39, 2002.

[13] M. Greiner, I. Bloch, O. Mandel, T. W. Hänsch, and T. Esslinger. Exploring Phase Coherence in a 2D Lattice of Bose-Einstein Condensates. *Phys. Rev. Lett.*, 87:160405, 2001.

[14] S. Gupta, K. Dieckmann, Z. Hadzibabic, and D. E. Pritchard. Contrast interferometry using Bose-Einstein condensates to measure h/m and alpha. *Phys. Rev. Lett.*, 89:140401, 2002.

[15] B. DeMarco and D. S. Jin. Onset of Fermi degeneracy in a trapped atomic gas. *Science*, 285:1703, 1999.

[16] C. A. Regal, M. Greiner, and D. S. Jin. Observation of Resonance Condensation of Fermionic Atom Pairs. *Phys. Rev. Lett.*, 92:040403, 2004.

[17] M. W. Zwierlein, C. A. Stan, C. H. Schunck, S. M. F. Raupach, A. J. Kerman, and W. Ketterle. Condensation of Pairs of Fermionic Atoms near a Feshbach Resonance. *Phys. Rev. Lett.*, 92:120403, 2004.

[18] M. W. Zwierlein, J. R. Abo-Shaeer, A. Schirotzek, C. H. Schunck, and W. Ketterle. Vortices and superfluidity in a strongly interacting Fermi gas. *Nature*, 435(7045):1047–1051, 2005.

[19] M. Vengalattore, J. M. Higbie, S. R. Leslie, J. Guzman, L. E. Sadler, and D. M. Stamper-Kurn. High-resolution magnetometry with a spinor Bose-Einstein condensate. *Phys. Rev. Lett.*, 98:200801, 2007.

[20] C. J. Pethick and H. Smith. *Bose-Einstein Condensation in Dilute Gases*. Cambridge University Press, Cambridge, United Kingdom, 2002.

[21] D. M. Stamper-Kurn. *Peeking and poking at a new quantum fluid: studies of gaseous Bose-Einstein condensates in magnetic and optical traps*. Ph.d. thesis, Massachusetts Institute of Technology, 2000.

[22] E. P. Gross. *Nuovo Cimento*, 20:454, 1961.

[23] L. P. Pitaevskii. *Soviet Physics JETP*, 13:451, 1961.

[24] B. Eiermann, P. Treutlein, T. Anker, M. Albiez, M. Taglieber, K.-P. Marzlin, and M. K. Oberthaler. Dispersion Management for Atomic Matter Waves. *Phys. Rev. Lett.*, 91(6):060402, 2003.

[25] M. Albiez, R. Gati, J. Folling, S. Hunsmann, M. Cristiani, and M. K. Oberthaler. Direct Observation of Tunneling and Nonlinear Self-Trapping in a Single Bosonic Josephson Junction. *Phys. Rev. Lett.*, 95(1):010402, 2005.

[26] D. J. Heinzen. Ultracold atomic interactions. In M. Inguscio, S. Stringari, and C.E. Wieman, editors, *Bose-Einstein condensation in atomic gases*, Proceedings of the International School of Physics "Enrico Fermi," Course CXL, pages 351 – 390. IOS Press, Amsterdam, 1999.

[27] S. Inouye, M. R. Andrews, J. Stenger, H.-J. Miesner, D. M. Stamper-Kurn, and W. Ketterle. Observation of Feshbach Resonances in a Bose-Einstein Condensate. *Nature*, 392:151–154, 1998.

[28] D.-I. Choi and Q. Niu. Bose-Einstein condensates in an optical lattice. *Phys. Rev. Lett.*, 82(10):2022–5, 1999.

[29] T. P. Meyrath, F. Schreck, J. L. Hanssen, C.-S. Chuu, and M. G. Raizen. *Phys. Rev. A*, 71:041604(R), 2005.

[30] B. P. Anderson and M. A. Kasevich. Macroscopic Quantum Interference from Atomic Tunnel Arrays. *Science*, 282:1686, 1998.

[31] C. Orzel, A. K. Tuchman, M. L. Fenselau, M. Yasuda, and M. A. Kasevich. Squeezed States in a Bose-Einstein Condensate. *Science*, 291:2386, 2001.

[32] L. Mandel and E. Wolf. *Optical Coherence and Quantum Optics*. Cambridge University Press, Cambridge, United Kingdom, 1997.

[33] G. Nogues, A. Rauschenbeutel, S. Osnaghi, N. Brune, J. M. Raimond, and S. Haroche. Seeing a single photon without destroying it. *Nature*, 400:239, 1999.

[34] J. Vuckovic and Y Yamamoto. Photonic-crystals microcavities for cavity quantum electrodynamics with a single quantum dot. *Appl. Phys. Lett.*, 82:2374, 2003.

[35] A. Blais, H. R.-S. Huang, A. Wallraff, S. M. Girvin, and R. J. Schoelkopf. Cavity quantum electrodynamics for superconducting electrical circuits: an architecture for quantum computation. *Phys. Rev. A*, 69:62320, 2004.

[36] A. Wallraff, D. I. Schuster, A. Blais, L. Frunzio, R.-S. Huang, J. Majer, S. Kumar, S. M. Girvin, and R. J. Schoelkopf. Strong coupling of a single photon to a superconducting qubit using circuit quantum electrodynamics. *Nature*, 431:162, 2004.

[37] J. M. Raimond, M. Brune, and S. Haroche. Colloquium: Manipulating quantum entanglement with atoms and photons in a cavity. *Rev. Mod. Phys.*, 73(3):565, 2001.

[38] C. J. Hood, M. S. Chapman, T. W. Lynn, and H. J. Kimble. Real-time cavity QED with single atoms. *Phys. Rev. Lett.*, 80(19):4157, 1998.

[39] J. Ye, D. W. Vernooy, and H. J. Kimble. Trapping of single atoms in cavity QED. *Phys. Rev. Lett.*, 83:4987, 1999.

[40] C. J. Hood, T. W. Lynn, A. C. Doherty, A. S. Parkins, and H. J. Kimble. The atom-cavity microscope: single atoms bound in orbit by single photons. *Science*, 287:1447, 2000.

[41] J. McKeever, J. R. Buck, A. D. Boozer, A. Kuzmich, H.-C. Nagerl, D. M. Stamper-Kurn, and H. J. Kimble. State-insensitive cooling and trapping of single atoms in an optical cavity. *Phys. Rev. Lett.*, 90:133602, 2003.

[42] J. McKeever, A. Boca, A. D. Boozer, J. R. Buck, and H. J. Kimble. Experimental realization of a one-atom laser in the regime of strong coupling. *Nature*, 425:268, 2003.

[43] A. Boca, R. Miller, K. M. Birnbaum, A. D. Boozer, J. McKeever, and H. J. Kimble. Observation of the Vacuum Rabi Spectrum for One Trapped Atom. *Phys. Rev. Lett.*, 93:233603, 2004.

[44] P. W. H. Pinkse, T. Fischer, P. Maunz, and G. Rempe. Trapping an atom with single photons. *Nature*, 404:365, 2000.

[45] M. Hennrich, T. Legero, A. Kuhn, and G. Rempe. Vacuum-stimulated Raman scattering based on adiabatic passage in a high-finesse optical cavity. *Phys. Rev. Lett.*, 85:4872, 2000.

[46] A. B. Mundt, A. Kreuter, C. Becher, D. Liebried, J. Eschner, F. Schmidt-Kaler, and R. Blatt. Coupling a single atomic quantum bit to a high finesse optical cavity. *Phys. Rev. Lett.*, 89:103001, 2002.

[47] G. R. Guthohrlein, M. Keller, K. Hayasaka, W. Lange, and H. Walther. A single ion as a nanoscopic probe of an optical field. *Nature*, 414:49, 2002.

[48] A. B. Mundt, A. Kreuter, C. Russo, C. B. C, D. Leibfried, J. Eschner, F. S.-K. F, and R. Blatt. Coherent coupling of a single Ca-40^+ ion to a high-finesse optical cavity. *Applied Physics B - Lasers*, 76(2):117, 2003.

[49] J. A. Sauer, K. M. Fortier, M. S. Chang, C. D. Hamley, and M. S. Chapman. Cavity QED with optically transported atoms. *Phys. Rev. A*, 69:51804, 2004.

[50] A. Ottl, S. Ritter, M. Kohl, and T. Esslinger. Correlations and Counting Statistics of an Atom Laser. *Phys. Rev. Lett.*, 95(9):090404–4, 2005.

[51] A. Kuhn, M. Hennrich, and G. Rempe. Deterministic single-photon source for distributed quantum networking. *Phys. Rev. Lett.*, 89:067901, 2002.

[52] S. Gupta, K. W. Murch, K. L. Moore, T. P. Purdy, and D. M. Stamper-Kurn. Bose-Einstein Condensation in a Circular Waveguide. *Phys. Rev. Lett.*, 95(14):143201, 2005.

[53] K. W. Murch, K. L. Moore, S. Gupta, and D. M. Stamper-Kurn. Dispersion Management Using Betatron Resonances in an Ultracold-Atom Storage Ring. *Phys. Rev. Lett.*, 96(1):013202, 2006.

[54] K. L. Moore, T. P. Purdy, K. W. Murch, K. R. Brown, K. Dani, S. Gupta, and D. M. Stamper-Kurn. Bose-Einstein condensation in a mm-scale Ioffe-Pritchard trap. *Applied Physics B: Lasers and Optics*, pages DOI: 10.1007/s00340–005–2101–1, 2006.

[55] K. L. Moore, S. Gupta, K. W. Murch, and D. M. Stamper-Kurn. Probing the quantum state of a guided atom laser pulse. *Phys. Rev. Lett.*, 97:180401, 2006.

[56] A. K. Tuchman, R. Long, G. Vrijsen, J. Boudet, J. Lee, and M. A. Kasevich. Normal-mode splitting with large collective cooperativity. *Phys. Rev. A*, 74:053821, 2006.

[57] H. J. Metcalf and P. van der Straten. *Laser Cooling and Trapping*. Springer-Verlag, New York, 1999.

[58] A. Chikkatur. *Colliding and Moving Bose-Einstein Condensates: Studies of superfluidity and optical tweezers for condensate transport*. Ph.d. thesis, Massachusetts Institute of Technology, 2002.

[59] D. E. Pritchard. Trapping and Cooling Neutral Atoms. In D.C. Lorents, W.E. Meyerhof, and J.R. Peterson, editors, *Electronic and atomic collisions : invited papers*

of the XIV International Conference on the Physics of Electronic and Atomic Collisions, Palo Alto, California, 24-30 July, 1985, pages 593–604. Elsevier, New York, 1986.

[60] N. R. Newbury, C. J. Myatt, and C. E. Wieman. s-wave elastic collisions between cold ground-state 87Rb atoms. *Phys. Rev. A*, 51:R2680, 1995.

[61] K. B. MacAdam, A. Steinbach, and C. Wieman. A narrow-band tunable diode laser system with grating feedback, and a saturated absorption spectrometer for Cs and Rb. *Am. J. Phys.*, 60:12, 1992.

[62] W. Demtröder. *Laser Spectroscopy - Basic Concepts and Instrumentation*. Springer, New York, 2002.

[63] J. M. Higbie. *First Steps toward Precision Measurements using Multicomponent Bose-Einstein Condensates of Rb-87*. Ph.d. thesis, University of California, Berkeley, 2005.

[64] H. J. Lewandowski. *Coherences and correlations in an ultracold Bose gas*. Ph.d. thesis, University of Colorado, Boulder, 2002.

[65] K. L. Moore, T. P. Purdy, K. W. Murch, S. Leslie, S. Gupta, and D. M. Stamper-Kurn. Collimated, single-pass atom source from a pulsed alkali metal dispenser for laser-cooling experiments. *Review of Scientific Instruments*, 76:023106, 2005.

[66] L. E. Sadler. *Dynamics of a Spin 1 Ferromagnetic Condensate*. Ph.d. thesis, University of California, Berkeley, 2006.

[67] W. D. Phillips, J. V. Prodan, and H. J. Metcalf. Zeeman slowing. *J. Opt. Sci. Am. B*, 2:1751, 1985.

[68] T. E. Barrett, S. W. Dapore-Schwartz, M. D. Ray, and G. P. Lafyatis. Inverted Zeeman slower. *Phys. Rev. Lett.*, 67:3483, 1991.

[69] W. Ketterle, D. S. Durfee, and D. M. Stamper-Kurn. Making, probing and understanding Bose-Einstein condensates. In M. Inguscio, S. Stringari, and C.E. Wieman,

editors, *Bose-Einstein condensation in atomic gases*, Proceedings of the International School of Physics "Enrico Fermi," Course CXL, pages 67–176. IOS Press, Amsterdam, 1999.

[70] S. Chu, L. Hollberg, J. E. Bjorkholm, A. Cable, and A. Ashkin. Three-Dimensional Viscous Confinement and Cooling of Atoms by Resonance Radiation Pressure. *Phys. Rev. Lett.*, 55:48, 1985.

[71] M. Greiner, I. Bloch, T. W. Hänsch, and T. Esslinger. Magnetic transport of trapped cold atoms over a large distance. *Phys. Rev. A*, 63:031401, 2001.

[72] H. Mabuchi and A. C. Doherty. Cavity quantum electrodynamics: coherence in context. *Science*, 298:1372, 2002.

[73] Research Electro-Optics, Inc., 5505 Airport Blvd., Boulder, CO, 80301.

[74] Kimble H.J. Ye J. Hood, C. J. Characterization of high-finesse mirrors: Loss, phase shifts, and mode structure in an optical cavity. *Phys. Rev. A*, 64:033804, 2001.

[75] R. Folman, P. Krüger, D. Cassettari, B. Hessmo, T. Maier, and J. Schmiedmayer. Controlling Cold Atoms using Nanofabricated Surfaces: Atom Chips. *Phys. Rev. Lett.*, 84:4749, 2000.

[76] W. Hänsel, P. Hommelhoff, T. W. Hänsch, and J. Reichel. Bose-Einstein condensation on a microelectronic chip. *Nature*, 413:498, 2001.

[77] H. Ott, J. Fortagh, G. Schlotterbeck, A. Grossmann, and C. Zimmermann. Bose-Einstein Condensation in a Surface Microtrap. *Phys. Rev. Lett.*, 87:230401, 2001.

[78] D. R. Lide and ed. *CRC Handbook of Chemistry and Physics, 87th edition.* CRC Press, 2007.

[79] J. T. Watt and J. D. Plummer. Effect of interconnection delay on liquid nitrogen temperature CMOS circuit performance. *IEEE - Proceedings of the International Electronic Devices Meeting*, 87:393–396, 1987.

[80] J. Arlt, O. Marago, E. Hodby, S. A. Hopkins, G. Hechenblaikner, S. Webster, and C. J. Foot. Bose-Einstein condensation in a rotating anisotropic TOP trap. *Journal of Physics B-Atomic Molecular and Optical Physics*, 32(24):5861–5869, 1999.

[81] W. Ketterle and N. J. van Druten. Evaporative cooling of trapped atoms. In B. Bederson and H. Walther, editors, *Advances in Atomic, Molecular, and Optical Physics*, volume 37, pages 181 – 236. Academic Press, San Diego, 1996.

[82] P. W. H. Pinkse, A. Mosk, W. Weidmuller, M. W. Reynolds, and T. W. Hijmans. One-dimensional evaporative cooling of magnetically trapped atomic hydrogen. *Phys. Rev. A*, 57(6):4747, 1998.

[83] M. H. Anderson, J. R. Ensher, M. R. Matthews, C. E. Wieman, and E. A. Cornell. Observation of Bose-Einstein Condensation in a Dilute Atomic Vapor. *Science*, 269:198, 1995.

[84] W. Petrich, M. H. Anderson, J. R. Ensher, and E. A. Cornell. A Stable, Tightly Confining Magnetic Trap for Evaporative Cooling of Neutral Atoms. *Phys. Rev. Lett.*, 74:3352, 1995.

[85] A. S. Arnold. Adaptable-radius, time-orbiting magnetic ring trap for BoseEinstein condensates. *J. Phys. B*, 37:L29, 2004.

[86] D. W. Kerst and R. Serber. Electronic Orbits in an Induction Accelerator. *Phys. Rev.*, 60:53, 1961.

[87] T. Gustavson, A. Landragin, and M. Kasevich. Rotation sensing with a dual atom-interferometer Sagnac gyroscope. *Classical and Quantum Gravity*, 17:2385, 2000.

[88] M. G. Sagnac. *C. R. Acad. Sci.*, 157:708, 1913.

[89] J. A. Sauer, M. D. Barrett, and M. S. Chapman. Storage ring for neutral atoms. *Phys. Rev. Lett.*, 87:270401, 2001.

[90] S. Wu, W. Rooijakkers, P. Striehl, and M. Prentiss. Bidirectional propagation of cold atoms in a "stadium"-shaped magnetic guide. *Phys. Rev. A*, 70:013409, 2004.

[91] A. S. Arnold, C. S. Garvie, and E. Riis. preprint, arXiv:cond-mat/0506142.

[92] A. E. Leanhardt, A. P. Chikkatur, D. Kielpinski, Y. Shin, T. L. Gustavson, W. Ketterle, and D. E. Pritchard. Propagation of Bose-Einstein Condensates in a Magnetic Waveguide. *Phys. Rev. Lett.*, 89:040401, 2002.

[93] P. J. Martin, B. G. Oldaker, A. H. Miklich, and D. E. Pritchard. Bragg scattering of atoms from a standing light wave. *Phys. Rev. Lett.*, 60(6):515, 1988.

[94] P. L. Gould, G. A. Ruff, and D. E. Pritchard. Diffraction of atoms by light: the near–resonant Kapitza–Dirac effect. *Phys. Rev. Lett.*, 56(8):827, 1986.

[95] M. Kozuma, L. Deng, E. W. Hagley, J. Wen, R. Lutwak, K. Helmerson, S. L. Rolston, and W. D. Phillips. Coherent splitting of Bose–Einstein condensed atoms with optically induced Bragg diffraction. *Phys. Rev. Lett.*, 82(5):871, 1999.

[96] J. Stenger, S. Inouye, A. P. Chikkatur, D. M. Stamper-Kurn, D. E. Pritchard, and W. Ketterle. Bragg Spectroscopy of a Bose-Einstein condensate. *Phys. Rev. Lett.*, 82:4569, 1999.

[97] M. Saba, T. A. Pasquini, C. Sanner, Y. Shin, W. Ketterle, and D. E. Pritchard. Optical measurement of the phase of a Bose-Einstein condensate. *Science*, 307:1945, 2005.

[98] Y.-J. Wang, D. Z. Anderson, V. M. Bright, E. A. Cornell, Q. Diot, T. Kishimoto, M. Prentiss, R. A. Saravanan, S. R. Segal, and S. Wu. An Atom Michelson Interferometer on a Chip Using a Bose-Einstein Condensate. *Phys. Rev. Lett.*, 94:090405, 2005.

[99] O. Garcia, B. Deissler, K. J. Hughes, J. M. Reeves, and C. A. Sackett. Preprint arXiv:cond-mat/0603772 v2.

[100] P. L. Kapitza and P. A. M. Dirac. The reflection of electrons from standing light waves. *Prof. of the Camb. Philos. Soc.*, 29:297, 1933.

[101] S. Gupta. *Experiments with Degenerate Bose and Fermi Gases*. Ph.d. thesis, Massachusetts Institute of Technology, 2003.

[102] M. Abramowitz and eds. Stegun, A. *Handbook of Mathematical Functions with Formulas, Graphs, and Mathematical Tables*. Dover, New York, 1965.

[103] S. Wu, Y.-J. Wang, Q. Diot, and M. Prentiss. Splitting matter waves using an optimized standing-wave light-pulse sequence. *Phys. Rev. A*, 71:043602, 2005.

[104] K. Bongs, S. Burger, S. Dettmer, D. Hellweg, J. Arlt, W. Ertmer, and K. Sengstock. Waveguide for Bose-Einstein condensates. *Phys. Rev. A*, 63:031602(R), 2001.

[105] L. Salasnich, A. Parola, and L. Reatto. Effective wave equations for the dynamics of cigar-shaped and disk-shaped Bose condensates. *Phys. Rev. A*, 65(4):043614, 2002.

[106] K. Huang. *Statistical Mechanics*. Wiley, New York, second edition edition, 1987.

[107] J. Binney and S. Tremaine. *Galactic Dynamics (Princeton Series in Astrophysics)*. Princeton University Press, New Jersey, 1988.

[108] S. Turner, editor. *CAS - CERN Acclerator School: 5th General Accelerator Physics Course*. CERN, Geneva, Switzerland, 1994.

[109] S. Gupta, Z. Hadzibabic, J. R. Anglim, and W. Ketterle. Collisions in zero temperature Fermi gases. *Phys. Rev. Lett.*, 92:100401, 2004.

[110] E. Wigner. On the Quantum Correction For Thermodynamic Equilibrium. *Phys. Rev.*, 40(5):749, 1932.

[111] M. Hillery, R. F. O'Connell, M. O. Scully, and E. P. Wigner. Distribution Functions in Physics: Fundamentals. *Physics Reports (Review Section of Physics Letters)*, 106:121–167, 1984.

[112] H. Wallis, A. Röhrl, M. Naraschewski, and A. Schenzle. Phase space dynamics of Bose condensates: Interference vs. Interaction. *Phys. Rev. A*, 55:2109, 1997.

[113] N. Wheeler. Phase Space and Quantum Mechanics. Reed College, unpublished lecture notes.

[114] Y. S. Kim and M. E. Noz. *Phase Space Picture of Quantum Mechanics: Group Theoretical Approach*. World Scientific Publishing Company, New Jersey, 1991.

[115] R. N. Bracewell. Numerical Transforms. *Science*, 248:697–704, 1990.

[116] R. H. Dicke. Coherence in spontaneous radiation processes. *Phys. Rev.*, 93(1):99, 1954.

[117] S. Inouye, A. P. Chikkatur, D. M. Stamper-Kurn, J. Stenger, and W. Ketterle. Superradiant Rayleigh scattering from a Bose–Einstein condensate. *Science*, 285(July 23):571, 1999.

[118] S. Inouye, R. F. Löw, S. Gupta, T. Pfau, A. Görlitz, T. L. Gustavson, D. E. Pritchard, and W. Ketterle. Amplification of light and atoms in a Bose-Einstein condensate. *Phys. Rev. Lett.*, 85:4225, 2000.

[119] M. G. Moore and P. Meystre. Theory of Superradiant Scattering of Laser Light from Bose-Einstein Condensates. *Phys. Rev. Lett.*, 83:5202, 1999.

[120] W. Ketterle and S. Inouye. Does Matter Wave Amplification Work for Fermions? *Phys. Rev. Lett.*, 86(19):4203–4206, 2001.

[121] Y. Yoshikawa, Y. Torii, and T. Kuga. Superradiant Light Scattering from Thermal Atomic Vapors. *Phys. Rev. Lett.*, 94:083602, 2005.

[122] N. E. Rehler and J. H. Eberly. Superradiance. *Phys. Rev. A*, 3(5):1735, 1971.

[123] B. Saubamea, T. W. Hijmans, S. Kulin, E. Rasel, E. Peik, M. Leduc, and C. Cohen-Tannoudji. Direct measurement of the spatial correlation function of ultracold atoms. *Phys. Rev. Lett.*, 79(17):3146, 1997.

[124] R. Loudon. *The Quantum Theory of Light.* Clarendon, Oxford, 2nd edition edition, 1983.

[125] E. Jaynes and F. W. Cummings. *Proc. IEEE*, 51:89, 1963.

[126] R. J. Brecha, P. R. Rice, and M. Xiao. N two-level atoms in a driven optical cavity: Quantum dynamics of forward photon scattering for weak incident fields. *Phys. Rev. A*, 59:2392, 1999.

[127] M. Tavis and F. W. Cummings. Exact solution for an N-molecule-radiation-field Hamiltonian. *Phys. Rev.*, 170:379, 1968.

[128] D. W. Vernooy and H. J. Kimble. Well-dressed states for wave-packet dynamics in cavity QED. *Phys. Rev. A*, 56:4287, 1997.

[129] S. Leslie, N. Shenvi, K. R. Brown, D. M. Stamper-Kurn, and K. B. Whaley. Transmission Spectrum of an Optical Cavity Containing N Atoms. *Phys. Rev. A*, 69:043805, 2004.

[130] M. D. Lukin, S. F. Yelin, and M. Fleischhauer. Entanglement of Atomic Ensembles by Trapping Correlated Photon States. *Phys. Rev. Lett.*, Volume 84(Number 18):4232–4235, 2000.

[131] M. D. Lukin. Colloquium: Trapping and manipulating photon states in atomic ensembles. *Rev. Mod. Phys.*, 75:457, 2003.

[132] A. Kuzmich, W. P. Bowen, A. D. Boozer, A. Boca, C. W. Chou, L.-M. Duan, and H. J. Kimble. Generation of nonclassical photon pairs for scalable quantum communication with atomic ensembles. *Nature*, 423:731, 2003.

[133] H. W. Chan, A. T. Black, and V. Vuletić. Observation of Collective-Emission-Induced Cooling of Atoms in an Optical Cavity. *Phys. Rev. Lett.*, 90:063003, 2003.

[134] C. W. Chou, S. V. Polyakov, A. Kuzmich, and H. J. Kimble. Single-Photon Generation from Stored Excitation in an Atomic Ensemble. *Phys. Rev. Lett.*, 92:213601, 2004.

[135] D. A. Steck, 14 October 2003. Rubidium-87 D Line Data (unpublished, http://steck.us/alkalidata/).

[136] Puppe T. Schuster I. Syassen N. Pinkse P.W. H. Rempe G. Maunz, P. Normal-Mode Spectroscopy of a Single-Bound-Atom–Cavity System. *Phys. Rev. Lett.*, 94:033002–1 – 033002–4, 2005.

[137] J. McKeever, J. Buck, A. Boozer, and H. Kimble. Determination of the Number of Atoms Trapped in an Optical Cavity. *Phys. Rev. Lett.*, 93:143601, 2004.

[138] P. Berman, editor. *Cavity quantum electrodynamics*. Academic Press, Boston, 1994.

[139] E. Hecht. *Optics*. Addison-Wesley, Reading, 2nd edition edition, 1989.

[140] L. M. Duan, M. D. Lukin, J. I. Cirac, and P. Zoller. Long-distance quantum communication with atomic ensembles and linear optics. *Nature*, 414:413, 2001.

[141] A. S. Sorensen and K. Molmer. Entangling atoms in bad cavities. *Phys. Rev. A*, 66:022314, 2002.

[142] Y. Shimizu, N. Shiokawa, N. Yamamoto, M. Kozuma, T. Kuga, L. Deng, and E. W. Hagley. Control of Light Pulse Propagation with Only a Few Cold Atoms in a High-Finesse Microcavity. *Phys. Rev. Lett.*, 89:233001, 2002.

[143] A. I. Oliva, V. Sosa, R. de Coss, R. Sosa, N. Lopez-Salazar, and J. L. Pena. *Rev. Sci. Instruments*, 63:3326, 1992.

[144] K. W. Murch, K. L. Moore, S. Gupta, and D. M. Stamper-Kurn. in preparation.

[145] R. Grimm, M. Weidemüller, and Y. Ovchinnikov. Optical Dipole Traps for Neutral Atoms. Technical report, 1999.

[146] J. D. Miller, R. A. Cline, and D. J. Heinzen. Far-off-resonance optical trapping of atoms. *Phys. Rev. A*, 47:R4567, 1993.

[147] D. M. Stamper-Kurn, M. R. Andrews, A. P. Chikkatur, S. Inouye, H.-J. Miesner, J. Stenger, and W. Ketterle. Optical Confinement of a Bose-Einstein Condensate. *Phys. Rev. Lett.*, 80:2072–2075, 1998.

[148] S. Gupta, K. W. Murch, K. L. Moore, and D. M. Stamper-Kurn. in preparation.

[149] C.-S. Chuu, F. Schreck, T. P. Meyrath, J. L. Hanssen, G. N. Price, and M. G. Raizen. Direct Observation of Sub-Poissonian Number Statistics in a Degenerate Bose Gas. *Phys. Rev. Lett.*, 95:260403, 2005.

[150] J. Geremia, J. K. Stockton, and H. Mabuchi. Real-Time Quantum Feedback Control of Atomic Spin-Squeezing. *Science*, 204:270, 2004.